UNIVERSITY OF OKLAHOMA

GRADUATE COLLEGE

USING GROUND-BASED FIXED AND MOBILE WEATHER RADARS AND NUMERICAL MODELING TO EVALUATE HURRICANE STRUCTURE AND DYNAMICS AT LANDFALL

A DISSERTATION

SUBMITTED TO THE GRADUATE FACULTY

in partial fulfillment of the requirements for the

Degree of

DOCTOR OF PHILOSOPHY

By

AUSTIN ADDISON ALFORD
Norman, Oklahoma
2021

USING GROUND-BASED FIXED AND MOBILE WEATHER RADARS AND NUMERICAL MODELING TO EVALUATE HURRICANE STRUCTURE AND DYNAMICS AT LANDFALL

A DISSERTATION APPROVED FOR THE
SCHOOL OF METEOROLOGY

BY THE COMMITTEE CONSISTING OF

Dr. Michael Biggerstaff, Chair

Dr. Xugaung Wang

Dr. Cameron Homeyer

Dr. Naoko Sakaeda

Dr. David Jorgensen

Dr. Nikola Petrov

Table of Contents

Acknowledgements

My time at the University of Oklahoma has been the result of those that have supported my personal and academic interests. First and foremost, I must thank my incredibly loving, supporting, and talented parents, David and Cindy Alford, for inspiring my interests in the physical world. They have forever made my interests and aspirations their own, selflessly seeking to support me at my lowest and challenging me at my highest. This dissertation is dedicated to them without whom none of my journey would be possible.

Second, my time at the University has led me to meet my wife, partner, and equal, (soon-to-be Dr.) Rachel Miller. My journey has been made brighter in finding someone who shares in my passion for science, dedication to the pursuit of knowledge, and aspiration to support those in positions less than we have known to achieve their dreams.

Perhaps most influential to this dissertation, I thank Dr. Michael Biggerstaff for his guidance, kindness, and support from the moment he hired me as an undergraduate at this institution. An unwavering source of wisdom, Mike has given me the tools to succeed, challenged me to grow as a scientist, and afforded more opportunities for personal and professional growth than can be counted.

I also thank Mr. Gordon Carrie, Dr. Daniel Betten, and the other past and present group members in the SMART Radar program for their mutual dedication to the weather enterprise and being the highlight of my career at OU. My journey would also not be complete without the foundational support my three of my long-time mentors and confidants, Ms. Sarah Belle Day, Mr. Harry Ozier, and Mr. Samuel Williamson. Their influence upon my career trajectory has afforded my appreciation for learning and the pursuit of knowledge.

I also cannot thank my friends and family enough for their unwavering support, love, and kindness. In particular, I want to thank Shelby Bailey, Madeline Hensley, Dr. Matt Flournoy, Dr. Kenzie Krocak, Dr. Andrew Wade, Heather Wade, Andrew Rickels, Kristen-Perez Rickels, Dr. Elizabeth DiGangi, Dr. Stacey Hitchcock, Dr. Branden Katona, Mrs. Sydney Katona, and Michael Smith for their valued friendships that will forever remain the highlight of my life.

Finally, I would like to acknowledge the support of my Doctoral Committee, Drs. Xuguang Wang, Cameron Homeyer, Naoko Sakaeda, David Jorgensen, and Nikola Petrov, for their influence and guidance in my academic endeavors as well as the faculty and staff of the School of Meteorology and the College of Atmospheric and Geographic Sciences. I also thank Drs. Jun Zhang, Frank Marks, Shirley Murillo, Peter Dodge, Rob Rogers, and Paul Reasor of the Hurricane Research Division (HRD) for their supporting collaboration between the University and HRD, for their helpful discussions that improved this research, and for their contributions to this dissertation. Dr. Xu Lu and Dr. Xuguang Wang were also instrumental in contributing the Hurricane WRF run that facilitated the conclusion of this dissertation, for which I am deeply indebted. I also am grateful to Dr. David Nolan of the University of Miami for his insight into fluid dynamics and helping to improve this work. Finally, this dissertation is supported thanks in part to the gracious backing of the NASA Earth and Space Science Fellowship, the Nancy L. Mergler Dissertation Completion Fellowship, the National Institute for Standards and Technology, and the National Science Foundation.

Abstract

Hurricane observations during landfall in the United States have received relatively little attention in the research community compared to hurricanes observed over the open ocean. Aircraft-based observations using in situ and remotely sensed data have elucidated much about the structure and evolution of hurricanes. However, gathering high temporal (3-5 minutes) and high spatial (500-1000 m) resolution observations over contiguous spatial domains (e.g., 10,000 km^2) is not possible with aircraft due to instrumentation limitations, operational missions, and required flight paths in hurricanes. Using ground-based fixed and mobile Doppler weather radars afford continuous observations of processes that not only affect landfall, but also offer comparison to aircraft observations of processes that occur over the open ocean. In addition, hurricane landfalls have generally been under sampled due to aircraft observations being relegated to the open ocean for crew and aircraft safety.

The Shared Mobile Atmospheric Research and Teaching (SMART) Radars (SRs) are a pair of mobile Doppler, dual-polarization radars operated by the University of Oklahoma. Having sampled 14 landfalling tropical storms and hurricanes, datasets collected by the SRs likely provide key insight into hurricane dynamics and is the primary data source of this work. SR data, along with other fixed ground-based radars, in situ platforms, and satellite remote sensing, are combined to provide a comprehensive view of hurricane structure using dual-Doppler analysis, single Doppler observations, microphysical retrievals, and surface station network wind mapping. The primary datasets for this analysis includes Hurricanes Isabel (2003), Irene (2011), Matthew (2016), and Harvey (2017).

This dissertation presents a detailed analysis of asymmetric dynamic processes in the form of the excitation of vortex Rossby waves from asymmetric convection in the eye in

landfalling hurricanes and their impacts on the surface winds and rainfall experienced at landfall. Specifically, the verification of vortex Rossby wave theory is addressed by examining the propagation of rainbands radially outward of the hurricane eyewall. The impact of vortex Rossby waves on the symmetrization and intensity change in hurricanes is also assessed for the first time in high temporal and spatial resolution. The microphysical structure of vortex Rossby wave-induced rainbands through remotely sensed and in situ observations is also detailed. As vortex Rossby wave-driven processes are currently not well understood, this work concludes by examining a numerical simulation of Hurricane Harvey (2017) to compare observed vortex Rossby waves to those in this simulation.

Additionally, little is known regarding the evolution of the hurricane boundary layer at landfall. In order to assess the impacts of structures in the wind field arising from asymmetric dynamics, the hurricane boundary layer response to a step-function change in aerodynamic surface roughness inland must be understood. Using aircraft observations offshore and ground-based mobile and fixed radars onshore, the hurricane boundary layer is quantitatively examined, for the first time, from over the open ocean through the coastal transition. The verification of boundary layer models, which can be used to estimate surface winds from winds observed aloft, is vital the estimation of standardized surface winds. The transfer of momentum by turbulence on a variety of spatial scales can be examined to understand the evolution of the hurricane wind field aloft and relate it to surface winds observed in situ.

Chapter 1: Background

Landfalling tropical cyclones (TCs) represent a multifaceted hazard to life and property in the United States (Rappaport 2014). Forecasts of TCs have vastly improved in terms of the track of the center of circulation in recent decades, but have unfortunately lagged in terms of the intensity over the TC lifecycle (Braun et al. 2013; Emanuel 2018). As such, there have been ongoing efforts to enhance observations of processes critical to TC intensification (e.g., Gall et al. 2013), particularly rapid intensification (c.f., Rogers et al. 2017). A meticulous focus of these experiments is using aircraft such as the National Oceanic and Atmospheric Administration (NOAA) WP-3D Orion (P-3; Aberson et al. 2006) to study convective scale [O(1 km)] and mesoscale [O(10-100 km)] processes using detailed observations from dropsondes (Hock and Franklin 1999), the Stepped Frequency Microwave Radiometer (Uhlhorn and Black 2003), and the Tail Doppler Radar (Jorgensen et al. 2017). Utilizing these unique instruments, detailed views of asymmetric and symmetric convection, boundary layer processes, shear impacts to the vortex, and moist dynamics have yielded a deep understanding into the evolution of TC intensification and numerical model improvements (Corbosiero and Molinari 2003; Rogers et al. 2012; Montgomery et al. 2014; Montgomery and Smith 2016). Aircraft-based studies represent a platform from which much of the collective knowledge of TCs is known, but disproportionately represents a dearth of studies devoted to dynamics, hazards, and modeling verification at landfall where TCs are arguably most impactful. Above all else, the motivation for this dissertation is to apply the conceptual models of TC dynamics elucidated from primarily aircraft-based studies to a detailed understanding of TC hazards at landfall. This dissertation also aims to augment the understanding of TC intensity change process that are difficult to sample in high temporal resolution over the open ocean.

At the forefront of improving TC forecasts is the ability to accurately simulate convective scale and mesoscale processes that are integral to the intensity of a TC vortex (Rogers et al. 2012). A leading topic of this work is the vortex Rossby wave (VRW) response inherent to TCs. Similar to planetary Rossby waves, VRWs arise due to the radial gradient in vorticity. On the planetary scale, Rossby waves are restored by the north-to-south gradient in planetary vorticity (Holton and Hakim 2013). In TCs, VRWs are restored by the radial gradient in local or storm-relative vorticity and are affected little by planetary motions on their timescales (<1 h).

1.1. An Overview of Montgomery and Kallenbach (1997)

VRWs are thought to arise from asymmetries in the TC flow, often near the radius of maximum wind where the gradient in vorticity is strongest. Montgomery and Kallenbach (1997; MK97) was the first study to examine VRWs in depth through a relatively simple, shallow-water, asymmetric-balance model simulating a hurricane-like vortex. Their investigation aimed to examine two main points. The first was to seek an explanation for outward propagating rainbands in TCs near the eyewall that were also observed to propagate against the mean flow (MacDonald 1968). The second was to examine the response of the vortex state as disturbances or asymmetries placed within the model were symmetrized. While the two points can be viewed as separate, this work considers the symmetrization process in a more unified framework.

Asymmetries in the model flow were the source points for VRWs, which behaved similarly in a simple model framework to observed rainband propagation characteristics. Specifically, outward propagation radially of the modeled waves viewed in a potential vorticity (PV) framework was noted in MK97. High PV being expelled from the asymmetry source was noted to be sheared by the gradient of the horizontal flow, forming trailing spiraled filaments of

enhanced PV. The filaments spiraled into their source asymmetries and exhibited upwind propagation against the vortex flow as they evolved. These trailing spirals of relatively high PV were termed VRWs due to their azimuthal upwind propagation, similar to the upwind propagation character of planetary Rossby waves. The source of the enhanced PV spiral is itself not considered a VRW, but is considered here to be an integral part of VRW evolution. Moreover, the source asymmetry is likely integral to the evolution of the average vortex state, as the VRW response is the result of the symmetrization of the asymmetry.

While the wave itself propagates outward, a positive flux of momentum or PV is anticipated. MK97 discussed that if the wave can persist for sufficiently long periods, a local increase in momentum outside the initial asymmetry source is expected and can result in a stronger monopole vortex. The maximum velocity change was noted to occur just outside of the radius of maximum winds where the initial asymmetry was located due to the outward propagation of the modeled VRWs. However, the change across the original radius of maximum wind was indeed positive, implying VRWs may act to dynamically enhance the average vortex state. It is important to note that the simulations examined asymmetries *at the radius of maximum wind* in an idealized vortex, while asymmetries may exist at a variety of radii *near the radius of maximum wind* (e.g., across the eyewall of a real TC). It is also important to note that the model framework of MK97 was one in which PV was conserved, implying that non-conservative processes in a real TC must also be accounted for when considering VRW applicability to observations.

1.2. A Brief Overview of Vortex Rossby Wave Literature

After MK97, a majority of studies dealing with VRWs have focused on using idealized and full-physics numerical simulations to understand VRW impacts on spiral rainband formation and to understand wave-mean flow interactions through VRW processes, but with little attention paid to observations (Möller and Montgomery 2000; Reasor et al. 2000; Chen and Yau 2001; Wang 2002a,b; Chen and Yau 2003; McWilliams et al. 2003; Franklin et al. 2006; Braun et al. 2006; Corbosiero et al. 2006; Judt and Chen 2010; Wei et al. 2010; Hall et al. 2013; Menelaou and Yau 2014; Cotto et al. 2015; Gao and Zhu 2016; Guimond et al. 2020). Common to most studies is the motivation to explain modeled and observed rainbands in the inner core (defined here as the annulus bounding the radius of maximum wind and a radial distance three times that of the radius of maximum wind; Houze 2010). In observations and full-physics modeling, trailing spiraled rainbands outside of the eyewall are often located along regions of trailing spirals of enhanced PV. In studies such as (Wang 2002a,b), the maxima in PV and radar reflectivity were often separated by one-quarter of a radial wavelength, suggesting that the rainbands themselves were not solely responsible for generating PV through diabatic heating. Observations support this to a degree in studies of inner core rainbands from airborne platforms (Reasor et al. 2000; Guimond et al. 2020) such that vertical vorticity maxima were observed in the vicinity of reflectivity maxima rather than being co-located.

Attempts in the aforementioned studies to compare the azimuthal translation of rainbands to the dispersion relation in MK97 have been routinely made. In general, modeled rainbands were shown to propagate against the mean flow at speeds consistent with MK97. This has also been supported in the few observational studies that exist (Reasor et al. 2000; Corbosiero et al. 2006; Guimond et al. 2020), which have used limited observations in space and/or time to

validate the phase speeds of rainbands against MK97. The evidence presented using models and observations support that the simple, barotropic dispersion relation in MK97 is consistent with rainband propagation. However, given the limitations of the observational studies, there is a need to utilize more extensive observations in space and time to convincingly compare MK97 to observed rainband evolution. Moreover, observations of rainbands coupled to VRWs have never been observed from their formation to dissipation at high spatiotemporal resolution. Thus, it is difficult to validate the model representation of VRW processes sufficiently, including the kinematic structure of rainbands, the evolution of the PV field in a non-conservative environment, and the impacts VRW processes have on the symmetric vortex.

1.3. Wind Hazards Associated with Asymmetric Dynamics

Given that VRWs arise from asymmetries in the circular hurricane flow, it is also important to explore the potential impacts to the instantaneous wind field resulting from the asymmetries themselves. Additionally, the expected intensification of the TC vortex through VRW symmetrization in MK97 is imperative to assess via observations. One such asymmetry commonly observed in TCs is the mesovortex (Black et al. 1999; Wingo and Knupp 2016), which can be defined as a region of enhanced vorticity that is located radially inward of the radius of maximum wind. Often, these vorticity maxima are closed circulations and can be viewed through satellite observations. However, for the purpose of this work, the circulation need not be closed. Rather, this work will examine asymmetries in the hurricane flow that are defined by closed or open vortices propagating along the inner edge of the eyewall.

In Hurricane Harvey specifically, multiple mesovortices were noted at landfall and often represented regions of enhanced surface winds (Fernandez-Caban et al. 2019) as they passed a

given location. In fact, a 0.1 s gust exceeding 190 mph (~85 m s^{-1}) was observed by a University of Florida sonic anemometer during the passage of a mesovortex over the tower site. Similar extreme wind gusts have been observed in other hurricane mesovortices (Black et al. 1999). Often, these mesovortices are associated with reflectivity maxima and may be tied to regions of enhanced convection and stronger updrafts (Stern et al. 2016; Aberson et al. 2017). Besides the instantaneous impact of mesovortices upon the wind field, Aberson et al. (2017) specifically discussed the mixing of high potential temperature air from the eye toward the eyewall via a mesovortex encountered by the P-3. They concluded the exchange of high potential temperature air from the eye to the eyewall may be integral to intensification. However, the mixing process from radially outward of the eyewall toward the eye was not discussed. It is unclear if mesovortices just inside the radius of maximum wind are responsible for initiation VRWs or intensity change in general. Moreover, this process has not been studied at landfall, where instantaneous impacts of mesovortices are most impactful to communities. It should be noted that the mesovortices discussed herein are on the scale of 5 km, rather than the sub-kilometer vortices or misovortices referenced by works such as (Wurman and Kosiba 2018).

1.4. The Landfall Hurricane Boundary Layer

A critical aspect to understanding VRW process impacts, both instantaneous and time-averaged, is to examine the evolution of the wind field at landfall as the primary circulation becomes perturbed by interactions with land. Forecasts of TC intensity and the representation of primary processes leading to intensification and rapid intensification, including by VRWs, is also important to understand over the ocean. In particular, the evolution of the TC up to landfall and the representation of the wind field in forecasts during and after landfall is a function of not only

correct intensity forecasts as the TC evolves over the open ocean but also the parameterization of the hurricane boundary layer over land.

In a detailed study of the hurricane boundary layer at the land-ocean interface, Hirth et al. (2012) documented that onshore flow in Hurricane Frances (2004) responded to rapid increase in aerodynamic surface roughness from ocean to land in a manner consistent with an internal boundary layer response (Garratt 1990). Unfortunately, studies such as Hirth et al. (2012) did not examine the boundary layer structure over land to that over the ocean observed by the P-3, for example. Over the ocean, the hurricane boundary layer is often considered to follow a standard logarithmic profile below the height of the maximum wind (Powell et al. 2003; Smith and Montgomery 2014; Zhang et al. 2011). Studies devoted to comparing the hurricane boundary layer over land are often performed by retrieving the boundary layer wind profile through velocity-azimuth display techniques (Browning and Wexler 1968) and compared to the known composite structure of the over-ocean hurricane boundary layer (e.g., Giammanco et al. 2012). To date, no study has examined the hurricane boundary layer simultaneously over the land surface and compared to that observed over the ocean.

1.5. Research Questions

This dissertation presents a detailed analysis of hurricane dynamics at landfall related to VRW processes and their associated wind hazards. The intent of this work is to not only assess the impact of asymmetric dynamics processes at landfall, but also to expand the existing knowledge of VRW processes that take place over the open ocean. As such, five primary questions serve as the motivation for this work:

1. Are asymmetries (e.g., mesovortices) in the hurricane flow impactful to the near-surface, instantaneous wind field?
2. Are mesovortices integral to multi-scale interactions though VRW processes and on what time scales?
3. Are VRWs responsible for driving the formation of inner core rainbands at landfall and over the open ocean?
4. Are observed VRW processes replicated in state-of-the-art hurricane simulations?
5. How does the land surface affect the structure of the hurricane boundary layer and the mesoscale evolution of the near-surface wind field?

These questions are presented in broad context and will be expanded in greater detail in later sections.

The University of Oklahoma Shared Mobile Atmospheric Research and Teaching Radars (SRs; Biggerstaff et al. 2005) have collected data in no less than 14 landfalling hurricanes to date, which affords the ability to utilize multiple studies to address the above hypotheses. Datasets in Hurricanes Isabel (2003), Matthew (2016), and Harvey (2017) are sourced to explore the detailed evolution of VRWs and their parent asymmetries where possible. SR data are combined with coastal Weather Surveillance Radars – 1988 Doppler (WSR-88Ds; Crum and Alberty 1993) to retrieve three-dimensional flow in the above landfalling TCs, which serves as the primary datasets for this work. The data will also be compared to observations taken offshore by the National Aeronautics and Space Administration (NASA) Global Hawk (Naftel 2009) equipped with the High Altitude Imaging Wind and Rain Airborne Radar (Li et al. 2008). Comparing landfall datasets to data collected in TCs over the open ocean will help elucidate the differences and similarities of VRW processes observed at landfall to VRW processes over the

open ocean. Finally, observational datasets are compared to a novel simulation using the Hurricane Weather Research and Forecasting model (Gopalakrishnan et al. 2011) to examine the model representation of VRWs with Hurricane Harvey serving as a case study. This work will also utilize three-dimensional wind retrievals in Hurricane Irene (2011) to perform a high resolution (250 m) study of the hurricane boundary layer compared to the dropwindsonde-observed boundary layer offshore.

Chapter 2: Impacts of the Near-Surface Wind Field

2.1 Introduction

Landfalling tropical cyclones (TCs) can devastate coastal communities via wind and water damage (Rappaport, 2014). Storm surge and inland flooding historically have been the primary cause of TC-related deaths in the United States, while damage to built structures by extreme winds has created property losses that often exceed $10B (Huang et al., 2001; Klotzbach et al., 2018). In the past, the distribution of near-surface winds during TC landfall has been documented through surface measurements (Powell et al. 1996; Powell and Houston 1996; Krupar et al. 2016; Powell and Houston 1998) and dropsondes from aircraft (e.g., Rogers et al., 2017; Stern et al., 2016). Above the ground, psuedo-dual-Doppler and dual-Doppler wind retrievals from aircraft (Marks and Houze 1987; Houze et al. 1992; Reasor et al. 2000) and single and dual-Doppler analysis from surface-based fixed (Crum and Alberty 1993) and mobile (Wakimoto and Srivastava 2017) Doppler radars have documented the winds within TCs as well as boundary layer structure and evolution over land and coastal waters (Knupp et al. 2006; Lorsolo et al. 2008; Hirth et al. 2012; Kosiba et al. 2013).

Unlike sparse in situ surface observing platforms like the Automated Surface Observing Systems (Powell 1993), dual-Doppler radar-based wind retrievals provide nearly continuous spatial distribution of winds over mesoscale areas (c.f., Fernandez-Caban et al. 2019) while single-Doppler retrievals can discern low wavenumber components of the flow (Lee et al. 1999; Lee and Marks 2000). Although surface friction over land helps to decelerate TC airflow as the near-gradient wind balance is disrupted (Smith and Montgomery 2014), the primary vortex and meso-gamma and convective scale anomalies in the tangential and radial flow may still exhibit significant magnitudes (Black et al. 1999). Kilometer and sub-kilometer scale features can also

enhance the local wind field, magnifying the primary flow and lead to significant property damage at the surface (Powell and Houston 1996; Wurman and Kosiba 2018).

Since radars cannot measure winds near the surface for more than a few kilometers due to the Earth's curvature, relating damage at the surface to the retrieved winds aloft has generally been limited to correlating damage swaths on the ground with tracks of radar observed flow features aloft, particularly for tornadic storms (e.g., Burgess et al., 2002; Wakimoto et al., 2003). To better understand the impact of long duration wind events like TCs on built structures, quantitative estimates of the near surface winds (defined as one-minute average windspeed at 10 m altitude) are required (Sparks et al. 1994; Knight and Khalid 2015). Moreover, time series of near surface winds over a continuous, broad area can help to mitigate unnecessary litigation resulting from insured losses in areas affected by both extreme winds and floods or storm surge (Baradaranshoraka et al. 2017). Maps of the maximum near-surface wind and the time it occurred relative to water incursions would aid in targeting the most impacted areas for post-storm surveys and aid in understanding the scale of similarly caused losses.

In their study of Hurricane Rita (2005), Kosiba et al. (2013) demonstrated the utility of projecting the *radial* single-Doppler radar observed wind above 100 m to a 10-m estimated wind speed and validated the radial component projection using two in situ measurements. Attenuation of the X-band radar pulse limited the range of their analysis. To date, maps of spatially-contiguous estimated maximum near-surface winds over an area of $\sim 10^4$ km^2 using the total horizontal wind vector from dual-Doppler analyses have not been provided.

In this chapter, data from fixed and mobile Doppler radars are combined to produce wind retrievals during the landfall of Hurricane Harvey (2017). Hurricane Harvey produced extreme winds in the Rockport and Port Aransas, TX region and extensive flooding in eastern Texas and

western Louisiana (Blake and Zelinsky 2018). The radar-derived horizontal flow at 500-m altitude was projected to near the surface using a simple logarithmic profile with an aerodynamic surface roughness estimate at each grid point in the analysis. A logarithmic wind profile assumption is an appropriate method to reduce elevated wind measurements to near the surface when the measurements are at or below the altitude of the hurricane wind maxima (Franklin et al., 2003). The method used here was tested against radiosonde wind profiles and the radar estimated winds were validated against in situ measurements from a network of StickNets (Weiss and Schroeder 2008). The estimated winds agreed well with in situ observations. Additionally, several of the peak maximum surface winds coincided with paths of mesovortices that circulated around the eyewall of the hurricane. This is the first time that spatially contiguous maps covering 100 km X 100 km areas of the maximum near-surface winds during the landfall of a major hurricane have been presented.

2.2 Data and Analysis Methods

2.2.1 Radar

For this study, data from the Corpus Christi, TX National Weather Service (NWS) WSR-88D (KCRP) located at 27.7840°N, 97.5113°W was combined with the SR2 C-band mobile radar (Biggerstaff et al. 2005). SR2, located at 28.1480°N 97.4101°W, collected volumetric data between 2058 UTC on 25 August 2017 and 1630 UTC on 26 August. The locations of the instruments used in this study are shown in Figure 2.1. SR2 operated nearly continuously with the exception of two periods, 2305-2350 UTC on 25 August and 0140-0310 UTC on 26 August, during which the radar suffered antenna drive failures. The 42-km baseline between the two radars was oriented quasi-parallel to the Texas coastline. This arrangement afforded dual-

Doppler wind retrieval areas over land to the northwest of the baseline and over the immediate coastal areas and into the Gulf of Mexico southeast of the baseline. Only the southeastern area was examined for this study. While both radars are dual-polarization, only the radial velocity and radar reflectivity were used.

The velocity data were dealiased with the Python ARM Radar Toolkit (Helmus and Collis 2016) using the "region-based" method of dealiasing (see Alford et al. 2019a and Appendix 1). The data were further quality controlled subjectively using Solo3 (Oye et al. 1995). Following Betten et al. (2018), the radial velocity and reflectivity were interpolated to a Cartesian grid via a natural neighbor interpolation scheme (Sibson 1981). The analysis domain origin is located at KCRP with a horizontal and vertical grid spacing of 1.0 km. Horizontally, the analysis grid extended from 0 to 130 km in the zonal direction and -60 to 70 km in the meridional direction. Vertically, the grid started at 0.5 km and extended to 10.5 km. Dual-Doppler wind syntheses were performed approximately every five minutes using the variational retrieval method of Potvin et al. (2012).

A map of the maximum wind speed at 500 m for each grid point for two periods, one before the official landfall (about 0300 UTC on 26 August) and the other after, were constructed along with the time the maximum occurred for each grid point. The 500-m altitude was chosen to minimize the distance required to project winds to the surface while maintaining a broad region of coverage. Following Hirth et al. (2012), the aerodynamic roughness length z_0 (in m), was derived from Office for Coastal Management land cover maps (NOAA 2018) to project the 500-m winds to the near surface. Using a simple logarithmic profile shown in (2.1), the projected wind speed U_{Tower} (in m s^{-1}) at height z_{Tower} was calculated from the radar wind speed U_{500} (in m s^{-1}) at 500 m (z_{500}).

$$U_{Tower} = U_{500} \frac{\ln\left(\frac{z_{Tower}}{z_0}\right)}{\ln\left(\frac{z_{500}}{z_0}\right)} \qquad (2.1)$$

While there are uncertainties in the representativeness of a logarithmic wind profile within TC boundary layers (Smith and Montgomery 2014), especially as the internal boundary layer evolves (Hirth et al., 2012), a similar logarithmic profile was applied by Kosiba et al. (2013) to estimate near-surface winds during the landfall of Hurricane Rita. To appropriately filter the 30-m resolution surface roughness data to the scale of the radar retrieved wind analysis, the closest 10 surface roughness points at each StickNet site were averaged to obtain the z_0 value used in the projection. Winds were projected to both 10 and 2.25 m heights. Ten meters is the standard height used for NWS surface wind measurements while the StickNet anemometers, used for validation, were at a height of 2.25 m.

2.2.2 StickNets

Texas Tech University (TTU) deployed a fleet of 14 StickNet portable observing weather platforms in the landfall region of Hurricane Harvey. Each platform utilized an RM Young 05103 wind monitor to collect wind measurements at a sampling frequency of 10 Hz and at a measurement height of 2.25 m AGL. For the StickNet wind data used herein, each wind speed time history underwent a manual quality control inspection where suspect or erroneous data were removed from analysis. Ten and 30 s wind speed averages were then constructed centered on the time of maximum observed dual-Doppler wind speed at the grid point closest to the StickNet deployment location (Table 2.1). Site photos were taken both at the time of deployment and retrieval of the instruments to document the surrounding surface roughness, including signs of

localized flooding or damage during the event. The inner core of Harvey passed over the array of StickNets, seven of which were in the dual-Doppler retrieval region (Figure 2.1) and were used to validate the projection of the radar winds to the surface.

Using the advective time-to-space relationship for airflow, the spatial scales of the radar analyses corresponds to about a 30-sec average of winds measured at a point for the observed wind speeds. Hence, the in situ winds were averaged over a 30-sec period centered on the time of the radar recorded maximum wind at the point over each StickNet location.

2.2.3 Soundings

To evaluate the logarithmic wind profile assumption, data were used from two radiosonde soundings (Figure 2.2) launched from a mobile mesonet operated by the National Severe Storms Laboratory. The first sounding was launched at 1954 UTC on 25 August 2017 at 28.2640 °N, 97.3018 °W and the second at 0136 UTC on 26 August 2017 at 28.1597 °N, 97.4009 °W. The soundings employed a Vaisala RS41-SGP radiosonde with the signal received by the Vaisala MW41 base station. Technical specifications for the RS41-SGP include a temperature uncertainty of 0.3 °C, over a -95°C to +60°C range, a 0.5 s temperature response time, humidity observations accurate to within 4 percent, and an onboard pressure sensor with accuracy of 1 hPa.

The RS41-SGP derives wind speed and direction using a proprietary smoothing algorithm applied to the change in location determined from a GPS receiver. The derived winds have a stated accuracy of 0.15 m s^{-1} and 2°, respectively. Given the unknown nature of the smoothing algorithm, an unfiltered wind profile was derived for this study using recorded GPS

locations. To avoid regions of downdraft, where momentum mixing would affect the wind speed, data were removed when the ascent rate of the balloon was less than 2 m s^{-1}.

2.3 Wind retrievals at 500-m altitude

2.3.1 Single wind retrieval

At landfall, Hurricane Harvey was estimated to be a category four storm (58-70 m s^{-1}) by the National Hurricane Center (Blake & Zelinsky, 2018) with a maximum sustained wind of approximately 59 m s^{-1}. As shown in the 0320 UTC dual-Doppler wind field analysis, the area of extreme winds in Harvey was rather compact (Figure 2.3). At 500 m, dual-Doppler winds approached 70 m s^{-1} in the eyewall. While this observation appears extreme, examination of radial velocity in the lowest elevation angle sweeps from SR2 and KCRP revealed Doppler velocities exceeding 70 m s^{-1} at several locations during landfall (not shown). The strong winds (>60 m s^{-1}) in the western eyewall were confined to a narrow swath slightly upstream (clockwise) from a mesovortex (Figure 2.3b) that was similarly noted in Fernandez-Caban et al. (2019). Thus, the mesovortex winds do not necessarily represent the broader-scale mean wind. Due to the presence of this and other mesovortices circulating along the inner eyewall, the eyewall resembled a wavenumber four pattern in both reflectivity and vertical vorticity.

At a range of approximately 40 km from the center of circulation, the horizontal wind magnitude decreased to about 50 m s^{-1}. At approximately 50 km range, the horizontal wind decreased to about 40 m s^{-1}. Thus, at the time under consideration, the most extreme winds were largely confined to within 30 km of the center of circulation.

2.3.2 Distribution of maximum wind at 500-m altitude

To assess the distribution of the 500-m maximum wind, time series of analyses were conducted with the maximum wind speed magnitude and time of occurrence recorded at each data point. Two periods are included, one before official landfall (2058 UTC on 25 August to 0139 UTC on 26 August; Figure 2.4a, b) and one during landfall (0314 UTC – 0556 UTC on 26 August; Figure 2.4c, d). Recall that the SR2 radar was inoperable between 0140 UTC and 0310 UTC.

The eyewall path can be clearly distinguished in the maximum wind field prior to landfall (Figure 2.4a). Wind speeds near 70 m s^{-1} characterized the western portion of the eyewall. Southwest of the eyewall path, the maximum 500-m wind was generally less than 50 m s^{-1}. Similar to the analysis at 0320 UTC, the gradient in the maximum horizontal wind radially outward from the eyewall was readily discernable.

Distinct, arc-shaped swaths of localized wind maxima were also found as Harvey moved toward shore, including one late in the period that was oriented northwest-to-southeast (centered at x=50, y=-10 km in Figure 2.4a). Inspection of individual analyses indicated these swaths in the maximum wind field were the result of individual mesovortices in Harvey's eyewall. On the scale of the wind retrievals, the mesovortices created an additional 5-10 m s^{-1} of wind speed relative to the airflow at surrounding points. The temporal evolution of the maximum wind prior to landfall (Figure 2.4b) indicates that these local structures revolved cyclonically in time around the inner eyewall and were associated with the strongest observed winds.

During landfall (0314-0556 UTC; Figure 2.4c, d), the maximum wind field exhibited similar characteristics. The strongest winds were still confined to within 30 km of the center of circulation and sharply decreased radially outward. Moreover, the maximum winds at 500 m

over land appeared to be just as strong as the winds prior to landfall offshore. Subsections of the eyewall had 500 m maximum winds between 75 and 80 m s^{-1} during 0330 to 0345 UTC over Copano Bay and Rockport, TX (x=35, y=-35 in Figure 2.4c) where significant wind damage occurred.

The mesovortices likely responsible for the local enhancements in the maximum wind are thought to be associated with VRW processes (VRWs; MK97) due to their propagation against the mean flow (Gao and Zhu 2016; Wingo and Knupp 2016; Wurman and Kosiba 2018). VRWs are hypothesized to promote the redistribution of momentum in TC eyewalls (Wang 2002a,b; Montgomery and Kallenbach 1997; Gao and Zhu 2016). Alford and Biggerstaff (2017) found a similar mesovortex structure in the decaying eyewall of Hurricane Hermine (2016) during landfall that also locally intensified wind speed as the broader-scale primary circulation decreased in strength. While these observations are at 500-m altitude, the wind gusts observed by Fernandez-Caban et al. (2018) at the surface near one of these mesovortices implies that the mesovortices produce enhanced surface wind perturbations as well. Subsequent chapters will investigate the Hurricane Harvey dataset in more detail to elucidate the role of VRW relations to these mesovortex structures and in inner core rainband production.

2.4 Wind estimates near the surface

Diagnosis of maximum winds in landfalling TCs generally relies on over-ocean dropsonde observations of the near-surface wind field, and projections of in situ measurements from airborne platforms, such as the NOAA P-3, to the near-surface (Franklin et al. 2003). Here, the surface roughness lengths derived from land use maps obtained from the Office for Coastal Management (Figure 2.5) are used to project the 500-m maximum winds to 10 m, which

corresponds to the height of standard surface wind measurements conducted by the National Weather Service, and 2.25 m, which corresponds to the height of the anemometers on the StickNets.

2.4.1 Validation of the wind projections

To evaluate the logarithmic wind profile assumption, unfiltered wind speed data from two mobile surface-based soundings released in an outer rainband at 1954 UTC and within the inner core at 0136 UTC were examined (Figure 2.6). Both profiles indicate that the 500-m altitude was below the level of maximum wind, which would suggest that a logarithmic wind profile is appropriate (Franklin et al. 2003). Indeed, the unfiltered winds fit a logarithmic wind speed profile reasonably well. Using an average of the surface roughness around the launch site, extrapolations of the sounding-observed 500-m wind to 10 m led to differences of about 4 m s^{-1} (~25 percent) compared to the sounding-observed 10-m wind. Using an average of surface roughness along the path of the balloon as it rose from the surface to 500 m improved the estimated wind profile fit for the later, inner core, sounding but did not appreciably change the earlier sounding estimated wind speed profile. Indeed, the surface roughness associated with the least-squares fit of the unfiltered wind for the later sounding was close to the average surface roughness following the balloon location. In contrast, the least-squares fit surface roughness for the earlier sounding taken in an outer rain band was significantly higher than the nearby average, the average following the balloon, or the single surface roughness value at the launch site.

Further validation of the results from applying the logarithmic profile was accomplished by projecting the radar maximum winds to the seven StickNet locations in the radar domain (Table 2.1). The 30-second average winds from the StickNets were compared against the radar projections using (2.1) with the surface roughness estimate taken from the average of the closest

10 points to each StickNet location. Comparing the radar projections to the in situ measurements led to a root mean squared error of 3.9 m s^{-1} and an average radar high bias of 2.3 m s^{-1}, which is close to the sounding data projection.

While the number of validation points is low, the greatest error occurred in low surface roughness locations. These locations were very close to the shoreline. Hence, many of the closest surface roughness points were over water. Using dual-Doppler analyses, Hirth et al. (2012) showed that there is a rapid decrease in the boundary layer wind speed as air crosses the ocean-land interface. Thus, the radar-estimated maximum winds near the coastline (within 300 – 500 m) may be overestimated by ~20 percent. Elsewhere, the errors were about 10 percent of the in situ measured wind speed at 2.25 m.

2.4.2 Spatially Continuous Projections

The 500-m maximum wind fields between 2058-0139 UTC and 0314-0556 UTC were projected to 10 m using the same procedure as for the validation (Figure 2.7). A combined map is shown in Figure 2.8. The surface roughness values used in the projection are shown in Figure 2.5. Since the aerodynamic surface roughness is assumed to be constant over the open water, the near-surface projection does not consider changes in sea surface roughness that were likely present (Powell et al. 2003). Otherwise, the impact of surface roughness variability on the near surface wind estimates is apparent (Figure 2.7). Airflow over open water was significantly stronger than along the coast and inland. Maxima of 45-50 m s^{-1} in the projected wind can be seen offshore both in the Gulf of Mexico and in Aransas Bay in association with the path of the eyewall and embedded mesovortices. Indeed, a large swath of strong flow (greater than 45 m s^{-1}) crossed the National Wildlife Preserve on Matagorda Island (area enclosed in black circle in

Figure 2.7a) between 0100 and 0130 UTC on 26 August (Figure 2.7b). Examining individual analyses (not shown) revealed that the strongest wind was associated with the path of a mesovortex. Fortunately, that part of the barrier island is not populated. Elsewhere, winds over the barrier islands of the Texas coast were 30-35 m s^{-1} as the northwestern portion of the eyewall moved on shore near 0130 UTC.

During the latter part of landfall (Figures 2.7c, d) the strongest winds (about 50 m s^{-1}) were found in Copano Bay (x= 40 km, y=-35 km in Figures 2.7c). Several locations along the shore of Copano Bay experienced winds in excess of 45 m s^{-1}, including the towns of Bayside and Holiday Beach (western circles in Figure 2.7c). Another local maximum, around the same timeframe, was found between Aransas Pass and Rockport, TX in association with tracks of mesovortices (Figure 2.4c). Around 0600 UTC, another swath of winds in excess of 45 m s^{-1} occurred in an unpopulated area (easternmost black circle in Figure 2.7c). While the presence of the strongest projected winds were largely confined to near the coast where the surface roughness might be underestimated, these maxima do extend 1-5 km inland. In the United States, a 1-min average wind speed at 10 m height is used to classify hurricane strength. The spatial extent of the maximum winds shown here suggest that Harvey was, at best, a category three (50-58 m s^{-1}) hurricane at landfall. It is important to note, however, that the SR2 radar was off-line during a portion of the landfall and the wind record here is incomplete. Nevertheless, the radial velocity data from KCRP did not indicate stronger winds were present during the time SR2 was unavailable.

2.5 Conclusions

In this chapter, data from a mobile C-band SMART radar were combined with the Corpus Christi, TX WSR-88D radar to examine the maximum winds that occurred before and after the landfall of Hurricane Harvey. Individual dual-Doppler wind retrievals, conducted about every 5 minutes, were used to construct a map of the maximum wind magnitude and time of occurrence at 500 m for every grid point in the radar domain. Aerodynamic surface roughness estimates were applied within a logarithmic wind profile projection to extrapolate the 500-m radar maximum winds to wind speeds near the surface.

The technique was evaluated using soundings from a mobile platform and further validated against a small network of in situ anemometers. It was found that the projected radar wind speeds were within 10-20 percent of the in situ measurements when examining 30-sec anemometer averages, which is consistent with the time-space conversion for the observed flow and the ~1 km spacing of the radar data. The errors were largest for small surface roughness estimates, which likely reflects the inclusion of open-water values in estimating the average roughness for near-shore locations.

The projected wind speeds indicate that Hurricane Harvey was, at most, a category three storm at the time of landfall, with a few locations around Copano Bay and near Rockport, TX having large enough regions of winds in excess of 45 m s^{-1} to have produced a one-minute average wind of Category 3 strength. More importantly, the strongest winds found in the analysis were associated with tracks of individual mesovortices that circulated cyclonically around the eyewall of Hurricane Harvey. It is believed that these mesovortices were associated with VRW processes during landfall. At the scale of the radar wind retrievals, the mesovortices enhanced the flow by 5-10 m s^{-1} relative to surrounding areas. Strong vertical drafts in mesovortices

(Wingo and Knupp 2016), may mix high momentum parcels toward the surface at scales that were not examined in this chapter. Moreover, the logarithmic wind profile used to project the radar winds to the near the surface may not be well suited to flow within and underneath mesovortices. Given observations of extreme gusts in such events (Black et al. 1999; Fernandez-Caban et al. 2019; Wurman and Kosiba 2018), it is believed that the analysis presented here may underestimate, rather than an overestimate of smaller scale wind maxima associated with mesovortices, or other wind gusts associated with a time scale of less than 30 seconds.

Regions of enhanced surface winds, especially in mesovortices, demonstrates that the presence of local maxima are vital to understanding regions of maximum wind damage and the landfall structure of TCs. Spatially and temporally continuous observations from dual-Doppler analyses can capture these maxima, signifying that such datasets would be useful in other TC landfalls and wind engineering assessments. Indeed, a study is currently underway to relate damage to built structures to the dual-Doppler derived wind attributes presented here. Additionally, a time series of wind maxima associated with landfalling storms may help to better separate property losses from winds to those caused by surge and inland flooding. The dual-Doppler derived wind fields can also be used to validate high-resolution numerical simulations of Harvey. Further characterization of the atmospheric boundary layer wind profile during hurricane landfall and a greater number of in situ measurements are needed to refine the wind projection method and yield more robust validation of radar estimated wind maxima at the surface.

2.6 Figures

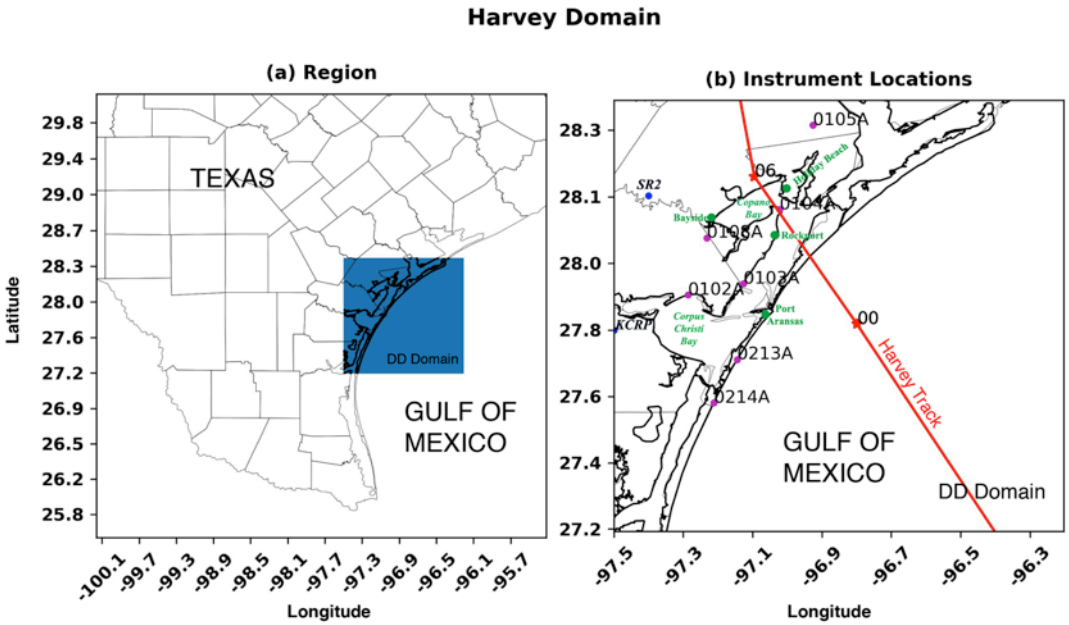

Figure 2.1. (a) Large-scale view of the analysis area with the dual-Doppler analysis domain outlined in blue. (b) Detailed view of the analysis domain with locations of the radars (KCRP and SR2) marked by blue dots, StickNet locations with magenta dots, cities mentioned in the text with green dots, and the Corpus Christi and Copano Bays in green italicized text. The track of the center of circulation of Hurricane Harvey is overlaid in red with red markers showing the times at 00 and 06 UTC.

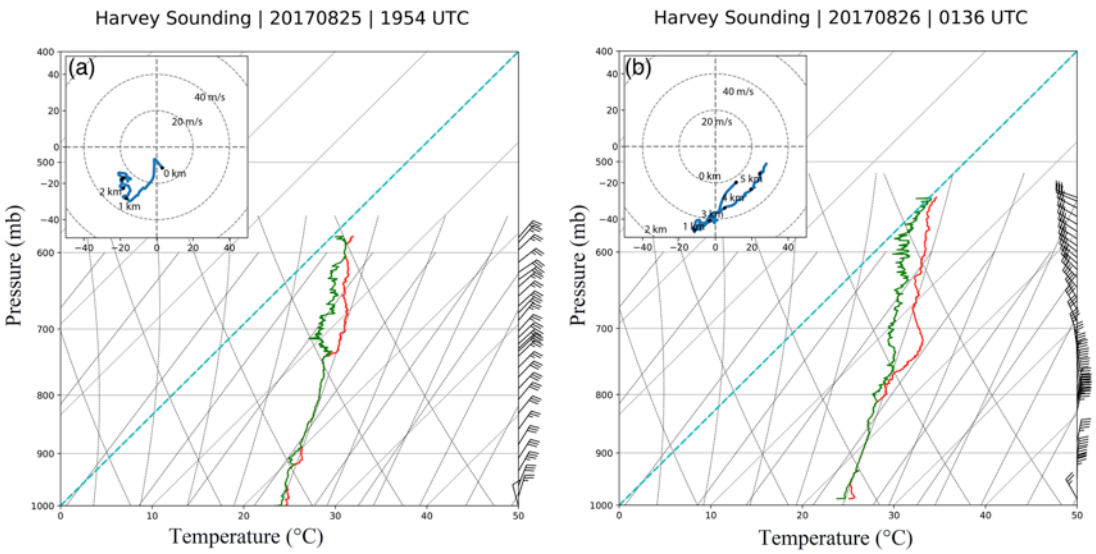

Figure 2.2. SkewT-logP plot of the atmospheric soundings taken in the outer bands of hurricane Harvey at (a) 1954 UTC on 25 August and (b) 0136 UTC on 26 August. The hodographs, indicating the value of the wind components as a function of altitude, are inserted in the upper left side of each sounding plot. In the hodograph, the black points indicate height in km as denoted by their corresponding labels. The winds shown here are the filtered winds produced by the Vaisala propritary smoothing algorithm.

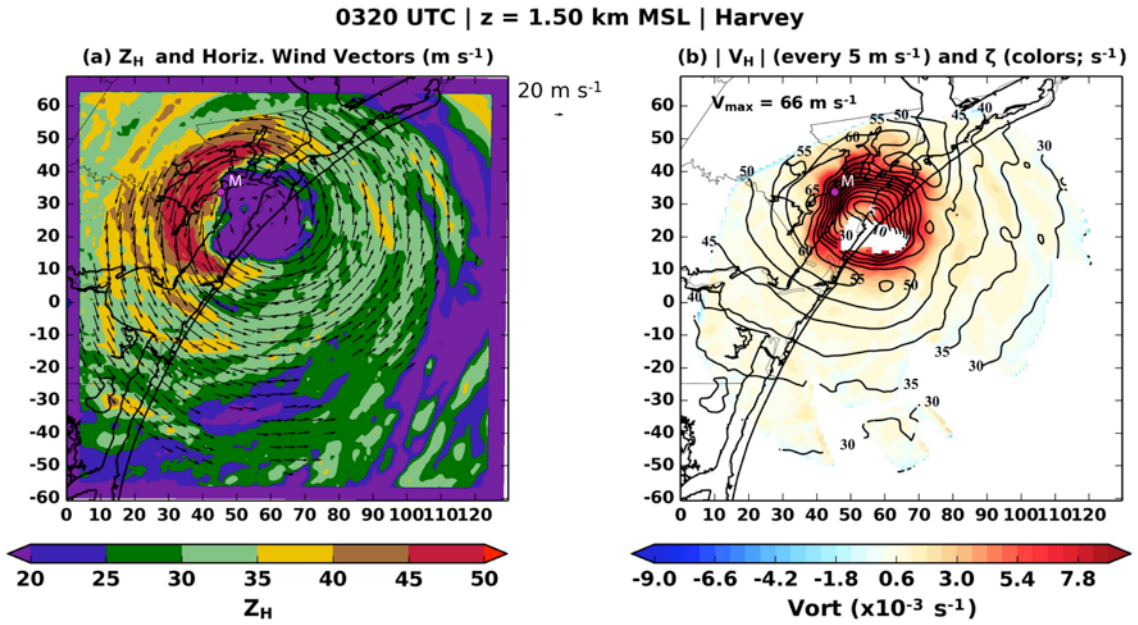

Figure 2.3. Dual-Doppler analysis at 0320 UTC during Hurricane Harvey's landfall. (a) The color-filled contours show radar reflectivity (Z_H, in dBZ) every 5 dB. The ground-relative wind vectors indicate the magnitude and direction of the horiztonal wind with a reference vector shown in the top right part of the figure. (b) The black contours indicate the magnitude of the horizontal wind every 5 m s^{-1}. The color-filled contours are vertical vorticity X10^{-3} s^{-1}. The "M" indicated the location of the mesovortex discussed in the text.

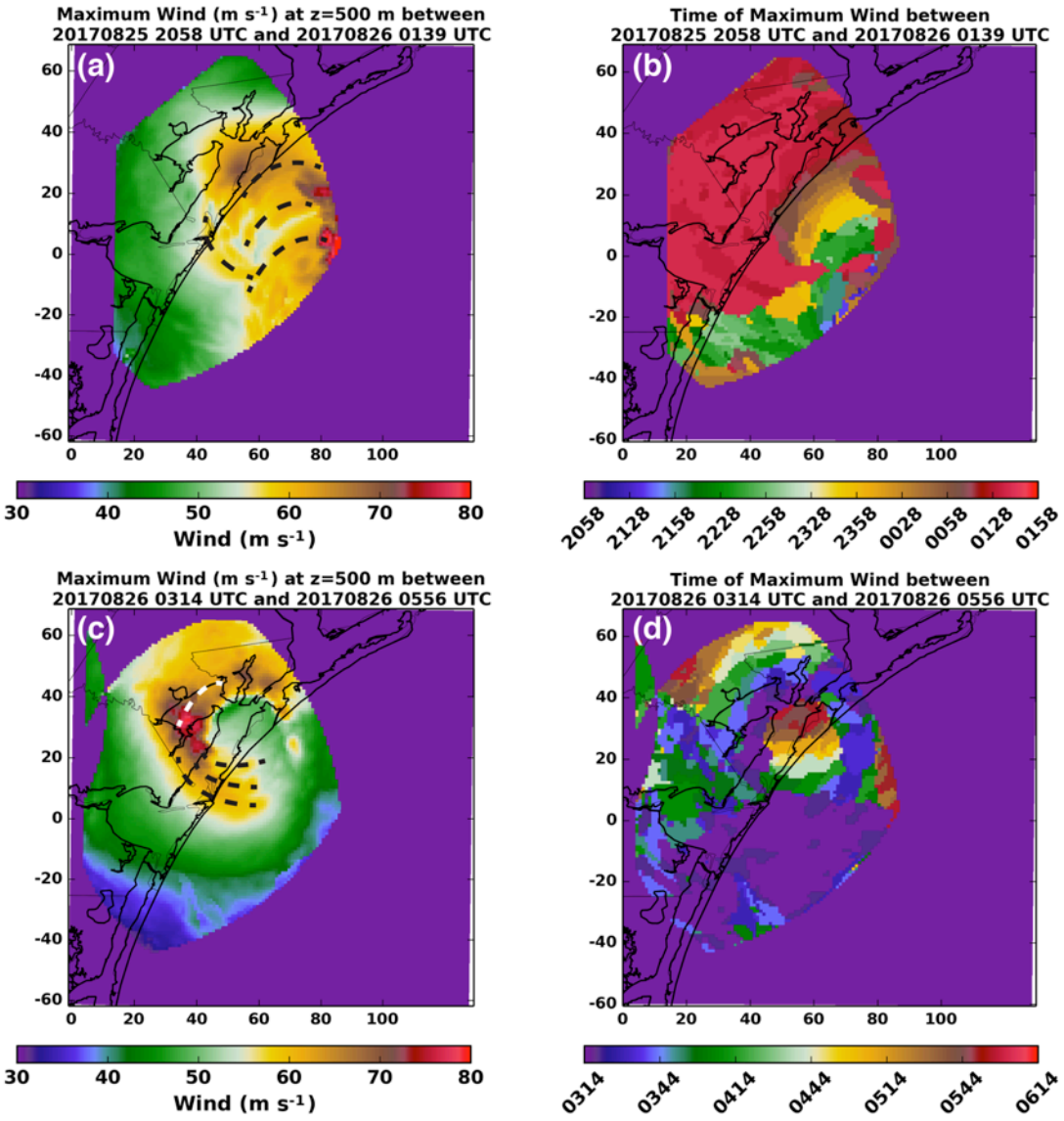

Figure 2.4. In (a) the maximum horizontal wind that occurred at each grid point between 2058 and 0139 UTC is shown for the 500 m altitude analysis. The abscissa is east-west distance from KCRP while the ordinate is the north-south distance from KCRP. (b) shows the time at which the maximum wind occurred at each grid point. (c) and (d) are similar, but for the 0314-0556 UTC period. The dashed lines in (a) and (c) denote mesovortex tracks clearly distinguishable in the individual wind retrieval analyses.

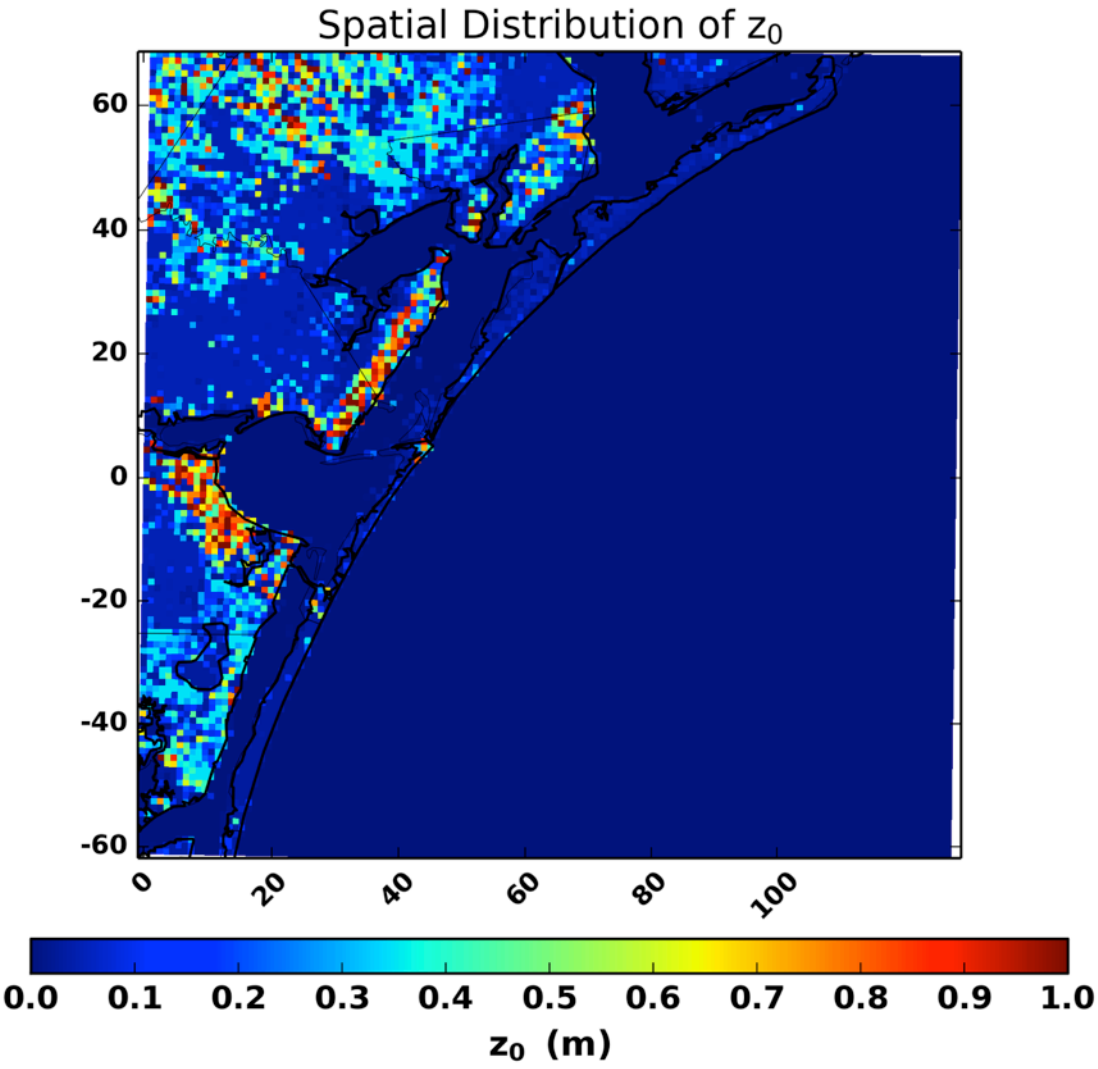

Figure 2.5. Map of the aerodynamic surface roughness estimates (in m, according to the color scale) used to project the radar observed wind at 500 m to both 10 m and 2.25 m altitudes.

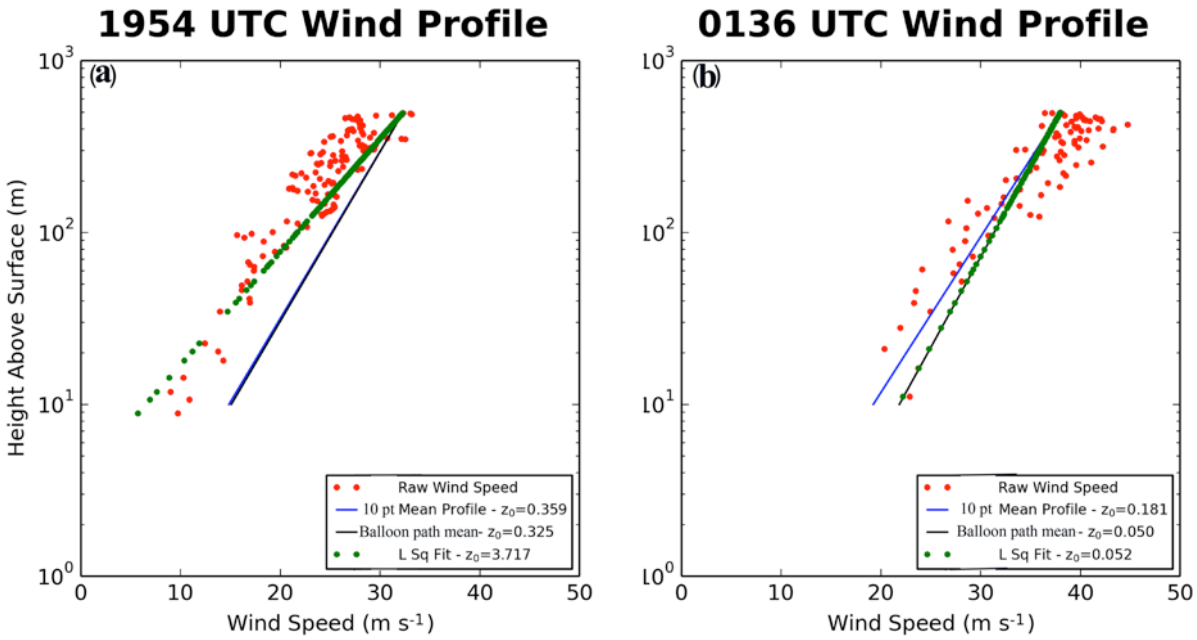

Figure 2.6. Unfiltered winds, for balloon ascent rates greater than 2 m s^{-1}, in the lowest 500 m of the radiosonde soundings taken at (a) 1954 UTC on 25 August 2017 and (b) 0136 UTC on 26 August 2017. The blue (black) lines show the projected wind profile for the 10-point average (along balloon path average) surface roughness. The green line is the least-squares best fit to the unfiltered winds.

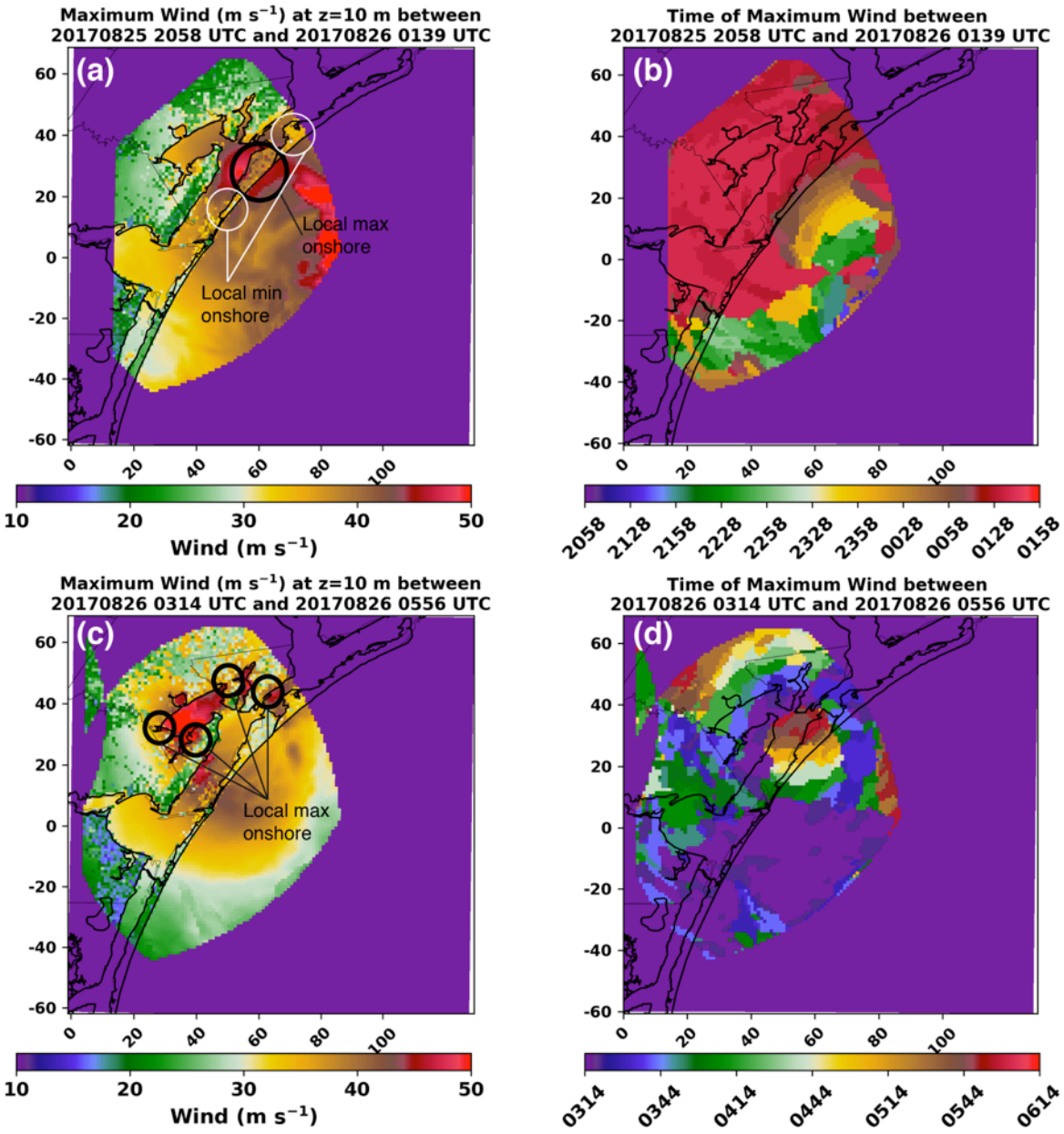

Figure 2.7. (a) The maximum 10 m wind experienced between 2058 and 0139 UTC on 25-26 August. (b) The time at which the maximum wind in (a) occurred. (c) The maximum 10 m wind experienced between 0314 and 0556 UTC on 26 August. (d) The time at which the maximum 10 m was observed in (c). For (a) and (c), the 10 m wind was projected from the 500 m wind. The circles in (a) and (c) denote regions of maxima and local minima in winds as discussed in the text.

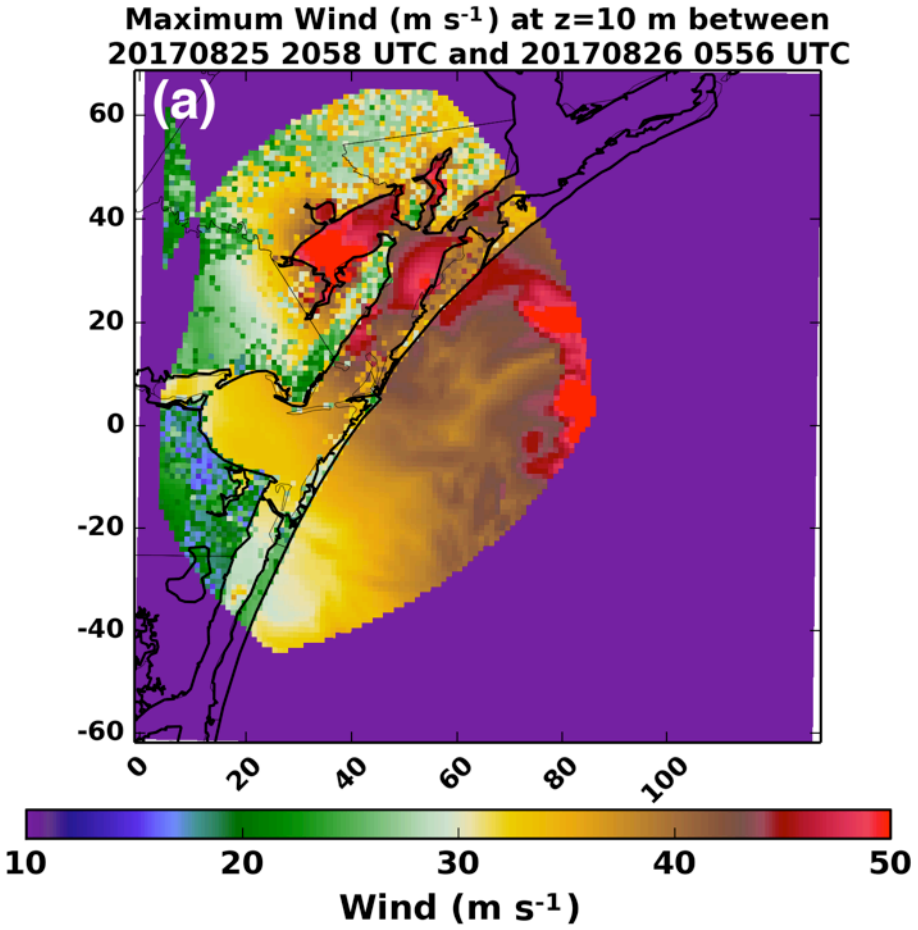

Figure 2.8. Map of estimated maximum winds at 10-m altitude combining the two time periods of the analysis. Note that the SR2 radar was down from 0140-0310 UTC on 26 August 2017.

2.7 Tables

Table 2.1. Details of the radar-derived wind speed validation data over each StickNet site.

Tower Name	***Latitude (degrees)***	***Longitude (degrees)***	***DD Max Wind Time (UTC)***	***10 s StickNet Wind at DD Max Wind Time (m s^{-1})***	***30 s StickNet Wind at DD Max Wind Time (m s^{-1})***	***Radar Projected Wind (m s^{-1}), 10 nearest points***	***Average (10 nearest points) Surface Roughness at Tower (m)***
0102A	27.87936	-97.29433	0408	21.4	20.7	24.3	0.209
0103A	27.90926	-97.13204	0330	28.3	29.0	31.3	0.142
0104A	28.11096	-97.02672	0133	26.2	28.3	28.6	0.299
0105A	28.33900	-96.92954	0450	31.8	30.0	31.8	0.061
0108A	28.03384	-97.23983	0334	30.0	28.8	34.9	0.049
0213A	27.70409	-92.13087	0133	29.4	29.4	25.7	0.182
0214A	27.58605	-97.21806	2350	22.4	22.1	27.8	0.013

Chapter 3: Observed Initiation of Vortex Rossby Waves from Asymmetric Convection

3.1 Introduction

As shown in Chapter 2, the hurricane wind field at landfall can be highly asymmetric (Schroeder et al. 2009; Krupar et al. 2016; Fernandez-Caban et al. 2019; Alford et al. 2019b). Asymmetries in Hurricane Harvey's eye and eyewall exhibited wind speeds that augmented the background wind by 5-10 m s^{-1} in an instantaneous sense. It is unclear, however, the mechanism by which the winds increased and how the asymmetries may contribute to the longer-term intensity of TCs.

Recently, research has focused on understanding the energy cascade between physical scales of motion in order to understand TC intensity changes and a better understanding TC inner core dynamics (Rogers et al. 2012; Montgomery and Smith 2016). However, obtaining such observations is often difficult and has precluded a unified framework of the TC energy cascade (Hogsett and Zhang 2009). Interactions between the convective and vortex scales are particularly important to understand TC evolution (Rogers et al. 2012). As discussed in Chapter 1, a leading mechanism prescribed to lead to intensity change in a dynamical framework is vortex Rossby wave excitation and propagation. This chapter examines VRWs in additional detail.

First mentioned by MacDonald (1968) and Guinn and Schubert (1993), Rossby-type waves were thought to be active in TCs and be associated with rainbands in the inner core (i.e., the annulus bounded by the eyewall and a radius three times that of the maximum wind). Macdonald (1968) attributed the upwind propagation of rainbands against the mean tangential flow in TCs to Rossby wave-like dynamics, similar to that of a planetary Rossby wave. Extending the suggestion made by MacDonald (1968), Guinn and Schubert (1993) hypothesized that the well-established radial potential vorticity (PV) gradient in TCs could act as a waveguide

and support the existence of Rossby waves in TCs. However, it was not until MK97 that the term "vortex Rossby wave" (VRW) was coined. Utilizing a Wenzel-Kramers-Brillouin analysis, MK97 showed that VRWs could exist arising from asymmetries in a barotropic vortex. As the prescribed asymmetries evolved, wave energy propagated radially outward on the radial gradient of storm-relative vorticity and was filamented by the horizontal shear of the vortex. In turn, it was shown that as the VRWs propagated outward, they fluxed momentum (or PV) inward. The symmetrization process is thought to result in a stronger vortex as the outward-propagating waves fluxed PV inward while the wave energy propagated outward. The work of MK97 was later extended to three-dimensions in Möller and Montgomery (2002), describing the vertical propagation of VRWs in addition to their radial propagation. Gao and Zhu (2016) derived the dispersion relation of VRWs in a baroclinic framework, showing that the dispersion relation takes the same form as in MK97 but in pseudoheight coordinates.

Cotto et al. (2015) demonstrated that given an asymmetry near the RMW of a TC, momentum/PV exchange could occur between the regions adjacent to the RMW (i.e., from the RMW into the eye or from the RMW radially outward). Given a sufficient net flux of momentum inward from the eyewall region toward the eye, the RMW could in this manner contract leading to TC intensification. In MK97 and Gao and Zhu (2016), it is noted that a net inward flux of potential vorticity is possible during the VRW axisymmetrization process. MK97 specifically noted that VRWs fluxed momentum such that the tangential wind increased just outside the RMW, while the maximum positive change in vorticity was just inside the RMW. Overall, this resulted in a stronger monopole vortex in their simulation. Studies such as Nolan et al. (2007) have also utilized full physics, three-dimensional simulations to examine in depth the role of asymmetric convection on vortex intensity changes. Whereas Cotto et al. (2015) found

asymmetries would act to enhance the symmetric vortex, Nolan et al. showed that the disruption of the vortex by asymmetric convection led to an overall weakening of the primary circulation. The primary mechanism for weakening was related to the asymmetric distribution of latent heating, suggesting symmetric latent heating is vital to TC intensification.

VRWs have been primarily studied in a modeling framework with emphasis upon convectively coupled rainbands that are thought to be the result of VRW excitation and propagation radially outward of the hurricane eyewall (MK97; Wang 2002a,b; Franklin et al. 2006; Judt and Chen 2010). Observations of the excitation of VRWs by asymmetric convection in the eyewall and their related rainbands have not been well documented yet. Specifically, the excitation of VRWs at their sources (asymmetries in the flow) have not been observed and it is not clear if rainband formation is also coincident. Most observations are limited to aircraft-based wind retrievals over the open ocean and are restricted in their temporal sampling of VRW-driven rainbands (e.g., Reasor et al. 2000; Fischer et al. 2020). In addition, there are no observational studies to the authors' knowledge focusing on the impact of VRWs to either intensity change or rainband structure at landfall.

In this chapter, asymmetries in the eyewall of Hurricane Harvey (2017) is examined at landfall. Disruptions to the hurricane vortex are expected during the landfall process and may present a greater number of asymmetries than typically seen over the ocean. Nevertheless, such asymmetries observed over the ocean in shallow waters offer unprecedented opportunity to examine the vortex-scale asymmetric convective evolution in a high spatiotemporal framework, expanding upon the mesoscale wind maxima described in Chapter 2. This chapter also focuses on the asymmetric convection thought to lead to the excitation of VRWs and the possible mechanisms for intensity change associated with asymmetric convection.

3.2 Data & Methods

3.2.1 Instrumentation

The C-band (5-cm wavelength) SR2 from the University of Oklahoma currently operates with a half-power beam width of 1.5° and in simultaneous transmit and receive (STaR) dual-polarization mode (Doviak et al. 2000) . C-band radar is an optimal remote sensing tool in a hurricane environment, as attenuation in the contiguous precipitation field is mitigated and a relatively high degree of radial resolution is retained (Knupp et al. 2006; Hirth et al. 2012; Alford et al. 2019a,b; Fernandez-Caban et al. 2019; Alford et al. 2020).

In Major Hurricane Harvey, the dual-Doppler retrieval region between SMART radar 2 (SR2) and the WSR-88D in Corpus Christi, TX (KCRP) captured the evolution of Harvey both offshore and during the landfall (Figure 3.1). Dual-Doppler retrievals were available approximately every five minutes, similarly synchronized with KCRP. The dual-Doppler retrieval region extended offshore where processes in and near the eyewall were captured prior to landfall. Further details about the deployment and data collection may be found in Alford et al. (2019a).

3.2.2 Analysis Technique

The SMART radar data and WSR-88D data gathered from the National Centers for Environmental Information (NCEI) were processed objectively through the Py-ART Toolkit available from the Atmospheric Radiation Measurement (ARM) Climate Research Facility (Helmus and Collis 2016). The region-based method of Py-ART objectively dealiases the radial velocity V_R field, while also mitigating noise and incoherent second trip echoes. The data were

also examined subjectively to correct aliasing not captured by the algorithm using Solo3 (Oye et al. 1995). See Alford et al. (2019a) and Appendix 1 for additional details.

After editing, data were interpolated to a Cartesian grid using a natural neighbor interpolation technique (Sibson 1981) described in Betten et al. (2018) and in Biggerstaff et al. (2021, submitted to *Geoscience Data Journal*). Data from all hurricanes were interpolated to a 1 km spaced grid in the horizontal and the vertical. V_R data were smoothed with a Gaussian filter with a sigma of 1. To objectively retrieve the three-dimensional wind, the gridded data were passed into a three-dimensional variational data assimilation (3DVAR) dual-Doppler wind retrieval algorithm (hereafter, DDA; Potvin et al. 2012a). A more complete record of the interpolation and dual-Doppler technique may be found in Alford et al. (2019a).

3.2.3 Center-Relative Projections

To characterize the storm-center-relative components of the hurricane flow, objectively-identified centers of circulation were found using a modified ground-based velocity track display (GBVTD) technique (Lee et al. 1999; Lee and Marks 2000; Bell and Lee 2012). The original GBVTD technique relies on fitting the low wavenumber component of a hurricane vortex by utilizing single Doppler velocity information. Reflections, contractions, and expansions of a simplex triangle with each vertex representing a hypothetical center of circulation are tested individually to maximize the projected circulation around a closed circuit given the observed Doppler velocities. In other words, the vorticity field at the radius of maximum wind is maximized to find the center of circulation.

However, the GBVTD method can be strongly biased by asymmetries in the hurricane vortex (e.g., mesovotices), such that the simplex-found center is aligned toward vorticity maxima

observed in the Doppler velocities. In the case of Hurricane Harvey, the primary dataset used in this work, multiple mesovortices have been noted and are representative to strongly asymmetric flow (see Chapter 2). The self-consistent technique of Bell and Lee (2012) was tested on the dataset, as it constrains the location of the center of circulation using the derived temporal consistency of the radius and magnitude of maximum wind. While this version of the algorithm greatly improved center locations, strongly asymmetric storms such as Harvey at landfall are still difficult to resolve in the GBVTD framework. As such, a modified version of the GBVTD technique is summarized here and is used exclusively to objectively define the center of circulation at each dual-Doppler time.

An initial guess for the center of circulation was retrieved from the Hurricane Research Division's center fix following the method of Willoughby and Chelmow (1982) at each DDA time (Available at https://www.aoml.noaa.gov/hrd/Storm_pages/harvey2017/harvey.trak). Starting with the initial guess of the center, a simplex triangle is defined with 1 km sides around the initial guess. Each vertex represents a hypothetical center of circulation and is allowed two possible actions original to the GBVTD method: contraction or reflection. From each vertex, an annulus representing the eyewall and region of maximum wind is defined from $20 < r < 30$ km, where r is the radius from center of circulation. The hypothetical tangential wind computed from the DDA horizontal velocity information is averaged over each annulus centered on each vertex. Utilizing the total wind tended to bias the resulting center of circulation toward mesovortices and asymmetries. To eliminate such bias that is inherent in the algorithm, the azimuthal annulus over radii of 20-30 km was chosen to smooth out local maxima in the vicinity of the radius of maximum wind. The relatively large annulus also assures better performance when only portions of the inner core are within the dual-Doppler retrieval region. The original method retrieved the

Fourier coefficients around individual radii (usually 1 km in width) to estimate the low-wavenumber components of the actual flow. While this approach could be applied to the actual tangential wind observations here, a simple azimuthal average across a larger annulus was preferred, due to the lack of a complete view of the eyewall in the early analyses. After retrieving the average tangential wind at each vertex, the simplex triangle is allowed to follow the contraction or reflection steps summarized in Lee and Marks (2000; see their Section 3) such that the simplex vertices are aligned with the average maximum wind (i.e., maximizing the circulation/vorticity). When the sides of the simplex are less than 0.05 km, the vertices' locations are averaged to define a final simplex center as the new spatial location of the center of circulation.

There is a natural tendency for the analyzed centers of circulation at each dual-Doppler time to progress in time in a non-linear (or non-smooth) fashion due to the asymmetric nature of real hurricane flows. This topic was discussed in detail in Bell and Lee (2012), who used the temporal evolution of the center of circulation, the radius of maximum wind, and the magnitude of the maximum tangential wind to statistically constrain the final center chosen for each analysis time. Here, a simpler approach to smooth out the analyzed centers at each dual-Doppler time is used. As dual-Doppler analyses are conducted every ~5 minutes, a more simple, running, linear Savitzky-Golay filter is applied to the x and y locations independently in order to reduce the small scale variations in either the x or y locations of centers of circulation. The smoothing is performed over a temporal window of 9 dual-Doppler times centered on the analysis time in question. The Savitzky-Golay filter was set to allow linear extrapolation at the beginning and ending times for each curve fit, of which there were three to account for the breaks in analyses (see Figure 3.1b).

3.3 Asymmetric Structure of Harvey's Eyewall

3.3.1 Mesovortex Structures

Hurricane Harvey made landfall on the Texas coastline near Port Aransas at approximately 0300 UTC on 27 August 2017. Prior to and after landfall, Harvey's eyewall was largely asymmetric at times, wherein multiple mesovortices (Black et al. 1999) and asymmetric structures were observed (Wurman and Kosiba 2018; Alford et al. 2019b; Fernandez-Caban et al. 2019). Because of the lack of scatterers within the eye, the presence of a mesovortex cannot be readily concluded with certainty for each asymmetry observed. However, for the purpose of this work, the terms mesovortex and asymmetry are used interchangeably as the ultimate goal is to quantify more broadly asymmetric dynamic processes on a landfalling hurricane.

Over the dual-Doppler period observed between SR2 and KCRP, the asymmetries in Harvey's eye and eyewall are readily apparent in three-dimensional wind retrievals. In Figure 3.2, three dual-Doppler analyses are shown at 26 August 2108 UTC (Figures 3.2a, 3.2b), 27 August 0029 UTC (Figure 3.2c, 3.2d), and 27 August 0351 UTC (Figures 3.2e, 3.2f). Radar reflectivity observations at 2108 UTC and 0351 UTC (Figures 3.2a and 3.2e) show a wavenumber 1 type asymmetry in Harvey's eyewall with higher wavenumber perturbations visible along the inner edge of the eye (annotated by white arrows in the figures). Coincident with the reflectivity perturbations, maxima in the vertical vorticity field (Figures 3.2b, 3.2f) are visible with values often exceeding 8×10^{-3} s^{-1}. In contrast at 0029 UTC (Figure 3.2c), the radar reflectivity is more symmetric. However, two distinct maxima in the vorticity field can be seen in Figure 3.2d in the northwest and southeast portions of the eyewall.

The asymmetries noted in Figure 3.2 have vertically coherent structure as well. In Figure 3.3, three-dimensional (3D) isosurfaces of vertical vorticity (Figures 3.3a, 3.3c, and 3.3e) and

isosurfaces of vertical velocity (Figures 3.3b, 3.3d, and 3.3f) are displayed. Deep vorticity maxima in Figure 3.3 are clearly visible associated with the surface vorticity maxima annotated in Figure 3.2. In general, it appears that the columns of enhanced vorticity tilt upwind and lean radially outward. In addition, almost all of the near-surface vorticity maxima (selective annotations by arrows in Figure 3.3) are flanked by downwind (counter-clockwise) downdrafts and radially outward and upwind (clockwise) updrafts. Similar structure was found in Wingo and Knupp (2016), who performed a careful examination of mesovortices in the eyewall of Hurricane Ike (2008). During Ike's landfall, it was found that the primary updrafts associated with mesovortex structures were located radially outward and clockwise upwind of the vorticity maximum. Although it was not discussed in detail, their results showed evidence of downdrafts leading the mesovortex structures as well.

3.3.2 Eyewall Vorticity Structure

Focusing on the 0029 UTC analysis as an example, the local absolute vertical vorticity tendency through advection (Figure 3.4a) and the sum of the tilting and stretching vorticity terms (Figure 3.4c) are examined. In general, the magnitude of the advection term is similar to that of the sum of the stretching and tilting terms. It should be noted that the tilting term specifically was approximately an order of magnitude less than that of stretching at the analysis levels sampled. Thus, neglecting friction and baroclinicity, advection and stretching of vertical vorticity are the primarily contributors to the asymmetries in vorticity. The maxima in the vorticity centers tend to reside on the interior portion of the eyewall where the gradient in the horizontal wind is large, which may imply that the vortices arise from the growth of barotropic instabilities. Relatively large advective values of vorticity in the tangential direction are expected and can be ascertained

from Figure 3.4a compared to Figure 3.4b, the radial component of vorticity advection. The maxima in the total advection term is exclusively counter-clockwise downwind of the vorticity maxima, which are denoted by the black Xs. The magnitude of the radial component of vorticity advection is comparable to the total advection in regions of mesovortices and relatively weaker elsewhere. The enhancement of radial advection near the mesovortices suggest that these eyewall asymmetries are likely efficient at vorticity redistribution, at least in the case of Hurricane Harvey. Thus, asymmetries' effect upon the structure of the eyewall and their potential impact to rainband formation, if any, needs to be examined.

3.3.3 Radial Advection of Potential Vorticity (PV)

As discussed in Chapter 3.1, idealized modeling of VRWs suggests that the waves are excited by initial potential vorticity (PV) perturbations in, for example, the eyewall near the radius of maximum wind. Thus, a PV framework is used here to examine the excitation of VRWs and the feedbacks of the symmetrization process (MK97) on the primary vortex. As potential temperature is not available on the scale of the wind field, a simplified, barotropic definition of *PV* is employed (3.1), where ζ *is* the relative vertical vorticity, f is the planetary vorticity, and z is the analysis height above mean sea level in meters. From (3.1), (3.2) shows the advection of *PV* by the radial component of the center-of-circulation relative wind $\overrightarrow{u_r}$ derived in Cartesian coordinates such that $\vec{u}_r = (|\overrightarrow{u_r}|sin\theta, |\overrightarrow{u_r}|cos\theta)$ where θ is the angle (0° points north and increases clockwise) to an analysis point from the center of circulation.

$$PV = \frac{\zeta + f}{z} \tag{3.1}$$

$$-\overrightarrow{u_r} \cdot \nabla_h PV = -|\overrightarrow{u_r}|sin\theta \frac{\partial PV}{\partial x} - |\overrightarrow{u_r}|cos\theta \frac{\partial PV}{\partial y} \tag{3.2}$$

While radial advection accounts for only one component of *PV* redistribution, it is examined exclusively here because VRWs are thought to primarily impact the main vortex through the radial transport of *PV*. Hence, the tendency of *PV* at the scale of the dual-Doppler analyses associated with asymmetries is used.

In Figure 3.5, the advection of *PV* by the radial wind according to (3.2) is shown for each of the analysis times considered in Figure 3.2. Associated with the localized vorticity maxima are regions are radial outward (positive values) and radial inward (negative values) advection of *PV*, maximized in the vicinity of the vorticity maxima in Figure 3.2. In general, radial inward advection is found counterclockwise downwind of mesovortex centers and radial outward advection is found upwind. All else being equal, mesovortices here act to induce an inward transport of *PV* from the eyewall downwind and an outward transport of *PV* upwind. It was noted in MK97 that the symmetrization process could contribute to the local enhancement of the winds radially inward of the asymmetries. In Chapter 2 specifically, evidence of enhanced velocities associated with mesovortex passage relative to the background flow was presented, representing a potential instantaneous impact to the character of the hurricane flow. Thus, it appears that the inward directed component of *PV* transport by asymmetries can explain temporary enhancements to the background flow. However, the simple transport of high *PV* from the eyewall toward the eye does not explain the VRW mechanism of vortex intensity changes on longer time scales.

3.4 Wave-Mean Flow Interactions

3.4.1 Computational Framework

A key component of understanding tropical cyclone intensity change relies on quantifying the contribution of asymmetric feedbacks upon the mean vortex state (Rogers et al. 2012). To date three-dimensional observations in a high temporal resolution framework of asymmetric dynamics processes in the eyewall of TCs over the ocean or at landfall are almost non-existent. A fortuitous observing opportunity during the landfall of Hurricane Harvey (Fernandez-Caban et al. 2019) afforded the opportunity to examine the effects of asymmetric mesovortex structures upon the symmetric (azimuthally averaged) vortex. Specifically, eyewall asymmetries likely excited VRWs that radially advected PV and momentum which may affect the intensity of the mean vortex.

In Chapter 3.3, the kinematic, instantaneous structure of mesovortices on the interior portion of Harvey's landfall prior to and during landfall was documented. Downwind of mesovortices, PV advection was favored directed from the eyewall toward the center of circulation. Alternatively, upwind of a mesovortex, PV advection occurred preferentially radially away from the center of circulation. Past studies such as Chen and Yau (2003) have investigated the contribution of asymmetric flux of PV to the total intensity change of the mean-vortex state. In their simulation of a landfalling hurricane, asymmetric eddy fluxes tended to counteract the progression of the mean TC intensity. In other words, during intensification prior to landfall, the eddy flux by asymmetric vorticity sources was shown to promote a reduction in the tangential wind at the radius of maximum wind. At landfall, as intensity was decreasing, the eddy flux tended to counteract the spindown of the vortex by accelerating the wind at the radius of maximum wind.

Here, the observed eddy flux contribution to the mean tangential wind (hereafter referred to as "eddy flux") is estimated. The eddy flux at an altitude of 500 m is evaluated, as the rearrangement terms in the prior vorticity analysis were an order of magnitude greater at 500 m versus any other analysis level. As discussed in multiple theoretical studies of vortex Rossby waves (MK97; Möller and Montgomery 2000; Gao and Zhu 2016), an inward transport of *PV* is expected toward the radius of maximum wind by VRWs wherein spinup near the radius of maximum wind is anticipated through wave-mean flow interaction. The general methodology of MK97 is followed, where the time-integrated eddy flux is used to estimate the change of the mean tangential wind δV_{eddy} as a function of radius r (3.3). The eddy flux is the azimuthal average (denoted by the overbar) of the product of perturbation vorticity (ζ') and perturbation radial wind (u_r'). This simple formulation was applied in MK97's barotropic framework to examine the wave-mean flow interaction of VRWs on the state of the vortex and typically holds true if the perturbations are relatively small. In other words, the radial transport of vorticity is used to estimate the barotropic eddy contribution to intensity change.

$$\overline{\delta V_{eddy}}(r) = -\int \overline{u_r'\zeta'}\, dt \qquad (3.3)$$

Chen and Yau (2003) noted that while barotropic eddy fluxes cannot be neglected, the contribution of symmetric latent heating on the strength of the primary vortex was greater than eddy fluxes. Unfortunately, thermodynamic impacts on the hurricane structure cannot be evaluated via dual-Doppler analysis. Therefore, the contribution of vorticity flux in (3.3) is compared to the change in the azimuthally averaged tangential wind V as a function of r and time t by computing the observed *total* change in the mean tangential wind δV_{obs} as a function of radius (3.4).

$$\overline{\delta V_{obs}(r)} = \int \overline{V(r, t+\Delta t)} - \overline{V(r,t)}\, dt \qquad (3.4)$$

Because SR2 experienced two ~1 hour failures, the change in the tangential wind is evaluated for each observational period (26 August 2058 UTC-26 August 2310 UTC, 26 August 2350 UTC – 27 August 0140 UTC, and 27 August 0310 – 27 August 0600 UTC) separately.

3.4.2 Eddy Flux Contribution to Changes in Mean Tangential Wind

Figure 3.6 shows δV_{eddy} (thin lines) and δV_{obs} (thicker lines) as a function of r^*, which is the radius from the center of circulation (r) normalized by the radius of maximum wind (RMW), The RMW was calculated as the radius at which the azimuthally averaged tangential wind was maximized relative to the center of circulation for each dual-Doppler time. In Figure 3.6a, the change in the tangential wind is shown almost exclusively when Harvey's eyewall was offshore. Thus, the results are interpreted in an over-water context. In Figure 3.6b (3.6c), Harvey's eyewall was partially (halfway to completely) onshore. Hence the results are interpreted as being strongly affected by land.

In Figure 3.6a, δV_{eddy} is maximized just inside the RMW ($r^* \sim 1$) while Harvey's eyewall was offshore. From near $0.8 < r^* < 1.2$, the eddy flux contribution is positive, as is the observed change in the tangential wind (δV_{obs}). However, δV_{eddy} is greater than δV_{obs}, suggesting that the integrated intensity change was moderated by other factors. While this temporal period is considered to be representative of the eyewall over water, Harvey on the whole was interacting with land, which may have been detrimental to significant intensification. Nevertheless, the wave-mean flow interactions observed via dual-Doppler kinematics appear to suggest that vorticity perturbations near the eyewall over water contributed positively to the spin up of the tangential wind, rather than being detrimental. This analysis does not consider the convection associated with these vorticity anomalies, wherein asymmetric latent heating may at least

partially offset the positive contribution of kinematic feedbacks. Furthermore, it appears that the eddy flux contribution is negative in the near inner core region ($1 < r^* < 2.2$) outside the eyewall and positive in the far inner core ($r^* > 2.2$). Neglecting the exact location of the maximum in eddy fluxes, these results are similar to those found in MK97, where VRWs outside the RMW tended to flux momentum toward the RMW resulting in an increase near the RMW and decrease radially outward. The location of the maximum in the eddy flux in Fig. 3.6a is slightly inward of the RMW, where the simulation of MK97 suggested the maximum should be just outside of the RMW. However, the location of the asymmetries in MK97 was peaked at $r^*=1$, where the observed peaks of the mesovortices and asymmetries in Harvey's eyewall were just inside the RMW.

As Harvey began making landfall (Figure 3.2b), the observed rate of intensification was largely quiescent from $0.75 < r^* < 1.6$. At the RMW, the observed change to the tangential wind was on the order of +0.5 m s^{-1}. Elsewhere, changes were very small over this time period with negative observed changes for $r^* > 1.5$ and $r^* < 0.9$. With the exception of normalized radii less than ~0.9, eddy flux changes between +1 to +8 m s^{-1} were computed for most radii. The maximum observed change (δV_{obs}) is near r^* equal to 1.05, which coincides with a local maximum in the eddy flux contribution to the tangential wind change. However, the magnitude of the eddy flux contribution is, again, greater than the observed change. Similar to when Harvey was offshore (Figure 3.6a), it is likely that asymmetric latent heating and/or land-induced vortex spindown accounts for the offset. Assuming that land interaction accounts for at least some of the offset, this result suggests that the eddy fluxes indeed offset the vortex spindown tendency induced by landfall.

As Harvey's eye moved further over land (Figure 3.6c), the observed change in the tangential wind for nearly all normalized radii is largely negative as is the eddy flux contribution. During this time period, the eyewall became highly asymmetric (e.g., Figure 3.2e) with multiple asymmetries and pronounced mesovortices propagating around the eye and eyewall (c.f., Wurman and Kosiba 2018; Fernandez-Caban et al. 2019). While it was noted in Chapter 3.3 and in Chapter 2 that these particularly intense perturbations account for regions of enhanced winds exceeding 75 m s^{-1} at times at 500 m altitude, their time integrated effect upon the symmetric vortex is largely negative (Figure 3.6c). The most significant reduction in the tangential wind is noted at the RMW. Although negative in magnitude, a nearby local maximum in the eddy flux exists (at approximately $r^* = 0.95$), suggesting that the decay of the RMW is likely dominated by factors other than wave-mean flow interactions observed in this analysis. Interestingly however, the observed change in the tangential wind and the eddy flux contribution tends toward positive values at radii < ~0.8. While difficult to observe in a dual-Doppler analysis due to the lack of scatterers in the eye, this trend may imply that during the decay of Harvey there was a tendency by the mesovortices to flux high momentum near the RMW inward into the eye, resulting in a local increase in the mean tangential wind within the eye.

3.5 VRW Initiation

3.5.1 A PV Perspective

In VRW literature (e.g., MK97; Möller and Montgomery 2000; Gao and Zhu 2016), it is shown that VRWs transport PV radially inwards toward the asymmetry source, while wave energy propagates outward on the radial gradient of vorticity. The eddy fluxes discussed above suggest a spinup of the tangential wind just inside the RMW and a decrease in the tangential

wind radially outward of the RMW while Harvey was offshore, resembling in part the hypotheses of MK97. As the eddy flux contribution resembles VRW processes, it stands to reason that VRWs and any associated rainbands may exist radially outward of the eyewall, and the symmetrization of asymmetries may result in outward propagating VRWs. The next chapter will examine the propagation of rainbands that may be associated with outward propagating VRWs in Hurricane Harvey and other landfalling hurricanes. Here the source of one outward propagating wave is examined, rather than the resultant rainbands themselves. In this particular chapter, secondary rainbands (rainbands near the eyewall; e.g., Houze 2010) are assumed to be formed from VRWs based on limited observational evidence (Reasor et al. 2000; Corbosiero et al. 2006) to which this study will lend evidence. As an example, Figure 3.7 shows a rainband that developed exterior of Harvey's eyewall. In Figure 3.7a, the rainband at 2115 UTC (annotated by the thick black curve) is immediately adjacent to the eyewall. In Figure 3.7b, an azimuthally elongated region of vertical vorticity on the order of 2.5-5.0 $\times$ 10^{-3} s^{-1} can be seen radially inward of the rainband's reflectivity maximum. Notably, the vorticity maximum also appears to intersect with the eyewall upstream of local maximum in the eyewall vertical vorticity field (denoted by the "X" in Figure 3.7b). In the same vicinity, the reflectivity field in the eyewall shows a pronounced "notch," which is typical of asymmetric structures within the eyewall in this analysis. At 2120 UTC (Figures 3.7c, 3.7d) the rainband appears to have intensified and separated more from the eyewall reflectivity continued to be associated with an azimuthally-elongated vorticity maximum that also appeared more separated from the eyewall.

To examine possible mechanisms of the initial rainband development, the simple framework of PV redistribution is once again employed. Figure 3.8a shows the formative stage of this particular rainband at 2108 UTC (one dual-Doppler analysis prior the analysis in Figures

3.7a and 3.7b), outlined by the solid black curve. Figure 3.8b examines the radial PV advection where positive values again indicate radial outward advection. Radially inside the reflectivity maximum, radial PV advection at 500 m altitude is strongly positive and associated with the vorticity anomalies previously discussed in Chapter 3.3. At 2115 UTC (Figures 3.8c and 3.8d), the area of positive radial PV advection apparently increased in magnitude and occupied a larger azimuthal portion of the inner-eyewall region. Near the point of intersection between the eyewall and the rainband (annotated by a "+" in Figures 3.8c and 3.8d), the advective tendency changes sign, suggesting that the rainband is in question in a region of outward PV advection. This implies that the upwind portion of the vorticity center in the eyewall may induce PV transport from the eyewall radially outward, resembling the initial progression of outward propagating VRWs in the barotropic framework of MK97. Additionally, it was shown in Wang (2008) that low wavenumber disturbances in hurricanes became highly deformed (i.e., filamentation) in the shear of the horizontal wind, particularly exterior of the eyewall. Here, the rainbands and the associated vertical vorticity maxima appear to elongate azimuthally in time, suggesting that they are being deformed in the horizontal shear. It is not surprising in this case, given that the radial profile of the azimuthally-averaged tangential wind (Figure 3.9a) decreases rapidly as a function of radius outside of the RMW. Indeed, the radial shear of the tangential wind [$\partial\overline{v_\theta}/dr$, where r is the radius and $\overline{v_\theta}$ is the azimuthally averaged tangential wind] in Figure 3.9b is maximized inside the RMW and is minimized at a radius of 27 km from the center of circulation, just beyond the RMW. Thus, it appears here that from a PV-perspective the filamentation of PV transferred radially outward from the eyewall is the formative source of this particular rainband. While a rainband itself is expected to produce PV through diabatic processes, the initial PV

transfer from the RMW radially outward is likely rapidly filamented just beyond the eyewall, leading in part to the azimuthally extensive vorticity filaments seen in this analysis.

3.5.2 Vertical Motion and Vertical Vorticity

The kinematic structure of the VRW-induced rainbands is discussed in more detail in Chapter 4. Here, the kinematic structure of the formative stage of this rainband is explored in more depth. The 2108 UTC and 2115 analyses are of primary interest since they afford views of the vorticity field and vertical velocity field just beyond the eyewall. Figure 3.10 shows plan views of the formation of the rainband in question in terms of vertical velocity. For reference, the dashed magenta lines in Figure 3.10 denote the reflectivity maximum of the rainband. Just upwind of the region where the developing rainband intersects the eyewall, the vertical velocities at 4.5 km altitude (Figures 3.10b and 3.10d) are 3-5 m s^{-1}. As discussed previously, this is the region where the maximum radial vorticity advection was noted at the 0.5 km analysis level (see Figure 3.8). Clockwise (upwind) along the rainband, vertical velocities are generally positive on the radial inward side of the rainband and generally decrease upwind. This point is important in particular, as a study by Moon and Nolan (2015) suggested that upwind convective cells were often the dominant contributor to spiral rainbands near the eyewall. Hydrometeors advected downstream of the initial convection were suggested to form the spiral rainband shapes. In contrast, in this analysis updrafts appear to be located azimuthally along the forming rainbands. The rainbands themselves were found in the vicinity of eyewall asymmetries, and strong updrafts were not present upwind of the reflectivity bands. Past studies (Chen and Yau 2001; Wang 2002a,b) have suggested that outward propagating VRWs act to induce convergence in the boundary layer, initiating convective bands in their vicinity.

A vertical cross section through the forming rainband at 2108 UTC (Figure 3.11a) shows the vertical structure of the tangential wind (color-filled contours) and reflectivity (black contours every 5 dBZ starting at 20 dBZ; Figure 3.11b). Vertical continuity can be seen in the forming rainband structure with reflectivity values exceeding 45 dBZ between 0.5 and 2 km altitude at ~30 km range along the cross section. At lower levels, a local vorticity maximum can be seen in Figure 3.11c at about 28-29 km range (annotated in the figure) that tilts radially inward toward the eyewall vorticity column. However, at the lowest analysis levels, the vorticity maximum appears separated from the eyewall vorticity column. For the most part, the vertical velocity and vertical vorticity maxima are co-located in the eyewall. A secondary maximum in vertical motion can be seen over the low-level vorticity column, suggesting that the vorticity perturbation to the low-level wind field is inducing rising motion above it. In Figure 3.11d, the radial wind field is shown in color-filled contours with the vertical velocity field contoured as in Figure 3.11c. Convergence of the radial wind can be seen ahead of the vorticity center, suggesting that the perturbation to the wind field from the vorticity lobe separating from the eyewall enhanced convergence in the low levels of the analysis.

3.6 Discussion and Conclusions

This chapter examined asymmetries in the eyewall of Hurricane Harvey as it made landfall on the south Texas coast on 26 August 2017. Characterized by prominent asymmetries and mesovortices before and during the landfall process, the kinematic structure of mesovortices along the inner eyewall was examined. It was found that the mesovortices were characterized by deep, vertically coherent vorticity maxima often with downdrafts on their downwind side and updrafts upwind. In terms of vertical vorticity tendency, the stretching of vorticity dominated the

tilting terms, which are small due to relatively weak vertical drafts in the low levels, and was similar in magnitude in the total advection terms. Overall, the total advection vorticity tendency was dominated by the tangential wind. However, in the presence of mesovortices/eyewall asymmetries, it was found that the radial component of advection was comparable in magnitude to the total advection.

While PV in the eyewall is not conserved in a kinematic analysis due to the unresolved component of diabatic effects, the redistribution of vorticity in terms of absolute vorticity conservation was examined nevertheless. It was found that on the upwind (downwind) portion of mesovortices, outward (inward) advection of vorticity was favored. In terms of the instantaneous effect to the tangential wind, PV flux inward should promote positive perturbations to the tangential wind. It was noted in Chapter 2 that during Hurricane Harvey's landfall, the maximum winds across south Texas were associated with the tracks of mesovortices. At 500 m above ground and on the scale of the analysis, perturbations to the surrounding wind field in the presence of mesovortices were on the order of 5-10 m s^{-1}. This analysis corroborates these findings by offering some explanation for the local increase in the wind field in that the radial redistribution of PV is directly related to the change in the tangential wind.

Associated with the outward advection of PV from eyewall asymmetries, trailing filaments of vorticity and rainbands were found to develop radially outward of the hurricane eyewall similar to theoretical models of VRWs (MK97; Möller and Montgomery 2000; Gao and Zhu 2016) and full physics simulations of VRWs (Chen and Yau 2001; Wang 2002a,b; Franklin et al. 2006). This is a particularly unique finding, as no observational study has been able to continuously examine the evolution of PV anomalies in the eyewall and their relation to rainband formation. Thus, evolution of inner-core narrow rainband formation in Hurricane Harvey

strongly resembles the foundational works of VRW evolution in idealized numerical models. VRW-induced rainbands are examined in more detail for several hurricanes in Chapter 4.

In addition to the formation of inner core rainbands by VRWs, wave-mean flow interactions near the eyewall were found to promote intensity change in the primary vortex strength in a kinematic framework. While latent heating likely places a large control over the sign of the intensity change (Rogers et al. 2013), this analysis supports the general conclusions of MK97. In particular, the symmetrization of PV anomalies in the eyewall is shown to promote rainband formation exterior of the eyewall which then flux PV toward the eyewall. This analysis quantifies the total contribution to the intensity through the axisymmetrization of asymmetries as explained by VRW dynamics at various stages of Harvey's observed lifecycle.

Applying the simple framework of MK97, the time-integrated flux of vorticity was calculated at three stages of Harvey's landfall process. When the eyewall was offshore, the azimuthally averaged flux of perturbation vorticity was shown to be positive across the eyewall and negative just outside the eyewall. This positive contribution across the eyewall implies that, via wave fluxes, there exists a tendency for the tangential wind to increase toward the eyewall with a maximum just inside the RMW. In the second observational period (~one half of the eyewall onshore), the time-integrated eddy flux was still positive and wave interactions displayed a tendency to enhance the symmetric vortex near the eyewall, although the actual changes were negligible. Thus, prior to Harvey's official landfall just after 0300 UTC, asymmetric wave-mean flow interactions tended to be constructive to the symmetric vortex. In the final observational period (0310 – 0600 UTC), Harvey's eyewall had mostly moved onshore. At this point, the amplitude of the asymmetries had become significantly more prominent, likely due to the enhanced friction in the boundary layer onshore. The time-integrated effect of eddy

fluxes was shown to be destructive across the eyewall, but tended toward positive nearer the center of circulation. However, the lack of scatterers in the eye made it difficult to retrieve continuous observations close to the center of circulation. The minimum in eddy fluxes was at the eyewall, suggesting that the prominent mesovortices tended to extract PV from the eyewall and tended to advect it radially inward.

This analysis represents one of the first high spatiotemporal resolution analyses of wave-mean flow interactions in a landfalling hurricane. Based on the evidence described above, VRW processes are likely contributing to intensity change, but their effects in this case appear to be moderated by other controls to the symmetric vortex state. The distribution of latent heating in relation to the existing RMW (Rogers et al. 2013) likely strongly limits the ability of VRWs to control changes in the mean vortex strength. Further observations are needed to quantify the total contribution of VRW-dynamics to intensity change, but are likely positive given the results of this work. However, significant perturbations to the eyewall structure, like those observed after Harvey made landfall, are likely destructive to the symmetric vortex. Nolan et al. (2007) showed that asymmetric latent heating was the primary mechanism for destructive feedbacks upon the symmetric vortex, but this kinematic analysis suggests that extraction of PV from the eyewall was also a significant factor decreasing the intensity of the symmetric vortex after landfall. It is not clear if these results are a direct consequence of the landfall process or if the results are applicable to TCs over the ocean during periods of significant asymmetries in the eyewall.

3.7 Figures

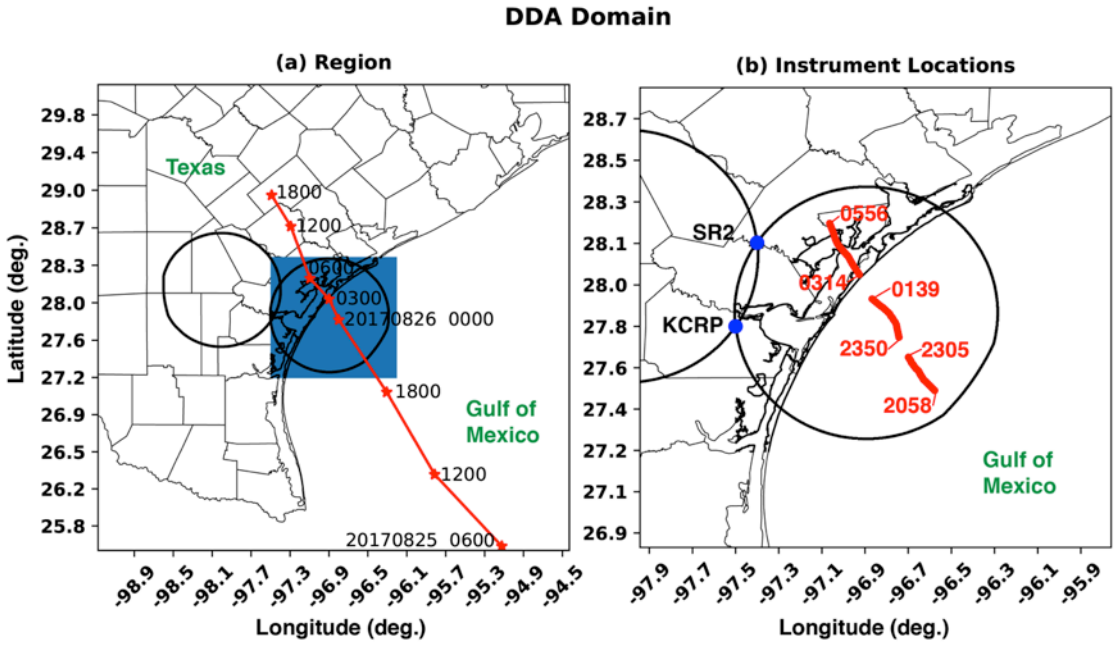

Figure 3.1. (a) Large-scale view of the dual-Doppler region. The black curves represent the 20° dual-Doppler cross-beam angle region. The red curve represents the National Hurricane Center's Best Track path of Harvey. The Best track dates and times are indicated by text. (b) A zoomed in view of the eastern dual-Doppler region is shown. SR2 and KCRP are shown with the blue markers. The red lines show the modified GBVTD-derived center locations of Hurricane Harvey. The beginning and ending of each temporal segment of available dual-Doppler analyses is marked.

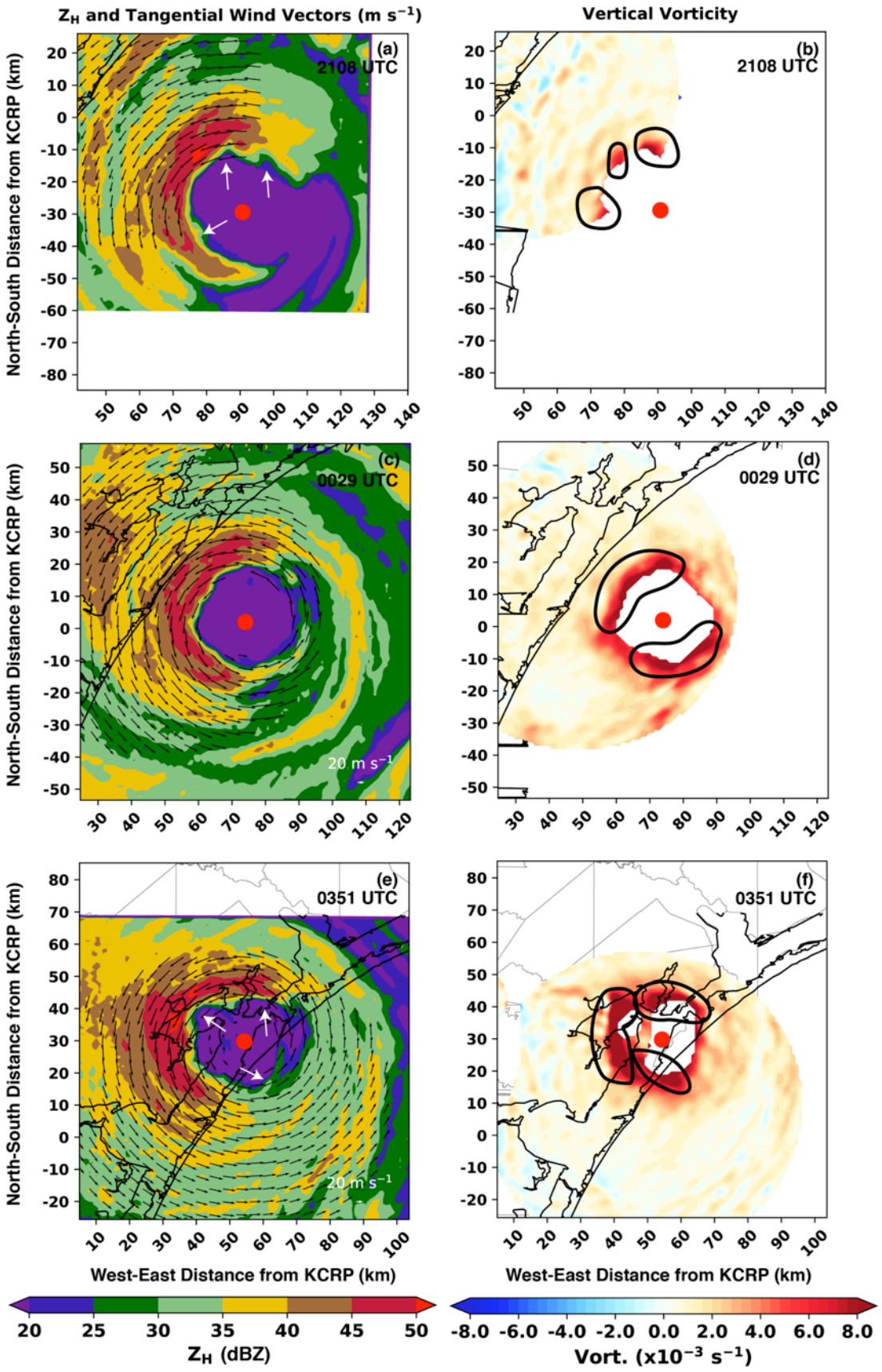
Z_H and Tangential Wind Vectors (m s^{-1})
Vertical Vorticity
(a)
2108 UTC
(b)
2108 UTC
(c)
0029 UTC
(d)
0029 UTC
(e)
0351 UTC
(f)
0351 UTC
20 m s^{-1}
20 m s^{-1}
North-South Distance from KCRP (km)
West-East Distance from KCRP (km)
20 25 30 35 40 45 50
Z_H (dBZ)
-8.0 -6.0 -4.0 -2.0 0.0 2.0 4.0 6.0 8.0
Vort. (x10^{-3} s^{-1})

Figure 3.2. Selected dual-Doppler analyses during the landfall of Hurricane Harvey are shown. (a) 2018 UTC radar reflectivity (dBZ) is displayed in the color-filled contours, and the tangential wind vectors relative to the center of circulation (red circle) are shown. (b) Vertical vorticity (s^{-1}) is shown in the color filled contours. As in (a), the red circle indicates the center of circulation. (c) and (d) are as in (a) and (b), but for the 0029 UTC dual-Doppler analysis. (e) and (f) are for the 0351 UTC analysis. In (b), (d), and (e), the black dashed contours indicate asymmetric vorticity maxima.

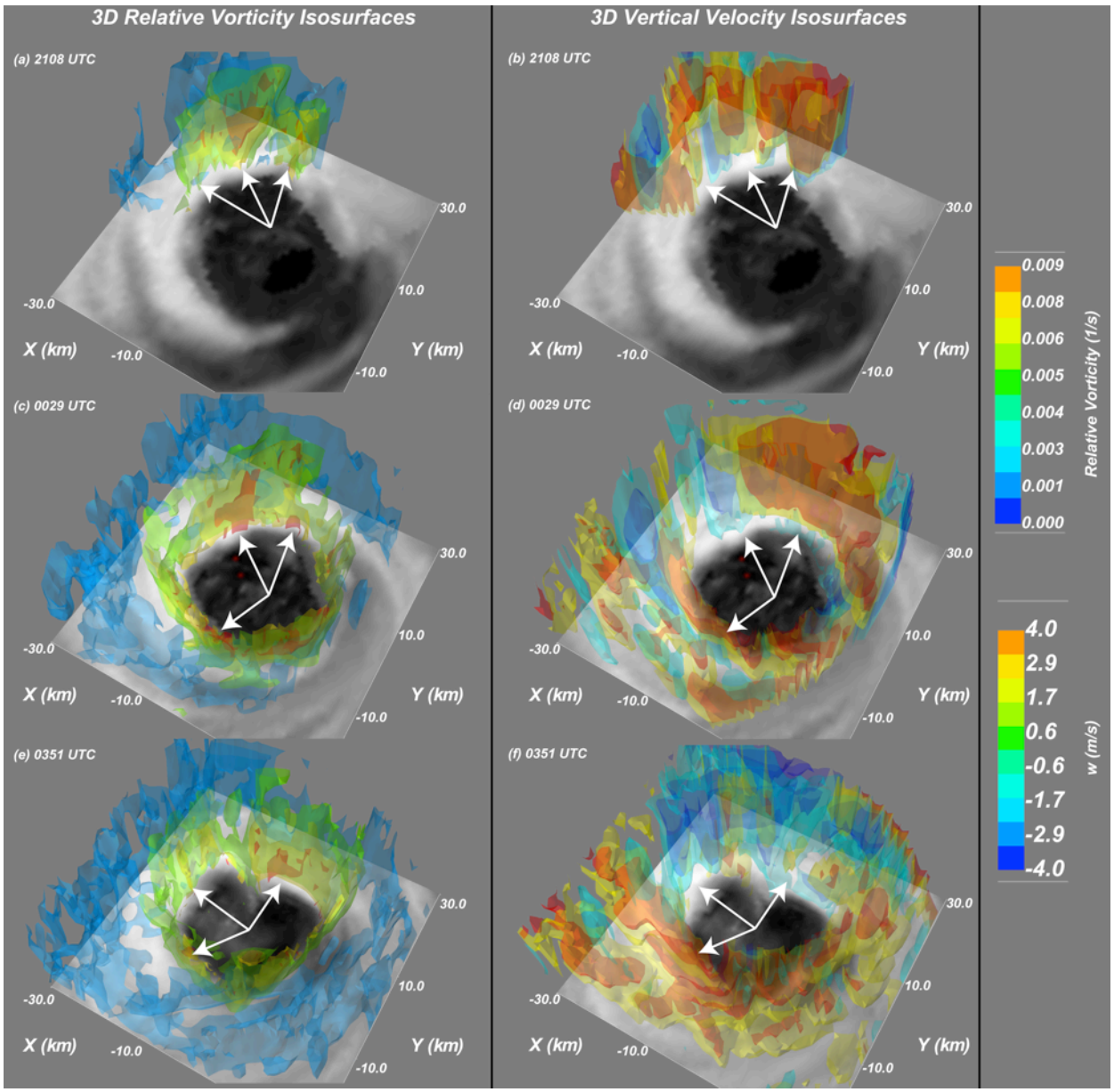

Figure 3.3. Three-dimensional kinematic data for dual-Doppler analyses conducted at 25 August 2108 UTC (a, b), 26 August 0029 UTC (c, d), and 26 August 0351 UTC (e, f) are shown. Three-dimensional isosurfaces of relative vorticity are shown in (a), (c), and (e) according to the colorbar on the right side of the figure. Similarly in (b), (d), and (e), isosurfaces of vertical velocity are displayed.

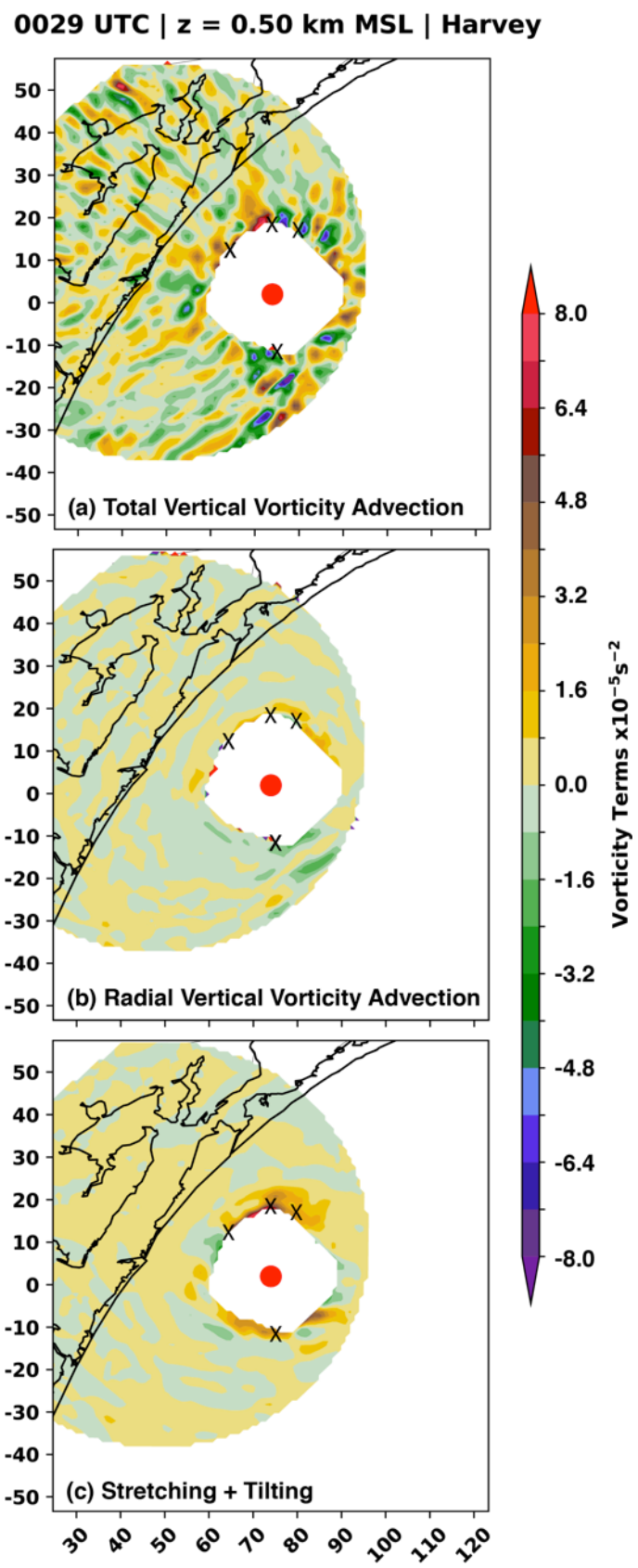
0029 UTC | z = 0.50 km MSL | Harvey
(a) Total Vertical Vorticity Advection
(b) Radial Vertical Vorticity Advection
(c) Stretching + Tilting
Vorticity Terms x10⁻⁵s⁻²
8.0
6.4
4.8
3.2
1.6
0.0
-1.6
-3.2
-4.8
-6.4
-8.0
50
40
30
20
10
0
-10
-20
-30
-40
-50
30
40
50
60
70
80
90
100
110
120

Figure 3.4. A vorticity budget at 0.5 km MSL is shown for the 0029 UTC dual-Doppler analysis. (a) The total vertical vorticity advection is displayed. (b) The radial component of the vorticity advection relative to the center of circulation (red circle in all subplots) is displayed. (c) The cumulative stretching and tilting terms of vorticity is shown. In all figures, the black Xs denote mesovortex locations.

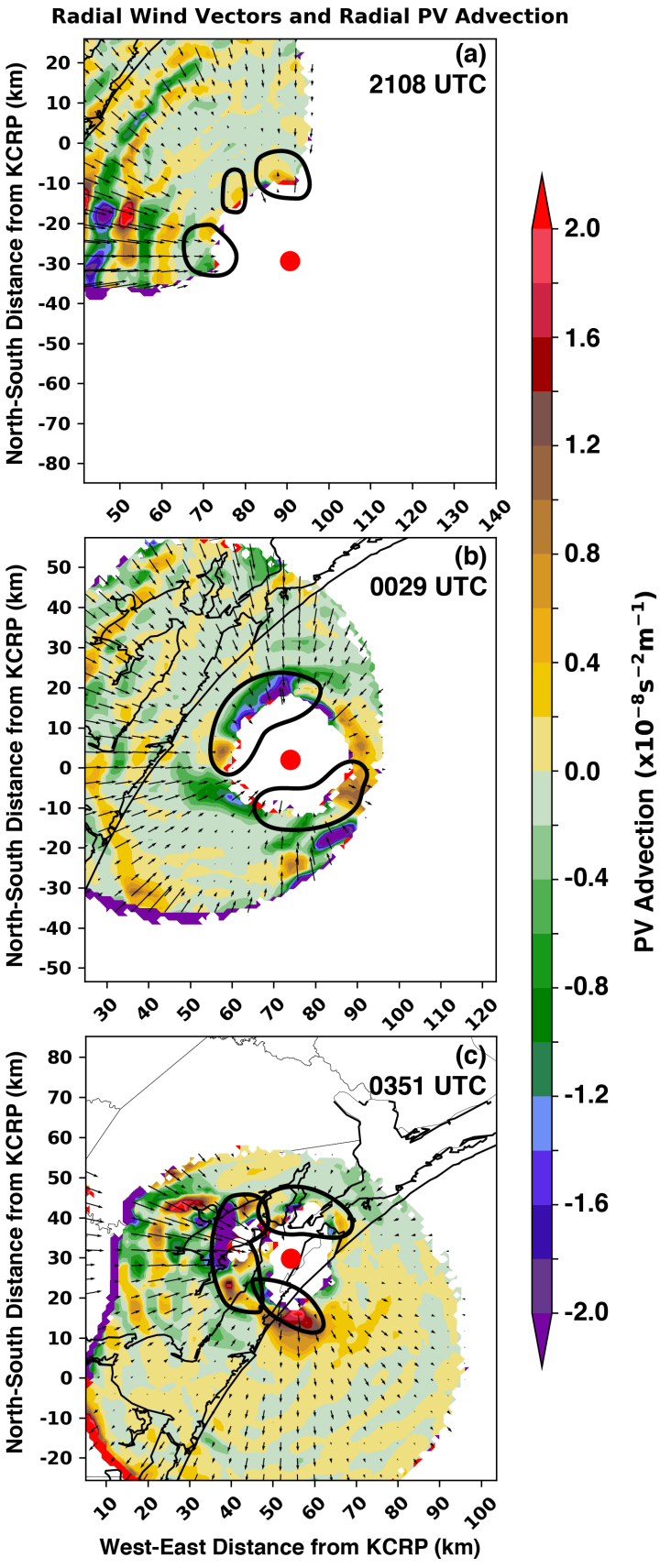
Radial Wind Vectors and Radial PV Advection
(a)
2108 UTC
(b)
0029 UTC
(c)
0351 UTC
North-South Distance from KCRP (km)
West-East Distance from KCRP (km)
PV Advection (x10⁻⁸s⁻²m⁻¹)
2.0
1.6
1.2
0.8
0.4
0.0
-0.4
-0.8
-1.2
-1.6
-2.0

Figure 3.5. The storm-relative radial PV advection term (color-filled contours) is shown along with storm-relative radial wind vectors for (a) 2109 UTC, (b) 0029 UTC, and (c) 0351 UTC. As in Figure 3.4, the red circle represents the objectively defined center of circulation. The thick black contours highlight mesovortices as in Figure 3.2.

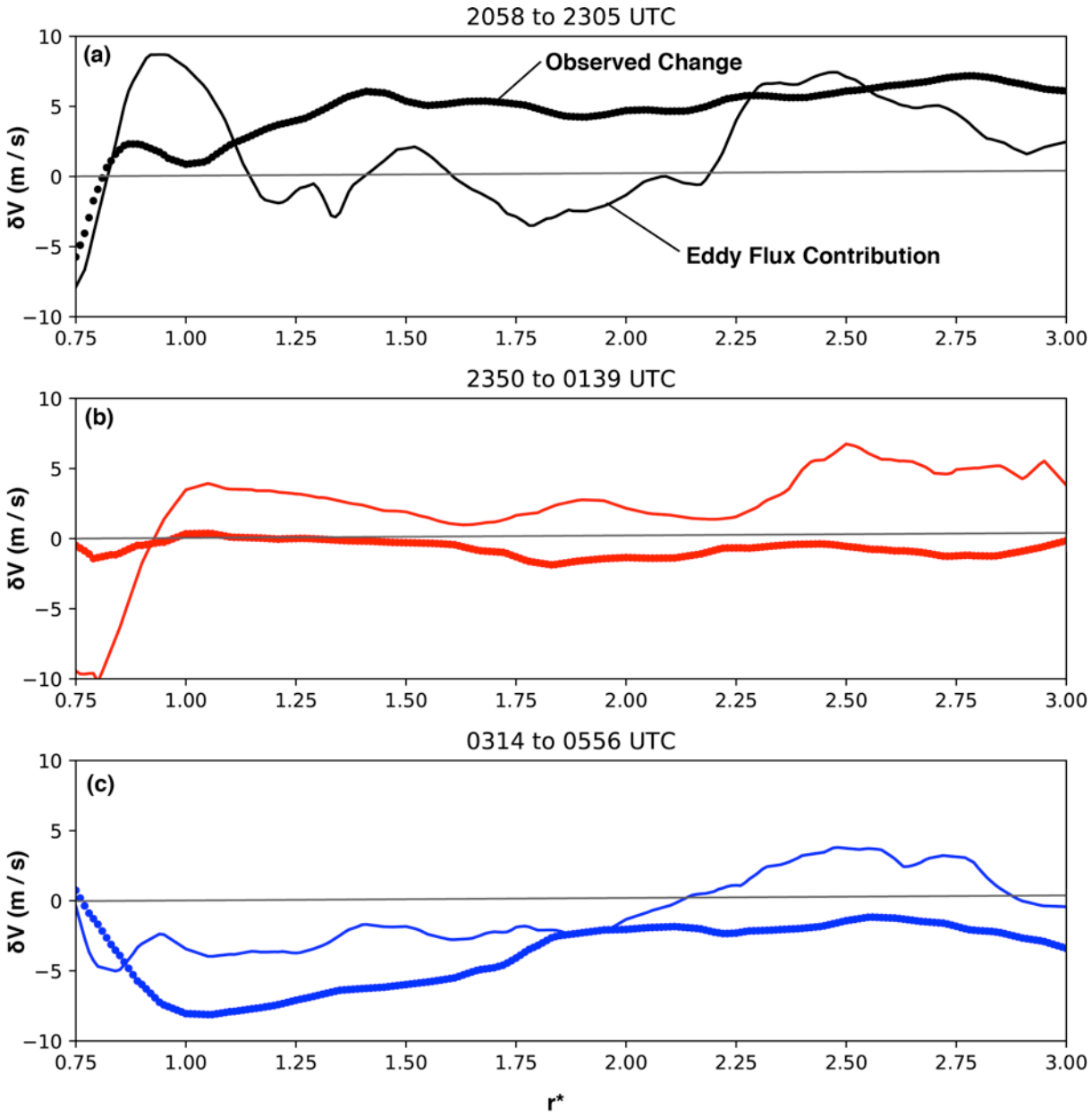

Figure 3.6. Azimuthally averaged profiles of cumulative tangential wind change (thick line) and the cumulative eddy flux (thin solid line are shown as a function of reference radius r^*. Each dual-Doppler time period surrounding outages of SR2 are shown separately for 2058-2305 UTC in (a), 2350-0139 UTC in (b), and 0314-0556 UTC in (c).

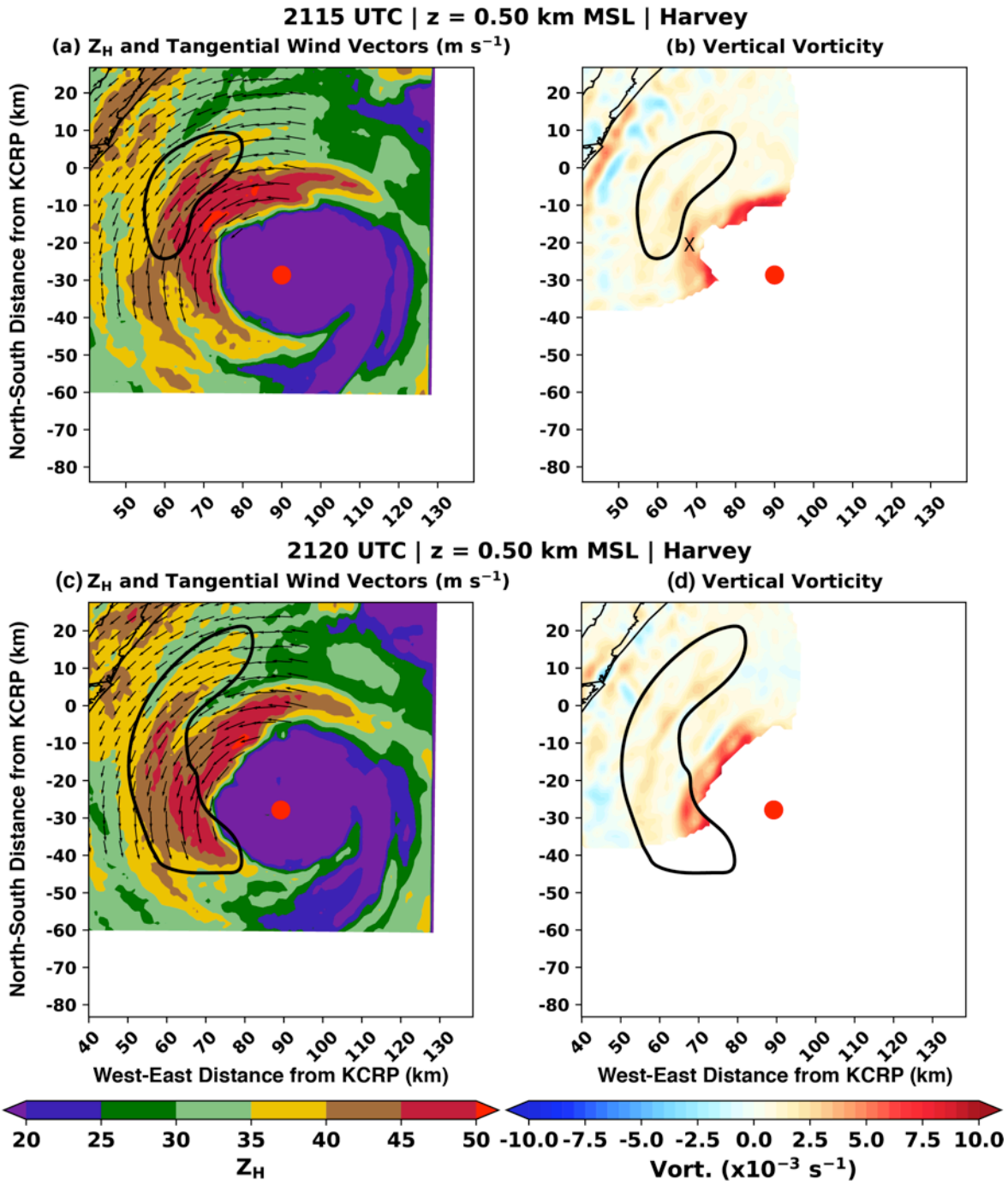

Figure 3.7. Dual-Doppler analyses at 2115 UTC in (a) and (b) and at 2120 UTC in (c) and (d) are shown. In (a) and (c), reflectivity (dBZ) and tangential wind vectors are shown. In (b) and (d), vertical vorticity is shown.

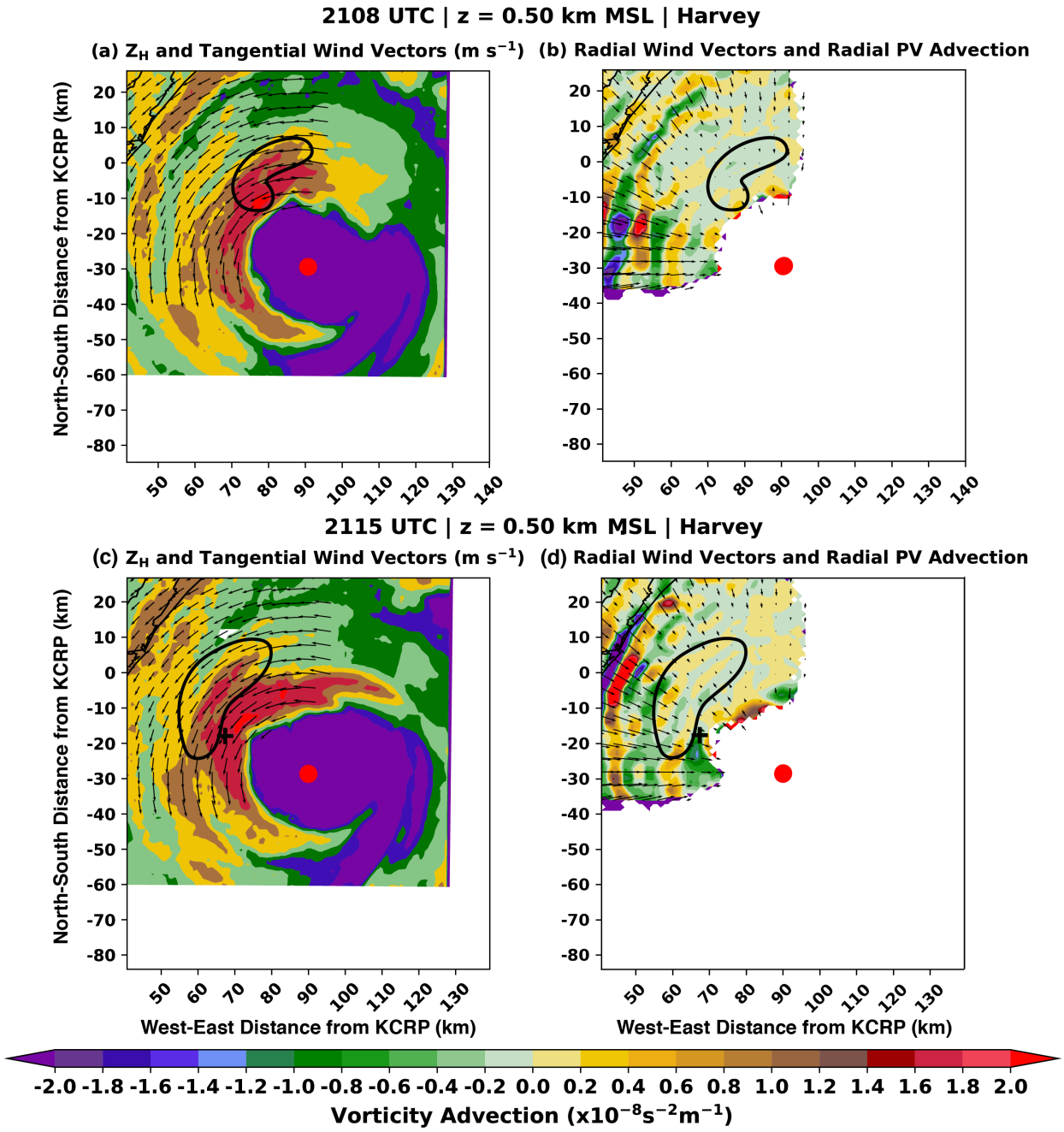

Figure 3.8. Dual-Doppler analyses at 2108 UTC in (a) and (b) and at 2115 UTC in (c) and (d) are shown. In (a) and (c), reflectivity (dBZ) and tangential wind vectors are shown. In (b) and (d), storm-relative radial PV advection (color-filled contours) and storm-relative radial wind vectors are shown.

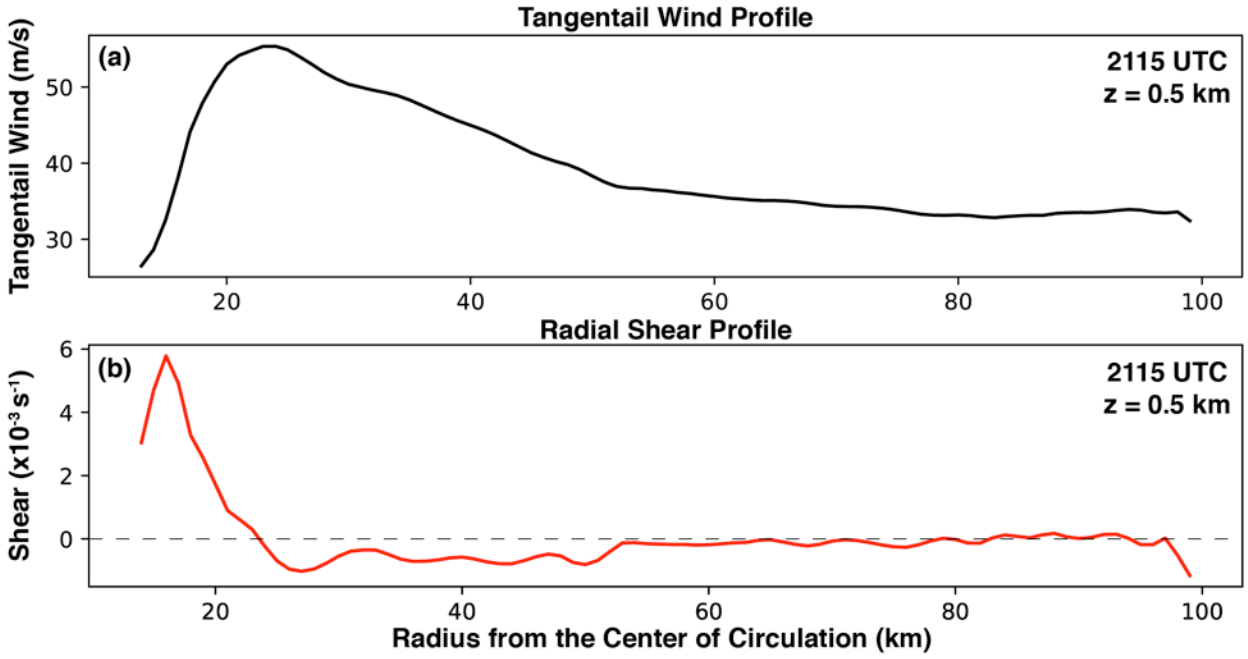

Figure 3.9. The radial profiles of the azimuthally averaged tangential wind (a) and the radial derivative of the azimuthally averaged tangential wind (b) are shown for the 2115 UTC analysis at an altitude of 0.5 km.

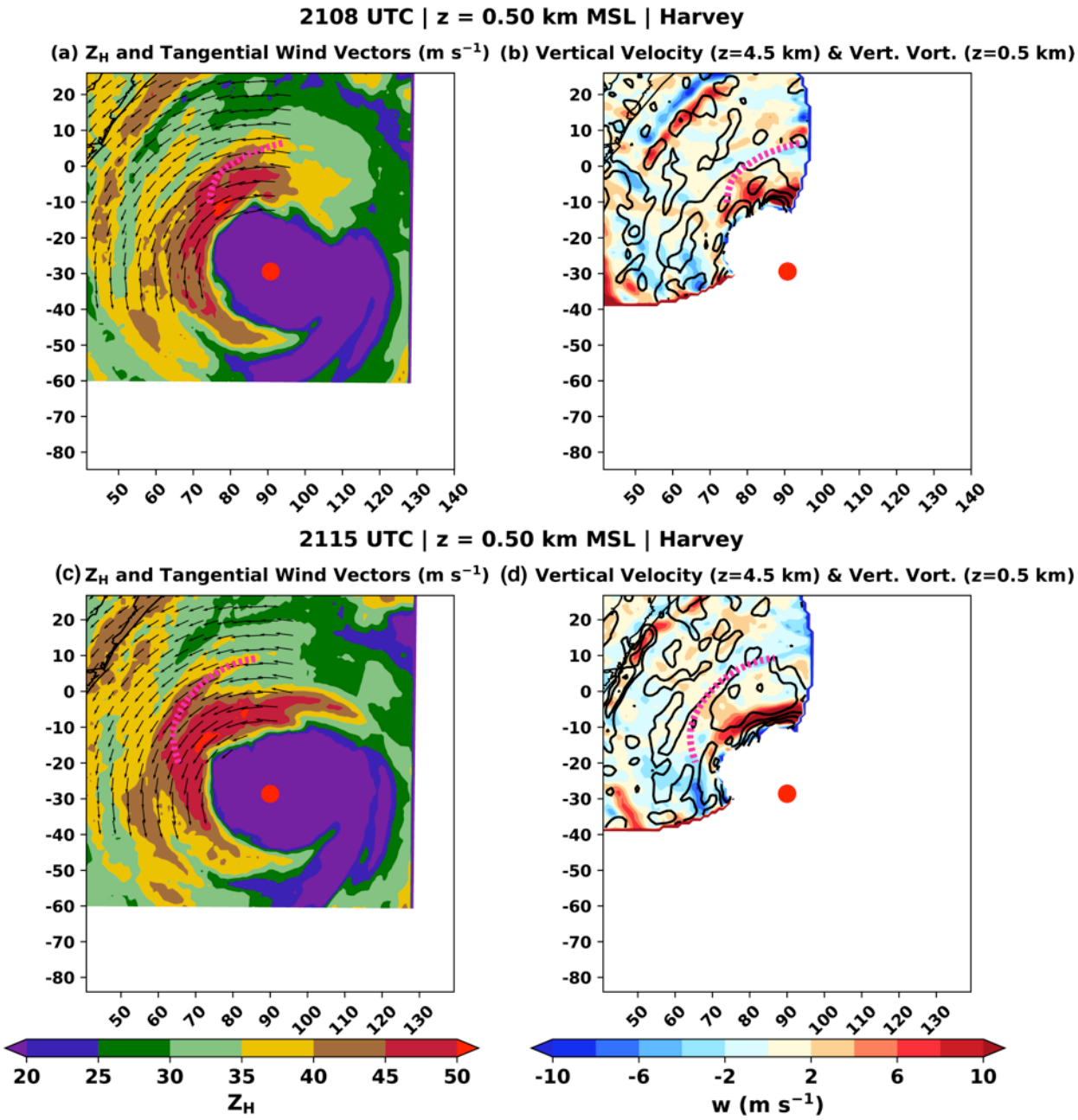

Figure 3.10. As in Figure 3.8, but (b) and (d) display the vertical velocity at 4.5 km altitude (color-filled contours) and vertical vorticity at 0.5 km altitude (black contours every 2×10^{-3} s^{-1} starting at 1×10^{-3} s^{-1}).

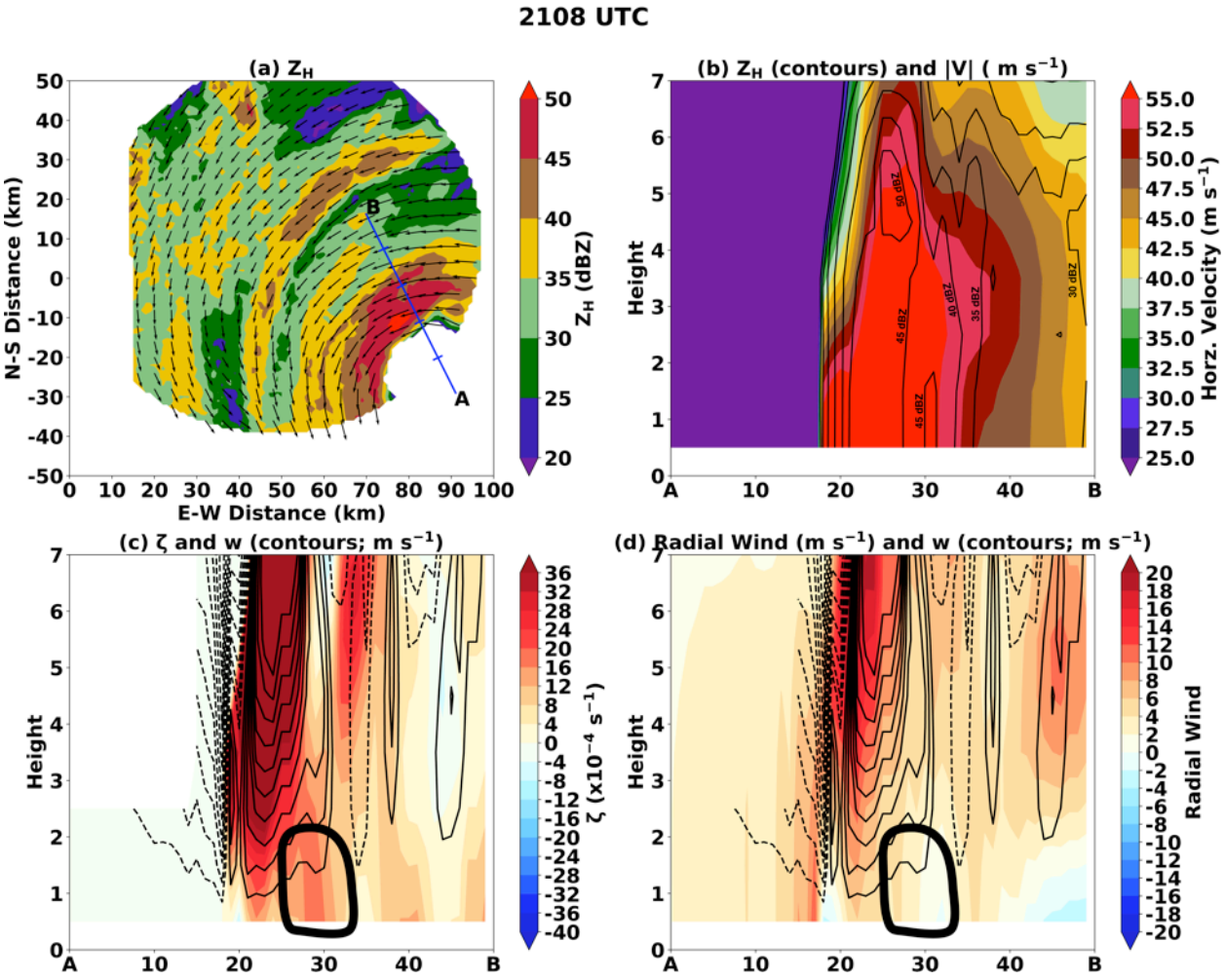

Figure 3.11. (a) The plan view of reflectivity and total wind vectors is shown. The blue line indicates the location of the cross section A-B, with ticks every 10 km along the cross-section for reference. In (b), the horizontal velocity magnitude with height along A-B is shown in the color-filled shading with reflectivity contours shown for reference. Similarly in (c), the color-filled shading represents the vertical vorticity in height along A-B. The solid (dashed) black contours are positive (negative) vertical velocity every 1 m s^{-1} with the 0 m s^{-1} line omitted. In (d), the color-filled shading represents the radial wind along the cross-section. The black contours are as in (c).

Chapter 4: VRW Evolution and Their Kinematic Character

4.1 Introduction

In Chapter 3, the influence of asymmetric dynamics in Hurricane Harvey (2017) was discussed. It was shown that asymmetries in the eyewall of Hurricane Harvey prior to and during landfall influenced the intensity (symmetric vortex) and were responsible for initiating at least one rainband outside the eyewall. The initiation of the rainband via this process was shown to be similar to VRW activity demonstrated in idealized numerical modeling studies (Montgomery and Kallenbach 1997; Möller and Montgomery 2000; Gao and Zhu 2016). Observed fluxes of potential vorticity (PV) in the low levels of the atmosphere were shown to be positive radially inward. But the PV flux impact on the primary vortex circulation was likely secondary to unmeasured latent heating influences. Thus, VRWs are a the mechanism by which PV is fluxed toward the eyewall and was shown to have at least some contribution to intensity change. Here, we examine the influence of VRWs on the production of narrow rainbands in the inner core of the hurricane. The initiation of rainbands by VRW processes is a common topic in the literature (e.g., Moon and Nolan 2015), but remains an unresolved subject. VRW-driven rainbands are essential to understand as they may contribute significantly to the total precipitation experienced by communities. Water-related fatalities, including inland flooding, during hurricane landfalls exceed those associated with wind in the United States (Rappaport 2014). Thus, understanding kinematic and microphysical processes that can lead to enhanced flooding are vital to improve model guidance and quantitative precipitation estimation.

Most discussion of VRW driven rainbands comes from idealized and full-physics simulations of TCs over the ocean (Möller and Montgomery 2000; Chen and Yau 2001; Wang 2002a,b; Chen and Yau 2003; McWilliams et al. 2003; Franklin et al. 2006; Braun et al. 2006;

Judt and Chen 2010; Wei et al. 2010; Hall et al. 2013; Menelaou and Yau 2014; Cotto et al. 2015; Gao and Zhu 2016). Outward-propagating waves modified by horizontal shear and restored by the radial gradient of storm-relative vorticity are thought to arise from asymmetries often near the TC eyewall (MK97). The waves, analogous to planetary Rossby waves, tend to propagate against the mean azimuthal flow, which has been a long-observed characteristic of rainbands near the eyewall (MacDonald 1968; Guinn and Schubert 1993). Seen as trailing spirals in the PV field, full-physics simulations have shown that spiraled PV structures induce boundary layer convergence on their radial-outward side, leading to updrafts tied to secondary rainbands (Houze 2010) near the eyewall (Chen and Yau 2001; Wang 2002a; Franklin et al. 2006; Hall et al. 2013). Due to the radial limit (i.e., the stagnation radius) to which the waves may propagate, rainbands beyond radii 2-3 times that of the radius of maximum wind (RMW) are not generally not attributed to VRW dynamics. This is because the stagnation radius represents a point where the radial gradient in storm-relative vorticity becomes very small and the wave energy is absorbed (Montgomery and Kallenbach 1997; Abarca and Corbosiero 2011; Cotto et al. 2015). Some studies have suggested that the shearing effect of the tangential wind gradient can often suppress VRWs with azimuthal wavenumbers greater than 3 or 4 (Wang 2008), suggesting that low azimuthal wavenumber disturbances in the vortex are the most likely to procure significant VRW propagation.

Limited observational evidence has supported the hypothesis that secondary rainbands are formed by VRWs processes. Reasor et al. (2000) showed that azimuthally elongated vorticity asymmetries were found in the presence of secondary rainbands in a study of Hurricane Olivia (1994). Although their airborne dual-Doppler analyses were taken at 30-minute temporal resolution, they were able to show that vorticity asymmetries explained by a dominant

wavenumber 2 structure were reasonably characteristic of barotropic VRWs. Radial wavelengths of 5-10 km were observed with the perturbations, which was similar to the wavelength structure of rainbands in the vicinity. Thus, rainbands were concluded to be associated with symmetrizing VRWs. Corbosiero et al. (2006) used the reflectivity structure of Hurricane Elena (1985) to document the azimuthal propagation speed of rainbands through the use of a coastal incoherent radar. The time-evolution of the radar reflectivity field associated with secondary rainbands was shown to support upwind propagation of the rainbands, consistent with VRW dynamics. Recently in a study of Hurricane Matthew (2016) over the ocean, Fischer et al. (2020) showed trailing spiraled vorticity features characteristic of numerical simulations and limited observations of VRWs. Similar to the work of Corbosiero et al. (2006), upwind propagation of the features was observed.

In contrast to the hypothesis involving VRW dynamics, some studies of secondary rainbands have suggested that VRWs are often not the primary mechanism by which they form. For example, Moon and Nolan (2015) performed a numerical simulation on Hurricane Bill (2009). Rainbands in their simulation were not associated with trailing vorticity spirals. Through use of a passive tracer in their simulations, the non-linear advection of the tracer field was shown to resemble trailing spiraled rainbands, suggesting VRWs are not necessarily responsible for rainband formation. Other hypotheses such as inertia-gravity waves have also been suggested to trigger rainband formation in TCs (e.g., Chow et al. 2002), but have generally received less attention recently due to the frequently observed upwind propagation of spiral rainbands.

Regardless of these other possibilities, VRWs have become a dominant hypothesis for secondary rainband formation based on numerical simulations, but have been observed very little in a kinematic framework, particularly at landfall. Additionally, full-physics modeling studies

focused on rainbands at landfall are very limited. Nevertheless, Hall et al. (2013) demonstrated that symmetrizing VRWs were instrumental in secondary rainband formation in Typhoon Morakot (2009). Orographic lift over Taiwan in the presence of the VRWs enhanced the vertical velocities and precipitation efficiency of secondary rainbands in their simulation. Given the dearth of observational studies of VRWs in general and no kinematic studies of VRWs at landfall, it is imperative to understand secondary rainband formation and validate numerical simulations. This chapter presents a summary of observations of hurricane landfalls taken by the SMART radars. In particular, this chapter will focus on the kinematic structure of secondary rainbands observed at landfall to compare existing literature regarding VRW-driven rainbands to observations in high temporal (~5 minutes) and spatial (1 km) resolution. Landfall observations will also be compared to observations taken over the open ocean as well to examine the general applicability to the observations at landfall to TCs over the ocean.

4.2 Data and Methods

4.2.1 SMART Radar Data

The Hurricane Harvey (2017) SMART radar dataset is optimal for examining VRW processes, as the primary vortex was compact, strong enough to be classified as a major hurricane at landfall, and the storm passed through the dual-Doppler lobe. In addition to Harvey, radar observations from Hurricanes Isabel (2003) and Matthew (2016) are included in this study of VRW-driven rainbands. Isabel was a much larger circulation with a broad annulus of precipitation preceding the eyewall. Like Harvey, the center of circulation passed through the heart of the dual-Doppler network. But Isabel was a weakening category 2 hurricane at landfall and had undergone a failed eyewall replacement cycle just prior to landfall (Beven and Cobb

2003). The outer eyewall dissipated upon landfall while a convective burst initiated a new partial inner eyewall (Curry 2010). Matthew made landfall as a category 1 hurricane in South Carolina (Stewart 2017). The SMART radars sampled Matthew while the storm was a weakening category 2 hurricane offshore of the Georgia-Florida border. The center of circulation grazed the outer edge of the dual-Doppler lobes. Hence, the Isabel and Matthew observations are more limited in their coverage, capturing rainbands mainly outside of the eyewalls in a section of the inner core rather than across the entire inner core. Nevertheless, the observations offer significant opportunity to compare rainband structures near landfall to a more complete view of the inner core in Hurricane Harvey and to develop more general conclusions than could be obtained from Harvey alone.

During Hurricane Isabel (2003), data were taken from both the SR1 and SR2 radars before their dual-polarimetric upgrade (Biggerstaff et al. 2017, 2021). Both radars were operated in quasi-time synchronization (i.e., there was a slight offset of generally less than 1 minute in the volume collection times of each radar) and collected both sector and 360° volumes in order to achieve a variety of data collection goals. As shown in Figure 4.1b, the dual-Doppler domain between both SRs was primarily over Pamlico Sound and the outer banks of North Carolina. As such, the observations characterize portions of Isabel that interacted with land and should be interpreted in such a context.

In Hurricane Matthew, the dual-polarization version of SR2 was quasi-time synchronized with the WSR-88D in Jacksonville, FL (KJAX). Specifically targeting inner core rainband evolution, data were collected in 150° sector volume scans with approximately two SMART radar volumes per volume collected by KJAX. Much closer to the coast than in the Isabel case, the position of SR2 and KJAX afforded a dual-Doppler retrieval region mostly over the Atlantic

Ocean (Figure 4.1c). As such, the observations from Matthew are more representative of those taken over the open ocean, albeit in a coastal area, rather than observations with significant land interactions.

In Major Hurricane Harvey (detailed in Chapter 3 of this dissertation), the dual-Doppler retrieval regions between SR2 and KCRP captured the evolution of Harvey both offshore and during the landfall. Dual-Doppler retrievals were available approximately every five minutes, similarly synchronized with the WSR-88D in Corpus Christi, TX (KCRP). The dual-Doppler retrieval region extended offshore (see Figure 4.1d) where processes in and near the eyewall were captured prior to landfall.

Each of the SR datasets discussed here were processed following the method of Alford et al. (2019a) and described in Appendix 1. In summary, all volumes collected by the SRs and the WSR-88Ds were objectively dealiased in the Python-Atmospheric Radiation Measurement Toolkit (Py-ART; Helmus and Collis 2016) and further quality controlled in Solo3 (Oye et al. 1995). The radar data (radar reflectivity and Doppler velocities) were interpolated to 1.0 km Cartesian grids following a Natural Neighbor interpolation technique (Sibson 1981) documented by Betten et al. (2018) and Biggerstaff et al. (2021). The Cartesian datasets for each case were then passed to a variational dual-Doppler analysis technique (Potvin et al. 2012) to retrieve the three-dimensional flow. Table 4.1 documents the specific dual-Doppler domain setup for each case.

4.2.2 HIWRAP Data

The High Altitude Imaging Wind and Rain Airborne Radar (HIWRAP; Li et al. 2008) is routinely flown aboard a NASA Global Hawk over mature TCs. It uses two dual-frequency, off-

nadir radars (antennas pointing at 30° and 40°) that sweep out conical surfaces below the aircraft track to sample a 10-20 km wide tropospherically deep swath beneath the aircraft. The fore and aft "looks" at any given point in space are used to perform wind retrievals. In this manuscript, the coplane method of Didlake et al. (2015) is employed. The technique is applied in a natural coordinate frame to directly retrieve two wind components (the along-track component and the along-radar-beam component) and then use mass continuity to retrieve the third (the cross-radar-beam component). Here, data from Hurricane Matthew were retrieved for 2 passes (Figures 4.2a and 4.2c) overtop Matthew on 7 October 2016 while it was moving north parallel to the Florida coast. The first (second) pass begins at 1306 UTC (1518 UTC) and ended at 1345 UTC (1600 UTC). At the time of the passes, the National Hurricane Center estimated Matthew to be a Category 3 (96-112 kt) hurricane (Stewart 2017). For the two passes, the region exterior of the eyewall was characterized by multiple rainbands (see nadir reflectivity in Figures 4.2b and 4.2d), which will be examined briefly for comparison to those observed closer to landfall.

4.3 Hurricane Harvey

While Hurricane Harvey is often remembered for its catastrophic flooding across southeast TX and southwest Louisiana after the initial landfall on 26 August 2017, the landfall itself is known for significant wind damage (Wurman and Kosiba 2018; Fernandez-Caban et al. 2019). Here the drivers of precipitation near the eyewall region in the form of weakly and moderately convective rainbands are examined. For reference herein, any use of "downwind" ("upwind") refers to counter-clockwise downwind (clockwise upwind) relative to the center of circulation of a hurricane.

4.3.1 Rainband Kinematics

To first set of inner core rainbands selected for comparison to past observations and simulations are taken from the dual-Doppler analyses conducted at 2120 UTC (Figures 4.3a and 4.4a-d) and 2249 UTC (Figures 4.3b and 4.4e-h) on August 25, 2017 from Hurricane Harvey while the eyewall and the inner core rainbands were off the coast. Outside of the eyewall several rainbands, encircled for reference by black contours in Figure 4.3 and cyan contours in Figure 4.4, are seen in their formative and mature stages.

At 2120 UTC, radar reflectivity and vertical velocity at 1.5 km (4.5 km) altitude and are overlain in Figure 4.4a (Figure 4.4c). The rainband outside the northwest portion of the eyewall is characterized by several updraft maxima along the band greater than 2 m s^{-1} at 4.5 km altitude (Figure 4.4c). These positive vertical drafts are seen in the northern portion of the band in the vicinity of 1.5 km reflectivity maxima. Downwind, vertical drafts become largely negative, but on the radially inward and outward peripheries of the band, rather than along the band's axis. In Figure 4.4b, vertical vorticity (color shading) at 1.5 km is shown. A clearly defined, azimuthally contiguous vertical vorticity maximum is clearly associated with the reflectivity band in Figure 4.4a. Several local maxima $>2\times10^{-3}$ s^{-1} along the band can also be seen. Aloft at 4.5 km altitude in Figure 4.4d, the vorticity maximum is less defined, but vorticity maxima generally exist downwind of local vertical velocity maxima in the northern portion of the mature band. Additionally, the updraft contour near the reflectivity maximum at 4.5 km altitude (Figure 4.4c) is radially inward from the maximum in reflectivity by several kilometers. Similarly, the vertical vorticity maximum is displaced radially inwards from the vertical velocity maximum. Previous modeling studies of VRW-driven rainbands have suggested that there exists a radial offset in the kinematic structures (vorticity and vertical velocity) such that the vorticity and vertical velocity

maxima are displaced by a one-quarter radial wavelength (hereafter referred to as wavelength unless otherwise noted). It appears that the rainband in question is similar in its kinematic structure to Wang (2002a).

Later at 2249 UTC, two rainbands are denoted in Figures 4.4e-h. The rainband to the southwest of Harvey's eye is more pronounced than the northern rainband that appears to be in its decaying stages. To the extent it can be analyzed, the rainband on the southern side is characterized by an azimuthally contiguous region of positive vertical velocities in the upwind portion of the band (Figure 4.4e, g), but with a less pronounced vorticity structure than the band examined at 2120 UTC. Nevertheless, there exists a general alternating updraft/downdraft structure with increasing radius in this region with similar perturbations in vertical vorticity offset by one-quarter of a wavelength (Figure 4.4h). It should be noted that this particular band decayed rapidly in reflectivity after this analysis.

The northern band in Figures 4.4e-h also displays several interesting features of note and appears to be in its formative stages. The rainband is relatively weak in reflectivity at 1.5 km (Figure 4.4e), but is associated with a distinct vertical vorticity maximum (Figure 4.4f). Aloft, the vertical velocity structure in the region resembles a pronounced wave-like structure radially outward of the eyewall, especially where the rainband has started to separate from the eyewall reflectivity (Figures 4.4 g, h). At 4.5 km, the 2 m s^{-1} updraft contour appears to be along the edges of the developing rainband with a downdraft, rather than updraft, close to the reflectivity axis (Figure 4.4g). This vertical velocity structure is in contrast to that observed in the other, more mature rainbands and may be the result of dynamical and microphysical influences of the eyewall convection. However, the magnitude of the wavelike vertical drafts decays radially outward from the developing rainband, similar to those observed away from the more mature

bands (Figure 4.4g). Co-located with the inner-most wave, an azimuthally contiguous region of positive vertical vorticity is seen at 1.5 km altitude (Figure 4.4d), which curves anticyclonically to intersect with a vorticity and reflectivity maximum in the eyewall, similar to the rainband shown in Chapter 3. The character of the vertical vorticity at 4.5 km altitude (Figure 4.4h) suggests that in this case, the vorticity observed aloft is nearly co-located with the vertical velocity maximum, rather than offset as shown in the more mature rainband.

The vertical structure of the northern region outlined in the 2249 UTC analysis is examined further through cross-section A-B shown in Figure 4.5a. In the vertical cross-section of reflectivity (Figure 4.5b), a rainband at 30-35 km range with reflectivity between 35 and 40 dBZ can be seen radially outward of the eyewall (where the eyewall is located between 20 and 30 km). The eyewall is denoted by a strong, radially outward-sloping updraft near 20 km range with the radar reflectivity axis radially outward from the updraft core (Figures 4.5a, c), similar to conceptual models of hurricane eyewalls (Houze 2010). Dynamically and microphysically forced downdrafts exist on both sides of the eyewall updraft. In particular, the radially outward downdraft, near 25 km range, is associated with a high reflectivity core where negative buoyancy from precipitation loading would be most expected. The radial divergence (Figure 4.5d) underneath this precipitation driven downdraft leads to strong low-level convergence farther radially outward, contributing to the moderately strong updraft that precedes the developing rainband. Low-level radial inflow from the environment through the inner core towards the eye is a common feature required to drive the hurricane's secondary radial circulation (e.g., Houze 2010; Zhang et al. 2011). A mid-to-low level convective downdraft in the high reflectivity of the eyewall is also a common feature. Hence, it is likely that most, if not all, developing rainbands

that form from an asymmetry in the eyewall initially have an updraft radially inward from the reflectivity axis of the rainband.

As noted in the plan view of vertical motion at 4.5 km, the reflectivity core of the rainband is associated with a strong downdraft. While microphysical factors like precipitation loading and melting aloft would likely be contributing to negative buoyancy in this region, it is likely that this downdraft is dominated by dynamic forcing associated with compensating subsidence and gravity waves from the eyewall, similar to the warm downdrafts observed outside the convective region of squall lines (Biggerstaff and Houze 1991; 1993; Sun et al. 1993). The likelihood that the initial updraft/downdraft couplet around the developing rainband is not purely driven by VRW dynamics is further supported by the coincidence of the vorticity maxima and minima with the updraft and downdraft, respectively (Figure 4.5c). Nevertheless, the role of VRW dynamics is clearly evident in the structure of vertical drafts and vertical vorticity farther outward from the initial stages of the rainband formation. Here, the vertical drafts precede the vorticity maxima by roughly one-quarter of their horizontal wavelength, in agreement with past work (Wang 2002a). Indeed, the updraft at ~ 46 km range is associated with a mature rainband.

Microphysically in the plane of the cross-section, the reflectivity maximum (~33 km range) is radially outward of the vertical velocity maximum (~29 km range). While some hydrometeors being grown in the updraft are falling out (approximately 28-31 km range), it is likely that hydrometeors are being advected radially outward toward the downdraft by the positive radial flow (i.e., the secondary circulation; Figure 4.5d) as they fall, leading at least a partial explanation for the offset of the maximum reflectivity radially outward of the updraft.

4.3.2 Comparison to VRW Dynamics

Discussed in detail in MK97, the dispersion relation for VRWs is generally derived for an idealized barotropic fluid. The extension of VRW dynamics to a three-dimensional baroclinic fluid was shown in Gao and Zhu (2016), which is more representative a real TC over the ocean than the simpler model of Montgomery and Kallenbach (1997). However, knowledge of the base-state profile of potential temperature, which cannot be derived from a dual-Doppler analysis, is required to compare observations of VRWs to the dispersion relation of Gao and Zhu (2016). Thus, as in previous studies (e.g., Corbosiero et al. 2006; Franklin et al. 2006) the VRW-like features seen here are compared to the barotropic dispersion relation (4.1) in terms of the angular velocity $\bar{\Omega} = \bar{v}/r$ (where v is the tangential wind and r is the radius from the center of circulation), ζ is the relative vertical vorticity, the radial wavenumber k, and the azimuthal wavenumber n. For reference, an overbar quantity denotes an average taken with respect to azimuth.

$$\omega = n\overline{\Omega} + \frac{n}{r}\frac{\frac{d\overline{\zeta}}{dr}}{k^2 + \frac{n^2}{r^2}} \qquad (4.1)$$

The radial wavenumber k is shown in Montgomery and Kallenbach (1997) to be the time-dependent radial wavenumber (4.2) where k_0 is the initial radial wavenumber and t is time.

$$k = k_0 - nt\frac{d\Omega}{dr} \qquad (4.2)$$

As in Franklin et al. (2006), (4.2) may be simplified by assuming an initial value problem, yielding $k = k_0$. From (4.1) and (4.2), a simple form of the azimuthal phase speed $c_{p\lambda} = \omega r/n$ of a Rossby wave may be obtained in (4.3).

$$c_{p\lambda} = r\overline{\Omega} + \frac{\frac{d\overline{\zeta}}{dr}}{k^2 + \frac{n^2}{r^2}} \qquad (4.3)$$

It can be easily shown that for typical profiles of the azimuthally averaged tangential wind, all terms in (4.3) are positive except the radial derivative of the azimuthally averaged vorticity. This implies that the azimuthal phase velocity of a VRW should be counter to the azimuthal mean flow, represented by $r\overline{\Omega} = \bar{v}$. Thus, in simplest terms, a VRW is expected to propagate counter to the mean tangential flow.

In MK97, the radius in (4.1) is deemed a "reference radius." Here, we calculate $c_{p\lambda}$ as a function of reference radius in order to elucidate the general azimuthal phase speed expected for a VRW for Harvey's average wind profile for varying radial wavelengths (5, 10, 15, and 20 km). As input into (4.1), the average tangential wind profile and the average vertical vorticity over all dual-Doppler analyses from 2058 UTC to 0000 UTC was computed. Figure 4.6 shows the profile of the storm-relative vorticity (Figure 4.6a) and the angular velocity (Figure 4.6b) computed from the dual-Doppler time-averaged profiles of tangential wind (Figure 4.6c). Integral to VRW dynamics, the radial gradient of storm-relative vorticity is shown in Figure 4.6d computed by taking the radial derivative of the average vorticity profile in Figure 4.6a. Using these inputs and assuming n = 2, the anticipated azimuthal phase speed was computed via (4.3) for radial wavelengths λ = 5 km, 10 km, 15 km, and 20 km. Adjusting n did not significantly change the computation of the expected phase speed. By varying the wavelength (wavenumber), the dependence of $c_{p\lambda}$ on the initial radius and initial wavelength can be seen, which varies most strongly in and just outside the eyewall (20-30 km radius). Compared to the average tangential wind, the instantaneous phase velocity is expected to be on the order of 5-20 m s^{-1} less than the background mean based on this simple, barotropic analysis. However, the exact phase speed may be drastically different from this relatively simple model through the incorporation of, for

example, baroclinic effects (Gao and Zhu 2016) and does not account for vertical propagation (Möller and Montgomery 2000; Gao and Zhu 2016).

The propagation of rainbands around a constant radius can be used to elucidate the approximate phase speed. While this has been done extensively in modeling studies, observational comparison of phase speeds of convectively coupled VRWs to three-dimensional kinematics is extremely limited in time and/or space (e.g., Guimond et al. 2020). Using the available dual-Doppler observations of Hurricane Harvey, a time series of the average tangential wind (i.e., symmetric component of the flow) was constructed at a constant radius of r = 35 km. It should be noted *kinematic* observations are not always available around the entire radius circle due to the radar beam geometry limitation upon dual-Doppler analyses. Nevertheless, observations were generally available over >180° of the radius circle for most times. Reflectivity observations were available for all portions of the radius circle, as they are not limited by dual-Doppler beam geometry. Thus, the kinematic data are used estimate the symmetric component of the circulation compared to the propagation of rainbands via reflectivity.

Figure 4.7 displays a Hovmoller diagram of reflectivity perturbation. The perturbation quantity was computed by subtracting the time-mean reflectivity for each azimuth (1° increments) from the total reflectivity field. This was done to eliminate the general wavenumber-1 asymmetry in the reflectivity field during Harvey's landfall (e.g., see Figure 4.3). In Figure 4.7, the dashed contours characterize the average tangential wind at various times through the dual-Doppler analysis observational period at 1.5 km altitude. The solid black contours were subjectively drawn to bring attention to particularly prominent rainbands noted to be rotating through the constant radius circle. For the most part, the swaths of reflectivity perturbation that are annotated appear to propagate slower than the average tangential wind, suggesting an upwind

propagation speed of most rainbands and consistency with VRW dynamics. Hence, most of the phase speeds, are consistent with the instantaneous solution to (4.3) described in Figure 4.6. It is plausible that diabatic and baroclinic effects that cannot be considered in this dataset account for any differences. Nevertheless, upwind propagation of rainbands in this case is remarkably consistent with past numerical modeling studies of VRW-driven rainbands (Chen and Yau 2001; Wang 2002a,b; Franklin et al. 2006; Abarca and Corbosiero 2011; Hall et al. 2013) and dissimilar to the expected characteristics of, for example, pure inertia-gravity waves (Willoughby 1977).

There are several rainbands in Figure 4.7 (e.g., ~330° and near 2200 UTC) of note that seem to propagate very near the average tangential wind speed as well. While VRW-driven rainbands are expected to propagate against the mean wind, Figure 4.6 supports that the fact that azimuthal phase speed of a VRW may be very close to the tangential wind for large radial wavenumbers (small radial wavelengths). Gao and Zhu (2016) additionally noted that in the case of limited baroclinicity, the vertical propagation of VRWs becomes limited and adheres closer to the barotropic solution of MK97. Thus, for a sufficiently small radial wavelength, a VRW itself may be expected to propagate close to the tangential wind speed. However, other solutions proposed by Moon and Nolan (2015) suggest that rainbands that propagate closer to the tangential wind are likely the result of convective structures and the associated hydrometeors being advected (non-linearly) in the hurricane flow. Their study noted a lack of trailing PV spirals specifically to conclude that rainbands in their simulation were not the result of VRW dynamics. However, in Hurricane Harvey most rainbands seen here are associated with trailing spirals of relative vorticity maxima, similar to those discussed in Chapter 4.3.1. While it is indeed plausible that some rainbands are not the result of convectively coupled VRWs, the

evidence described herein suggests that VRW-driven rainbands were indeed present near the landfall of Hurricane Harvey.

4.4 Additional Hurricanes

While Hurricane Harvey is one of the most well-sampled landfalling hurricanes to date (Fernandez-Caban et al. 2019), the question arises if the same rainband features observed in Harvey are generally seen in other landfalling TCs. The SMART radar program has captured several datasets that are ideal for comparison including the landfall of Hurricane Isabel (2003) and the near-coast passage of Hurricane Matthew (2016).

4.4.1 Hurricane Isabel (2003)

During Isabel's landfall, the SMART radars captured multiple rainband features to the northwest of the eyewall with the most prominent being between 1430 and 1500 UTC on 18 September 2003. Unlike in Hurricane Harvey, the radar task cycle was focused on objectives other than collecting volumes for three-dimensional wind retrieval, which makes the measurement of the propagation speeds of the rainbands difficult. Thus, observations focused on wind retrievals are only available to examine the particular rainband passages between 1440 and 1500 UTC. In Figure 4.8, two dual-Doppler analyses (1442 and 1452 UTC) are shown with the two particular rainbands to be examined annotated by cyan contours. Similar to previous analyses, reflectivity and wind vectors are shown in Figures 4.8a and 4.8c for 3.0 km altitude, and vertical velocity (4.5 km altitude; black contours) and vertical vorticity (3.0 km altitude; color-shading) are shown in Figures 4.8b and 4.8d.

Similar to that seen in Hurricane Harvey (Chapter 4.3.1), azimuthally-elongated rainbands exist radially outward of the hurricane eyewall (denoted by the white arrow in Figures 4.8a and 4.8c). Both rainbands are characterized by reflectivity values exceeding 45 dBZ at 3.0 km altitude. The rainband in the northwest portion of the domain is quite far from the eyewall and does not spiral into the eyewall in the dual-Doppler domain. However, the rainband nearer the eyewall (southeast portion of the domain) appears to spiral into the eyewall near a prominent reflectivity maximum, similar to the rainbands seen in Hurricane Harvey. Kinematically, both rainbands are characterized by vorticity maxima that are themselves azimuthally elongated and radially lag the reflectivity maxima. Interestingly and generally consistent with the mature rainband observations from Hurricane Harvey, the vertical velocity maxima (about 4 m s^{-1}) at 4.5 km altitude (black contours in Figures 4.8b and 4.8d) are radially outward of the vertical vorticity maxima. Along each band, there exists a strong degree of complexity in terms of the reflectivity, vertical velocity, and vertical vorticity structures, suggesting the larger-scale vertical motion is generally caused by VRW propagation but modified by meso-gamma scale (*O*[2-20 km]) kinematic and thermodynamic variability. It is also interesting to note that the prominent vertical motion generally resides in the upwind portion of the bands and subsides anti-cyclonically along the band, again generally consistent with the observations taken in Hurricane Harvey.

To further investigate the vertical kinematic structure as in Hurricane Harvey, a vertical cross section is shown through the southeastern rainband near the downwind edge of the 2 m s^{-1} updraft in Figure 4.9a, showing a 20 km-wide cross section (labeled A-B) through the band. In the vertical, reflectivity values are just above 45 dBZ at maximum (approximately 12 km range in the cross section) in the cross section and a radar bright band can be discerned at about 5-5.5

km in height, namely in regions exterior to the reflectivity maximum. The kinematic data in Figures 4.9c and 4.9d show a vertically coherent wave in the cross section. Specifically, vertical velocities (black contours) are maximized at about 9 km range with minima on either side of the updraft at 4 and 13 km range, suggesting an approximate radial wavelength for this particular wave of 9-10 km. Being situated at 9 km range, the vertical velocity maximum radially lags the reflectivity maximum (12 km range) through the depth of the column shown. At about 8 km range, the vertical vorticity maximum can be seen, which is maximized in the lowest 3.5 km of the analysis. There also exists a wind maximum in the lowest few kilometers of the analysis (Figure 4.9d) located radially inward of the reflectivity maximum but co-located with the updraft of the wave.

4.4.2 Hurricane Matthew (2016)

In Hurricanes Harvey and Isabel, the dual-Doppler retrieval region was in the downshear half of the two hurricanes. The most vigorous rising motion is generally anticipated in the downshear quadrants (DeHart et al. 2014), suggesting the observations summarized thus far are representative of being downshear. However, in Hurricane Matthew the dual-Doppler retrieval region, which was largely offshore of the Georgia coastline, captured several rainbands seemingly propagating off of the eyewall in the upshear left quadrant of Matthew. Indeed, the reflectivity structure of Matthew, being subjected to strong shear at the time, had become wavenumber 1 asymmetric (i.e., maximum reflectivities downshear and minimum reflectivities upshear).

Figure 4.10 shows two dual-Doppler analyses from 7 October 2016 at 2239 UTC (Figures 4.10a, 4.10b) and 2323 UTC (Figures 4.10c, 4.10d). Reflectivities within the dual-

Doppler domain were largely below 40 dBZ at both analysis times (Figures 4.10a, 4.10c) and several weak or dissipating rainbands annotated by cyan contours can be seen within the regions. The kinematic structure of these weakening rainbands is similar to that seen in Harvey and Isabel. In Figures 4.10b and 4.10d, the cyan contours overlaid as in 4.10a and 4.10c highlight azimuthally elongated regions of vertical vorticity exceeding 1.5 $\times 10$ s^{-1} parallel to the rainbands. This structure is similar to the VRWs seen in Harvey and Isabel in terms of vertical vorticity. However, in terms of vertical velocity the cases contrast one another. Here, vertical velocities across the entire domain are seen to be weak, with vertical velocities above 2 m s^{-1} at 5 km altitude present solely in the eyewall region. Along the rainbands themselves, regions of updrafts exceeding 1 m s^{-1} can be seen in the eastern two rainbands in Figure 4.10b and the western rainband highlighted in Figure 4.10d. The updrafts are not azimuthally aligned as in the other cases shown here and are located in the upwind portion of the bands in the northern part of the dual-Doppler domain.

The observations in Matthew afford the opportunity to examine the azimuthal phase speed of the rainbands as well as the vorticity features discussed. Unlike in Harvey where the vorticity field evolved very rapidly in azimuth and radial space, the vorticity features seen in Matthew are more slowly varying in time. Figure 4.11 shows an azimuthal Hovmoller diagram similar to that shown for Harvey. The vorticity perturbation is shown in the color-filled contours and the reflectivity perturbation every 5 dBZ is indicated by the black contours. Two magenta lines are drawn to point out two vorticity bands that rotate through the 40 km range ring from the center of circulation, verified in dual-Doppler analysis. The first between 2235 UTC and ~2250 UTC is the center vorticity feature seen in Figure 4.10a. The second line from 2245-2325 UTC is eastern-most band noted in Figure 4.10c.

The vorticity from the first band in the Hovmoller diagram clearly propagates slower than the mean wind (at 3 km altitude), as expected by VRW theory. The reflectivity perturbations are more difficult to discern, however, and it is unclear if the reflectivity band is propagating slower than the mean wind at 3 km. The second vorticity band shows similar propagation characteristics. However, the reflectivity perturbation maximum (+10 dBZ) propagates through the radius circle seemingly nearer the mean wind speed. The 5 dBZ contour does seem to expand in time, suggesting that the reflectivity band (at least a portion of it) may be propagating nearer the expected VRW phase speed. Thus, this may suggest that portions of the rainbands in Hurricane Matthew propagate as VRWs and some do not. This result was also found in the recent work of Guimond et al. (2020). Since rising motion was limited within the domain, it is likely that upwind convection may be formed along the VRWs (i.e., vorticity features), but become suppressed as it rotates downwind. The remaining hydrometeors tied to the dying convective cells may then propagate with the mean wind, giving rise to weak spiraled rainbands, similar to the work of Moon and Nolan (2015).

4.5 Over Ocean Observations

The numerical modeling studies cited herein indeed suggest that VRWs axisymmetrize convective scale and mesoscale asymmetries, which is supported by the observations here and in Chapter 3. However, the observations are shown near or during the landfall of Hurricanes Harvey, Isabel, and Matthew. It is reasonable to anticipate the higher degree of asymmetry in vortex-scale dynamics and in convective structures at landfall could lead to VRW response due to the influence of, for example, frictional disruption of the vortex. Thus, comparison of structures is necessary over the open ocean where frictional gradients are comparatively low.

Indeed recent observations of Hurricane Irma (2017; Fischer et al. 2020) and Hurricane Matthew (Guimond et al. 2020) using instrumented aircraft lend evidence that VRWs are active over the open ocean. Thus, data in Hurricane Matthew (2017) is briefly explored, as Matthew passed the central Florida coastline before entering the SR2-KJAX dual-Doppler domain described in Chapter 4.4b and was observed by the HIWRAP aboard the NASA Global Hawk.

Using HIWRAP, three-dimensional wind analyses were retrieved covering a ~20 km wide swath of Matthew's inner core. The first analysis from 1306-1345 UTC (Figures 4.12a and 4.12b) shows several rainband-like features radially outward of the eyewall. In this particular analysis, a detailed review of these rainbands can be found in Guimond et al. (2020), who showed that the rainbands behaved similarly to barotropic VRWs (Montgomery and Kallenbach 1997). Here, the kinematic structure in the vertical can be further compared to observations at landfall and an additional analysis from 1508-1600 UTC (Figures 4.12c and 4.12d) is also employed. Rainbands within about 50 km of the eyewall will be focused on here, since VRWs are generally confined to near the eyewall where the gradient of storm-relative vorticity is strongest (MK97). The reflectivity, vorticity, and vertical motion fields were averaged across-track.

In Figure 4.12a, four rainbands in reflectivity are denoted by dashed red contours and similarly denoted in Figure 4.12b by white dashed contours for reference. Each rainband appears to be associated with positive vorticity maxima in their vicinity, similar to over-ocean observations found by Reasor et al. (2000) and Guimond et al. (2020). In the 1306 UTC analysis particularly, the rainbands and vorticity maxima appear to be nearer one another, which suggests that the radial wavenumber increases as expected (MK97; Möller and Montgomery 2000). This occurs to a lesser degree in the 1518 UTC analysis, as several vorticity maxima are seen in the

analysis plane between 180-190 km along the track very near the eyewall. It is possible that several rainbands associated with VRWs were forming near the eyewall, which was more asymmetric during this analysis (see Figure 4.2c) and may decrease the radial wavelength between waves at initiation. Also similar to observations captured at landfall, the vorticity maxima associated with each band are maximized in the lowest 4-5 km of the analysis level.

While the vertical vorticity structure captured along the Global Hawk flight track in Matthew is similar to the vorticity structure of rainbands/VRWs at landfall, the vertical velocity observed is weaker than that captured at landfall. Besides the observations taken in the eyewall, the maximum vertical velocity in both analyses associated with the rainbands in question is near 3 m s^{-1}. There may be two possible explanations for the differences. The first explanation is that the vertical drafts over the ocean are weaker than at landfall. In general, it is anticipated that a difference in vertical velocities could be explained by thermodynamic differences (unlikely) or frictional convergence enhancing vertical drafts at landfall. However, the view of vertical motion in Harvey or Isabel, for example, does not suggest a significant difference in vertical velocities between land and ocean surfaces (see Figures 4.4 or 4.8 as examples). The more likely explanation is that rainband updrafts were often maximized in the upwind portion of the bands where the landfall analyses were often focused. Vertical velocities in the downwind portion of the bands in Harvey, Isabel, and Matthew were shown to be on the order of 0-3 m s^{-1}, much more consistent with the observations from HIWRAP. Coherent vertical vorticity structures were seen in the landfall analyses in the downwind portion of the bands as well without the presence of strong vertical drafts. The plan view of reflectivity from the Melbourne, FL WSR-88D suggests that both tracks were in the downwind portion of most bands, where vertical velocities could be weaker if the results of the landfall analysis can be generally applied. Thus, the general vertical

velocity differences are attributed to the regions of VRWs analyzed during landfall versus those observations take over the ocean.

4.6 Discussion and Conclusions

4.6.1 Summary and Key Conclusions

In Chapters 3 and 4, WSR-88D, and HIWRAP data were used to retrieve the three-dimensional wind field at very high temporal (~5 minutes) and spatial (~1 km) resolutions to examine the formative and mature stages of VRWs. Chapter 3 examined asymmetries in the eye and eyewall of Hurricane Harvey (2017) to examine the axisymmetrization process and examine the kinematics of both wave-mean flow interaction near the eyewall at landfall and VRW and rainband excitation near the eyewall from a potential vorticity perspective. This chapter focused on the kinematics of VRWs and their effect on rainbands in three TCs. Two of the cases, Harvey and Matthew, afforded the opportunity to approximate the azimuthal phase speed of the waves compared to the observed tangential flow for several hours continuously. Relative to other observational studies that are often limited to individual aircraft passes in TCs over the ocean with relatively low temporal resolution (Reasor et al. 2000; Fischer et al. 2020; Guimond et al. 2020), this study is the most comprehensive examination of VRW-driven rainbands to date.

Based upon the above results, the following key points are summarized in a conceptual model (Figure 4.13):

1. Established via the consistency of rainband phase speeds and the observation of trailing, spiraled vertical vorticity structures in multiple landfalling TCs (seen as trailing spiraled vorticity and reflectivity maxima exterior of the eyewall in Figure 4.13), VRWs are indeed present in observations and can be convectively coupled to rainbands. The upwind

propagation of the bands is consistent with the barotropic dispersion relation of MK97, strongly implying that the rainbands are the result of convectively coupled VRWs.

2. The VRWs observed here are generally excited by asymmetries in the eye and eyewall, which are themselves responsible for the simultaneous inward and outward transport of potential vorticity (see the curved red arrows in Figure 4.13). This process manifests simultaneously via the VRW response radially outward of the eyewall and the inward transport of potential vorticity. However, the inward transport of vorticity is not necessarily responsible for changes in intensity over long time scales and warrants further work.
3. VRWs, seen here in the vertical vorticity field, are associated with low level convergence in the low-level radial inflow that contribute to deep convective motions that are quasi-uniform along the bands and are maximized often in the upwind portion of the bands (see the vertical cross section in Figure 4.13). These rainbands are associated with the heaviest precipitation observed in the inner core.

As discussed in Chapter 4.1, there have been several explanations in recent years regarding the formation of secondary rainbands near hurricane eyewalls, most often attributed to VRW dynamics. Nevertheless, other explanations exist such as inertia-gravity wave propagation and non-linear advection of hydrometeors from upwind convective sources. No matter the explanation for rainband formation, most of the knowledge of secondary rainbands comes from numerical modeling studies due to their transient nature. Observations of such bands can be difficult over the open ocean, since aircraft may only sample a band once during its lifetime.

Using a relatively large (O[10,000 km^2]) dual-Doppler domain in all three cases examined here, rainbands exterior of the hurricane eyewall were observed to be associated with

azimuthally elongated, trailing vertical vorticity spirals that appear to wrap into the eyewall near convective asymmetries. These vorticity structures were observed to extend along the band identified by radar reflectivity and were often associated with updrafts that were stronger in the upwind portion of the bands. The vorticity maxima mostly radially lagged the reflectivity maxima and were often offset from the updrafts as well, similar to full-physics numerical modeling (Wang 2002a,b). In Hurricane Harvey, the rainbands were easily identifiable in Hovmoller diagrams and were shown to propagate against the mean tangential wind within the range of expected phase speeds defined by the barotropic phase speed relation in MK97. Nearly all rainbands were shown to propagate against the mean wind with some rainbands propagating near the mean wind. Even the rainbands observed propagating nearer the mean wind, however, were associated with trailing vorticity spirals, suggesting consistency with VRW-driven rainbands. It is indeed plausible that the intense radial gradient in vorticity (Figure 4.6) in Harvey increased the radial wavenumber (4.2) sufficiently quickly such that the intrinsic VRW phase speed was near the mean wind at times (i.e., k^2 in (4.3) becomes large). In Hurricane Matthew, the reflectivity and more easily identifiable vorticity maxima were shown to diverge in their phase speeds. The vorticity maxima, propagating clearly slower than the mean wind, were consistent with VRW dynamics. However, in the upshear portion of Matthew, it appears that some parts of the rainband reflectivity propagated with the mean wind while others did not. While not shown here, the depth of the observed VWRs were mostly beneath the melting level of the hurricane. Hence, precipitation processes aloft may have also modified the reflectivity field. The projection of the environmental shear upon the vortex as a whole likely suppressed convection in this region (DeHart et al. 2014), which would also aid in the collapse of VRW-rainbands in the reflectivity field. This indicates that the vertical drafts are limited by the

environmental shear, while the wave itself may still exist (e.g., vertical vorticity maximum propagating, but not giving rise to a rainband).

It is also important to note that the barotropic phase speed relation of MK97 seems to describe observed rainbands. Recently, Guimond et al. (2020) calculated the azimuthal phase speed in the same rainbands observed in Figure 4.12a, which resulted in remarkable consistency between the expected phase speed according to MK97 and the observed phase speed. This work shows similar results at landfall, where the rainbands observed were of differing radial wavenumbers, but fell into the expected range of phase speeds for Harvey's general wind profile. As the results here are shown between 1 and 5 km altitude, we anticipate the radial gradient in the vorticity profile should be relatively consistent to that over the open ocean. Chapter 6 will demonstrate that the hurricane wind profile is generally unaffected leading up to landfall above the boundary layer (generally the lowest 1 km), suggesting that MK97 may be applied with confidence to the wind profile aloft. Given the consistency of the kinematic observations from the landfalling cases observed by the SRs compared to Hurricane Matthew observed by HIWRAP, the general structure of VRWs observed here may be readily applied over the ocean where frictional gradients are low.

4.6.2 Rainfall and Wind Impacts

Given the kinematic observation of VRW-induced rainbands in multiple TCs, it is also worth briefly mentioning the impact VRW-driven rainbands have upon general conceptual models of TCs. While not necessarily intended as a general model of TC precipitation characteristics, Marks and Houze (1987) showed the inner core of a mature TC is generally characterized by stratiform-like precipitation and its associated mesoscale vertical draft/latent

heating characteristics. In general, the inner core of a mature TC has often been shown to be dominated by precipitation grown as small ice crystals are advected radially outward from the eyewall, grow by vapor deposition, and fall out when their size (terminal velocity) is sufficiently large to overcome the background vertical velocity, similar to mid-latitude mesoscale convective systems (c.f., Biggerstaff and Houze 1991). The latent heating associated with deposition growth above the melting level leads to a mesoscale updraft above the melting level. This general pathway of precipitation growth is indeed supported in a number of studies (e.g., Marks and Houze 1987; Houze et al. 1992; Braun 2006; Houze 2010). However, it is shown here that VRWs are impactful to both the precipitation and vertical velocity field (c.f., the vertical cross-section in Figure 4.13), suggesting added complexity to the inner core conceptual model of precipitation growth.

In all cases, weak yet tropospherically-deep vertical drafts were observed that were tied to rainbands in the inner core. Reflectivity values associated with precipitation not associated with rainbands were generally 20-35 dBZ, whereas rainbands were characterized by reflectivity values of 35-50 dBZ. Assuming the simple rain rate relationship between reflectivity Z [mm^6 m^{-3}] and rain rate R following Jorgensen and Willis (1982) where $Z = 350R^{1.35}$, non-rainband (rainband) precipitation can be expected to be between 0.4-5.1 mm hr^{-1} (5.1-65.9 mm hr^{-1}) in general. Using the National Weather Service Tropical Z-R relationship where $Z = 250R^{1.2}$, non-rainband (rainband) precipitation can be expected to be between 0.5-8.3 mm hr^{-1} (8.3-147 mm hr^{-1}). It is clear that the rainband precipitation can be expected to enhance rain rates by at least an order of magnitude for typical Z-R relationships. While it is not immediately clear if the rainbands contribute significantly to inland flooding, it is indeed plausible and is absolutely necessary to evaluate in terms of quantitative rainfall prediction (Hall et al. 2013). It is unclear if

numerical modeling sufficiently resolves VRW-driven rainbands to a reasonable degree and the precipitation associated with them. Prior to this study, it has been difficult to assess the kinematic structure of VRWs in sufficiently high resolution in order to evaluate numerical model representation of kinematic and microphysical processes. This dataset is certainly ideal for such comparison and will be the subject of Chapter 5.

In terms of impacts to the wind field, this concept was explored in Chapter 3 with a focus on the initial asymmetries observed in Hurricane Harvey. Based on Chapter 3, the mesovortices in Harvey were impactful to the instantaneous wind field, but less so to the intensity evolution. The mesovortices, which were shown to give rise to the VRW response, were the result of symmetrizing potential vorticity anomalies and were the focus of rainband formation. Given the results in Hurricanes Harvey and Isabel, Figures 4.5 and 4.9 showed contiguous vertical perturbations to the horizontal wind field associated with the waves. In addition, deep downdrafts were noted that extended to the bottom of the analyses. While it cannot be concluded that VRW-driven rainbands significantly perturb the surface wind field, it is within reason to anticipate some impact to the sustained wind following an ongoing study regarding gust factors in Hurricane Harvey in the vicinity of deep convection (M. Biggerstaff, personal communication). Further work is needed to understand the near-surface wind impacts of VRW-driven rainbands.

4.7 Figures

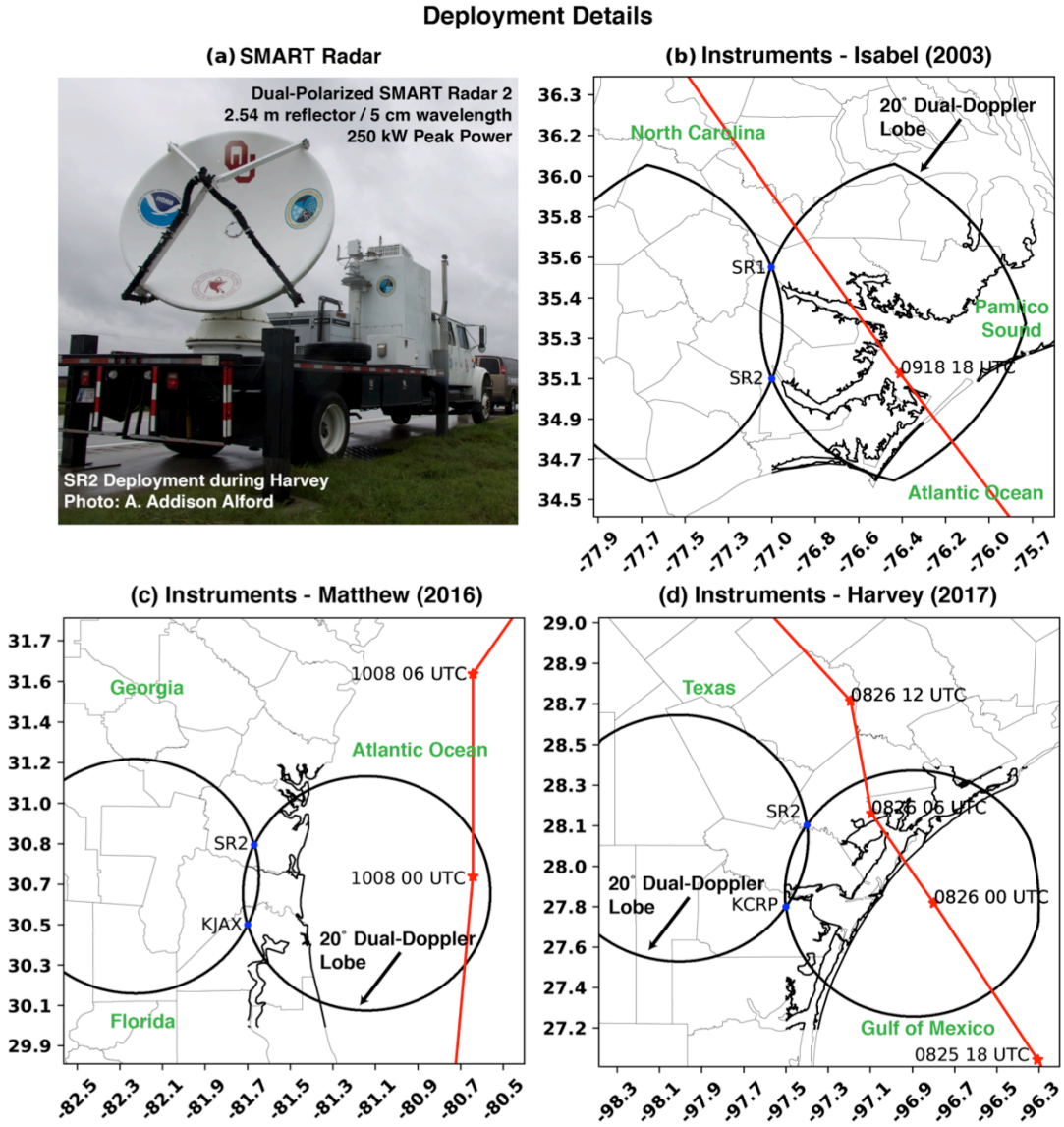

Figure 4.1. Dual-Doppler deployment details with the SMART radars. (a) Photo of SMART radar 2 (post-dual-polarization upgrade) during Hurricane Harvey. (b-d) The instrument locations during the landfalls of (b) Hurricanes Isabel, (c) Hurricane Matthew, and (d) Hurricane Harvey. In each figure, the red line indicates the National Hurricane Center Best Track position at 6-hr intervals. The black lines intersecting the radar locations denote the 20° dual-Doppler retrieval region.

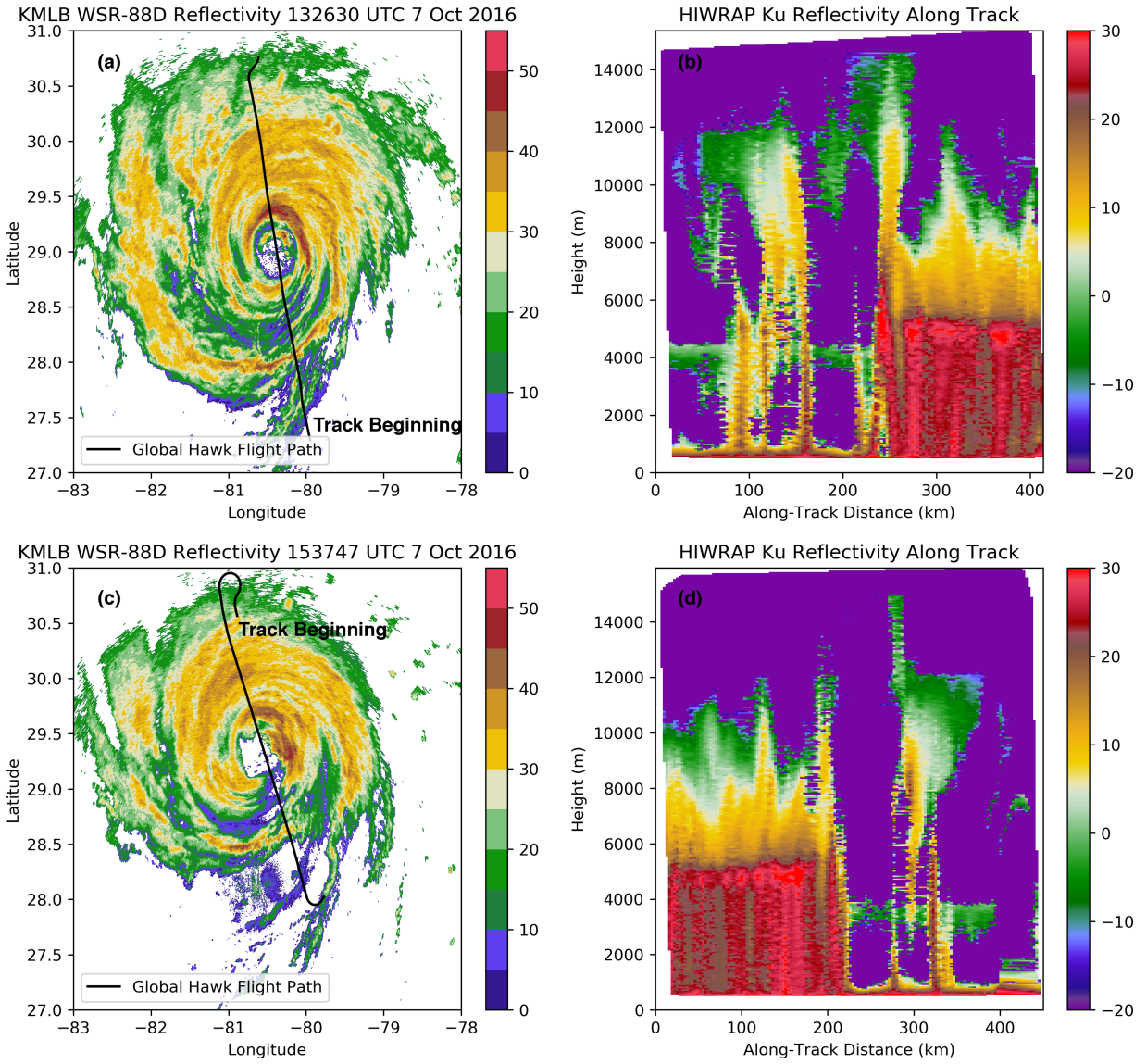

Figure 4.2. (a) The flight path of the Global Hawk (black line) overtop KMLB radar reflectivity (dBZ; color-filled contours according to the colorbar) is shown with the track beginning indicated. The flight spans 1306 UTC 7 October 2016 to 1345 UTC 7 October 2016. (b) The radar reflectivity (dBZ according to the colorbar) from the outer beam (40° off nadir) from the Ku radar is shown. The track is shown in (a). (c) As in (a), but for the flight spanning 1518 UTC 7 October 2016 to 1600 UTC 7 October 2016. (d) As in (b), but for the track shown in (c).

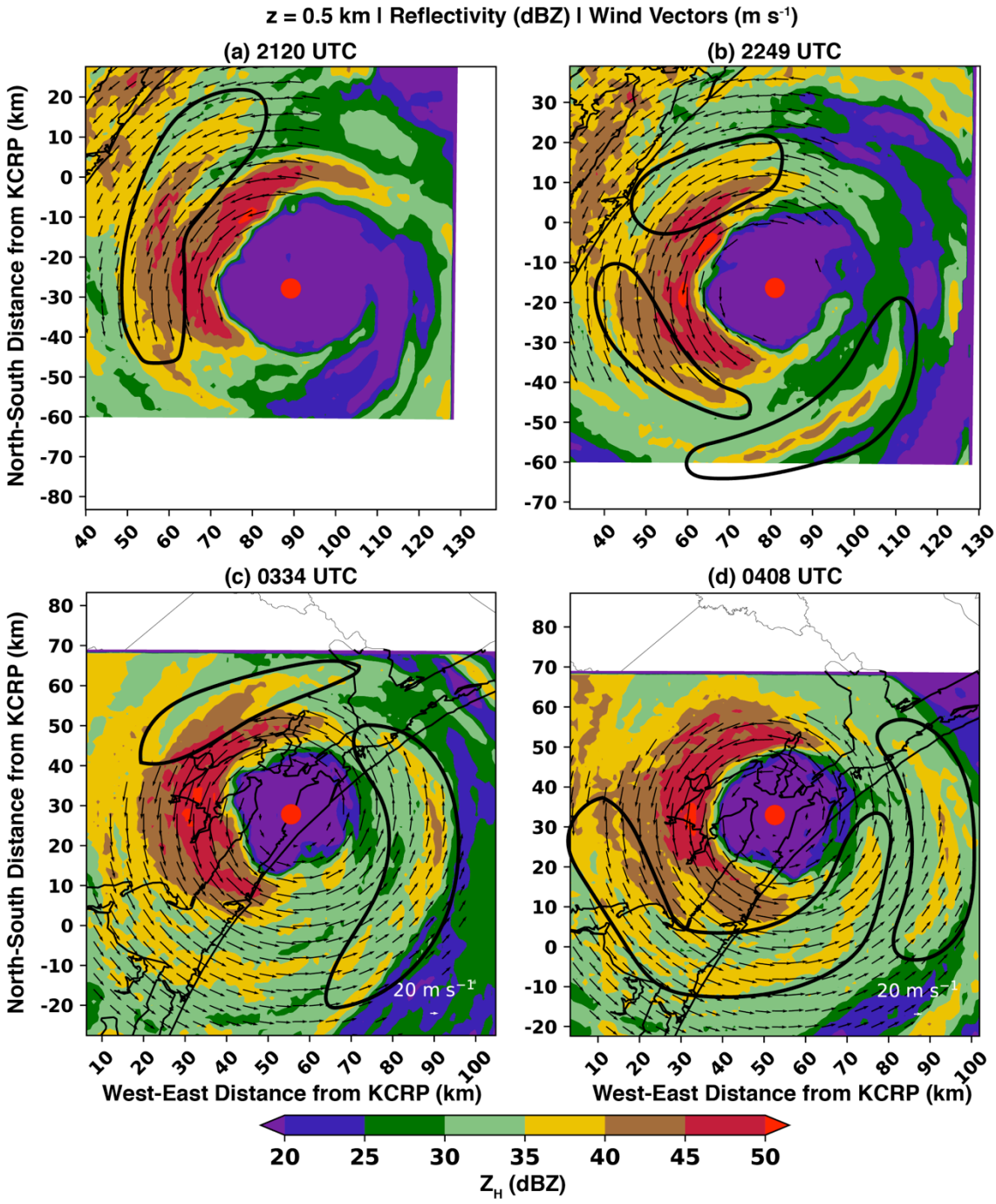

Figure 4.3. Radar reflectivity (color-filled contours; dBZ) and horizontal wind vectors (m s^{-1}) at four times to indicate rainbands that are likely convectively-coupled VRWs. The black contours encircle rainbands that will be examined in this study.

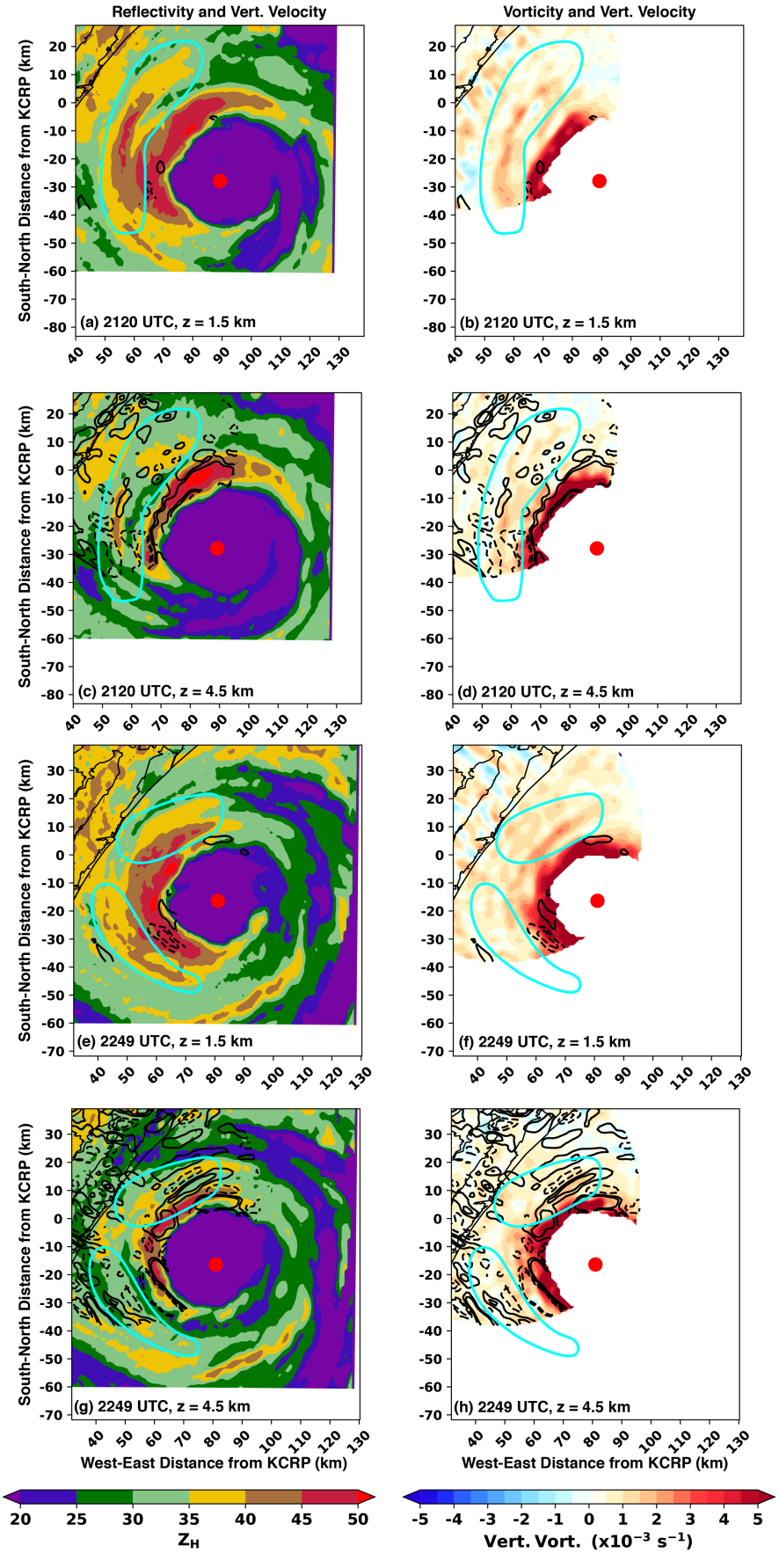
Reflectivity and Vert. Velocity
Vorticity and Vert. Velocity
South-North Distance from KCRP (km)
(a) 2120 UTC, z = 1.5 km
(b) 2120 UTC, z = 1.5 km
(c) 2120 UTC, z = 4.5 km
(d) 2120 UTC, z = 4.5 km
(e) 2249 UTC, z = 1.5 km
(f) 2249 UTC, z = 1.5 km
(g) 2249 UTC, z = 4.5 km
(h) 2249 UTC, z = 4.5 km
West-East Distance from KCRP (km)
20 25 30 35 40 45 50
Z_H
-5 -4 -3 -2 -1 0 1 2 3 4 5
Vert. Vort. (x10^{-3} s^{-1})

Figure 4.4. Dual-Doppler analyses for 2120 UTC are shown in (a) and (b), and analyses for 2249 UTC are shown in (c) and (d). (a) and (c) display radar reflectivity (color-filled contours) and vertical velocity denoted by solid (dashed) black contours for +2 and >+4 m s^{-1} (-2 and <-4 m s^{-1}). The reflectivity is shown for 1.5 km altitude and the vertical velocity is shown for 4.5 km altitude. The cyan contours are as in Figures 4.3a and 4.3b to denote the rainbands of focus for this analysis. In (b) and (d) the vertical velocity (m s^{-1}; black contours) at 4.5 km altitude and the vertical vorticity at 1.5 km altitude is shown according to the colorbar.

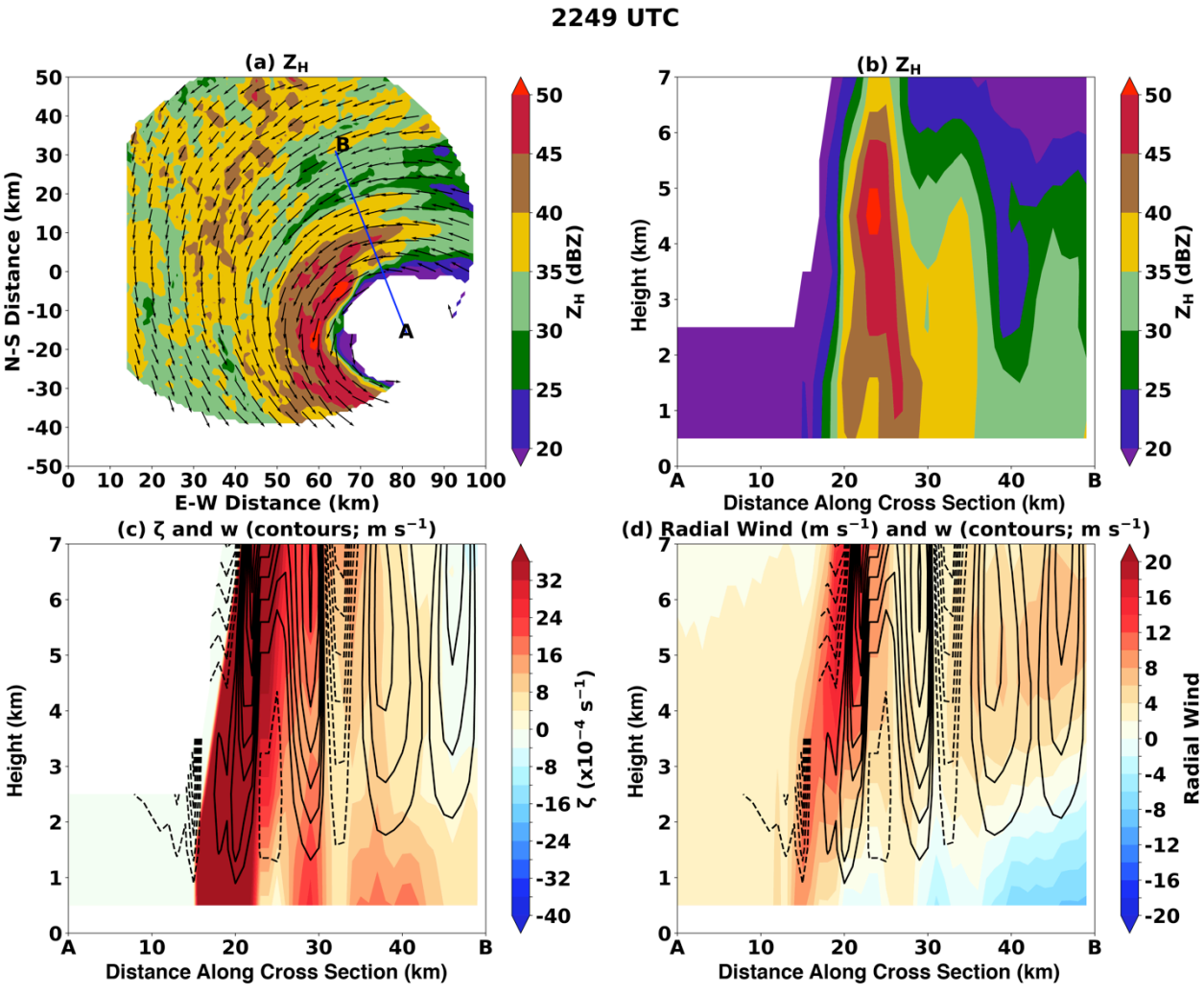

Figure 4.5. (a) A plan view of radar reflectivity at 0.5 km altitude is shown according to the

colorbar along with wind vectors (m s^{-1}). The blue line indicates the location of the cross section A-B, with the location of A corresponding to the derived center of circulation. (b) A vertical cross-section of radar reflectivity. (c) A vertical correction section of vertical vorticity according to the colorbar and vertical velocity (contours every 1 m s^{-1} with the 0 m s^{-1} omitted). (d) As in c, but the color-filled contours show the radial component of the wind relative to the center of circulation.

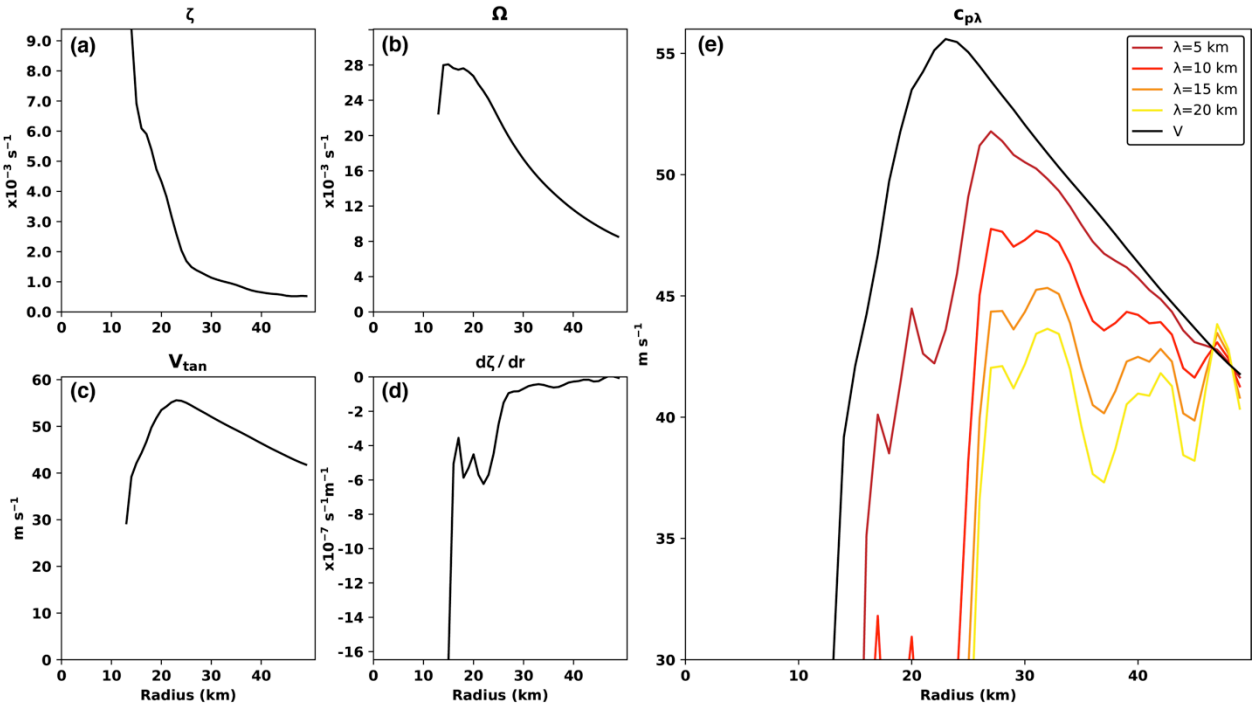

Figure 4.6. (a) The average radial profile of storm-relative vorticity. (b) The average radial profile of angular velocity. (c) The average tangential wind profile. (d) The average profile of the storm-relative vorticity gradient. (e) The azimuthal phase speed calculated based on (a) – (d) for varying radial wavelengths are compared to the tangential wind *v* (black contour) as a function of reference radius.

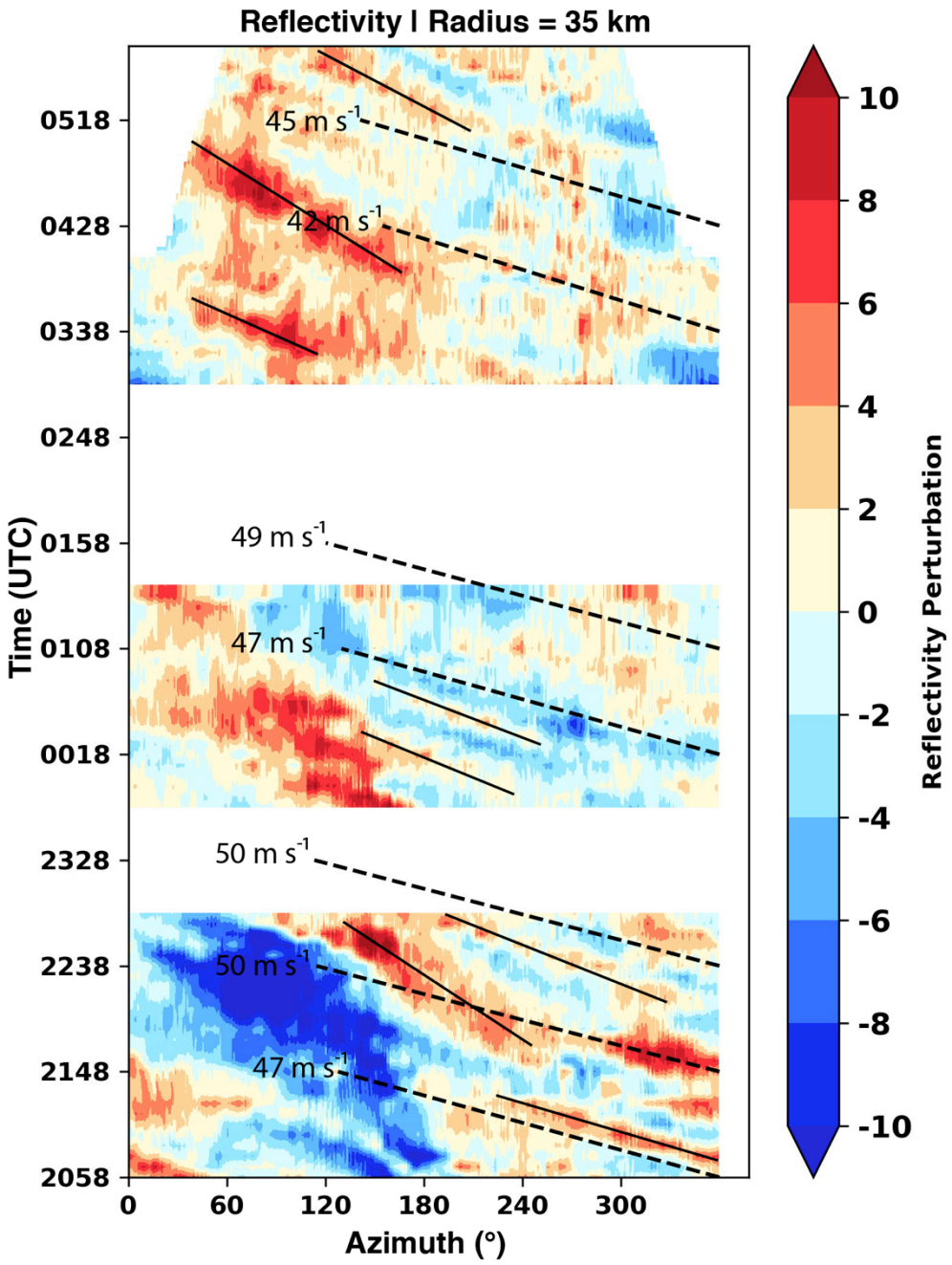

Figure 4.7. An azimuthal Hovmoller diagram from Hurricane Harvey is shown. The Hovmoller was constructed for a constant radius of 35 km from the center of circulation (i.e., outside of the eyewall). The Hovmoller displays the reflectivity perturbation (dBZ) relative to the time-mean average reflectivity at each azimuth. The dashed lines represent the average tangential flow calculated from the available observations of the observed wind for reference. The solid lines are

subjectively drawn to show reflectivity perturbations that are associated with prominent rainbands such as those discussed in Chapter 4.3.

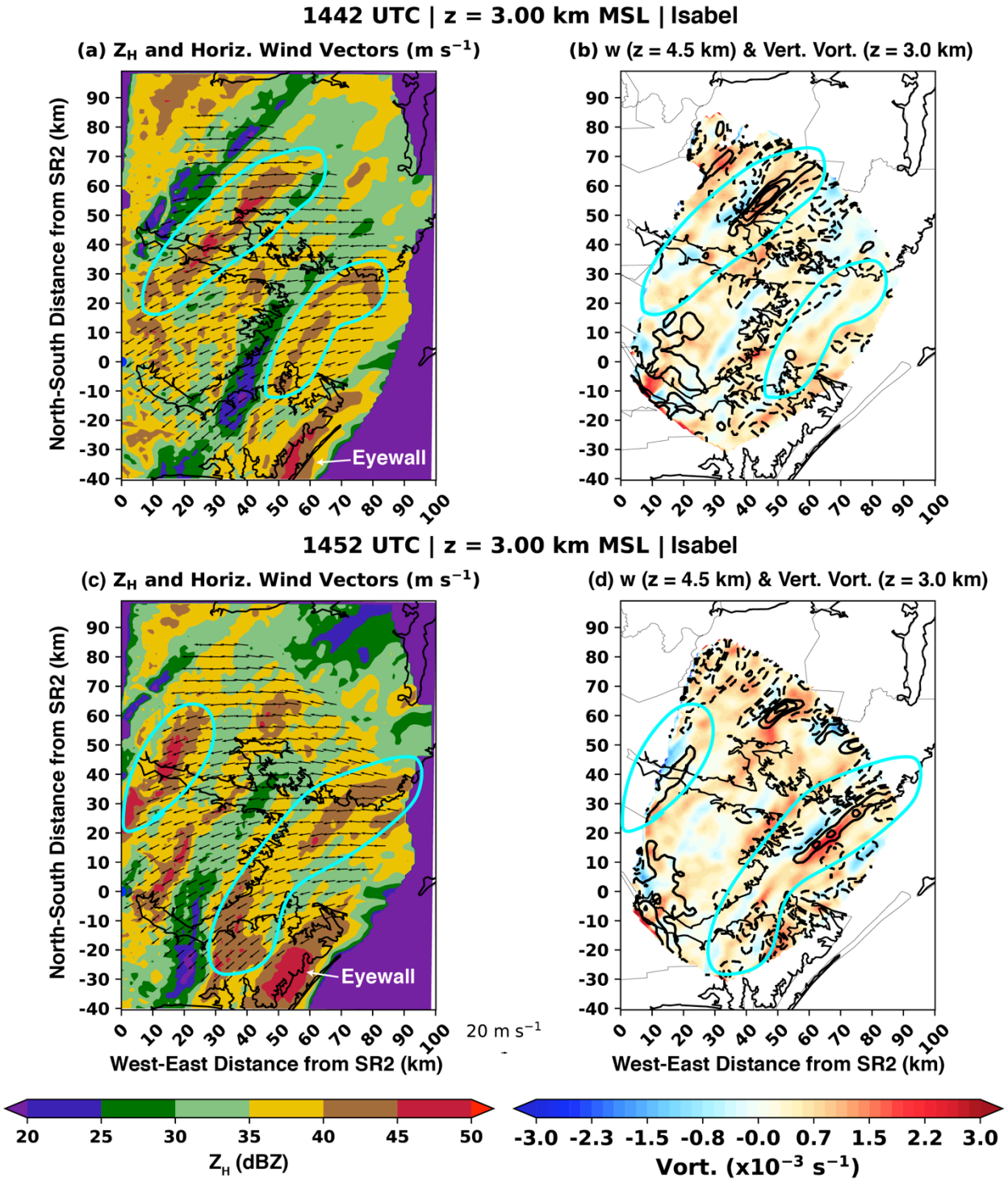

Figure 4.8. As in Figure 4.4, but for the 1442 UTC (a, b) and 1452 UTC (c, d) dual-Doppler analyses in Hurricane Isabel. The reflectivity and wind vectors in (a) and (c) and the vertical vorticity in (b) and (d) are shown for the 3.0 km altitude. In (b) and (d), the vertical velocity is shown at 4.5 km altitude. Note the change in the vorticity color scale compared to Figure 4.4.

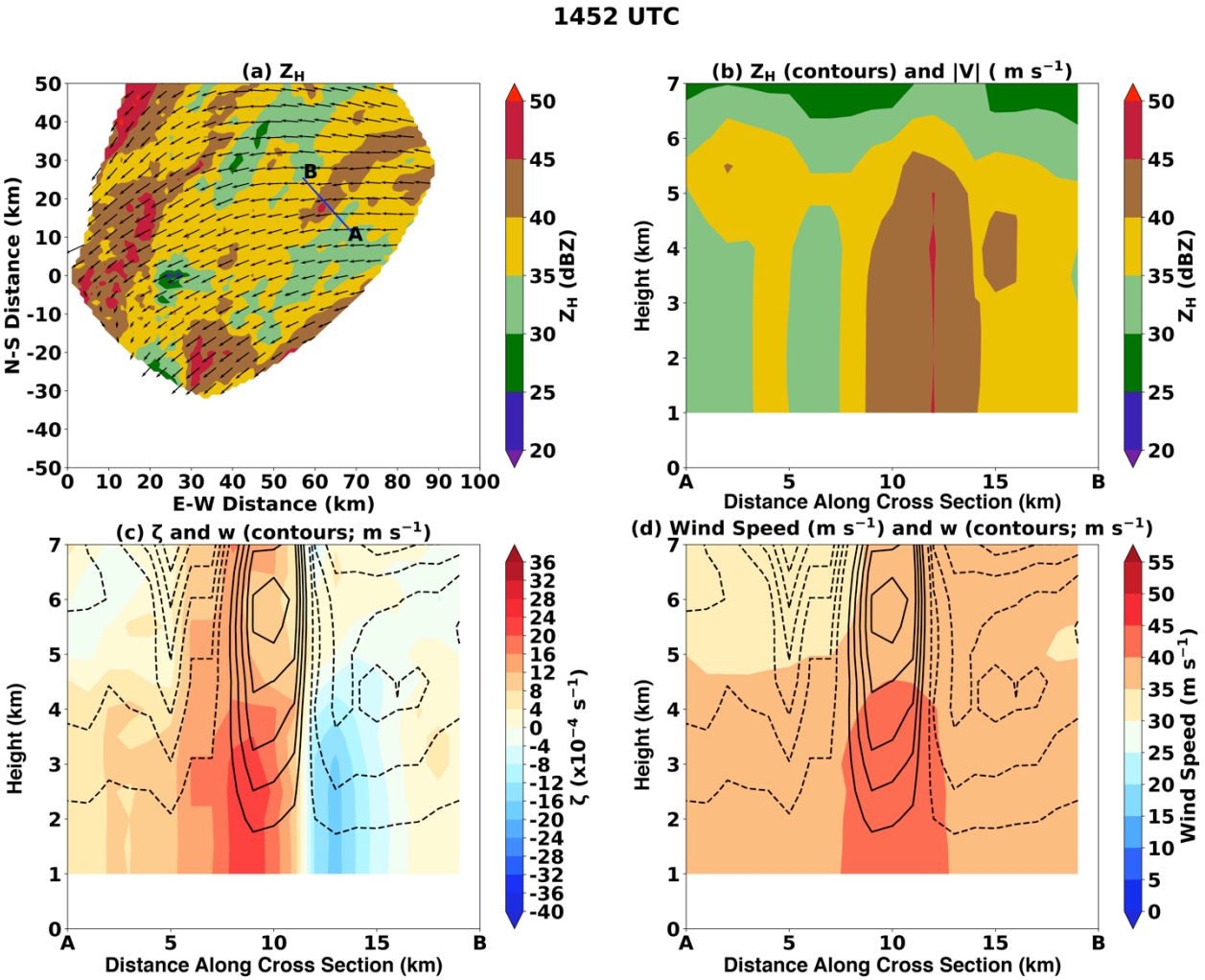

Figure 4.9. As in Figure 4.5, but for the 1452 UTC analysis in Hurricane Isabel. Note that (d) displays the total wind speed, rather than the radial wind speed.

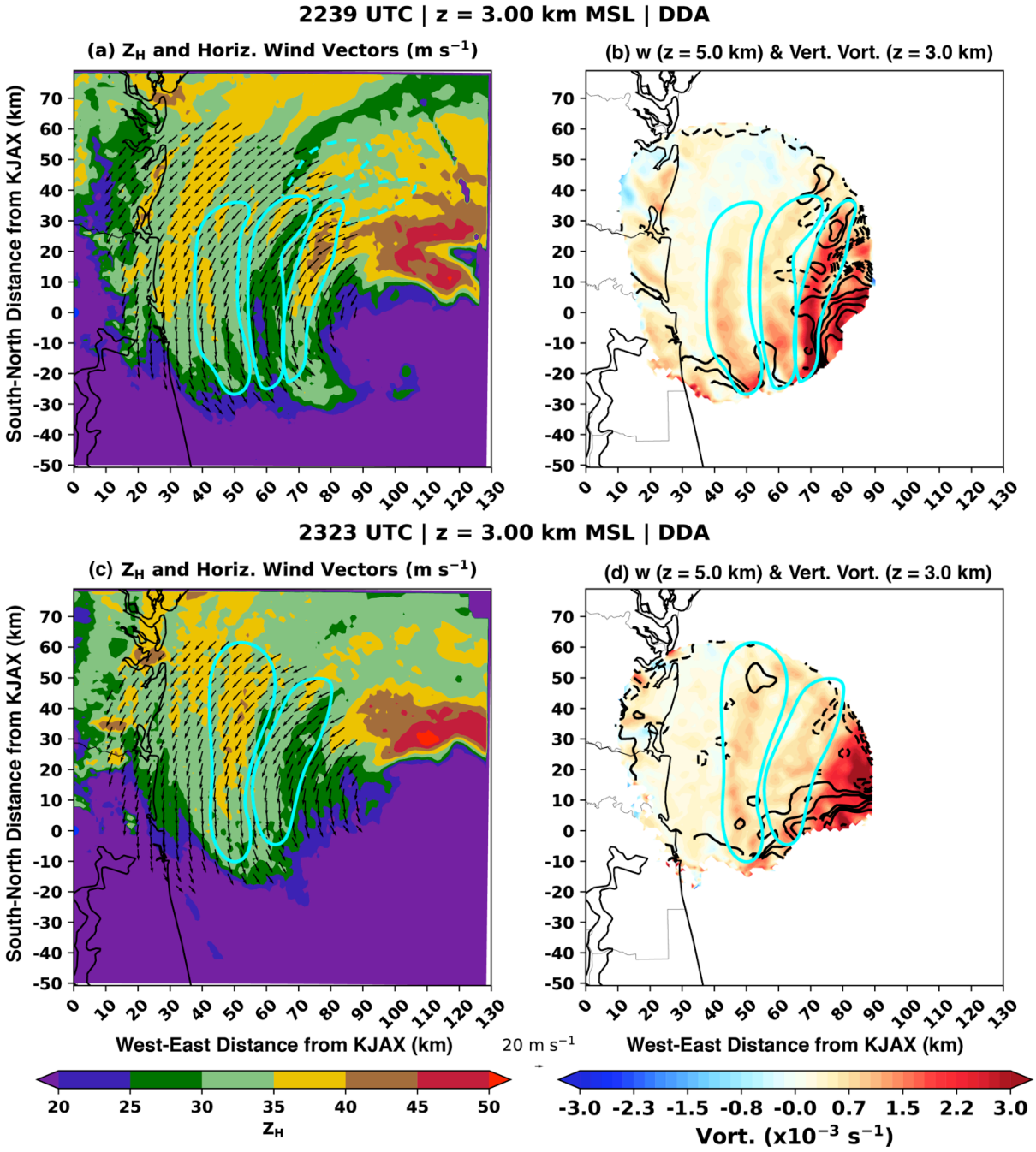

Figure 4.10. As in Figure 4.8, but for the 2239 and 2323 UTC dual-Doppler analyses in Hurricane Matthew. The blue cyan contours denote the presence of VRWs in reflectivity and vertical vorticity. The dashed cyan lines in (a) show the extension of rainband structures beyond the wind retrieval region that are likely associated with VRWs within the retrieval region. Unlike in Figure 8, the vertical velocities in (b) and (d) are every 1 m s^{-1} with the 0 m s^{-1} contour

omitted.

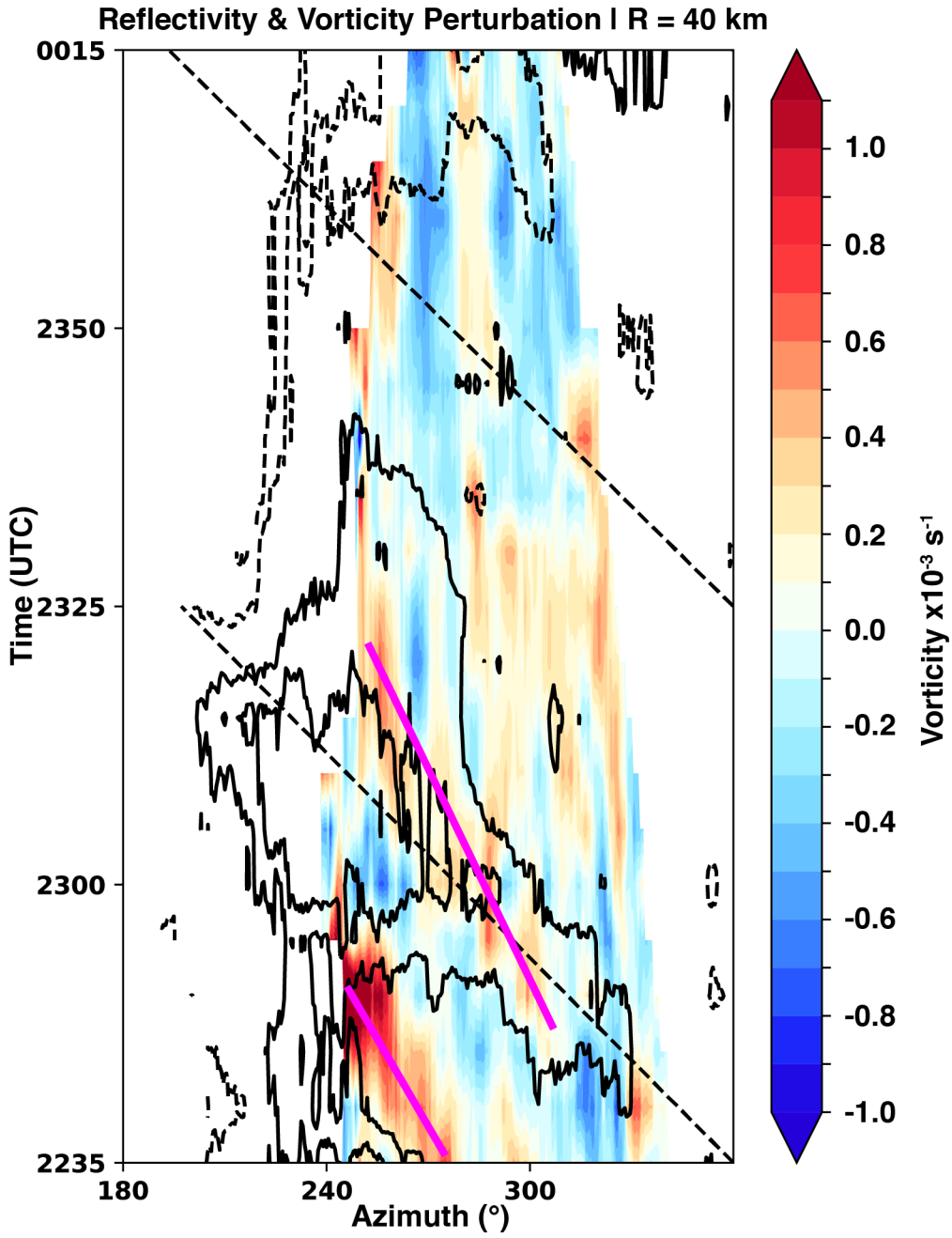

Figure 4.11. An azimuthal hovomller diagram from Hurricane Matthew. The color-filled shading shows the vertical vorticity perturbation relative to the time-mean average of vorticity at each azimuth. The black contours show the reflectivity perturbation every 5 dBZ with the 0 dBZ line

omitted. The magenta lines are drawn to show the phase speed of two vorticity features rotating through the constant radius circle relative to the mean wind (dashed black lines).

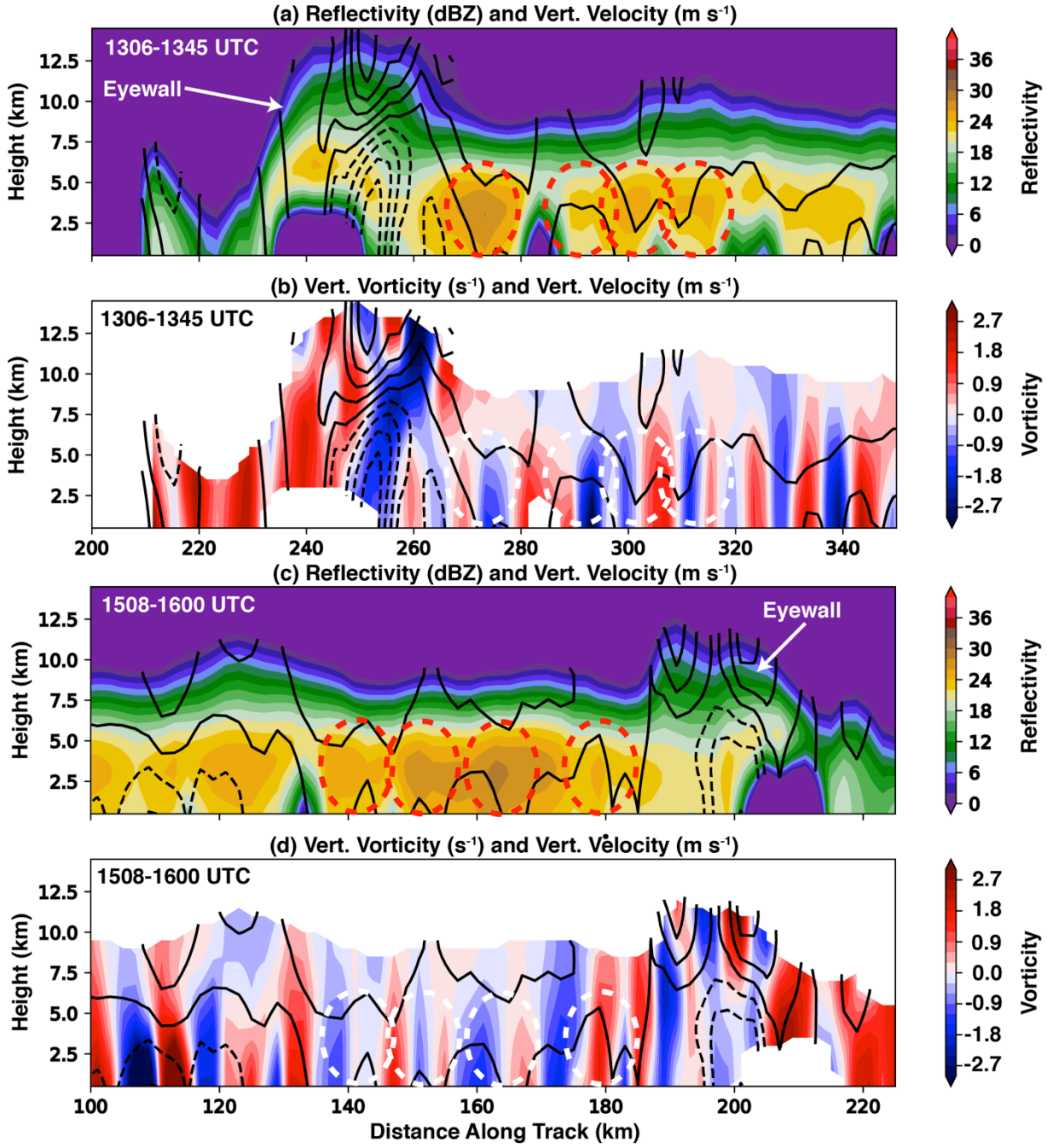

Figure 4.12. Wind retrievals are displayed from HIWRAP for the 1306 UTC (a, b) and 1518 UTC (c, d) analyses. (a) Reflectivity (dBZ; color-filled shading) and vertical velocity (m s^{-1}; every 1 m s^{-1} with the 0 m s^{-1} line omitted) are shown. (b) Vertical velocity is shown as in (a).

Vertical vorticity (s^{-1}) is shown according to the colorbar. (c) and (d) are as in (a) and (b) respectively but for the 1518 UTC analysis. All quantities were averaged across the track. In (a) and (c), the red-dashed contours identify rainbands of interest near the eyewall (labeled). Similarly, in (b) and (d) the dashed white contours are as in (a) and (c) for reference.

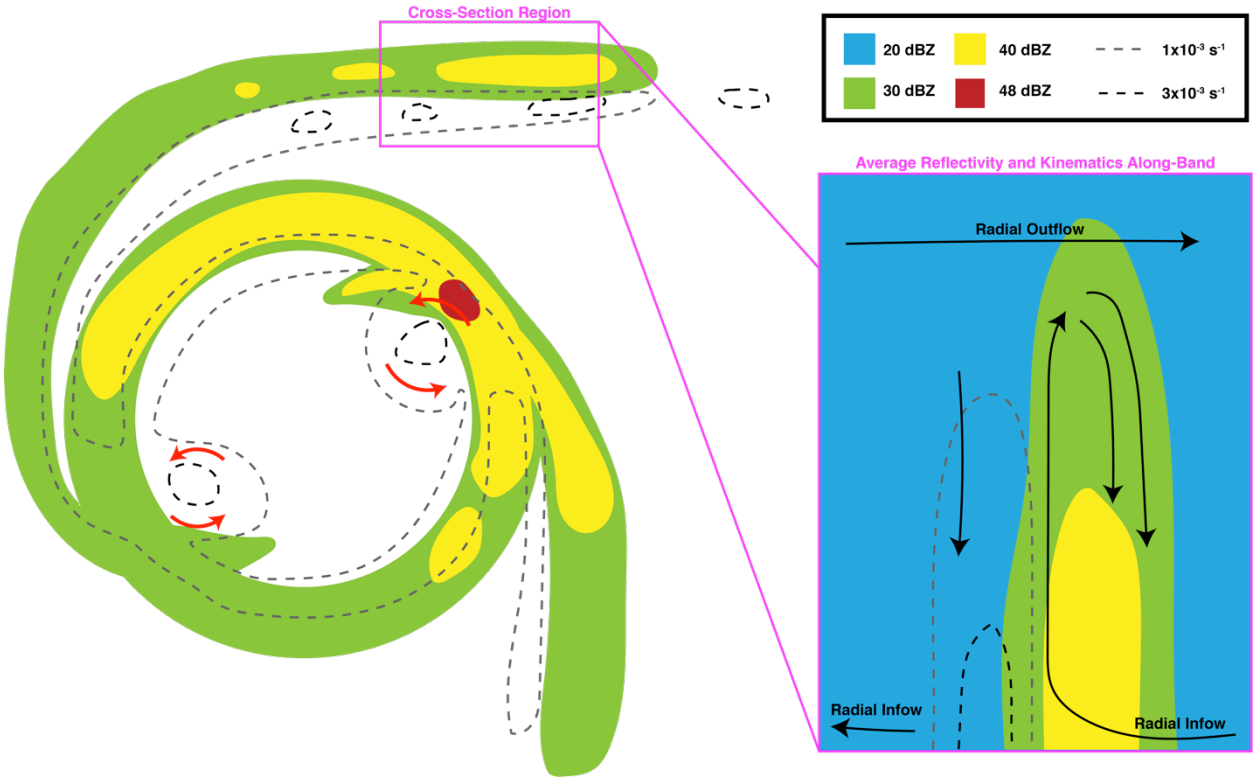

Figure 4.13. Conceptual model of VRW-induced rainband formation. The color-filled contours represent radar reflectivity (dBZ) according to the key and the dashed grey and black lines represent regions of constant vertical vorticity. The curved, red arrows simply highlight mesovortex structures integral to the VRW-rainband formation process. In the vertical cross section, average trajectories of radial infow, outflow, and vertical drafts are drawn to denote the observed vertical velocity structure relative to rainbands and the vorticity maxima associated with VRWs.

4.8 Tables

Table 1. Dual-Doppler domain details and radar pairs used in each hurricane case. The radar used as the origin of the domain is listed under "Radar 1" with the other radar listed under "Radar 2." In addition, the grid specifications including size and shape are listed. Finally, the baseline distance between the dual-Doppler pairs is listed.

Hurricane	**Origin Radar and Lat/Lon**	**2nd Radar and Lat/Lon**	**Δx, Δz (km)**	**x_{min}, y_{min}, z_{min} (km)**	**x, y, & z Dimensions**	**Baseline (km)**
Isabel	SR2 35.0772, -77.0483	SR1 35.5740, -77.0510	1.0, 0.5	0, -40, 1.0	100, 134, 15	52
Matthew	KJAX 30.4846, -81.7018	SR2 30.8405, -81.6695	1.0, 1.0	0, -50, 0.5	130, 130, 21	40
Harvey	KCRP 27.7840, -97.5113	SR2 28.1480, -97.4101	1.0, 1.0	0, -60, 0.5	130, 130, 10	42

Chapter 5: Evaluating Simulations of Hurricane Harvey (2017) at Landfall Using Ground-Based Dual-Doppler Analysis

5.1 Introduction

Numerical weather prediction is extensively used as both an operational (e.g., Vukicevic et al. 2013; Aberson et al. 2015) and a research (e.g., Abarca and Corbosiero 2011) tool to understand TC track, intensity, and evolution. The representation of physical processes on a variety of resolvable scales and in sub-grid scale parameterizations are integral to the realism of modeled TCs. Physical processes are the subject of intensive research of late as the computational ability to resolve kilometer and sub-kilometer scales improves (Nolan et al. 2009a; Cavallo et al. 2012; Gall et al. 2013; Zhang et al. 2015, 2018; Ko et al. 2020). As the ability of numerical models improves in resolving convective scale processes, it is essential to validate modeled physical processes, particularly those that are almost exclusively studied and understood via numerical modeling.

The Hurricane Weather Research and Forecasting (HWRF) model is a commonly utilized system for forecasting TC track and intensity and characterizing storm-scale evolution in a research setting. Evaluating the HWRF model is a task often approached by way of quantifying the error of operational and research based simulations in terms of the track of the center of circulation (e.g., Alaka et al. 2017, 2019), wind field distribution metrics (Nolan et al. 2021a,b), and the spatial distribution of precipitation (Tuleya et al. 2007; Ko et al. 2020). At present, a leading mode of evaluating HWRF has focused on capturing intensification and rapid intensification (RI) events and understanding the physical processes separating intensification and rapid intensification events from steady-state and weakening TCs (Gall et al. 2013). For example, Leighton et al. (2018) utilized a HWRF ensemble to examine factors leading to RI

events in some ensemble members compared to members that did not intensify. It was found that ensemble members with RI events were characterized by more contiguous azimuthal coverage of convection. They also found that positive eddy fluxes strongly contributed to spinning up the tangential winds in the mid and upper levels of the model simulation and were integral in aligning the vortex in the vertical (i.e., opposing the environmental shear). In order to characterize TC intensification in HWRF in a realistic way, Lu and Wang (2019, 2020) demonstrated the importance of both initializing the HWRF using sophisticated data assimilation (DA) analyses and of improving the diffusion and turbulent mixing parameterizations to maintain more realistic TC structure. Specifically, accurately simulating subgradient and supergradient features near the TC eyewall were shown to be critical to characterizing the intensity compared to observations. Thus, it is critical to evaluate asymmetric convective and dynamic processes in HWRF (Braun et al. 2006; Montgomery et al. 2015; Montgomery and Smith 2016) compared to observations, which is often difficult to do over the ocean.

VRW dynamics have been a long discussed topic in asymmetric dynamics that are thought to contribute to intensity change in TCs through the axisymmetrization of anomalies in the TC flow, namely in the vicinity of the radius of maximum wind (MK97; Möller and Montgomery 2000; Gao and Zhu 2016). As described in detail in Chapters 3 and 4, VRW processes can be separated in terms of their influences in secondary rainband (Houze 2010) formation and contributions to intensity change. While they occur simultaneously, the rainbands manifest as a result of the outward propagation component of wave energy (i.e., a VRW; Wang 2002a; Franklin et al. 2006; Cotto et al. 2015) while they converge angular momentum toward the VRW source asymmetries in the flow (MK97; Gao and Zhu 2016). In Chapter 3, it was demonstrated in an analysis analogous to that of MK97 that the flux of vorticity by eddies near

the radius of maximum wind in Hurricane Harvey acted to intensify the vortex over time (all else being equal), similar to the VRW response described in MK97. The inward flux of vorticity was shown to occur in the presence of simultaneously forming rainbands that manifested as a result of an outward directed flux of PV from Harvey's eyewall. The response of the PV transport radially outward from the eyewall induced convergence in the boundary layer such that tropospherically deep rainbands were formed. The PV was subsequently sheared into elongated bands coupled to rainbands, which were shown to propagate as VRWs in Chapter 4.

A purpose of Chapters 3 and 4 was to document VRW-driven rainband characteristics and symmetrization processes on the time-averaged vortex, similar to many modeling studies (Möller and Montgomery 2000; Chen and Yau 2001; Wang 2002a,b; Chen and Yau 2003; McWilliams et al. 2003; Franklin et al. 2006; Braun et al. 2006; Judt and Chen 2010; Wei et al. 2010; Hall et al. 2013; Menelaou and Yau 2014; Cotto et al. 2015; Gao and Zhu 2016). Unfortunately, the aforementioned studies were unable to compare their results to direct observations, due to the scarcity of spatiotemporally continuous observations (Reasor et al. 2000; Corbosiero et al. 2006; Fischer et al. 2020; Guimond et al. 2020). In fact, no study to date has been able to utilize observational kinematic datasets to evaluate VRW representation and processes in numerical models, namely HWRF.

This chapter summarizes a novel effort to investigate the realism of VRW structures in a high-resolution simulation of Hurricane Harvey (2017) using HWRF. The results of the simulation will be quantitatively compared to the available observations captured at Hurricane Harvey's landfall by SMART Radar 2 and KCRP. Utilizing the spatiotemporally continuous observations of Harvey near landfall from dual-Doppler analysis is indeed unique compared to the often temporally lower resolution wind analyses routinely captured by the NOAA P-3.

Perhaps more unique to this chapter is the ability to evaluate the structure of a major hurricane at landfall in unprecedented detail.

5.2 Data and Methods

5.2.1 HWRF Details

A single, deterministic HWRF run was performed using the 2018 implementation of HWRF (Biswas et al. 2018; https://www.emc.ncep.noaa.gov/gc_wmb/vxt/HWRF). Although one of the purposes of this work is to evaluate HWRF in terms of its ability to provide accurate forecasts, a more significant goal is to examine VRW dynamics and their associated physical processes in high spatiotemporal resolution in a model framework. Thus, the setup of HWRF was of a higher spatial resolution than the operational HWRF implementation in order to fully resolve VRWs in as much detail as possible.

The model configuration was similar to that used in (Lu and Wang 2019; see their Table 1 regarding their data assimilation-based runs). The HWRF run of Hurricane Harvey was initialized at 25 August 2017 1800 UTC when Harvey was offshore and integrated for 12 hours through landfall (0600 UTC on 26 August). Data were output every 2 minutes, providing unprecedented temporal resolution of modeled VRWs. The initial condition is produced by a cycled data assimilation experiment ingesting ground based radar observations using the HWRF hybrid EnVar system (Wang et al. 2013; Lu et al. 2017). Harvey was resolved on a triply nested grid with 0.036°, 0.012°, 0.004° (approximately 4, 1.3, and 0.45 km respectively) resolution on domains 1, 2, and 3 respectively. The inner most grid of 0.004° resolution (domain 3) has an average spatial resolution of 445 m in the horizontal. A total of 75 vertical eta levels were used with higher vertical resolution in the lower part of the model domain to resolve boundary layer

processes more efficiently. The model top was set at 10 hPa. The physics configurations were standard to HWRF and are summarized in Table 5.1. Additionally, Table 5.1 indicates the datasets incorporated into the EnVar system used to initialize the run.

5.2.2 Vortex Centers

As described in Chapters 3 and 4, the identification of the center of circulation is critical to assessing VRW processes, the contributions by eddies to the tangential wind, and examining the phase speeds of VRWs around a closed circuit. HWRF wind field data were extracted at each 2 minute model output interval at 500 m altitude. Using the Ground Based Velocity Track Display (GBVTD; Lee et al. 1999) method in Chapter 3.2.3, the hypothetical tangential winds over a 30 km wide annulus centered at a radius of 30 km from each simplex vertex were used to maximize the vorticity near the radius of maximum wind to define a center of circulation. At the beginning of the HWRF run, the center of circulation guess needed as input into the GBVTD method was defined as the 25 August 2017 1800 UTC Best Track center of circulation of Harvey. At each subsequent time, the first guess of the center of circulation was defined as the preceding GBVTD-defined center of circulation (e.g., the GBVTD center of circulation at 1800 UTC was used as the first guess for the 1802 UTC wind field).

Other methods to define the center of circulation often rely on either using the pressure minimum in the eye or the wind minimum in the eye (Nolan et al. 2021a). However, in order to remain consistent with Chapters 3 and 4, the enhanced GBVTD method was chosen. Examining the differences in the retrieved propagation characteristics and tangential/radial wind fields depending on the center-finding-method chosen is beyond the scope of this work. Furthermore,

pressure and wind field data in the eye are unavailable in the dual-Doppler analyses used as verification here.

5.3 Simulation Details

5.3.1 Comparison of General Reflectivity and Vorticity Characteristics

By using the state-of-the-art data assimilation techniques to initialize the HWRF run of Hurricane Harvey, an accurate representation of the environment and the vortex structure is expected. However, the simulation of Harvey was not anticipated to exactly follow the track and intensity evolution, as the sensitivity of the track and intensity evolution to the initial vortex location and structure was not examined. Rather, a reasonable characterization of the evolution just before landfall that is reasonably representative of an operational HWRF run used in forecasting was sought. Figure 5.1a shows the GBVTD-derived track (at 500 m altitude) from the model (blue line) from 25 August 2017 1800 UTC to 26 August 2017 0600 UTC versus the dual-Doppler observed track beginning at about 25 August 2017 2100 UTC to 26 August 2017 0600 UTC. In the first ~6 hours of the simulation, the model track follows the observed track quite well. Later leading up to landfall, the model solution takes Harvey to the north by about 20 km or less than the observed track.

In terms of intensity at the lowest comparable altitude (0.5 km altitude), the maximum tangential wind near landfall in the model is near 70 m s^{-1} (black curve in Figure 5.1b) versus maximum tangential wind estimates of 70-75 m s^{-1} at various dual-Doppler times (red circles in Figure 5.1b). The most significant difference between the model solution and the observed dual-Doppler winds is the intensity evolution post-landfall. In the model, landfall occurs at 0514 UTC, about 2 hours after the official landfall (Blake and Zelinsky 2018). After ~0500 UTC, the

tangential wind at 500 m altitude indeed begins trending downward, but at a rate significantly less than the downward trend in intensity after 0300 UTC in observations. Nevertheless, the intensity evolution prior to landfall indicates a steadily intensifying storm prior to landfall, which is supported by the observed dual-Doppler winds. Thus, by these simple metrics it is reasonable to conclude that the simulation performs relatively well prior to landfall for the purposes of validating the general character of rainbands and VRW processes.

In terms of the convective distribution, an often-neglected metric with which to evaluate numerical models and of particular interest to this work, the simulation also appears to be perform reasonably well. At an altitude of 0.5 km, the reflectivity progression of the HWRF run is comparable to that of the observations. When Harvey's eye and eyewall were over the open ocean (Figure 5.2a, 5.2b), the eyewall in the simulation was characterized by reflectivity values exceeding 50 dBZ (Figure 5.2a). Alternatively in observations, reflectivity values were characteristically less than 50 dBZ at the compared time. Stronger convective cells throughout the observations were noted with reflectivity values exceeding 50 dBZ. The strongest precipitation in the eyewall occurred on the western side of the eyewall in the HWRF run (Figure 5.2a) versus the northwest side in observations (Figure 5.2b). Several prominent rainbands can also be seen radially exterior of the eyewall and form trailing spirals, similar to observations. The reflectivity values at 0.5 km in the rainbands are larger in magnitude in the simulation than those observed, however.

Later in the simulation (observations) as Harvey approached the coast, the eyewall reflectivities were maximized in the southwest (northwest) portion, suggesting a continued offset in terms of the eyewall convection compared to observations (Figures 5.2c, 5.2d). Perturbations in the reflectivity field associated with vorticity maxima (e.g., as in Chapters 3 and 4) can be

seen in the observed reflectivity field but are not seen in the simulation. Similarly, the reflectivity field in the model (Figure 5.2e) is quite smooth and characterized by larger reflectivity magnitudes than observed (Figure 5.2f). Based upon reflectivity alone at these times, the HWRF run does not perform well in terms of resolving the prominent mesovortices characteristic of Harvey during the landfall process (Fernandez-Caban et al. 2019). Alternatively, the rainbands exterior of the hurricane eyewall appear to be reasonably characterized in terms of reflectivity, but are generally simulated with higher reflectivity values than observed (Figure 5.2).

In terms of kinematics, the observable vertical vorticity structure is smooth for nearly all times in the simulation (Figures 5.3a, 5.3c, and 5.3d). Values of vertical vorticity exceed $1x10^{-2}$ s^{-1} regularly within the radius of maximum wind. Alternatively in the observations where available in the eyewall, vertical vorticity values exceeding $1x10^{-2}$ s^{-1} were generally confined to isolated areas (asymmetries) and certainly did not cover an azimuthally extensive portion of the interior eyewall as seen in the simulation. Radially outward of the eye and eyewall, trailing spirals of vertical vorticity can be seen in the simulation (Figures 5.3a, 5.3c, and 5.3e) associated with the rainbands noted in Figures 5.2a, 5.2c, and 5.2e. Contiguous, azimuthally extensive vorticity maxima can also be seen in the observations and are often associated with reflectivity maxima. It appears the maximum vertical vorticity values in the simulated bands are generally consistent with observed bands, but the observed bands are more irregularly structured in azimuth compared to the smoothness of the modeled bands.

5.3.2 Vertical Rainband Structure

Knowing that the reflectivity field in the HWRF run is generally too high compared to observations implies several possible issues with the simulation. First a possible flaw is that the

vertical draft structure of the rainbands and convection are being poorly represented compared to observations, which could affect the rain drop size sorting (Didlake and Houze 2013; Feng and Bell 2019; Laurencin et al. 2020; Homeyer et al. 2021). Specifically, updrafts that are too strong in the model could lead to a bias of hydrometeors falling out to the surface at greater distances from their source updrafts than expected. Second is the possibility that the microphysics scheme used in HWRF is in need of improvement. In a recent study comparing two microphysics schemes with varying particle size distributions tested for each, Hristova-Veleva et al. (2021) determined that microphysics schemes with a lower mass-weighted mean diameter (i.e., more smaller droplets) tended to result in vastly improved representation of inner core microphysical and dynamical processes. Finally, the bias in the rotation of the simulated reflectivity could point to an issue with the representation of the synoptic environment. Namely, convection in the eyewall is particularly favored to maximize in vigor in the downshear right quadrant, and begin tapering off in the downshear left quadrant (DeHart et al. 2014). In terms of reflectivity distribution, Homeyer et al. (2021) showed that the shear projection onto the vertical motion in a sheared TC results in the largest droplets being found in the downshear right quadrant and smaller droplets being advected to the downshear and upshear left quadrants. Since the goal here is to assess the representation of asymmetric dynamic processes, the first two points will be considered in depth.

In Figure 5.4, HWRF analyses separated by 10 minutes are shown. Exterior to the Harvey's eyewall, several rainbands can be seen denoted by magenta contours in the figure. In this particular instance, the rainbands denoted appear to be rotating nearly opposite one another, consistent with a wavenumber 2 pattern in reflectivity. Clearly, the rainbands are associated with azimuthally extensive regions of rising motion (the vertical velocity is shown at 4.5 km altitude

via the black contours in the figure). The rainband that rotates clockwise from the western side of the eyewall around to the southeastern side of the eyewall appears to degrade in terms of reflectivity and vertical velocity with time, perhaps responding to the environmental shear being projected onto the vortex (i.e., the rainband rotates upshear). Radially inward of this particular band, an azimuthally extensive region of vertical vorticity can viewed that spirals into the eyewall near a vorticity maximum (Figures 5.4b, d). This is quite similar in broad terms to the rainbands seen in observations described in Chapters 3 and 4. Also similar to the observed character of rainbands in Harvey, there is a displacement between the vorticity maxima and the vertical motion/reflectivity maxima. In the simulation, the vorticity maxima generally reside radially inward of the rainbands and their associated updrafts approximately by one-quarter of a radial wavelength, consistent with other modeling studies of VRWs (Wang 2002a).

Unlike the observed rainband characteristics, the regions of rising motion generally exceed 5 m s^{-1} at the analysis level over much of the band's azimuthal extent. In Chapter 4, it was noted that vertical drafts exceeding 5 m s^{-1} were rare in most rainbands on the scales resolved in three landfalling hurricanes, suggesting the simulation may overestimate the vertical motions associated with convectively coupled VRWs. Specifically, unlike the observed rainbands, the maximum vertical motion seems to be much more azimuthally extensive along the band than observed in Chapter 4. Jorgensen et al. (1985) noted that vertical velocities of 5-10 m s^{-1} magnitude were commonly observed in situ in mature hurricane rainbands, but were confined to scales less than that observed/simulated here. Given that the vertical drafts driven by the VRW structures in Chapter 4 were rapidly sheared, it is likely that the more azimuthally extensive vorticity maxima (i.e. VRWs) here are responsible for the vertical motion response.

The vertical character of observed VRW-driven rainbands was also discussed in Chapter 4. In summary, narrow rainbands were shown to be associated with vertically coherent vorticity maxima radially lagging the rainband updrafts. In the HWRF run, the rainband to the west of the eyewall in Figures 5.4a and 5.4c (at 2200 and 2210 UTC) are examined in more detail in Figure 5.5. Figure 5.5 shows a cross section through the band. The cross section shows the eyewall of Harvey between 20 and 30 km range (Figures 5.5a, 5.5c) and the rainband in question between 40 and 50 km range. The eyewall is associated with a deep updraft extending upwards of 14 km altitude and a deep vertical vorticity column inside the eyewall, which is maximized in the lowest kilometer of the cross section. The rainband, alternatively, is characterized by a narrow vertical updraft in the plane of the cross section that is maximized near 5 km altitude. Highlighted by the dashed magenta lines in the figure, low-level vorticity maxima can be seen radially inward from rainbands at low altitudes. Progressing in range, the vorticity maxima become nearly co-located with the rainbands and the vertical drafts in the middle levels, similar to the rainbands assessed in Chapter 4. Nevertheless, the vorticity maxima lag the vertical velocity maxima by a few kilometers. This kinematic structure is similar to that of the VRW-driven rainbands observed in Hurricane Harvey. The modeled rainbands with be further compared to VRW theory in Chapter 5.4.

Contrasting the observed VRW-rainband characteristics is the lack of downdrafts seen in the plane of the analysis on the scales analyzed. The plan view of the rainbands in Figures 5.4 also confirms that downdrafts are relatively scarce near rainbands. With the exception of the eyewall, downdrafts in Figure 5.4 (representing the 4.5 km altitude vertical velocity) fail to exceed -1 m s^{-1}, which is unlike the observed rainband characteristics. Additionally, the observed rainbands were often situated between the updraft and downdraft maxima, whereas the rainbands

in the HWRF run are nearly co-located with the updraft. This points to deficiencies in the microphysics scheme utilized here. The offset of rainbands radially outward of the vertical drafts in the observations suggests that hydrometeor fallout occurs preferentially on the radial outward gradient of the vertical drafts. In the HWRF run, the nearly co-located vertical draft and reflectivity maximum suggests drops growing in the updrafts easily overcome their terminal velocity and quickly fall through the updraft. Again, noted by Hristova-Veleva et al. (2021) microphysics schemes utilizing smaller mass-weighted mean diameters often produced more realistic inner core structure. So, while the nature of the rainbands is similar to observed VRW-driven rainbands in terms of their vorticity and updraft characteristics, the microphysical representation and downdrafts of the bands are not.

5.4 VRW Propagation Characteristics

The above kinematic comparison shows that the rainbands in the HWRF run were generally similar to that observed, with differences noted in the microphysical and downdraft representation of the bands. Alternatively, the kinematics leading to rainband formation seem to be quite similar to that observed. The rainband processes detailed in Chapter 4 were shown to be indicative of VRWs in Hurricane Harvey and were similar in other presented cases over the ocean and at landfall. Thus, a more detailed comparison of the modeled rainbands to VRW theory is warranted.

A Hovmoller diagram was constructed using the vertical vorticity at 0.5 km altitude in HWRF. The diagram was constructed using a range circle at 25 km from the center of circulation. Every 30 minutes, the dashed lines in Figure 5.6 show the average tangential wind representative at 25 km from the center of circulation, just beyond the eyewall. Comparing the

propagation of vorticity maxima through the range circle (Figure 5.6a), it appears that most of the maxima are propagating slower than the tangential winds analyzed at 0.5 km altitude. The propagation speeds of the bands through the circle appear to vary in time and space, sometimes approaching the tangential wind magnitude. A clear wavenumber 2 type response can be seen to be dominant in the Hovmoller diagram, suggesting that the wavenumber 2 mode is dominant in the model. This is similar to the character of the reflectivity field described earlier in Chapter 5.3.2. In terms of reflectivity (Figure 5.6b), similar features are noted in the 25 km radius circle. Most reflectivity maxima propagate slower than the mean tangential wind, suggesting that the vorticity maxima associated with rainbands are VRWs similar to those observed. There is indeed complexity in the propagation characteristics in the Hovmoller diagrams, which is difficult to evaluate in an observational framework with limitations in the spatiotemporal continuity of observed kinematic and reflectivity properties (see Chapter 4). The variation in propagation speed implies various modes of propagation are being observed in the radius circle (MK97).

MK97 showed that for varying azimuthal wavenumber n VRW responses, the frequency ω at which VRWs are expected to propagate changes. While the Hovmoller diagrams (Figure 5.6) suggest an azimuthal wavenumber $n = 2$ dominant response, a more complete analysis can be performed through fast Fourier transform (FFT). The dispersion relation for barotropic VRWs is shown in (5.1) where Ω is the angular velocity at a radius r, ζ is the vertical vorticity also at r, and k is the initial radial wavenumber (i.e., the inverse of the radial wavelength; see Chapter 4). For reference, an overbar quantity denotes an average with respect to azimuth.

$$\omega = n\overline{\Omega} + \frac{n}{r}\frac{\frac{d\overline{\zeta}}{dr}}{k^2 + \frac{n^2}{r^2}} \qquad (5.1)$$

Considering the Hovmoller diagram is constructed in azimuth-time space and considering (5.1), a FFT F is used to decompose the vorticity and reflectivity (Z_H) fields via (5.2) and (5.3) where θ is the azimuth in radians and t is time in seconds:

$$F(n,\omega)=\frac{1}{4\pi^2}\iint \zeta(\theta,t)\exp\left(-i(n\theta+\omega t)\right)d\theta dt \qquad (5.2)$$

$$F(n,\omega)=\frac{1}{4\pi^2}\iint 10^{\frac{Z_H}{10}}(\theta,t)\exp\left(-i(n\theta+\omega t)\right)d\theta dt \qquad (5.3)$$

The FFT, containing the amplitude and phase information through the real and imaginary components of F, can be evaluated in terms of power P shown in (5.4). P can be interpreted in wavenumber-frequency space to ascertain the dominant wavenumber modes of vorticity and reflectivity at the 25 km radius. In (5.4), the subscripts R and I denote the real and imaginary components of F respectively.

$$P(n,\omega)=\left|F_R^2(n,\omega)+F_I^2(n,\omega)\right| \qquad (5.4)$$

The resulting power spectrum in logarithmic units (base 10) is shown in Figure 5.7 via the color mesh plot as a function of n (x-axis) and ω (y-axis). The FFTs here were calculated for wavenumbers 0-4. VRWs are typically expected to be dominant at low azimuthal wavenumbers (MK97). Higher order VRWs are not expected due to the dampening effect of the horizontal shear (Wang 2008). Frequencies ranging from 0.002 s^{-1} to 0.009 s^{-1} were evaluated based on applying the azimuthal-average, time-average profile of angular velocity and vorticity to (5.1). In other words, frequencies of VRWs (depending on the radial wavenumber) are expected to be greater than the angular velocity (~0.002 s^{-1}).

To compare the dominant wave modes to the VRW dispersion relation, the dispersion relation in (5.1) can be compared to the Fourier transform power directly. Traces of the dispersion relation in wavenumber-frequency space are shown in Figure 5.7 for radial wavelengths of 5, 10, 15, and 20 km. In the vorticity FFT (Figure 5.7a), the traces of the dispersion relation can be seen to overlap with the largest magnitudes of *P*, with the maximum power for wavenumber 1 occurring at low frequencies (0.002 – 0.003 s^{-1}). The simple calculation of the azimuthal phase speed $c_{p\lambda} = r\omega/n$ can be applied, which suggests that wavenumber 1 VRWs at low frequencies and wavenumbers (n = 1) propagated at approximately 50 m s^{-1}. In the wavenumber 2 mode, the frequencies between 0.002 – 0.005 s^{-1} are clearly dominant relative to higher frequencies at $n = 2$. The range of expected phase speeds covers a wide range (25 m s^{-1} – 62.5 m s^{-1}) with the fastest end of the phase speeds occurring for the highest frequencies, but lowest relative power. This suggests that some waves were propagating near the tangential wind, which was calculated to be 64.3 m s^{-1}. The expected VRW propagation also varies with the radial wavelength. In Figure 5.7a, the dispersion relation trace for varying radial wavelengths suggests that the power spectrum is consistent with VRWs of radial wavelength between 10 and 15 km at azimuthal wavenumbers 1 and 2, which is consistent with the radial scales of the modeled rainbands and their associated vorticity maxima. The local power maximum at 0.002 s^{-1} and $n = 2$ is indeed peculiar, but likely not representative of the rainbands examined here since the higher order radial wavelengths (>20 km) needed to satisfy (5.1) are not observed. Additionally, the $n = 0$ mode, while displaying large powers, is not discussed here and is related to the azimuthally averaged component of vorticity.

The reflectivity power spectrum in Figure 5.7b shows similar results to that of the vorticity power spectrum with several important differences. Like the vorticity analysis, the $n = 1$

mode is maximized from 0.002 – 0.003 s^{-1}, consistent with the VRW dispersion relation. At n = 2, there is a maximum at $\omega = 0.002\ s^{-1}$ that is similarly not explainable by VRW properties on the scales observed here. However, there is better overlap between the frequency space at n = 2 for frequencies of 0.004-0.005 s^{-1} with the VRW dispersion relation for VRWs of order 5-15 km radial wavelengths, consistent with phase speeds of (50-62.5 m s^{-1}). Again, this is quite consistent with the radial scales of rainbands seen in observations and similar to phase speeds noted for observed VRWs in Chapter 4 and other studies (Guimond et al. 2020).

To compare the power spectrum analysis directly to the *observed* VRW characteristics (5.3) was applied to the observational reflectivity data using in the Hovmoller analysis from Chapter 4 (see Figure 4.7). The observed vorticity was not evaluated due to the dual-Doppler limitations on the spatial extent of the vorticity field. The reflectivity data were evaluated at a constant range circle of 35 km. As input into (5.1), estimated time-averaged values of the angular velocity and the range derivative of vorticity of $1.4\times10^{-3}\ s^{-1}$ and $-1\times10^{-7}\ s^{-1}\ m^{-1}$ respectively were also taken from Chapter 4 (see Figure 4.6). Similar to the power spectrum from the HWRF run (Figure 5.7), there are large magnitudes of power observed across the n = 0 mode, related to the azimuthally averaged components of reflectivity which are expected to be relatively large for a mostly symmetric hurricane. However, the largest values of power are seen in the n = 1 and 2 modes are at frequencies of $0.001s^{-1}$ and $0.002s^{-1}$ respectively. These both correspond to phase speeds near 35 m s^{-1} and are remarkably consistent with the trace of the VRW dispersion relation for radial wavelengths of 10-15 km. For reference, the average tangential wind was on the order of 48-50 m s^{-1}. The radial scales of the observed VRW-driven rainbands were indeed on the order of 10-15 km, suggesting that the observed bands were consistent with VRW propagation. Thus, the consistency with the VRW dispersion relation of the dominant power spectra seen in

the HRWF run and observations suggest that rainband propagation is indeed consistent with VRW dynamics.

5.5 Asymmetric Contributions to Intensity Change

Finally, the contributions of VRW dynamics to intensity change in the HWRF run is compared to the observed character of asymmetric dynamics observed at landfall. The time-averaged contribution to intensity change by wave-mean flow interaction is first evaluated. As in Chapter 3, the flux of perturbation vorticity ζ' by the perturbation radial wind *u'* is evaluated. Smith et al. (2017) decomposed the tendency of the tangential wind into average and eddy components to examine the contributions of various processes in an evaluation of HWRF simulation of Hurricane Earl (2010). Equation (5.5) shows the time rate of change contributions to the azimuthal tangential wind in terms of the radial wind *u*, Coriolis parameter *f*, vertical velocity *w*, pressure *p*, density *ρ*, and sub-gridscale diffusion coefficients *D*. As in previous equations, an overbar quantity denotes an average with respect to azimuth and a prime quantity denotes the perturbation with respect to the azimuthal mean.

$$\frac{d\bar{v}}{dt} = -\bar{u}\left(\overline{f+\zeta}\right) - \overline{w}\frac{d\bar{v}}{dz} - \overline{u'\zeta'} - \overline{w'\frac{dv'}{dz}} + \overline{\frac{-\partial p'}{\rho r d\lambda}} + \overline{D} \qquad (5.5)$$

The terms on the righthand side of (5.5) represent in order the mean radial flux of the absolute vorticity, the mean vertical advection of the mean tangential wind, the radial eddy vorticity flux, the mean vertical advection of the perturbation tangential wind, the mean azimuthal perturbation pressure gradient force per unit area, and the horizontal and vertical diffusive tendency respectively. Here, the upscaling energy cascade (i.e., wave-mean flow interaction) is represented by the eddy terms of (5.5). As discussed in Smith et al. (2017), VRWs cannot be described in terms of azimuthally averaged dynamics (i.e., the azimuthal-mean terms), but can

nevertheless affect the azimuthally-averaged state of the vortex. Since much of the analysis being performed here is in the lowest levels of the HWRF run, the eddy vorticity flux will dominate the vertical advection of the perturbation tangential wind. Smith et al. (2017) also noted the pressure gradient terms are quite small due to the limited variability of density. Thus, the radial eddy vorticity flux is of primary focus as in Chapter 3. Similar to Chapter 3, the contribution of the time rate of change of the azimuthally averaged tangential wind due to the radial eddy vorticity flux $\bar{v}_{eddy}$ as a function of time is evaluated following (5.6).

$$\frac{\partial \bar{v}_{eddy}}{\partial t} = -\overline{u'\zeta'} \qquad (5.6)$$

As a function of radius, the eddy vorticity flux term was shown to change as a function of time through landfall in observations (Chapter 3). When Harvey's eyewall was over water in observations, the eddy flux contribution to intensity change was noted to be positive at an altitude of 0.5 km between r* ≈ 0.8 to r* ≈ 1.2. This suggests that the horizontal vorticity flux by eddies acted to the spinup of the tangential wind at low altitudes via wave-mean flow interaction. The process of rainband formation in the vicinity of asymmetries in the eyewall and the subsequent evolution of the vorticity field was shown to be representative of VRW initiation in MK97. Later in Chapter 4, the rainbands were shown to propagate as VRWs, suggesting that the flux of vorticity was at least partially explained by VRW dynamics.

Here in the HWRF run, the vertical distribution of the eddy vorticity flux (in m s^{-1} h^{-1}) is shown as a function of radius and height for two time periods: 25 August 2200-2230 (Figure 5.9a) and 26 August 0230-0400 (Figure 5.9b). For reference, the radius of maximum wind at 0.5 km altitude for each time period was 23 km and 20 km respectively. In Figure 5.9a, there is a region of positive velocity tendency (5.6) at radii where the VRW-driven rainbands were seen in Figure 5.4. The positive tendency is maximized at altitudes lower than 1 km between ~23 and 30

km radius, suggesting that the eddy contribution to the tangential wind was positive in a limited area just outside of the eyewall. This corresponds well to the rainbands associated with VRWs that spiraled into the radius of maximum seemingly near asymmetries in reflectivity and vertical vorticity. However, just within the radius of maximum wind between approximately 12 and 23 km range, a significant minimum less than -9 m s^{-1} h^{-1} is evident. This feature is likely associated with the radial flux of the intense vorticity values over a large portion of the eyewall in asymmetries rotating inside the radius of maximum wind during this period (visible in Figure 5.4). Compared to the observable character of vortices in Hurricane Harvey, the time-averaged affect was indeed smaller than -10 m s^{-1} h^{-1}. However, for periods when Harvey was observed over water, negative tendency of the eddy contribution to the tangential wind was observed within the maximum wind. In observations *at the radius of maximum wind*, the eddy flux term was positive. Alternatively in the HWRF run, the positive tendency is located *outside* the radius of maximum wind. This suggests that the wave fluxes in the HWRF run are offset compared to the observations.

To confirm this offset of the radial vorticity flux term, a second period of tangential wind tendency was examined later in the model solution prior to landfall on 26 August 0230 UTC to 26 August 0400 UTC (Figure 5.9b). Similar to Figure 5.9a, a deep column of negative (positive) tangential wind tendency forced by the radial vorticity flux can be seen inside (outside) 20 km range at low altitudes. Interestingly during this period, the eddy flux term contributed positively to the tangential wind for all radii sampled beyond 20 km range below approximately 1.75 km altitude. This is analogous to the observed character of Harvey just before landfall (Figure 3.6b), which suggested positive contributions by eddies to the mean tangential wind occurred for similar radii outside the radius of maximum wind. However, the change in sign of the eddy flux

contribution occurs at the radius of maximum wind in the HWRF run, rather than inside the radius of maximum wind as in observations. This finding is particularly significant, as the observed eddy vorticity flux suggested that VRWs acted to spinup the tangential wind at the radius of maximum wind, rather than outside it. This idea is explored further in the next section.

5.6 Summary and Discussion

This chapter has documented some of the characteristics of VRW-driven rainbands compared to the high spatiotemporal resolution observations of Hurricane Harvey near landfall. Specifically, rainbands arising from VRW-like structures were shown to evolve similarly to observations in terms of the vertical vorticity and updraft structure but were dissimilar to observations in terms of microphysics and downdraft character. The vorticity spirals associated with rainbands were shown to propagate as VRWs at phase speeds expected by the barotropic dispersion relation, similar to observations. The time-integrated effect of the VRWs however, was shown to be quite dissimilar to observations in terms of the upscaling energy cascade through the radial vorticity flux effect on the tangential wind. The rate of change of the symmetric intensity due to the radial vorticity flux was shown to be strongly negative interior of the radius of maximum wind. Outside the radius of maximum wind at both time periods, the wave flux tended to be positive at low altitudes. The observations suggest that wave-mean flow interactions act to enhance the vortex at the radius of maximum wind, but the HWRF run did not reproduce this result.

In terms of the rainbands seen in the HWRF run, it is likely that improvement in the microphysics scheme is required. It has been documented recently that microphysics schemes often overestimate the mass-weighted mean droplet diameter (Hristova-Veleva et al. 2021).

Inferred hydrometeor trajectories in the observed VRW driven rainbands in Chapters 3 and 4 suggest that hydrometeors generally grow in the radially inward updrafts, are likely advected radially outward by the secondary circulation of the TC, and fall out on the radial outward gradient of vertical velocity toward the deep downdrafts leading the rainbands. In the HWRF simulation, alternatively, the hydrometeors fell through the core of the vertical drafts, suggesting that the terminal velocity of the hydrometeors were able to overcome the velocities of the drafts (~4-5 m s^{-1} in the mid altitudes). Thus, it is likely that droplets are too large in the simulation. Retrievals of the drop size distribution were not performed here using the observed polarimetric data to evaluate the HWRF run but is a subject of future work that likely would act to improve the model microphysics scheme.

In terms of the VRW-driven rainband kinematics, the HWRF simulation generally represents the symmetrization process described in Chapters 3 and 4 and in MK97 quite well. Trailing spiraled vorticity maxima were shown to be coupled with rainbands and their vertical drafts, similar to the observed rainbands. The phase speeds matched well with the barotropic dispersion relation and were shown to manifest at similar wavenumbers to observations. This finding is particularly unique, as no study has been able to compare the results of VRW propagation seen in numerical modeling to observations of the same TC.

Perhaps the most difficult issue to diagnose in this simulation is the representation of eddy fluxes in HWRF compared to observation. In the simulation, the tangential wind tendency was positive outside the radius of maximum winds at low altitudes and strongly negative inside the radius of maximum wind. However, observations of Hurricane Harvey suggest that wave-mean flow interactions act to augment the tangential wind at the radius of maximum wind. The smoothness of the vorticity and reflectivity character discussed previously suggests the validity

of the simulation is partially a function of the diffusion scheme utilized in HWRF. The asymmetries in the hurricane eyewall were notably less pronounced in the simulation, while the maximum values in vorticity were much more azimuthally extensive than observed. Outside the eyewall, the VRW structures were significantly more homogeneous in azimuth compared to observations.

The horizontal diffusivity coefficient K_h in HWRF is a function of the horizontal mixing length L_h (Zhang et al. 2018). Previous HWRF runs have tuned L_h to be on the order of 800 m, which is a suggested mixing length consistent with observations from aircraft in TCs for the current operational implementations of HWRF (Zhang et al. 2015). Increasing L_h results in a suppressed radial gradient in momentum and potential temperature but decreasing L_h can result in an artificially intense vortex. The horizontal scale of previous studies using HWRF (e.g., Lu and Wang 2019) have been on the order of 2 km in the innermost nested domains. To properly scale the diffusion coefficient to ~800 m, the "coac" parameter may be tuned following (5.7) wherein *coac* is the dimensionless horizontal diffusion coefficient and *dx* is the minimum grid spacing (Janic 1990; Zhang et al. 2018).

$$L_h = \sqrt{0.1coac}\, dx \qquad (5.7)$$

For simulations at 2 km spatial resolution, a value of *coac*=1.2-1.6 is typically used. Here, a value of 2.6 was used, which resulted in a L_h of approximately 230 m for the smaller grid spacing used in this study.

In a recent study by Wang et al. (2021), a formulation for a new length scale was proposed for HWRF, which is dependent on the horizontal grid scale and formulated in terms of shear and stretching of the local horizontal wind. Given the available observations, Wang et al. showed it is likely such a formulation will improve the representation of the sub-grid scale

diffusion, which is noted to vary depending on the location with a TC (Zhang and Montgomery 2012). Zhang and Marks (2015) also specifically note that the eddy flux of momentum is sensitive to the choice of the horizontal mixing length. In terms of the observed VRW character here viewed from wave-mean flow interactions, it is likely that the perturbation quantities (5.6) are significantly impacted by the horizontal diffusion scheme. Specifically, the formulation of Wang et al. (2021) and limited observations (e.g., Zhang and Montgomery 2012) suggest that the horizontal diffusivity should scale with both wind speed and shearing, which are maximized near the radius of maximum wind. Thus, horizontal mixing may account for the offset in placement and magnitudes in the horizontal flux terms compared to observations. No matter the formulation of the diffusion scheme chosen, this work highlights the importance of accurately implementing sub-grid scale physics parameterizations. While larger-scale dynamical responses (i.e., VRW formation and propagation) in the model accurately represented observations, their impacts to smaller scale (perturbation eddy fluxes) were less successful. Future work will be required to investigate the sensitivity of the eddy structure to the horizontal length scale at high resolutions.

5.7 Figures

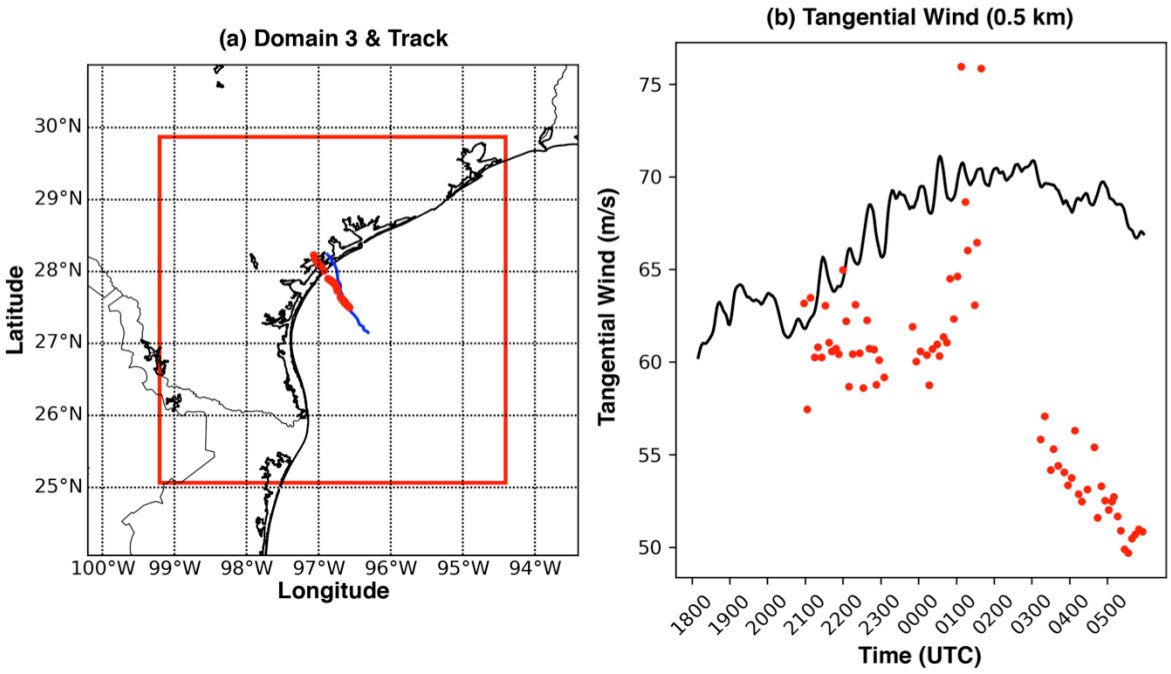

Figure 5.1. The domain details of the HWRF run of Harvey compared to dual-Doppler wind retrievals. (a) The red box shows the geographic location of domain 3 for the HWRF simulation. The blue line (red circles) show the GBVTD derived centers of circulation in time for the HWRF run (dual-Doppler analyses). (b) The comparison of the maximum tangential wind evolution at 0.5 km altitude between the HWRF run (black line) and dual-Doppler analyses (red circles) is shown.

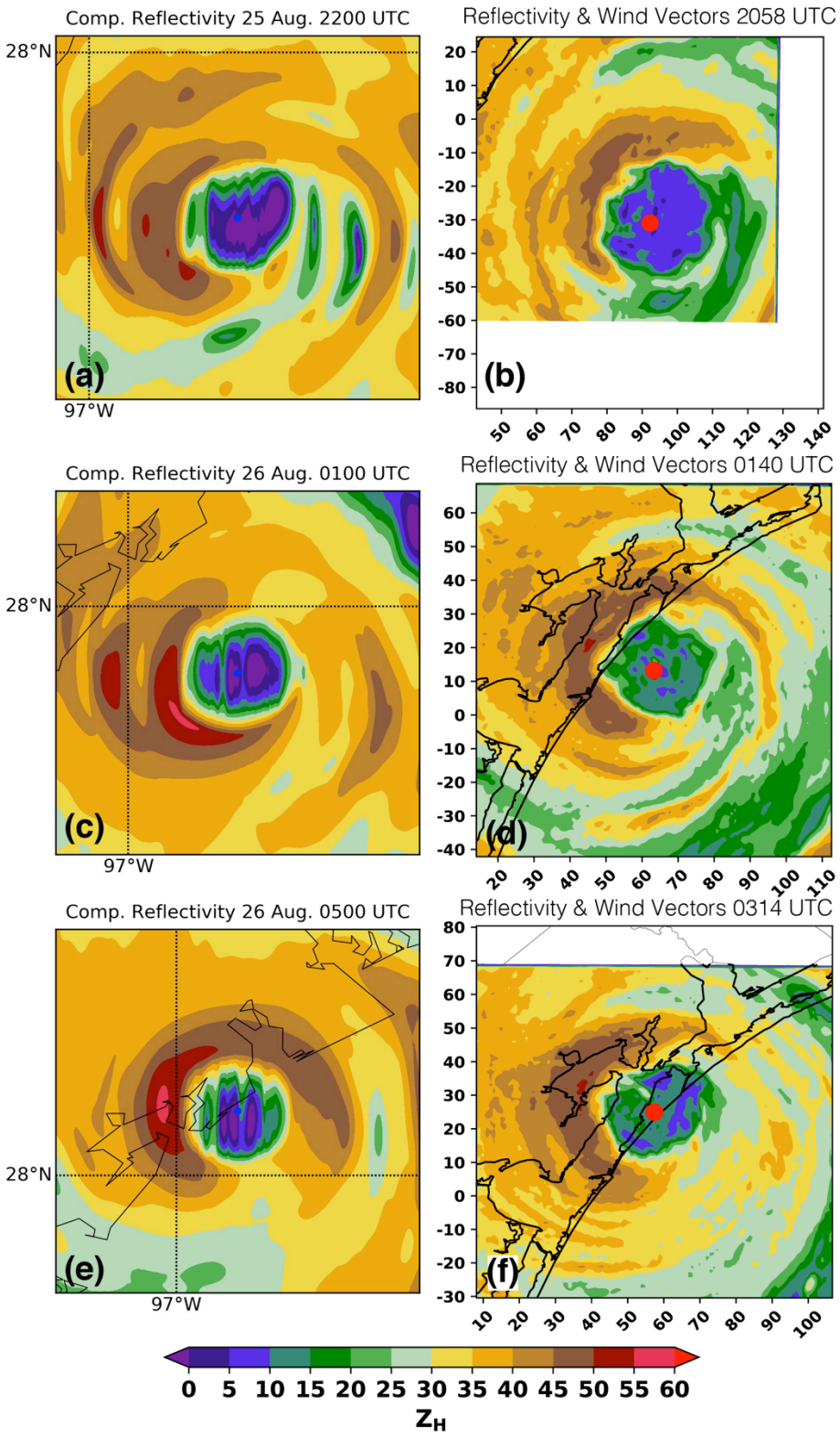

Figure 5.2. The temporal evolution of the HWRF run of Hurricane Harvey is shown compared to observations. In the left column (a, c, e) reflectivity at 0.5 km altitude is shown according to the

colorbar from the HWRF simulation. In the right column (b, d, f) the observed reflectivity at 0.5 km altitude according to the colorbar is shown. The first, second, and third rows of the figure display the model results at 2200 UTC, 0100 UTC, and 0500 UTC compared to the 2058 UTC, 0140 UTC, and 0314 UTC analyses respectively.

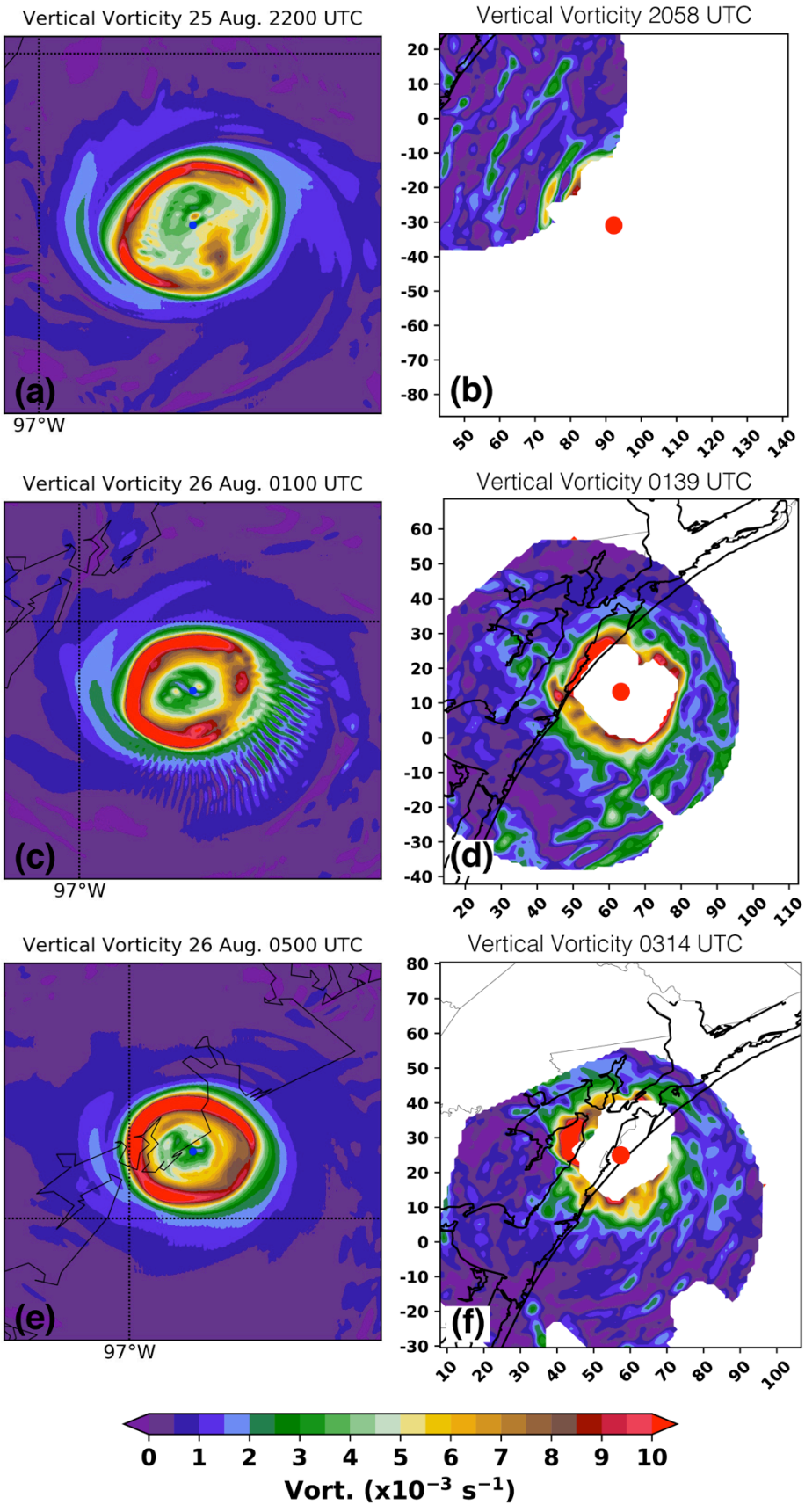
Vertical Vorticity 25 Aug. 2200 UTC
(a)
97°W
Vertical Vorticity 2058 UTC
(b)
Vertical Vorticity 26 Aug. 0100 UTC
(c)
97°W
Vertical Vorticity 0139 UTC
(d)
Vertical Vorticity 26 Aug. 0500 UTC
(e)
97°W
Vertical Vorticity 0314 UTC
(f)
0 1 2 3 4 5 6 7 8 9 10
Vort. (x10⁻³ s⁻¹)

Figure 5.3. As in Figure 5.2, but for the vertical vorticity field at 0.5 km from the HWRF run (left column) versus the observed vertical vorticity (right column).

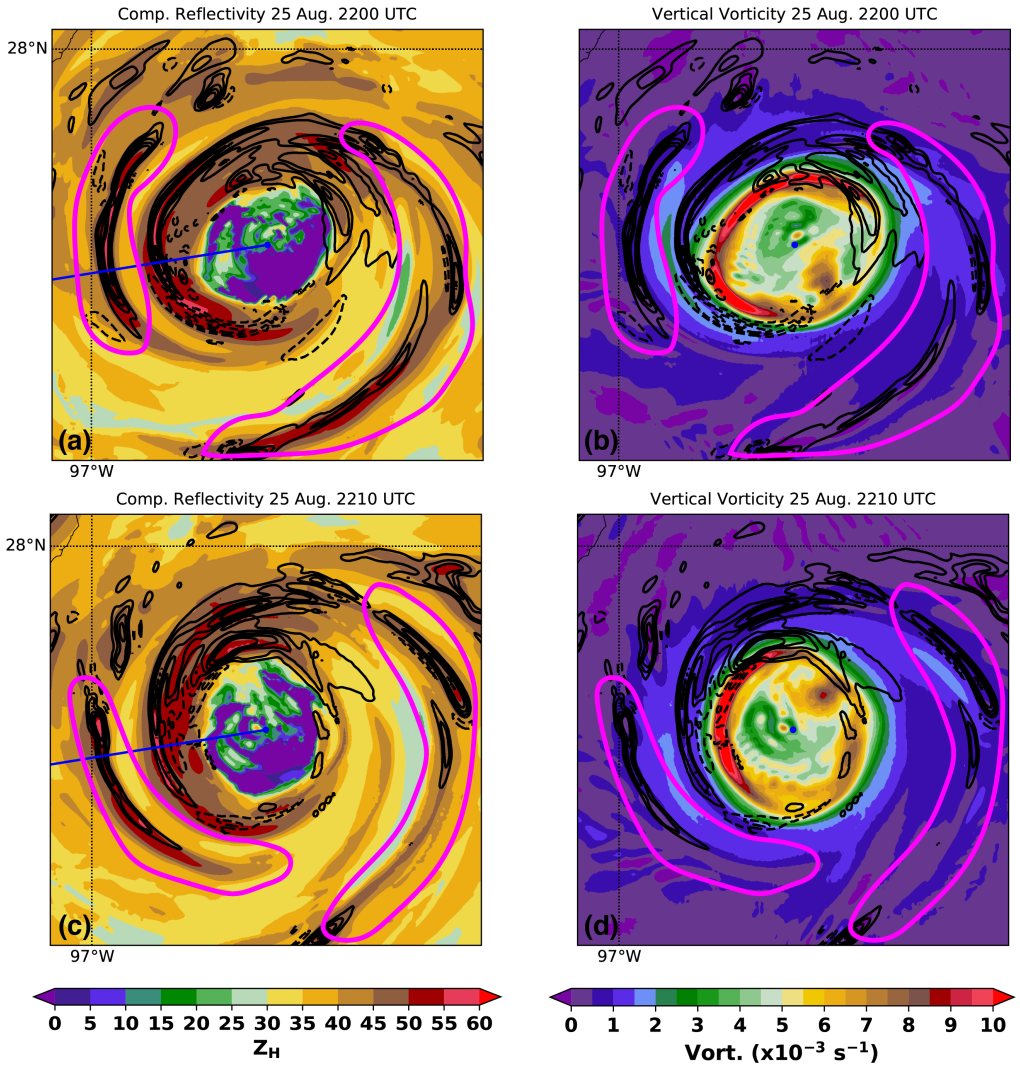

Figure 5.4. Output at 2200 and 2210 UTC in the HWRF run is shown. In the left column, the composite reflectivity (dBZ) is shown according to the colorbar. In the right column, vertical vorticity at 0.5 km altitude is shown according to the colorbar. In all plots, the black contours show vertical velocity at 4.5 km altitude every 1 m s^{-1} with the 0 m s^{-1} contour omitted. In (a) and (c), the blue line shows the location of the cross section in Figure 5.5

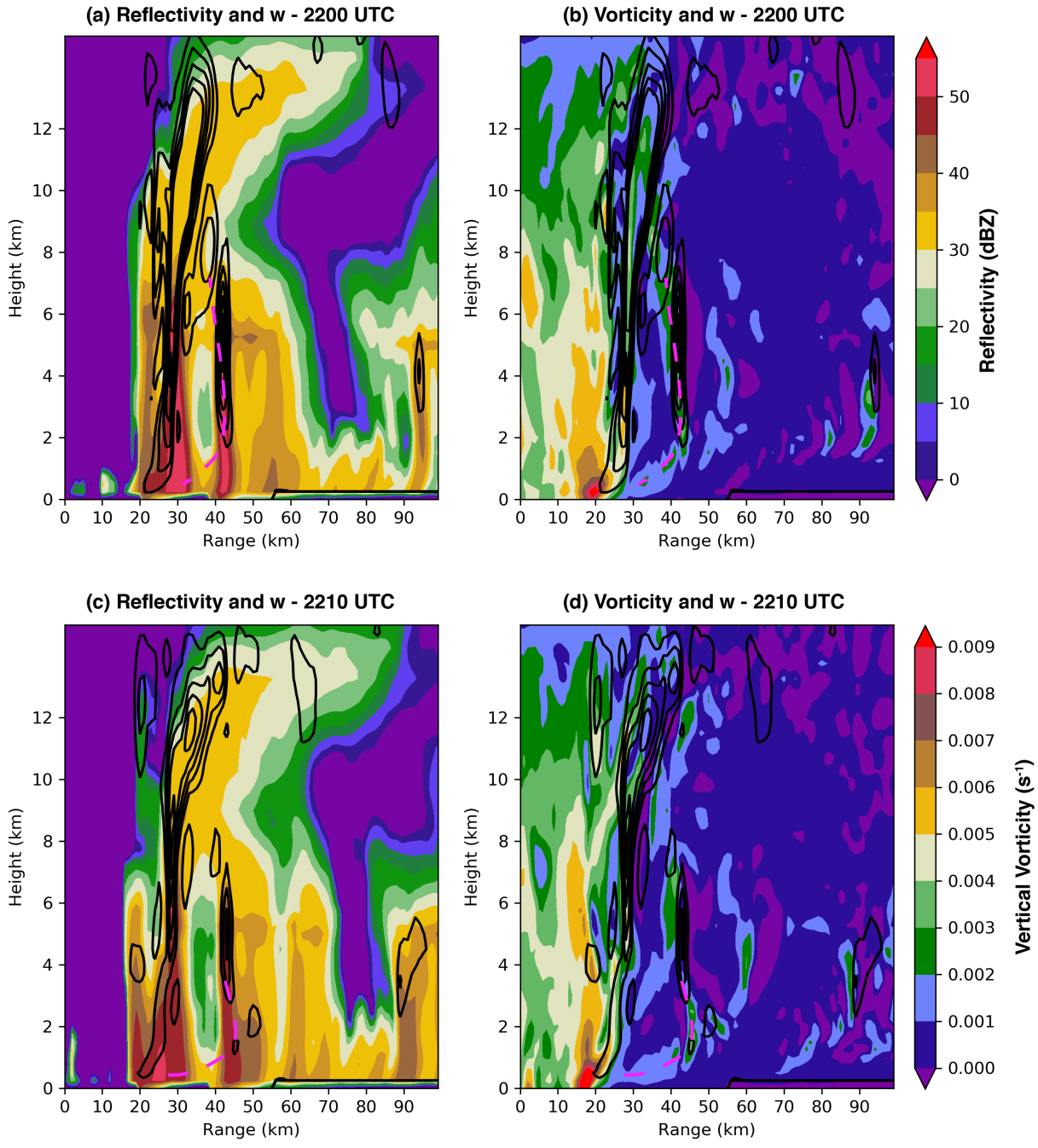

Figure 5.5. Vertical cross-sections of vertical vorticity (color-filled contours) taken at 260° from north starting at the center of circulation are shown. The black contours represent the vertical velocity every 1 m s^{-1} with the 0 m s^{-1} contour omitted. The magenta curve follows rainband that

propagates radially outward in the plane of the cross-section. For reference, the blue lines in Figures 5.4a, c denote the location of the cross-section.

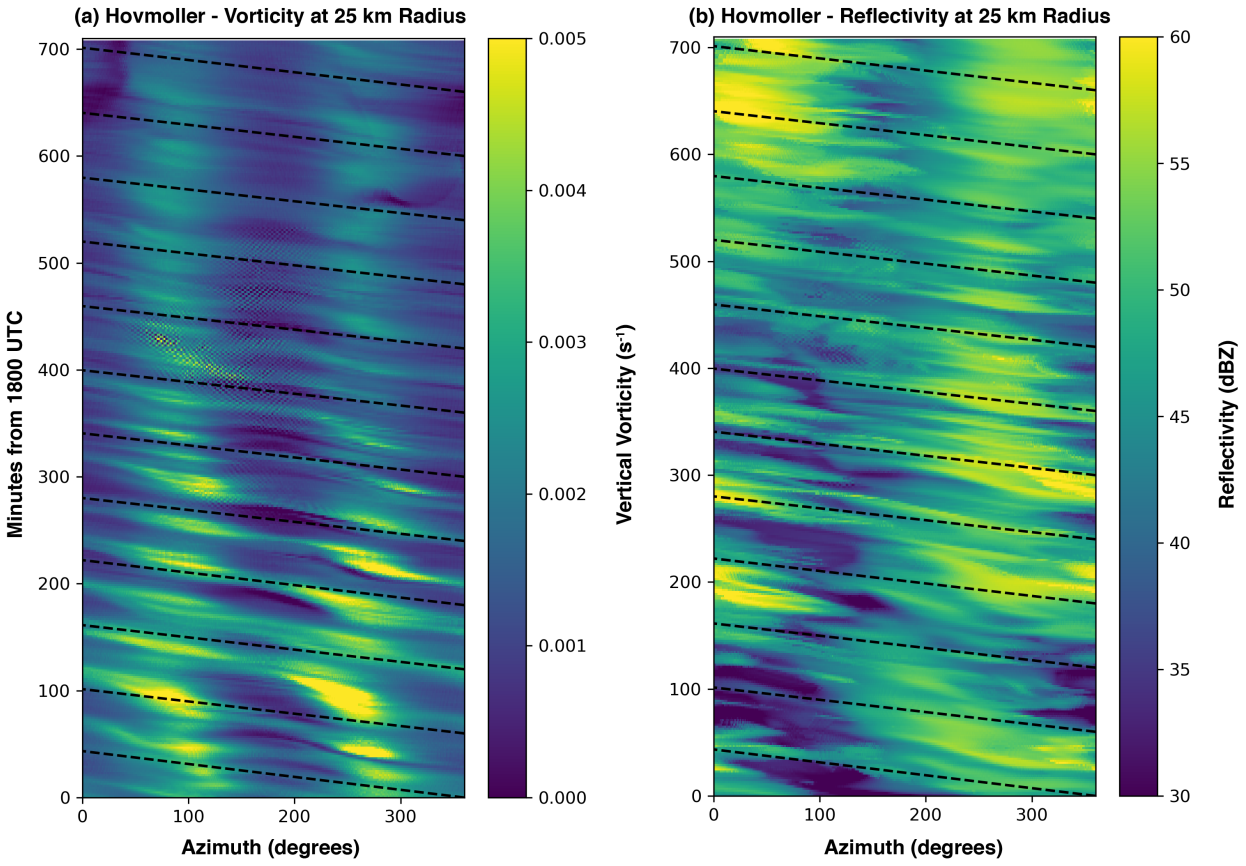

Figure 5.6. A Hovmoller analysis at a radius of 25 km from the center of circulation is shown. (a) displays the evolution of the vertical vorticity field (0.5 km altitude). (b) shows a similar analysis but for the composite reflectivity field. In both panels, the dashed black lines represent the magnitude of the azimuthally-averaged tangential wind.

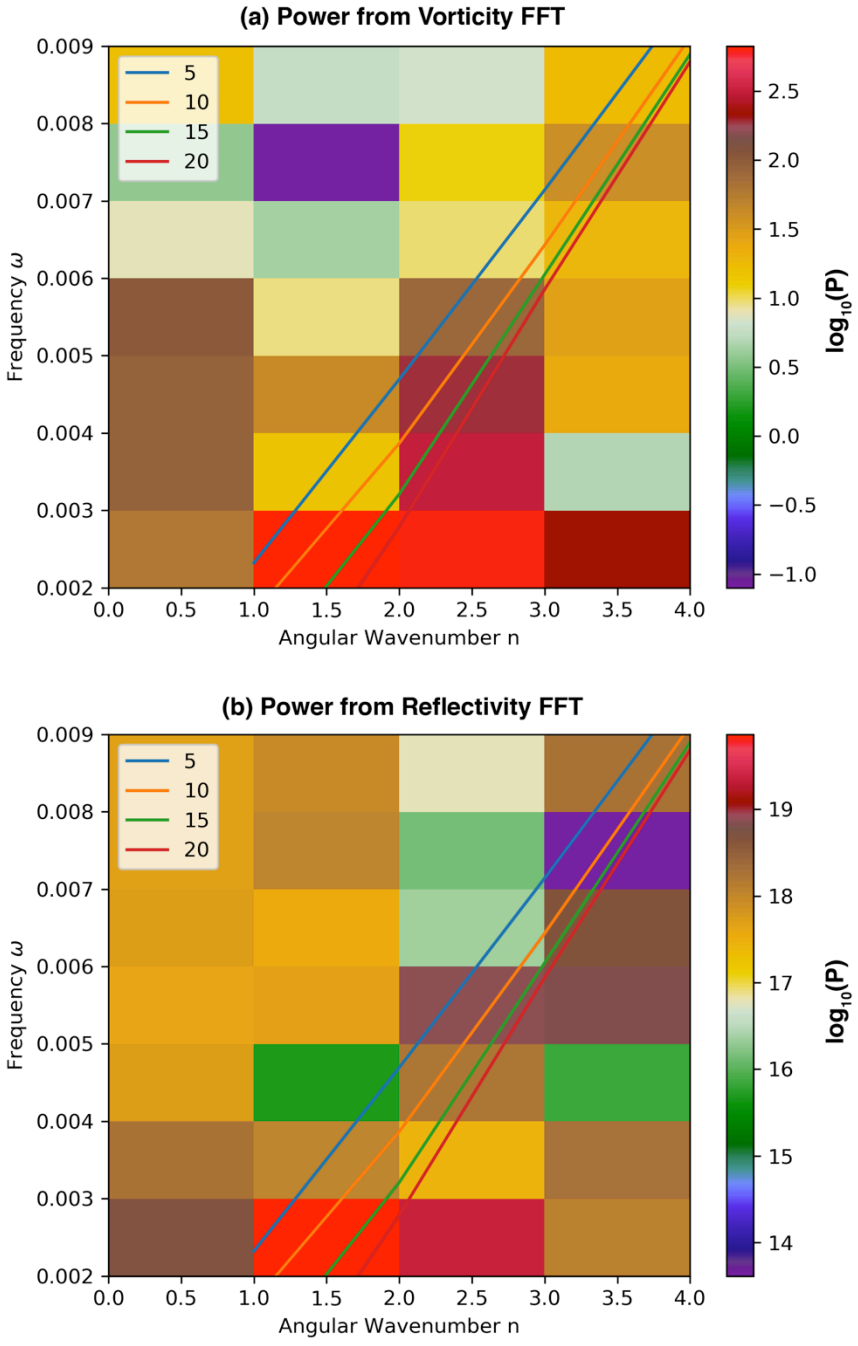

Figure 5.7. The power spectrum from the FFT analyses of vorticity (a) and reflectivity (b) are shown. The lines represent the VRW dispersion relation traces for the wavelengths (in km) according to the inset legends.

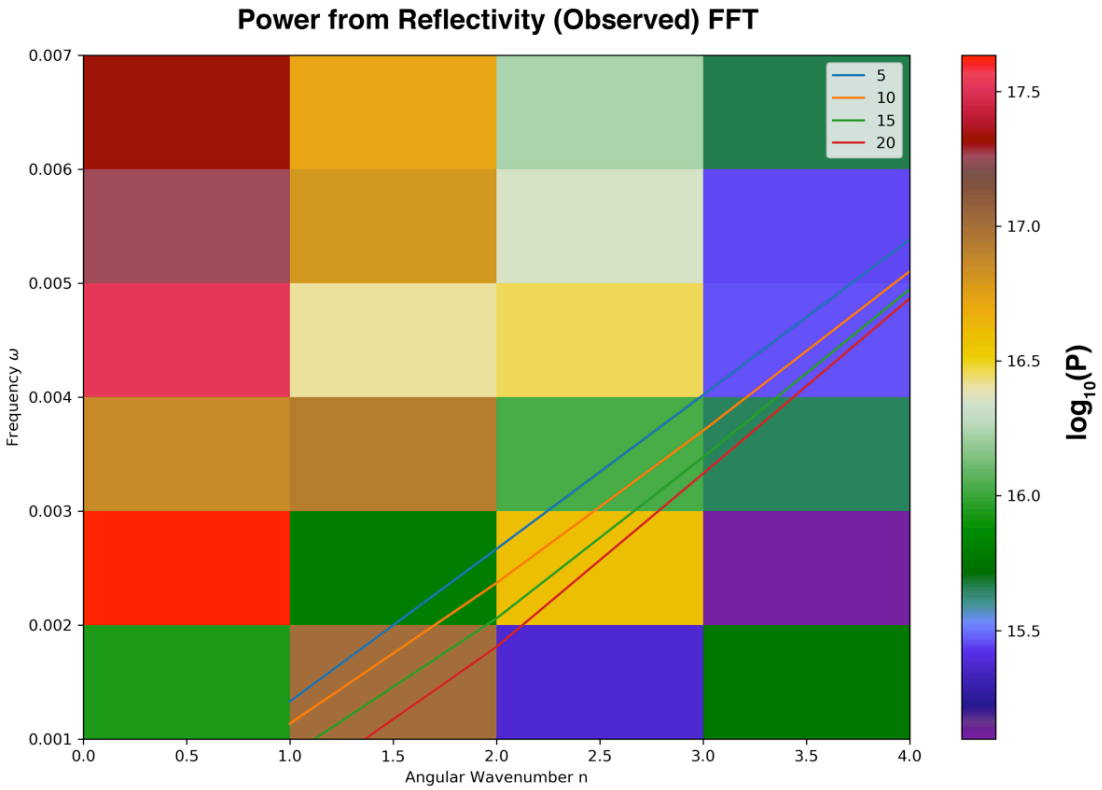

Figure 5.8. Similar to that shown in Figure 5.7b, a Fourier power spectrum of the *observed* reflectivity field discussed in Chapter 4 is shown.

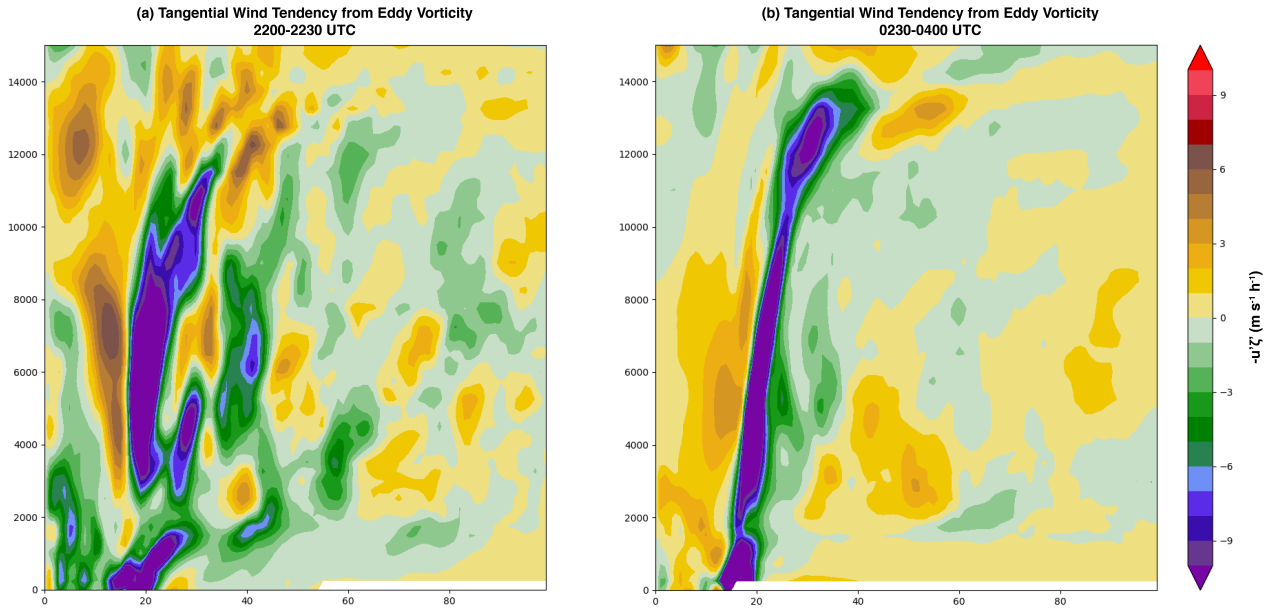

Figure 5.9. The time rate of change of the mean tangential wind due to the eddy vorticity flux is shown according to the colorbar. (a) Shows the mean rate of change on 25 August from 2200-2230 UTC in the HWRF run. (b) Is as in (a), but for 26 August 0230-0400 UTC.

5.8 Tables

Table 5.1. Details of the HWRF simulation of Hurricane Harvey.

Model Parameter	Details
Horizontal Resolution on Domains 1, 2, 3	0.036°, 0.012°, 0.004°
Microphysics parameterization	Ferrier-Aligo microphysics scheme
Cumulus parameterization	The Scale-Aware Simplified Arakawa-Schubert (SASAS)
Surface parameterization	HWRF modified surface layer scheme
Land surface model	Noah land surface model
Boundary layer parameterization	HWRF PBL scheme
Radiation parameterization	RRTMG longwave and shortwave radiation schemes
Data Assimilation Observations	Coastal WSR-88D Radial Velocity, TDR, flight level observations, SFMR, and operational observations (atmospheric motion vectors; radiosondes; dropwindsondes; aircraft reports; surface ship and buoy observations; surface observations over land; Pibal winds; wind profilers; /radar- derived velocity–azimuth display wind; WindSat scatterometer winds; integrated precipitable water derived from the global positioning system; satellite radiances from HIRS, AIRS, IASI, GOES, AMSU-A, MHS, and ATMS)
Inner/Intermediate/Outer Domain Input	6-hourly dual-resolution 3DEnVar assimilation of observations above; DA performed on 0.011° background grid with a 40-member ensemble of 0.033° resolution; analyses interpolated onto domains 1-3 to perform high resolution run for this study. See Lu and Wang (2021; in preparation for *Monthly Weather Review*).

Chapter 6: Observed Characteristics of the Hurricane Boundary Layer at Landfall

6.1 Introduction

Understanding the distribution of winds, intensity change, and tropical cyclone (TC) structure requires comprehensive knowledge of the storm's atmospheric boundary layer (hereafter referred to as the Hurricane Boundary Layer [HBL]; e.g., Montgomery et al. 2014). The structure of the HBL can influence the vertical distribution of momentum through turbulent fluxes, which in turn can influence the horizontal distribution of the maximum wind experienced at any one location, particularly during landfall (Wurman and Winslow 1998; Alford et al. 2019b). Due to the increase in aerodynamic surface roughness over land versus that over the open ocean, sustained wind speeds are expected to decrease while the dynamic boundary layer is expected to increase in depth (Elliott 1958; Garratt 1990; Tang and Tan 2006; Hirth et al. 2012; Williams 2019).

Observations of the mean HBL structure over the open ocean are generally plentiful (Wang et al. 2015; Zhang et al. 2011). High vertical resolution (10-20 m) dropsonde (Hock and Franklin 1999) observations have been collected by several airborne platforms including the National Oceanic and Atmospheric Administration's (NOAA's) WP-3D Orion and G-IV jet (Aberson et al. 2006) operated by the NOAA Aircraft Operations Center, the C-130 Hurricane Hunter aircraft operated by the United States Air Force (USAF; e.g., Franklin et al. 2003), the HIAPER aircraft operated by National Science Foundation (NSF; UCAR/NCAR 2005), and the DC-8 and Global Hawk operated by the National Aeronautics and Space Administration (NASA; Naftel 2009). Such observations have documented the vertical thermodynamic and kinematic structure of TCs over large mesoscale regions across the entire cyclone and surrounding environment. The mean structure of the HBL has been elucidated through individual and

composite dropsonde observations over hurricanes of varying strengths and varying degrees of symmetry (e.g., Franklin et al. 2003; Kepert 2006; Zhang et al. 2011, 2013). In general, it has been found that the top of the dynamic HBL (i.e., the level at which the hurricane radial inflow is 10% of its peak value) decreases with height with decreasing radial distance from the center of circulation (Zhang et al. 2011; Giammanco et al. 2012). Wind profiles often exhibit a distinct peak (or jet) within the dynamic HBL, usually near the inner core of the tropical cyclone (Giammanco et al. 2012). Numerical modeling studies have focused on replicating the HBL as observed in nature, often finding that the representation of the HBL is highly sensitive to model diffusion and HBL parameterization schemes (e.g., Xiaodong and Zhemin 2006; Bryan and Rotunno 2009; Nolan et al. 2009a,b).

In contrast to the open water HBL, the structure of the HBL across the land-water interface across the coast is not as well documented. Observations over the land surface are limited by aircraft flight safety concerns while the sparse nature of profiling systems over land limit where vertical profiles of the boundary layer may be retrieved. Nonetheless, a few observational studies have been performed (Morrison et al. 2005; Lorsolo et al. 2008; Giammanco et al. 2012; Hirth et al. 2012; Ming et al. 2014). Hirth et al. (2012) found that an internal boundary layer (IBL; c.f., Garratt 1990) formed across the land-ocean interface during the landfall of Hurricane Frances (2004). The IBL resulted from the surface roughness discontinuity across the coastal transition. In general terms, the IBL forms due to a discontinuity in, for example, aerodynamic surface roughness (e.g., an ocean-land interface) as flow passes across the discontinuity (e.g., Garratt 1990; Savelyev and Taylor 2005). All else being equal downwind of the discontinuity, the boundary layer adjusts to the new surface roughness characteristics such that the IBL grows until it represents the complete depth of the fully adjusted

boundary layer (see Hirth et al. 2012, their Figure 6). In Hirth et al. (2012), the complexity of the coastal environment and the attendant adjustment of the HBL were examined. Across the coastal interface, the modeled empirical growth of the IBL was observed to be less than expected. Due to inhomogeneities in surface roughness and the added complexity of coastal islands, the structure of the growing boundary layer was far from homogeneous in their analyses. In addition, significant backing of the low-level (400-500 m) winds was observed in their analyses, with changes in wind direction of 15-20° immediately inland.

Using velocity-azimuth display (VAD) profiles, Giammanco et al. (2012) demonstrated that the evolution of onshore and offshore flow denoted by normalized boundary-layer mean wind profiles were relatively similar. Specifically, the reduction in the boundary layer height with decreasing storm-center-relative radial distance was found for both onshore and offshore regimes. Jet-like features were observed in profiles in both regimes as well, largely tied to regions near the radius of maximum wind (RMW). However, significant differences were found in onshore and offshore wind profile structures for the same normalized radial distances. Surface roughness and upwind terrain characteristics were found to change the vertical structure of the boundary layer significantly. The authors also made mention of jet-like features in outer rainbands, similarly found in Knupp et al. (2006). Neglecting storm-relative space, Krupar et al. (2016) used VAD profiles to estimate the surface wind speed in 17 hurricane landfalls. It was found that WSR-88D site-specific constructions of linear regression equations yielded the most accurate surface wind estimates. However, the authors acknowledged that VAD retrievals are limited in assessing HBL characteristics across large spatial regions and emphasized the need for spatially contiguous observations from, for example, dual-Doppler analyses across the coastal region.

Ming et al. (2014) documented fluctuations in HBL structure with the passage of outer rainbands in Typhoon Morakot (2009). Downdrafts associated with rainbands tended to reduce the height of the tangential wind maximum. Contrary to most studies, Ming et al. found that the tangential wind maximum in the outer rainbands was above the height of the dynamic HBL and suggested the observation could be the direct result of landfall processes. However, no study has been able to address the change of the height of the tangential wind maximum while observing both onshore and over water boundary layer structure and the transition between the two. If the observation of the tangential wind maximum above the boundary layer is generally applicable to TC landfalls, then the landfall HBL transition is likely important in the vertical momentum structure observed over land. In particular, the projection of momentum aloft via turbulence on a variety of spatial scales has been shown to be fundamental in the magnitude of gusts observed at the surface (Morrison et al. 2005; Lorsolo et al. 2008; Kosiba and Wurman 2014). Furthermore, individual convective processes such as rainbands are also likely fundamental to the observed vertical distribution of momentum. However, a comparison of the HBL in rainbands to that of the inner core and eyewall has not been examined within an individual storm.

In this study, the transition of the HBL, specifically the structure of the sustained wind, during the landfall of Irene (2011) will be documented quantitatively using over-ocean dropsonde observations, land-based VAD retrievals from ground-based Doppler radars, and dual-Doppler wind retrievals. The study is unique in that the observations over land and water were collected within the same time period. Flow regimes in the outer bands, the inner core, and eyewall can also be directly compared. Moreover, one set of VAD winds is from a frequency-agile Doppler radar with a temporal resolution of approximately 30 s and can be used to extend the information extracted from dual-Doppler analyses (available every 10 min). Additionally, the

dual-Doppler domain includes portions of the coastal interface. Hence, for the first time, the mean HBL can be examined near simultaneously from over water, through the coastal transition, and inland. Specifically, the transition of the tangential wind maximum will be shown as the HBL changes in response to the coastal surface roughness discontinuity. The coastal transition, in particular, is herein documented with high temporal and spatial resolution across a limited domain within ± 10 km from the land-water interface and extended through dropsonde and VAD analyses.

6.2 Data and Methods

Noted in Avila and Cangialosi (2012), Hurricane Irene (2011) began as a tropical wave originating off the coast of Africa on 15 August and became a tropical storm on 21 August east of Dominica. At its most intense period, Irene struck the Bahamas as a Category 3 hurricane (50-58 m s^{-1}) before moving north and beginning to weaken. On 27 August, Irene made landfall near Cape Lookout, NC as a Category 1 storm (estimated 38.6 m s^{-1} maximum sustained 1-min wind at 10 m altitude). In addition to flooding and wind damage experienced in North Carolina, Irene produced tremendous inland flooding in parts of New England before making its extratropical transition at higher latitudes.

During its landfall in North Carolina, simultaneous observations by the NOAA aircraft and ground-based mobile and stationary radars afford the retrieval of boundary layer structure over the open ocean, in coastal waterways, and onshore. At the time of simultaneous observations prior to and during landfall, Irene was considered a Category 1 hurricane with a maximum sustained wind of ~38 m s^{-1}. The observational period (00 to 13 UTC) encompasses

the outer bands, inner core (generally the annulus bounded by the RMW wind to a radial approximately three times that of the RMW), and eyewall (c.f., Houze 2010).

6.2.1 Dropsondes

GPS dropwindsondes (here referred to as "dropsondes") are commonly released by the NOAA P-3 to characterize vertical structure of temperature, relative humidity, pressure, and horizontal and vertical wind speeds and directions in hurricanes (e.g., Franklin et al 2003; Halverson et al. 2006; Stern et al. 2016; Rogers et al. 2017). The details of a dropsonde and its measurement errors can be found in Hock and Franklin (1999) and Zhang et al. (2011, Section 2b). Here, the dropsonde kinematic data are especially useful for characterizing the vertical structure of the HBL winds and are exclusively utilized for consistency with other datasets described below. In addition, the depth of the boundary layer is calculated according to the dynamic definition recommended in Zhang et al. (2011).

During Hurricane Irene, the NOAA P-3, the NOAA G-IV (Aberson and Franklin 1999), and Air Force Reconnaissance aircraft conducted a series of flights near landfall that will be the focus of this study (see Figure 6.1a, 6.1c). Dropsondes used in this study were limited to 27 August 2011 to be representative of the environment over water in close proximity to available land-based instrumentation. All dropsondes were processed using the National Center for Atmospheric Research's (NCAR's) Atmospheric Sounding Processing Environment (ASPEN) software as described in Zhang et al. (2013). The fallspeed of a typical dropsonde is 12-14 m s^{-1} and the sampling rate is 2 Hz, yielding 5-7 m vertical sampling. The 2-Hz sample was filtered over 5-s intervals in ASPEN, yielding approximately 10-m resolution.

6.2.2 SMART Radar and Morehead WSR-88D

SMART Radar 2 (SR2) was deployed to Michael J. Smith airfield near Beaufort, NC prior to Hurricane Irene's landfall. SR2 (located at 34.7331°, -76.6619°) operated continuously for approximately 15 hours between 2100 UTC on 26 August and 1215 UTC on 27 August 2011. While SR2 collected data to achieve a variety of science objectives, SR2 radar volumes that were appropriate for performing dual-Doppler analysis with the nearby WSR-88D (Crum and Alberty 1993) in Morehead City, NC (KMHX; located at 34.7760°, -76.8762°) were collected every 10 minutes.

Level II data for KMHX were retrieved from the National Centers for Environmental Information (available at https://www.ncdc.noaa.gov). Dual-Doppler analyses were conducted between 0000 UTC and 1215 UTC on 27 August. While SR2 collected data beginning at 2100 UTC on 26 August, KMHX data between 1800-2359 UTC on 26 August were unavailable, and hence no dual-Doppler analyses were performed. The radial velocities from both radars were objectively dealiased using the region-based dealiasing method available in the Python-ARM Radar Toolkit (Py-ART; Helmus and Collis 2016; see Appendix 1 for additional details). SR2 was operated in staggered pulse repetition time (PRT) mode (Torres et al. 2004), which extends the unambiguous Doppler velocity interval. Errors associated with the staggered PRT method were corrected (Alford et al., in preparation) after the radial velocity data were dealiased using a technique similar to Alford et al. (2018).

The radar reflectivity (Z_H) and Doppler velocity (V_R) data were interpolated to a Cartesian grid using a Natural Neighbor interpolation (Sibson 1981) method documented in Betten et al. (2018). The Cartesian grid had an origin set to the location of KMHX, with minimum x, y, and z distances of 5, 5, and 0.2 km and maximum x, y, and z distances of 50, 50, and 10.2 km,

respectively. The 20-km baseline between the radars provided high spatial resolution over the analysis domain, and horizontal and vertical spacing were set to 250 m and 200 m, respectively. Because the southern dual-Doppler domain was largely affected by ground-clutter from Morehead City, the northern dual-Doppler lobe, which extended over a salt water inlet and open fields, were exclusively used here (Figure 6.1b).

The interpolated data were passed into a three-dimensional variational (3DVAR) dual-Doppler analysis technique documented by Potvin et al. (2012). This technique is designed to heavily weigh the observed radial velocity fields when storm-topping echoes are not available (i.e., when the column total mass continuity is under sampled). As the dual-Doppler domain is relegated to below the storm tops at times, this technique is heavily favored for the retrieval of the horizontal winds, rather than traditional, iterative techniques that require better sampling of a column's total divergence profile.

In addition to dual-Doppler analysis, range height indicator scans (RHIs) were collected by SR2. However, the azimuths over which the RHIs were taken varied at the discretion of the radar operator. To provide a more consistent set of vertical cross-sections, RHIs were developed from the volumetric scans over a 15° azimuthal sector every 3°, yielding five total RHIs per volume. The radial velocity field was dealiased manually in all cases using Solo3 (Oye et al. 1995).

6.2.3 RaXPol Data

The Rapid X-band dual-polarization radar (RaXPol; Pazmany et al. 2013; Pilke et al. 2013) was deployed nearly co-located with SR2 in Beaufort, NC. Using a frequency-agile transmitter, RaXPol collects data at a maximum azimuthal antenna rotation rate of 180° s^{-1}.

During the landfall of Irene, RaXPol operated at 120° s^{-1}, yielding one elevation scan every 3 s (excluding time to transition the antenna to the next elevation). RaXPol primarily operated between 00 and 05 UTC, affording high temporal resolution Doppler velocity retrievals of the HBL within 30 km of the radar's location (34.7300°, -76.6570º) during the landfall of Irene's outer bands. The data were similarly processed through Py-ART's region-based dealiasing scheme. These data were analyzed using a velocity-azimuth display (VAD) technique described below.

6.2.4 Coastal VADs

The VAD technique described in Browning and Wexler (1968) was used to construct representative profiles of the boundary layer wind structure from Doppler radar. The technique involves using Doppler velocity observations around constant radii circles to retrieve the mean flow at constant heights. The fit of Fourier coefficients to the radial velocity observations assumes that the flow characteristics around a constant radial circle vary at most linearly across the circle.

The vertical resolution of the constructed vertical profiles is dependent on the radial resolution of the radar data. Profiles were constructed for both KMHX and RaXPol radial velocity observations. KMHX collected data at 250-m radial resolution. Using radial velocity data between 0.15 km and 8.0 km from KMHX, VADs with an average resolution of ~7 m in the vertical were obtained and a maximum resolution of ~85 m. Thus, data were linearly interpolated to 15 m vertical resolution. The temporal resolution was approximately every 5 min for VADs retrieved between 0000 and 1300 UTC on 27 August. RaXPol obtained radial velocity data at much higher temporal and radial resolutions. The vertical resolution varied between 15 and 75

m, so the VAD profiles were linearly interpolated to a resolution of 15 m in the vertical. Radar volumes were obtained approximately every 30 s, yielding high temporal resolution observations of the boundary-layer wind profiles. The observation period of RaXPol was largely confined to 0000 to 0500 UTC, during which time the outer bands of Irene were moving on shore.

6.3 Open Water Dropsonde Profiles

To facilitate compositing of the HBL vertical profiles within the storm's dynamic framework, observations of the *RMW* based on stepped frequency microwave radiometer (SFMR; e.g., Uhlhorn and Black 2003) data were used to normalize the radial distance from the center of circulation *(r)* relative to the RMW using (6.1).

$$r^* = \frac{r}{RMW} \qquad (6.1)$$

Total wind speed dropsonde observations from 27 August 2011 prior to and during Hurricane Irene's landfall were composited for the lowest 1200 m altitude by the normalized radius r^*. Dropsondes with drop points $0.8 < r^* < 3$ and distances between 0 and 100 km from the nearest point on the coast were retained for this study. This method yielded 10 dropsondes taken within 50 km of the nearest coastline (near coast) and 7 dropsondes between 50 and 100 km of the coastline (far coast; Figure 6.1a). The wind speeds are also normalized by the mean 10-500 m wind speed observed by each dropsonde unless otherwise noted.

Although a relatively small sample for each set of coast-relative distances, Figure 6.2 shows the mean normalized profiles for the near and far coast dropsondes. All profiles were taken within 100 km of the coastline and over the North American continental shelf. One dropsonde (highlighted in Figure 6.1) was dropped just beyond the continental shelf, but is

retained as it was very near the gradient in bathymetry. Hence, the dropsonde profiles are assumed to be representative of shoaling wave conditions (Powell et al. 2003), where drag coefficients are increased relative to deep water (e.g., beyond the continental shelf). Each profile shows normalized wind speed maxima well above the surface. In addition, both regions exhibit mean 10-m normalized winds that are less than 0.8 of the 0-500 m mean flow, similar to past studies (e.g., Kepert 2001). The composite profiles yield several results of note. First, the normalized wind speeds in the lowest 100 m of both near and far coast profiles are significantly more variable than other winds below 500 m, with standard deviations on the order of 0.10-0.15 of the normalized mean wind speed. A similar increase in the variability of the normalized profile was recorded in Giammanco et al. (2012). Secondly, while the magnitudes of the mean 10 m wind speed normalized by the 0-500 m mean are similar for the near coast (0.79; Figure 6.2a) and far coast (0.76; Figure 6.2b), the structure of the normalized profiles differ strongly aloft. The near coast profiles exhibit their maximum values around 600-800 m altitude while the far coast wind speeds are maximized at approximately 400 m. The "jet" structure exhibited by both profiles is consistent with previous observations of the HBL observed well over water (e.g., Zhang et al. 2011; Giammanco et al. 2012).

The robustness of the limited observations taken on 27 August was compared using all the dropsondes in Hurricane Irene between 26-28 August 2011 and for $0.8 < r^* < 3.0$ (shown as red lines in Figure 6.2). However, to generate a larger sample, dropsondes were not delineated according to their coast-relative distance (i.e., dropsondes over the open ocean, well away from the coast were retained). In total, 42 profiles were retained for comparison to the near and far coast profiles (see red lines in Figure 6.2; referred to as the all-profile-mean). The profile structure below 400 m delineated by coast-relative distance represented the all-profile-mean

well. Specifically, the normalized wind speeds at 10 m for the near and far coast profiles were quantitatively similar to the all-profile-mean (differences of ~0.02 to 0.03). In addition, the 10-400 m layer for both near coast and far coast profiles are quantitatively representative of all profiles (differences generally less than 0.05). The height of the maximum normalized wind for all dropsondes was 600-800 m, which matched the near coast profile well. In addition, normalized differences of approximately 0.03-0.05 above a height of 600 m exist for near coast profiles, suggesting the entirety of the near coast profile was generally representative of the dataset. However, some differences aloft were noted in the far coast profiles. The far coast profile appeared to suggest a height of the maximum normalized wind to be near 400 m. It is unclear if the differences between all profiles and the far coast profile were due to sampling differences or the smaller number of dropsondes (7 in total). The differences in sample space are hypothesized (particularly sondes dropped at varying r^*) to be a more plausible reason for differences in the profiles, rather than the sample size itself.

The observed dropsonde wind profiles can be decomposed into tangential and radial wind components by projecting the wind direction into a storm-center-relative framework using the method of Willoughby and Chelmow (1982). Uncertainty in the exact center of circulation can affect the estimation of the radial wind more strongly than the tangential wind. Nevertheless, the approach has been used in previous studies (e.g., Giammanco et al. 2012) successfully, as it is based upon center-fixes collected by aircraft operations at higher temporal frequency than National Hurricane Center Best Track estimates. The characteristics of the tangential wind component in the soundings are largely similar to those of the full wind profiles described above (see Figure 6.3a and b). In contrast, the radial wind profiles (Figure 6.3c, 6.3d) exhibit significantly greater variability, likely due to the azimuthal variability in the radial wind. Based

on the composite mean, the near coast (0-50 km) profiles (Figure 6.3c) suggest that the boundary layer height, h_{inflow} ,is approximately 1000 m with the peak tangential (and peak full) wind speed near 800 m altitude (Figure 6.2a). This is consistent with past observational studies, which have demonstrated that the maximum tangential wind is often located within the inflow layer as shown here (Vickery et al. 2009; Zhang et al. 2011; Montgomery et al. 2014). To examine the transition of the boundary layer from the open ocean to the coast, vertical wind profiles were derived from the dual-Doppler analyses.

6.4 Coastal Composite Profiles

Since the dual-Doppler domain includes both water and land surfaces, a classification of "land" or "water" was assigned for each dual-Doppler grid point (Figure 6.4a) using the Basemap function in Python (available online at https://matplotlib.org/basemap). The distance (regardless of wind direction) from the coast was calculated (negative values in Figure 6.4b indicate inland and positive indicate over coastal waterways). For each dual-Doppler grid point, a vertical profile normalized by the 0-600 m mean wind (slightly different from the dropsondes in Chapter 6.3 due to the differing vertical resolution) was constructed. In general, profiles were taken between 10 km inland and 5 km over water (-10 km to +5 km) of the coastline. A subset of the dual-Doppler lobe (shown in Figure 6.1a) was used in this region. Within the observation period, the mean wind direction across the dual-Doppler domain was between ~70° to ~110° (winds from the east), indicative of onshore flow in the dual-Doppler domain. Since the dual-Doppler subdomain is relatively small, the water versus land profiles are assumed to be taken approximately in the same storm-center relative space. However, differences are readily apparent

in the mean winds over land and over water as expected with domain-averaged 0-600 m wind speeds less over land than over water (Figures 6.4c, 6.4d).

6.4.1 Over Water HBL Structure

To examine the coastal transition of the boundary layer throughout the dual-Doppler observation period, the over land and over water profiles were further delineated into subsets representing the distance to the nearest point of coastline. Negative distances indicate profiles over land and positive distances indicate profiles over water. As shown in Figure 6.4, the water surfaces used here are confined to coastal waterways that experienced easterly flow throughout the dual-Doppler period. At times depending on the exact wind direction, flow may have undergone transition off of land surfaces into the coastal waterways. Nevertheless, flow was generally in an onshore regime across the domain as a whole.

The result over the full ~12 h period of the dual-Doppler analysis is shown in Figure 6.5. The near-shore profiles retrieved by dropsondes in Figure 6.2 showed a maximum in normalized wind speed above 600 m. Similarly, the dual-Doppler-derived mean profiles just off the coastline indicate the maximum wind speed was between 400 and 800 m in altitude. Indeed, the general structure of the dual-Doppler normalized winds from 0-5 km over water appears similar to the dropsonde-measured boundary layer profiles over water. Specifically, winds between 400-800 m generally exceed the boundary layer mean wind by a few percent. Winds between 200-400 m are generally near 100% of the boundary layer mean wind or just slightly less than the mean wind speed, similar to dropsonde composites. The profiles in the 0-2.5 km range bins change relative to the 2.5-5.0 km range bins, suggesting the HBL may begin to “feel” the shoreline in the 0-2.5

km bins. However, it is unclear if this is due to smoothing performed in the interpolation and dual-Doppler analysis, or if the HBL begins adjusting near the shore.

To explore the changes seen in the mean profiles over water nearing the coast, RHIs taken by SR2 are employed. Although RHIs can only resolve the one-dimensional wind directly toward or away from the radar perspective, RHIs of the boundary layer can corroborate the mean structure of the coast-relative boundary layer generated from dual-Doppler analysis. Shown in Figures 6.6a and 6.6b, a single RHI taken at 1009 UTC along a rainband exterior of the eyewall (approximately perpendicular to the coast) shows a maximum in V_R (Doppler velocity) between 500-1000 m altitude within 8 km range, where 8 km approximately represents the radar-relative range to the coast (excluding the barrier islands). Beyond 8 km, the V_R maxima appear to be below 500 m altitude. Additionally, V_R appears to be relatively constant below 500 m altitude beyond 8 km. Clearly, the structure of V_R in the plane of the RHI changes abruptly at the coast, rather than transitioning just over water as in the composite dual-Doppler analysis results. Inland from the coast, the maximum V_R increases in height to between 500 and 1000 m above radar level within approximately 2-3 km of the coastline, similar to what is seen in the dual-Doppler analysis mean. Below 500 m, the magnitude of V_R decreases, likely from both the backing of the boundary layer wind and the reduction in the magnitude of the boundary layer wind. Figure 6.5b corroborates that backing in the plane of the RHI is likely, as the coast-relative mean wind direction in over water bins in the mean is 80-90° compared to onshore values of 70-80° in the lowest 500 m of the atmosphere. This transition occurs rapidly inland of the coastline, suggesting that IBL growth is a function of the discontinuity of surface roughness from water to land surfaces, similar to the results found in Hirth et al. (2012).

An additional RHI (Figure 6.6c, 6.6d) was examined 10 minutes (0959 UTC) prior that was further southwest over a similar portion of the coastal region. Doppler velocities were weaker in this case, as the plane of the RHI was not oriented nearly parallel to the boundary layer wind. Nevertheless, at approximately 6 km range (corresponding to the coastal region) in Figures 6.6c and 6.6d, the Doppler velocities show a decrease in the V_R field below 500 m and a similar growth in the depth of the weaker V_R structure as in the RHI taken at 1009 UTC. There exists an additional perturbation in V_R at approximately 8.5 km range, which corresponds to the barrier islands shown in the inset in Figure 6.6d. As at 1009 UTC, the change in the V_R field appears to exist coincident with the coastal interface, suggesting that the HBL winds adjust to the underlying surface while the residual V_R maximum above retains its character.

6.4.2 Inland HBL Structure

Onshore, rapid changes in the boundary layer mean winds can be seen beginning in the first range bin inland from the coast (Figure 6.5a). An immediate increase in the altitude of the normalized maximum wind can be seen relative to the over water structure. Winds below 400 m fall below 95% of the boundary layer wind speed. Further inland, winds fall to about 90% of the mean wind at ranges of -10 to -7.5 km. Over land, the height of the maximum tangential wind (Figure 6.7a) appears to shift from heights of 400-800 m over water to 800-1000 m onshore, suggesting that the surface roughness transition at the coast influences the height of the maximum wind.

The actual tangential wind speed profile (Figure 6.7a) shows a qualitatively similar structure to the normalized total wind (Figure 6.5a), but the actual radial wind speed profile (Figure 6.7b) shows the most significant changes relative to the normalized wind. Rather than

using a normalized wind value, which is more heavily affected by values between -1 and 0 m s^{-1} (division by a small number), the full radial wind is shown to demonstrate the rapid transition in boundary layer structure across the coast (Figure 6.7). Between 2.5 and 5 km over water, the maximum radial inflow in the mean is between 200 and 400 m altitude and changes little toward shore, but increases in magnitude over land. As expected, the radial wind onshore should increase for the same total wind speed, as the degree of imbalance between the Coriolis, centrifugal, pressure gradient, and frictional forces is disrupted relative to over the open ocean.

The height of the mean boundary layer (defined by the height at which the radial inflow is 10% of its peak value; Zhang et al. 2011) appears to be above the height of the maximum tangential wind for over water profiles. Figure 6.7b shows that the transition between boundary layer inflow (negative velocities) and outflow (positive velocities) is generally between 600-1000 m altitudes. Between -5 and +2.5 km distance from coast the height of the inflow layer appears to increase relative to the surrounding bins. However, the inflow from 800-1000 m is very weak and is near the 10% criteria, suggesting that by definition the inflow depth is relatively constant across the coastal interface in this analysis. On the other hand, further inland the vertical distance between the maximum tangential wind and the top of the inflow layer appears to diminish from over water to onshore. Between -10 and -5.0 km, the height of the maximum tangential wind resides in the mean outflow layer, which is above the HBL top.

6.4.3 Coastal Composite Change

Since the evolution of the normalized winds is a function the mean wind, it is useful to characterize the HBL transition in terms of the maximum normalized wind to more comprehensively view the HBL transition at the coastal interface. A time-averaged VAD profile

from KMHX taken over the same period as the dual-Doppler analyses is used as a proxy for the HBL downstream of the -10 to -7.5 km range bin in Figure 6.5a. The individual VADs used in the composite were normalized by the 200-600 m wind to be consistent with the dual-Doppler normalized profiles. Then, for each composite profile (KMHX and each range bin in Figure 6.5a), the maximum normalized wind was found and the profile was shifted such that the maximum normalized wind was represented by a value of 1.0 (Figure 6.8a). It is clear that the profiles above 800 m altitude adjust little, while the profiles below evolve rapidly as a function of inland distance. This is indicative of IBL growth, as expected across the coast. The top of the "kink" in the profile below the otherwise unaffected winds aloft can be used as a proxy for the height of the growing IBL, which suggests rapid growth of the IBL within 5 km of the coast and relatively slow growth further inland.

However, the adjustment of the HBL to the inland surface roughness regime implies that the HBL wind profile through the coastal transition may deviate from a logarithmic profile (or log-linear profile). Over the ocean on average, dropsonde profiles suggest that the HBL is indeed log-linear (e.g., Franklin et al. 2003; Powell et al. 2003; Giammanco et al. 2013). This notion is examined via the dual-Doppler coastal-composite analyses by computing the aerodynamic surface roughness needed to maintain a log-linear profile between 200 m (the lowest available dual-Doppler wind measurement) and the height of the maximum wind (calculated for each profile as a function of distance from the coast). This calculation is done via the time-average full wind speed, not the normalized wind speed. Following the general technique of Kosiba et al. (2013) and Alford et al. (2019) using a wind speed at 200 m V_{200} and the maximum wind speed (V_{max}) a height of z_{max}, the aerodynamic surface roughness z_0 can be calculated by solving for z_0 in (6.2) to obtain (6.3).

$$V_{200}\ln\left(200/z_0\right)=V_{max}\ln\left(z_{max}/z_0\right) \quad (6.2)$$

$$z_0=\exp\left(V_{max}\ln(200)-V_{200}\ln(z_{max})\Big/V_{max}-V_{200}\right) \quad (6.3)$$

The resulting z_0 are indicated in Figure 6.8b, which range from <0.001 for over water surfaces and 0.001 to 0.37 for over land surfaces, which appear to be reasonable averaged across relatively large spatial areas with complex land use conditions. More importantly, the profiles between 200 m and z_{max} remain mostly log-linear, suggesting that the IBL through the coastal transition remains representative in general of a logarithmic boundary layer.

6.5 Temporal Evolution of the Coastal HBL

Previous studies often employ the use of mean profiles (as above) to assess the structure of the HBL, either over land or over water. However, the evolution of the HBL in storm-center-relative space has not been examined quantitatively to date. Here, the temporal evolution of the HBL over land compared to that observed over water is examined using dual-Doppler analyses and available VAD retrievals from RaXPol and KMHX.

6.5.1 Dual-Doppler Analysis Results

Using a time series of area-averaged normalized vertical wind profiles, the transition of the mean boundary layer wind speed and depth over land and over water in the dual-Doppler domain can be ascertained. As the wind speeds are discussed in their normalized forms, the area-mean 0-600 m winds are shown in Figure 6.4c (6.4d) for land (water) surfaces. However, each dual-Doppler profile at each dual-Doppler analysis grid point is normalized by its own 0-600 m mean wind. Thus, the mean winds shown in Figures 6.4c and 6.4d are for general context only. In Figure 6.9, time periods from approximately 0000 UTC – 0716 UTC on 27 August represent

the outer bands of Irene, 0716 UTC – 1046 UTC represents the inner core, and 1046 – 1206 UTC represents the eyewall. These spatial regions were defined by the spatially averaged r^* over the dual-Doppler domain. Normalized radii larger than 3 were considered to be outer bands, 1.5 – 3 was considered inner core, and 0.8 – 1.5 was considered eyewall. Within each of these regions, the structures of the profiles for each regime (outer bands, inner core, and eyewall) differ strongly from one another. The normalized 0-1200 m wind profiles indicate that the strongest boundary layer winds are generally experienced between 400 and 1200 m heights for all inland profiles, but the height of the maximum wind descends with decreasing radial distance (increasing time) to the eyewall, namely in the inner core and eyewall regimes. Below the inland maximum winds (Figure 6.9a), the normalized wind at the lowest analysis level between 0000-0700 UTC (outer bands) is generally weaker than in the inner core and eyewall regimes. Additionally, the winds above the maximum in the inner core and eyewall regimes decrease rapidly, which is generally not seen in the outer band regime, indicative of a jet-like profile in the eyewall of Irene. A similar trend is seen in over water profiles, but with stronger mean-wind-relative reductions above the wind maximum during the inner core and eyewall, indicative of a more pronounced wind maximum (i.e., jet-like profile; Figure 6.9b). This trend has been observed in over water mean profiles in other studies (Franklin et al. 2003; Giammanco et al. 2012). The inner core regime after ~0700 UTC for both land and water profiles shows greater temporal consistency of a jet-like profile in the boundary layer and a gradual decrease in the height of the maximum wind toward the eyewall. As mentioned, the eyewall exhibits a more classic "jet" profile (e.g., Kepert 2001) with maximum normalized winds near 400 m heights over water and 600-800 m inland. Thus, the dual-Doppler analyses reveal unique HBL structures in the outer band, inner core, and eyewall regimes that are qualitatively similar inland and over

water, but quantitatively different especially in the lowest analysis levels, where the decay of the wind below the maxima is much greater for inland profiles. In addition, the normalized wind speeds at 200-400 m are notably less than 0.9 for most inland profiles (excluding the eyewall) and generally greater than 0.95 for over water profiles.

Wind direction for land and water surfaces in the vertical was also examined (Figures 6.9e, 6.9f). In all regimes, wind directions over land varied between ~60° and ~90° (from north) at the lowest analysis levels and turned clockwise with height. Similar trends were seen in the over water profiles of wind direction (Figure 6.9f). While above 600-800 m little difference was found quantitatively in the wind direction for each domain subset, below 600 m altitude a counterclockwise change in the wind direction of 10-20° onshore was observed, similar to the results of Hirth et al. (2012). However, the magnitude of the counterclockwise wind direction change from over water to over land profiles is generally greater in the outer bands and the outer edge of the inner core (differences of 10-15° from 0000-0830 UTC) than in the inner core and eyewall regimes (5-10° from 0835-1200 UTC).

Several transient maxima in the 200-400 m normalized wind can be seen both over land and over water in the outer band regime (Figures 6.9a, 6.9b), suggesting that the winds relative to the boundary layer mean increase in, perhaps, rainbands. Changes in the wind direction (Figures 6.9e, 6.9f) and relative peaks in area-averaged wind speeds (Figures 6.4c, 6.4d) can also be seen corresponding to changes in the low-level wind structure. Area-averaged radar reflectivity was computed to provide a proxy for periods when the dual-Doppler domain was under the influence of outer rainbands. For low-level (<400 m) normalized wind maxima in the outer band regime (annotated by arrows in Figure 6.9), reflectivity was generally reduced relative to its surrounding values, suggesting that low-level normalized wind maxima (Figures 6.9a, 6.9b), domain-

averaged 0-600 m mean wind (Figures 6.4c, 6.4d), and wind direction changes (Figures 6.9e, 6.9f) were experienced on the edges of rainbands (Figures 6.9c, 6.9d). When the area-averaged reflectivity was at a local maximum, the normalized winds often maximized aloft. This result is similar to the results of Ming et al. (2014), who showed that downward turbulent fluxes were often maximized on the exterior of rainbands, leading to the downward transport of high momentum. Retrieved vertical velocity was also explored, but did not show significant trends in an area-averaged sense.

6.5.2 RaXPol VAD Profiles

To explore the structure of the outer-band regime in greater detail, the structure of the HBL can be examined through VAD retrievals approximately every 30 s to 1 min during the RaXPol operational period. The radial and temporal resolution of RaXPol affords the opportunity to explore the low-level perturbations to the HBL structure (Figure 6.9) and increases in the area-average winds (Figure 6.4) that may be associated with rainbands. While turbulence on a variety of scales can also influence the vertical distribution of momentum (Morrison et al. 2005; Lorsolo et al. 2008; Kosiba and Wurman 2014; Zhang et al. 2008, 2011), rainbands are focused on here. Based on the time series of dual-Doppler domain averaged HBL structure, it was shown that local maxima in the normalized wind profiles were often associated with gradients in the domain-averaged reflectivity.

In Figure 6.10, a similar time series is shown for 0000 UTC to 0500 UTC documenting the VADs retrieved from radial velocity observations. Figure 6.10a shows the time series of VAD-derived winds from 0-1200 m at 15 m vertical resolution. Local maxima (minima) in the low levels can be seen and are denoted by solid (dashed) rectangles in Figure 6.10a. During these

periods, winds in the lowest 100 m of the profiles tend to be between 15-20 m s^{-1} relative to surrounding local minima of 10-15 m s^{-1}. These local minima appear to be sometimes in the presence of local maxima aloft, suggesting that high momentum air is seen during these periods at lower levels relative to surrounding times through the observed column.

The reflectivity structure observed by RaXPol was examined in context of these wind maxima (minima) to deduce if rainband and convective structures were responsible for these perturbations to the wind field. For the example times denoted in Figure 6.10a, the wind maxima (minima) are highlighted in Figure 6.10b over the vertical reflectivity structure. During the periods of local wind maxima denoted in the figure, rainband passage is observed in the vertical structure of the reflectivity. To a degree in the low levels (denoted by black rectangles in Figure 6.10a) and in the upper levels (denoted by black ovals in Figure 6.10a) of the VAD profiles, the wind maxima appear to be offset from the reflectivity maxima, suggesting that many of the local wind maxima are experienced on the edges of deep convection. One maximum between 0033 and 0045 UTC appears to be in a core of reflectivity, which resembles precipitation-induced downdrafts previously seen in airborne kinematic retrievals of convection in the outer bands (Barnes et al. 1983, 1991). This suggests larger-scale kinematics of rainbands and/or convective scale kinematics are responsible for the low-level perturbations to the wind field. Particularly for the local maxima observed aloft, these appear to resemble the wind field perturbations observed by the spatially averaged time series of dual-Doppler analyses in the outer bands (Figure 6.9). Since the perturbations exist primarily on gradients in reflectivity where downdrafts are anticipated, the downward flux of high momentum as in Ming et al. (2014) is likely an important mechanism for the local enhancements to the near-surface winds. It has also been observed that gust factors are higher in rainbands (e.g., Schroeder et al. 2009; Giammanco et al. 2016), to

which this analysis lends support. As the dual-Doppler composite results and VADs represent horizontal scales of flow larger than, for example, HBL rolls (e.g., Kosiba and Wurman 2014), the results here are predominantly associated with larger-scale (i.e., rainband) processes. Nevertheless, smaller-wavelength features in the HBL can also contribute perturbations to the HBL wind structure, which will be discussed in Chapter 6.6.

6.5.3 KMHX VAD Profiles

The coastal WSR-88D was downstream from the profiles discussed in Chapter 6.4b, suggesting that its time varying mean profiles can be used to characterize wind profiles further inland relative to those within 10 km of the coastline (approximately 18 km from the nearest saltwater inlet to KMHX's north). A time series of VADs from KMHX (Figure 6.11) was constructed to compare the normalized boundary layer winds to the dual-Doppler area-averaged time series shown in Figure 6.9a. Indeed, the KMHX VADs replicate the regimes observed in the dual-Doppler results well. Between 0000 UTC and around 0730 UTC, the normalized winds are maximized near 1000 m. Between ~0730 UTC to ~1030 UTC, the inner core regime shows maximum winds between 600–850 m, similar to the dual-Doppler analysis results. Finally, the eyewall regime after ~1030 UTC shows the maximum normalized wind near 700 m initially and decreases in height to 300-500 m nearer 1200 UTC. Relatively stronger normalized flow also characterizes the low levels of the retrievals compared to earlier times. However, the magnitude of the ~200 m normalized wind is greater in the VADs than in the dual-Doppler analysis results due to the contribution of the winds below 200 m to the 0-500 m boundary layer mean wind. The VAD winds near 200 m are characterized by values near 100% of the mean wind rather than 0.9 or less in the dual-Doppler analyses (Figure 6.9a). The lowest analysis level (representative of

50-65 m altitude) suggests that the winds in the outer bands fluctuate between 50-60% of the mean wind (with similar time varying perturbations seen to those characterized by the RaXPol VADs and dual-Doppler time series). In the inner core and eyewall, however, the magnitude of the 70-120 m normalized wind increases to 65-75% of the boundary layer mean at times.

Delineated by distance to the center of circulation, Figures 6.12 and 6.13 show the VAD-derived boundary layer winds averaged over time for radial and tangential profiles, respectively. Unlike the dropsonde profiles (Figures 6.3c and 6.3d), the radial winds derived from KMHX exhibit a layer of maximum radial inflow above the surface (generally between 200 and 400 m). The normalized tangential profiles (not shown) indicate that the 200-400 m winds are generally 90-100% of the boundary layer mean wind, similar to the dual-Doppler and VAD results discussed previously. The dual-Doppler coast-relative composites suggest that the maximum tangential wind speed first resides in or near the top of the inland HBL within 5 km of the coast, but transitions to above the HBL 5-10 km inland. Given that KMHX is downstream of the dual-Doppler observations and further inland, the maximum tangential wind speed should also be expected to reside near or above the HBL. Indeed, within 100 km of the storm's center of circulation (Figures 6.12a, b and 6.13a, b), the height of the inflow layer and the maximum tangential wind speed is approximately at the same altitude (600 m). For profiles taken farther away from the storm center, (Figures 6.12c, d and 6.13c, d), maximum tangential wind height (800-1000 m) is well above the top of the HBL. This suggests that the vertical displacement between the maximum tangential wind and the top of the HBL increases with distance from the center of circulation over land.

6.6 Discussion and Conclusions

As found in Ming et al. (2014) and Marks et al. (2020), the height of the boundary layer over land is increased relative to over-ocean boundary layer structure and resides above the inflow layer. Prior studies such as Ming et al. (2014) suggest that the tangential wind maximum above the inflow layer is a direct consequence of the adjustment of the HBL to changing surface characteristics (i.e., IBL growth). However, the process by which the HBL transitions across the coastal region was not documented. Hirth et al. (2012) showed that the coastal region represents a discontinuity in surface roughness. Their work focused on HBL change observed inland, but offered limited comparison of the HBL structure over water.

Here, using high spatial-resolution observations of the HBL relative to the coastline, the transition of the boundary layer characteristics at the coastal interface were examined, which resulted in several key conclusions:

1. Using a unique dropsonde, dual-Doppler, and VAD dataset, quantitative differences in the HBL winds were documented. It was shown that the evolution of the HBL was qualitatively similar over water and over land, but their magnitudes were significantly different for all regimes (outer bands, inner core, and eyewall).
2. Past studies focused on VAD or boundary layer profiler (i.e., point profiles) retrievals have shown that downdrafts on the periphery of outer rainbands can lead to a reduction in the height of the maximum wind. Based on the mean structure throughout the dual-Doppler domain corroborated by coincident VAD retrievals, this dataset suggests that rainbands are indeed responsible for an enhancement in the lower HBL winds.
3. VAD-based studies have suggested that the maximum wind over land resides atop the HBL, rather than within it as over the open ocean. The data herein document that the

growth of the IBL is directly responsible for mixing out the previous tangential maximum over the open ocean, wherein the tangential winds above the newly adjusted IBL/HBL become the maximum.

4. As the IBL grows, the wind profile below the maximum likely remains mostly logarithmic as the HBL responds to the inland, large-scale surface roughness change.

Figure 6.14 summarizes the key observations that resulted from this analysis. Between 0 and 5 km over water the maximum tangential wind was observed to reside in the inflow layer (HBL; see Figure 6.7) similar to past observations near the coast and over shallow and deep water (e.g., Zhang et al. 2011; Hirth et al. 2012). In the first 5 km inland of the coast, the height of the maximum tangential wind (Figure 6.7a) is still within the inflow (boundary layer; Fig 6.9b) as the HBL responds to the discontinuity in surface roughness at the coast (i.e., IBL growth; Figure 6.14). However, these results suggest that the residual boundary layer does not immediately adjust to the underlying surface, similar to the results of Hirth et al. (2012). Thus, for a period the tangential wind maximum may continue to reside in the inflow layer until the HBL over land has fully adjusted to its underlying surface (Figure 6.14). RHIs from SR2 support that the adjustment of the HBL begins rapidly in the first few kilometers inland of the coast, similar to the mean coast-relative profiles. The V_R maximum observed in the lowest 500 m of the RHIs over water appeared to increase in height onshore where the IBL growth was occurring. Alford et al. (2019) and Fernandez-Caban et al. (2019), for example, showed that in convective perturbations in the eyewall can represent the strongest winds during the landfall process. Downdrafts in the region may more readily project stronger momentum aloft in the near-coastal regions toward the surface prior to the full adjustment of the HBL to the increased surface

roughness inland of the coast. While most observational studies suggest that gust factors immediately inland of the coast do not significantly depart from the mean, Giammanco et al. (2016) support the notion that the wind maximum within the HBL is, perhaps, an upper bound on the magnitude surface winds. Additional data are needed, however, to fully explore this idea. However, changes in the boundary layer structure in time (Figures 6.9 and 6.10) are indeed noted in the outer bands, where rainband passage procures the strongest winds in the low levels relative to their boundary-layer means in a domain-wide sense. This study focused on larger scale structures that can be examined through the mean HBL structure, rather than kilometer and sub-kilometer features that also impact the vertical distribution of horizontal momentum (Morrison et al. 2005; Lorsolo et al. 2008; Zhang et al. 2008; Kosiba and Wurman 2014). This topic will be addressed in future work.

This work augments the mean profile studies referenced herein, which show a strong reduction in the near-surface boundary layer wind relative to its peak aloft. Here, it is found that periods of convection result in greater linearity of the boundary layer profile over water above 200 m as shown by dual-Doppler analysis (e.g., Figure 6.9). While dual-Doppler observations cannot be used to directly retrieve the standardized 10 m wind, the result suggests that pre-convective periods may procure the strongest near-surface winds in the outer bands, supported by the lower-level retrievals procured by RaXPol and KMHX VADs. Based on past studies, greater downward momentum flux on the edges of convection in the outer bands is likely responsible for the transition of a sharply decreasing profile relative to the boundary layer maximum wind to a gradual reduction in the boundary layer wind relative to its above maximum. In contrast, perturbations to the low-level winds were not seen in the inner core regime, but the height of the maximum wind was indeed reduced between the outer bands and the inner core.

The eyewall regime transitioned to a strong jet-like profile with a maximum below 500 m in this case. The highest normalized winds in the lowest 100 m of the atmosphere were found in the eyewall regime retrieved by VADs from KMHX. Although addressed to some degree, it is still unclear how the winds near the surface (10 m altitude) evolve relative to the mean winds aloft due to a lack of high resolution (e.g., 200-250 m resolution) dual-Doppler analyses (Krupar et al. 2016). While Krupar et al. (2016) found that a logarithmic profile did not represent the HBL as well as a linear-regression fit, this work suggests a log-profile was generally applicable in Hurricane Irene at dual-Doppler analysis levels. Thus, future work should focus on characterizing the complete boundary layer structure from the surface through the top of the HBL onshore and near the shore. As the Texas Tech University StickNets and FCMP 10-m towers were available during the landfall of Irene, this dataset is ideal for comparison in a future study.

This work represents a high spatiotemporal resolution observational case study in a gradually weakening TC, but emphasizes for the need of additional observations of the boundary layer during TC landfalls. The general conclusions from this work should be studied in stronger storms to assess the generality of the results across various TC intensities. Over the open ocean, boundary layer structure is not only a function of radial distance from the eyewall or shear-relative quadrants, but also a function of TC intensity. Thus, similar results may also apply at landfall.

6.7 Figures

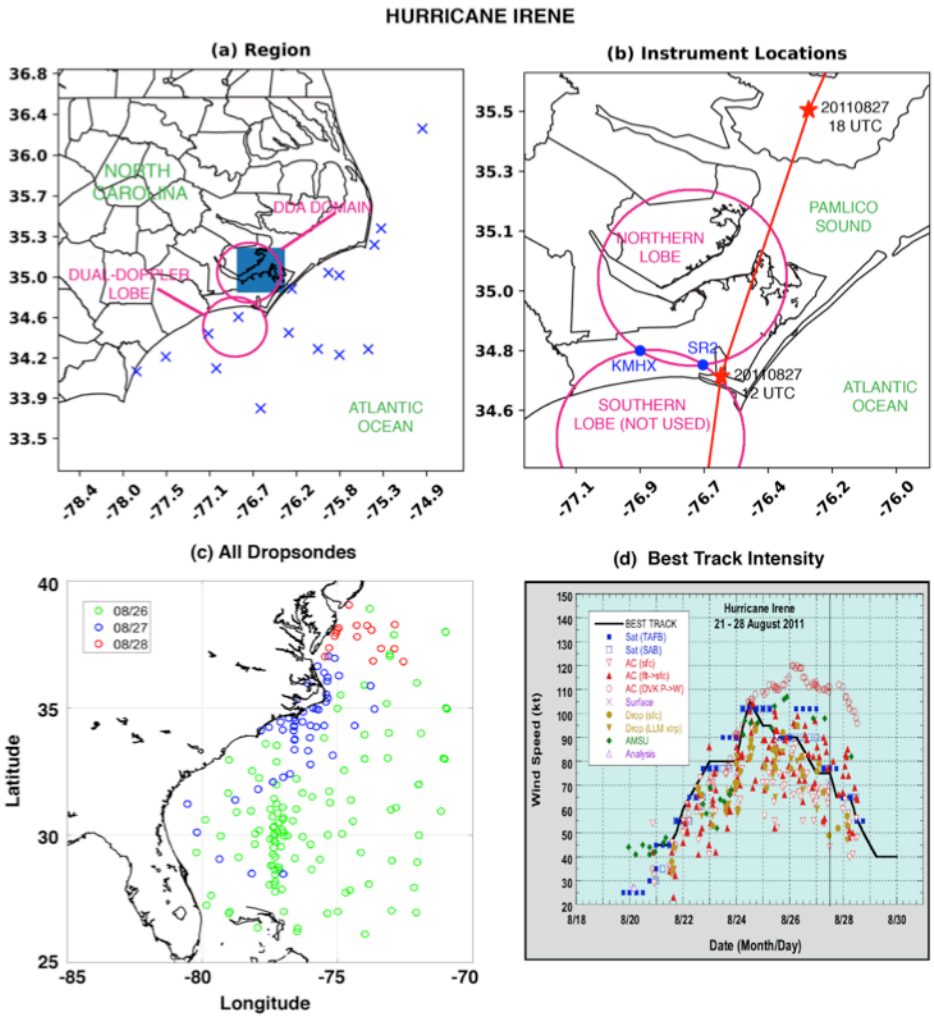

Figure 6.1. Details of the observation, instrumentation, and dual-Doppler domain locations. (a) A large view of the region over which observations were collected. The blue x's indicate locations of dropsondes released by the NOAA P-3 within 100 km of the coast that were used in this study. (b) A detailed view of the dual-Doppler lobes (magenta lines) and the locations of KMHX and SR2 (blue circles). RaXPol was co-located with SR2. The red line indicates the Best Track locations of Irene with synoptic dates and times indicated by the red stars. (c) The locations of dropsondes released by the NOAA P-3, G-IV, and Air Force C-130 are shown colored by date. (d) The National Hurricane Center Best Track intensity in time (figure courtesy of Avila and

Cangialosi 2012).

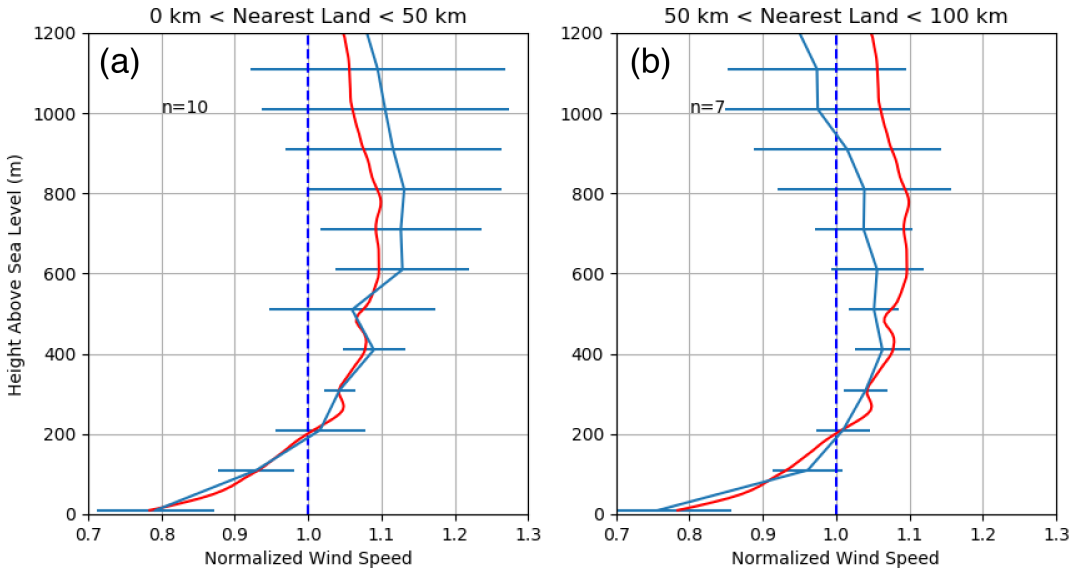

Figure 6.2. Normalized dropsonde profiles taken (a) from 0-50 km of the nearest point on the coast and (b) 50-100 km of the nearest point on the coast. The dashed blue line indicates a normalized wind speed of 1.0. The cyan line shows the mean of *n* profiles taken for each distance subset on 27 August 2011. The red line indicates the mean of all dropsondes profiles regardless of date. Error bars are ±1 standard deviation.

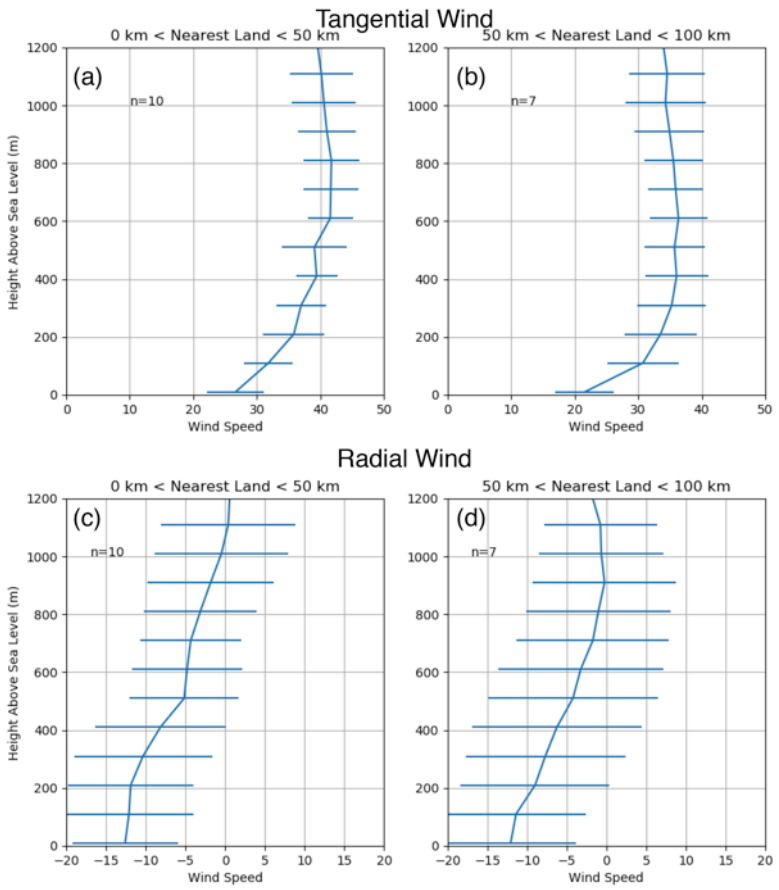

Figure 6.3. Dropsondes profiles of non-normalized (a-b) tangential and (c-d) radial wind (relative to the SFMR/Best Track-derived center of circulation) on 27 August 2011. Unlike Figure 6.2, the actual wind speed values are shown instead of the normalized wind (values in m s^{-1}).

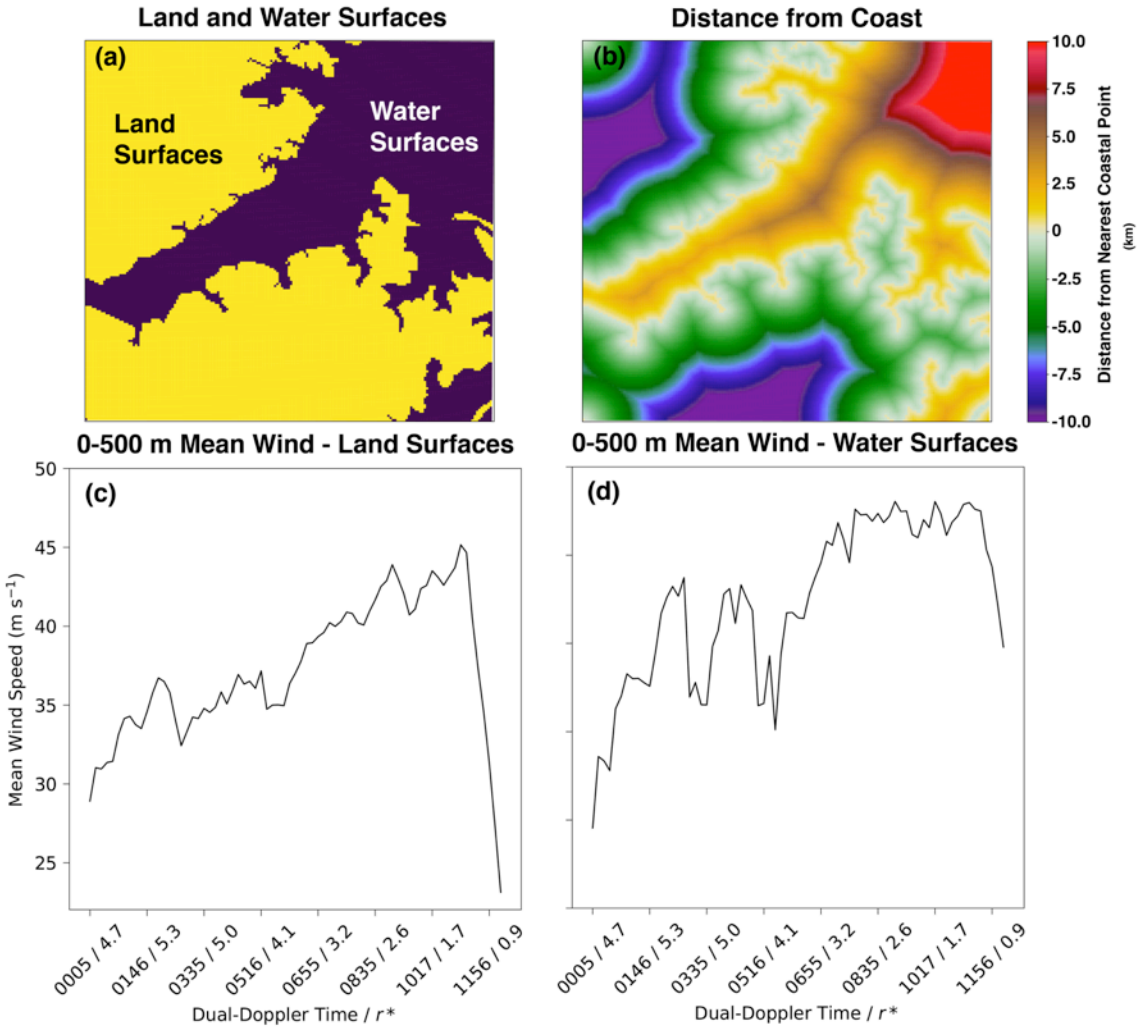

Figure 6.4. Details of the dual-Doppler domain land and water surfaces. (a) Land surfaces are shown in yellow and water surfaces are shown in purple. (b) For each grid point in the dual-Doppler domain, the distance to the nearest coastal point is shown according to the color bar values (in km). Positive values indicate distances of water surfaces from the coast. (c) A time series of the area-average 0-600 m wind speed across the dual-Doppler domain is shown strictly for land surfaces. (d) As in (c), but for water surfaces. In (c) and (d) the x-axis shows the dual-Doppler time and the domain-mean r^*.

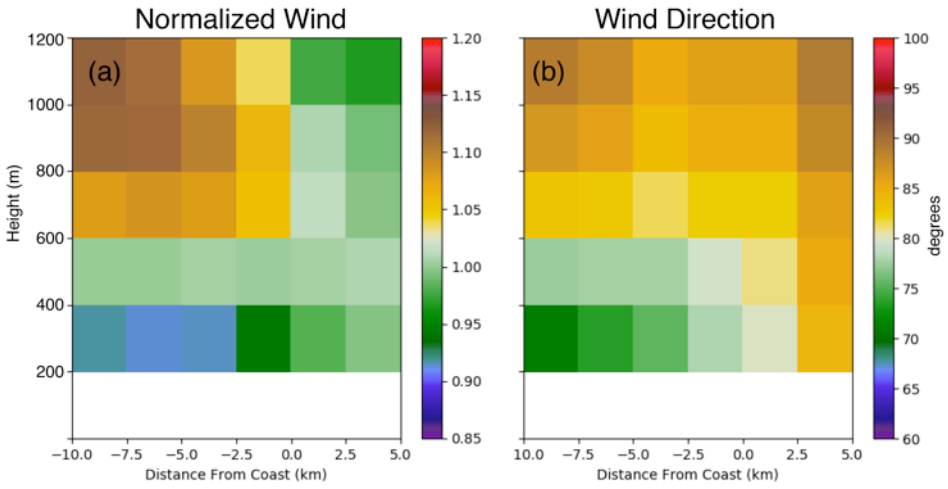

Figure 6.5. (a) Coast-relative normalized wind profile averaged in time and distance from the coast for all dual-Doppler profiles between 0000-1215 UTC. Positive distances from the coast indicate increasing distance over water surfaces within the dual-Doppler domain. (b) As in (a), but for the wind direction according to the color bar (in degrees from north).

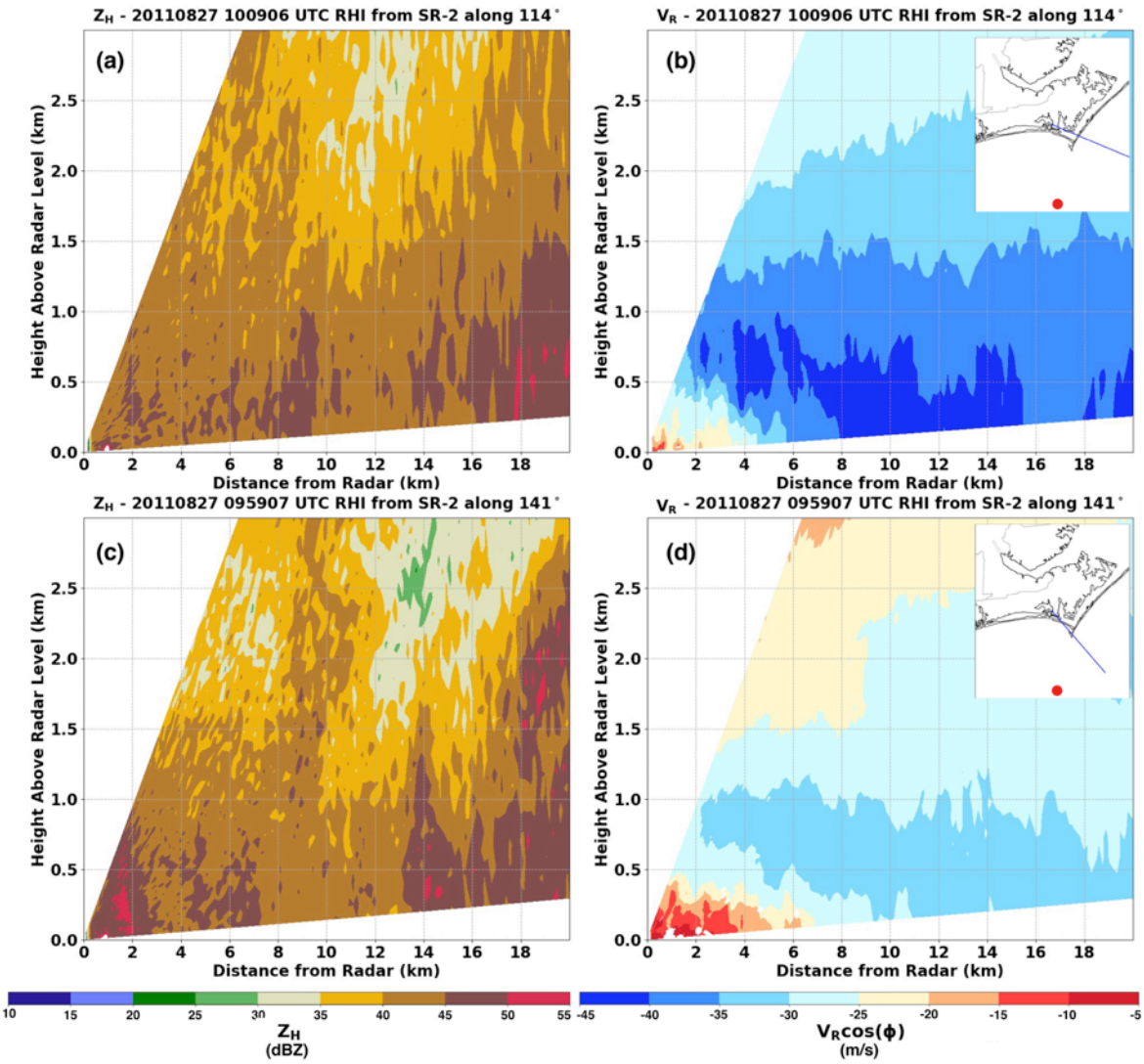

Figure 6.6. RHI from SMART radar 2 along an azimuth of (a, b) 114° from north at 1009 UTC and (c, d) 141° from north at 0959 UTC. (a, c) Radar radial velocity is shown projected into the horizontal according to the elevation along which it was taken. (b, d) A plan view of the RHI (blue line) and the 10 UTC location of Irene's center (red circle) overlain upon a map of the coastal region. It should be noted that at 1009 UTC (0959 UTC) the 8 km (6 km) range is approximately representative of the shoreline of the greater continental region and 18 km (8.5 km) is approximately the shoreline of the North Caroline barrier islands.

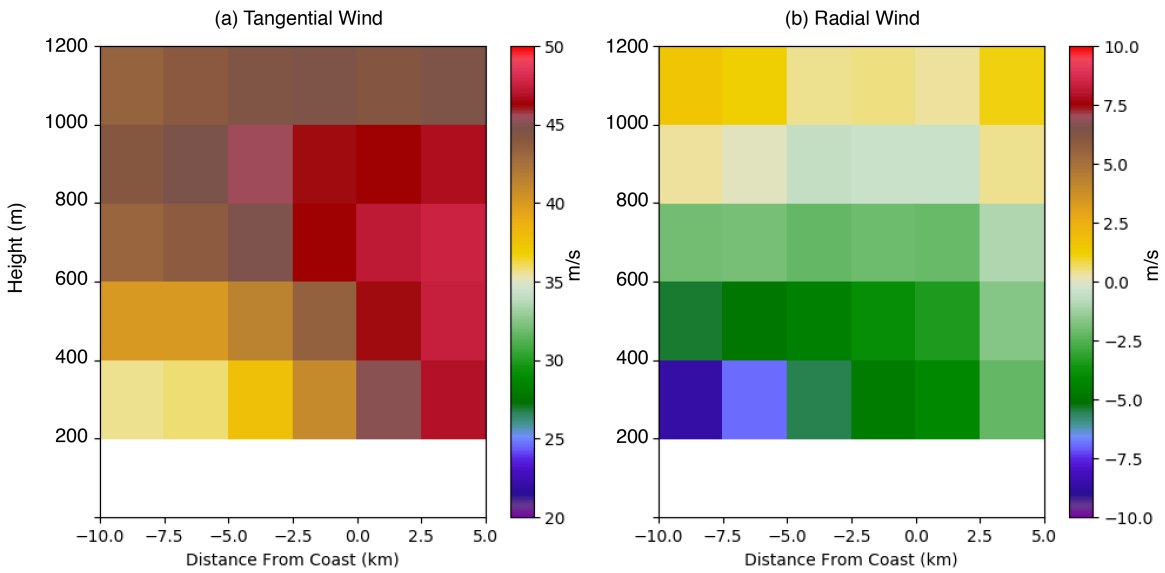

Figure 6.7. Full (not normalized) average coast-relative (a) tangential and (b) radial wind speeds (m s^{-1}) according to the color bars. Negative values indicate storm-relative inflow in (b).

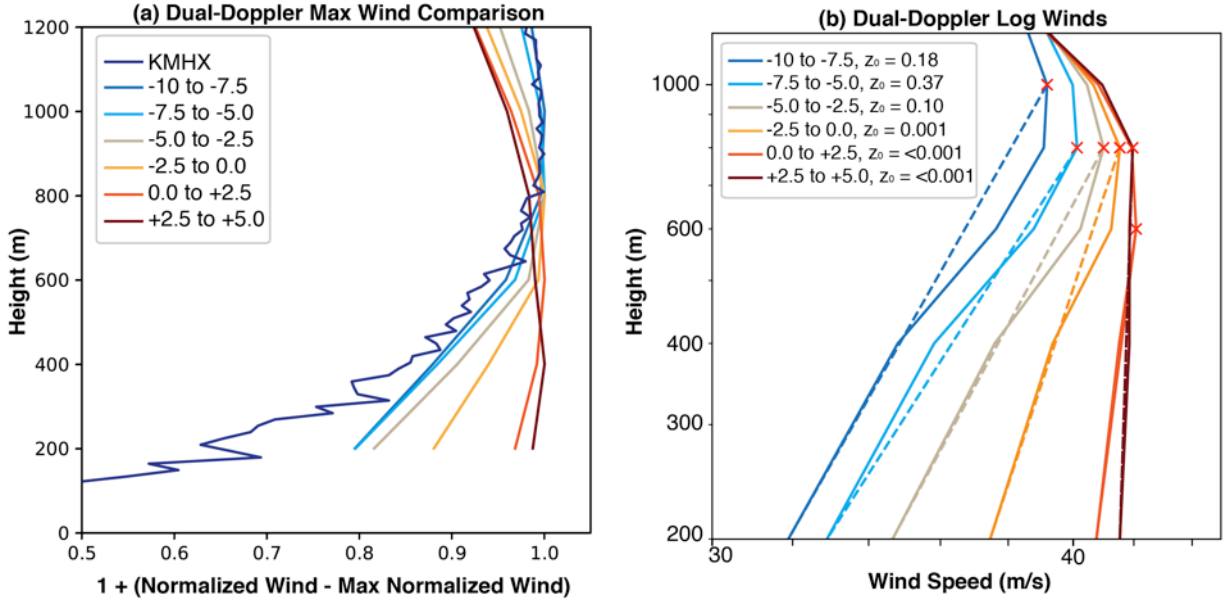

Figure 6.8. (a) A comparison of the coast-relative normalized boundary layer profiles from Figure 6.5 and an average boundary layer normalized profiles for VADs retrieved from KMHX. The coast relative distance is indicated according to the contour color in the inset legend. A value

of 1.0 indicates the maximum wind. (b) The mean boundary layer winds (full; solid curves) compared to a logarithmic profile constructed between the maximum wind (red crosses) and 200 m. The roughness length z_0 is shown in the legend and represents the value required to maintain a log-linear profile between the maximum wind and the 200 m wind.

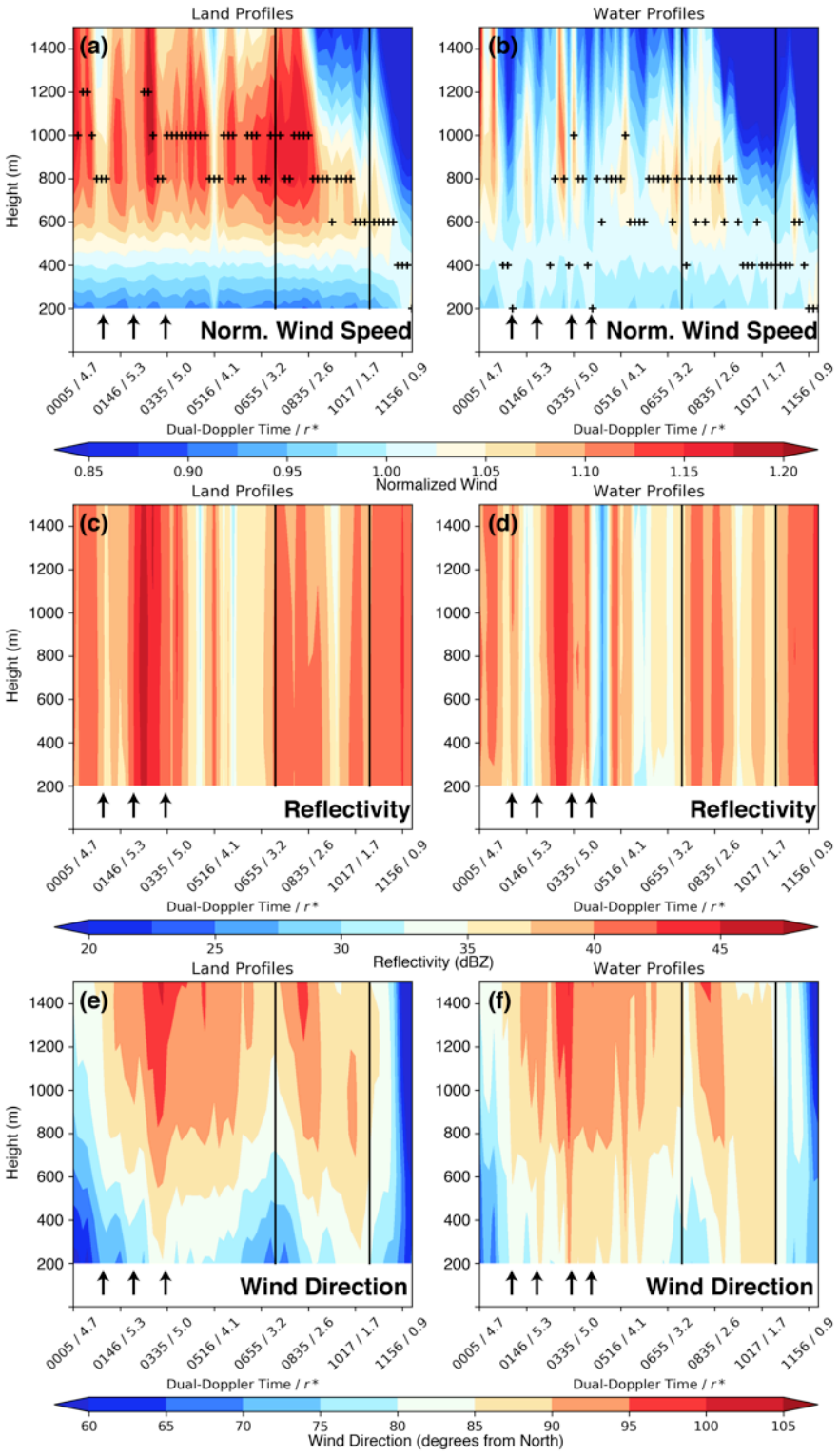

Figure 6.9. Normalized wind profiles (a) over land and (b) over water within the dual-Doppler analysis domain subset shown in Figure 6.4. The labels along the x-axis indicate the dual-

Doppler time and the area-mean normalized-radius r^*. Profiles are constructed for each dual-Doppler time (x-axis) in height (y-axis). The values of the normalized wind are shown according to the colorbar at the bottom of the figure. The black lines indicate the separation of the outer bands/inner core regime at $r^* = 3.0$ and the separation of the inner core/eyewall regime at $r^* = 1.5$. The black +'s indicate the height of the maximum normalized wind. (c) and (d) display land and water profiles of area-mean reflectivity, respectively. (e) and (f) show the area-mean profiles of wind direction with height for land and water profiles, respectively. The arrows in the figure depict periods of increased normalized winds in (a) and (b), their corresponding periods of changing reflectivity in (c) and (d), and their corresponding changes in wind direction in (e) and (f).

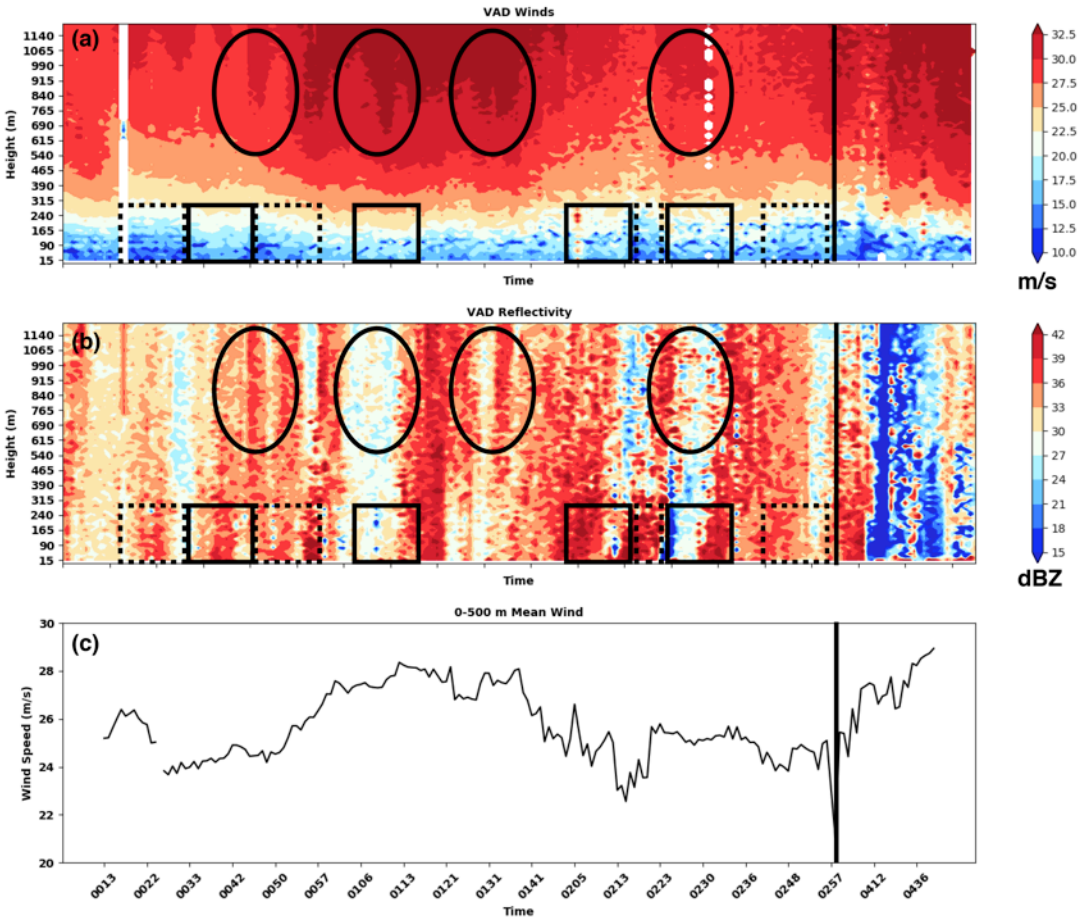

Figure 6.10. Time series of RaXPol observed HBL structure from 0013 UTC to 0500 UTC. (a) VAD-derived winds as a function of height (y-axis) over time (x-axis). Wind speeds (total) are shown according to the colorbar to the right of (a). (b) As in (a), but for the vertical profile of radar reflectivity. (c) The VAD-derived 0-500 m mean wind is shown for context. In both (a) and (b), the black rectangles (dashed rectangles) indicate example periods during which there are local wind maxima (minima) in the lower part of the VAD profiles. The black ovals indicate periods of wind maxima in the upper part of the VAD profiles. The vertical black line denotes a temporal gap in RaXPol data.

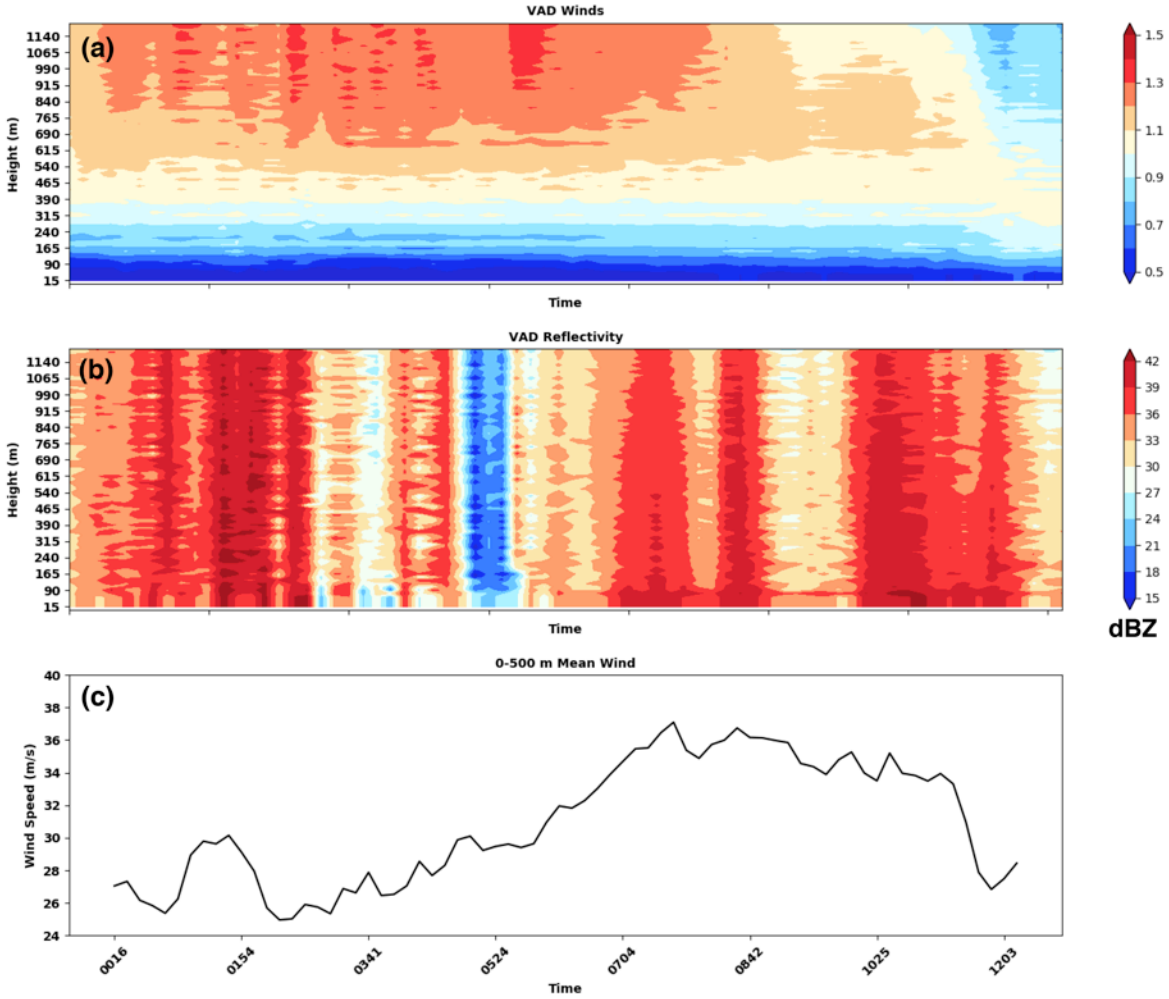

Figure 6.11. Time series of KMHX VAD profiles as in Figure 6.10. (a) As in Figure 6.10a, but for the normalized wind.

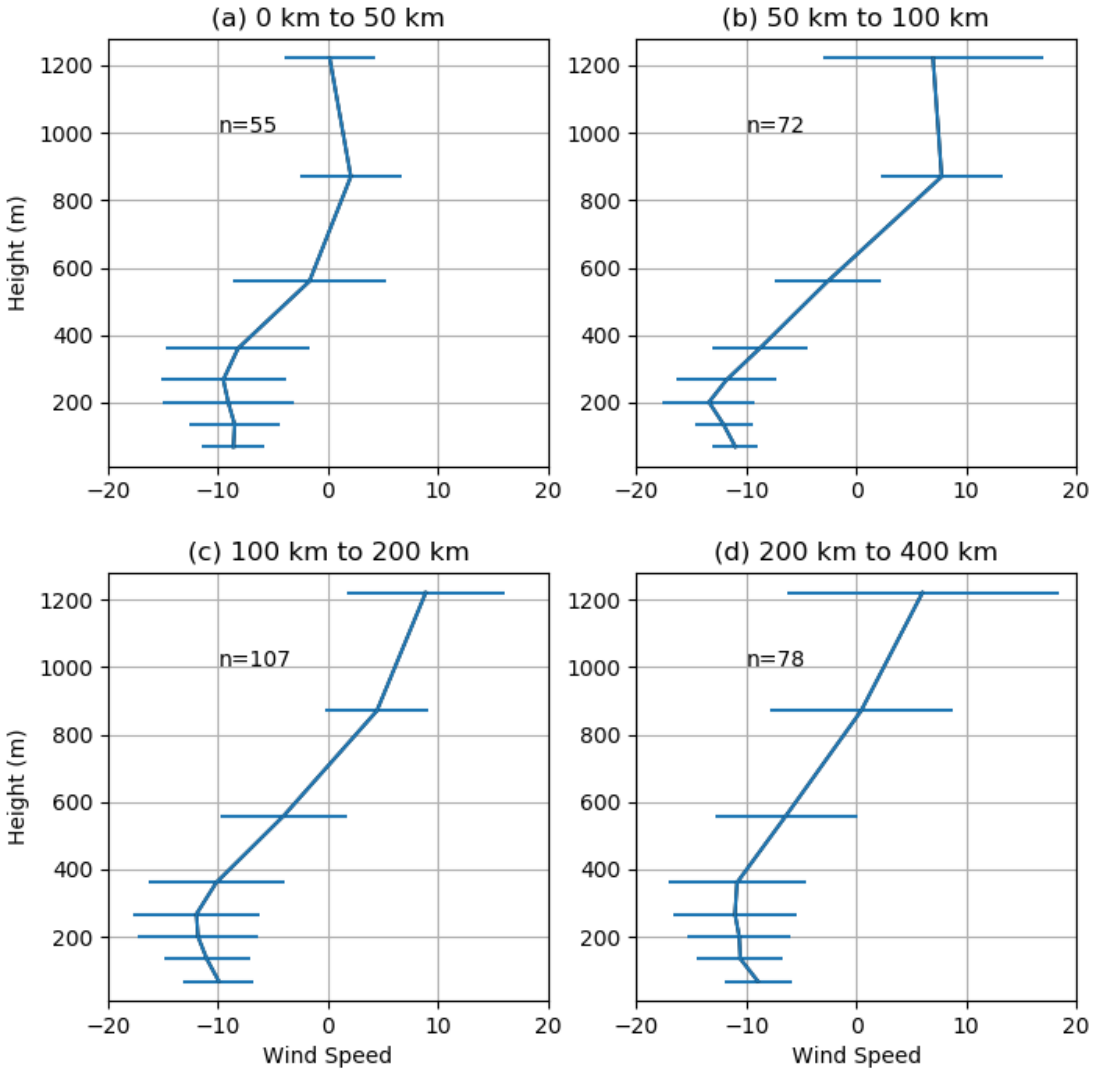

Figure 6.12. Radial wind profiles derived from the KMHX VAD analysis. Profiles are shown (a) 0-50 km, (b) 50-100 km, (c) 100-200 km, and (d) 200-400 km from the center of circulation of Irene. Wind speeds are shown in m s^{-1}.

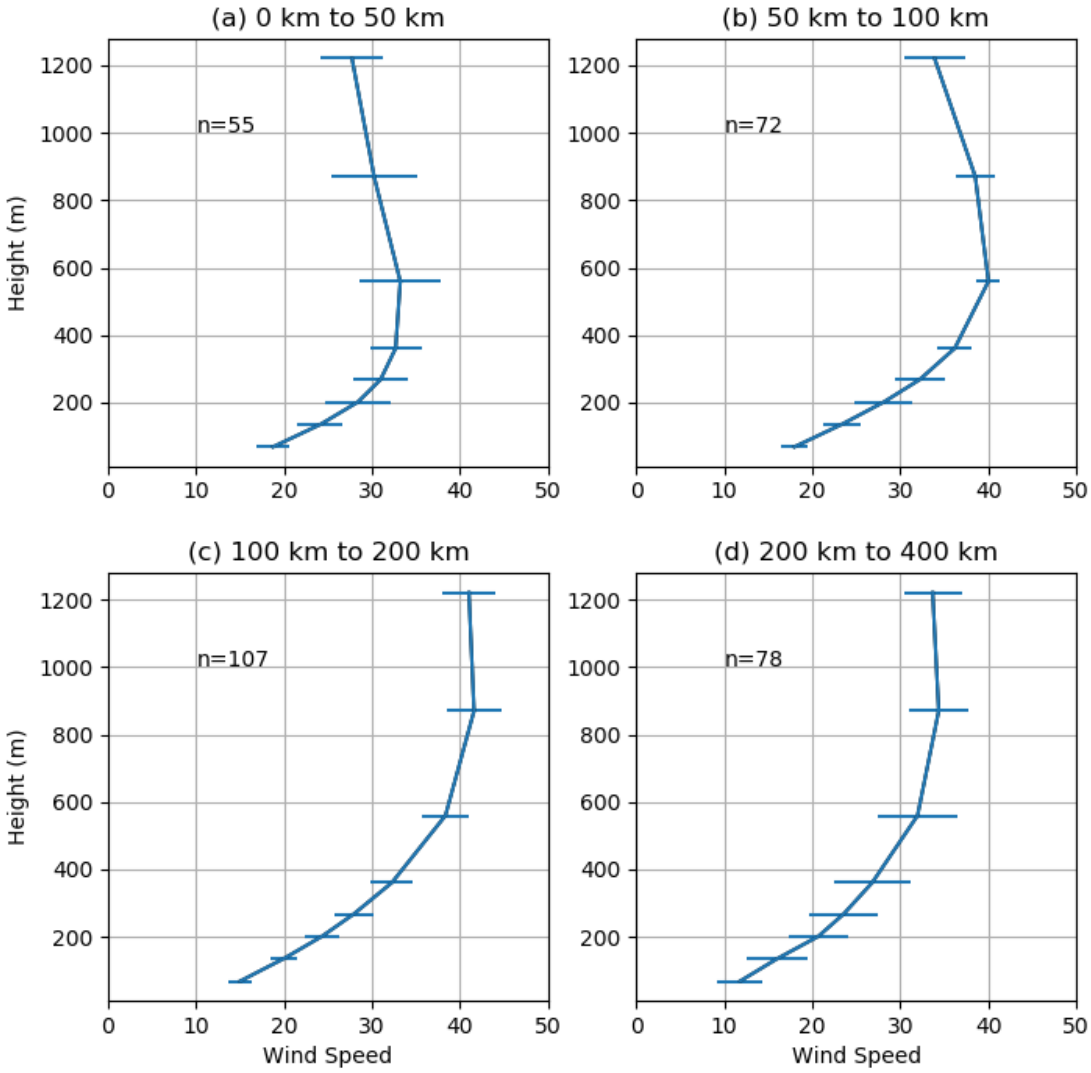

Figure 6.13. As in Figure 6.12, but for the tangential wind.

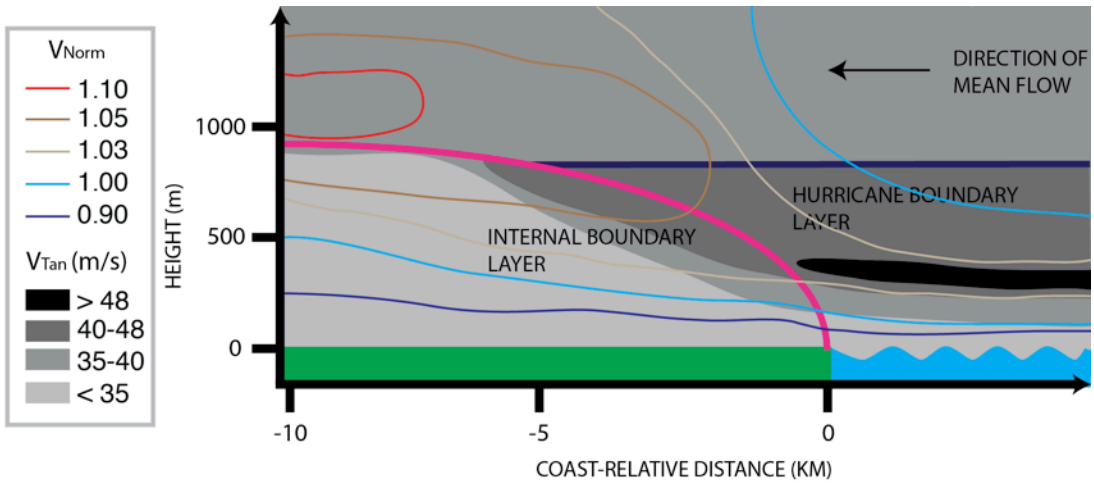

Figure 6.14. Conceptual model of the HBL transition across the coastal-interface for Hurricane Irene. The dark blue line represents the height of the pre-existing HBL that results from HBL dynamics over the open ocean. The magenta curve represents the growth of the internal boundary layer response to the surface roughness discontinuity at the coast. The tangential wind V_{tan} is shown via the color-filled contours according to the legend. The line contours according to the legend indicate the approximate value of the mean state of the coast-relative normalized wind V_{Norm}. In the figure the mean flow is directed from right to left (toward coast).

Chapter 7: Conclusions

7.1 Summary

This dissertation has presented an analysis of hurricane dynamics, convective structure, and boundary layer character at landfall. Using SMART Radar dual-Doppler analyses with coastal WSR-88Ds, NSSL-launched radiosonde, Texas Tech StickNet, NASA Global Hawk, and the University of Oklahoma RaXPol Radar datasets, a detailed review of VRW dynamics and wind impacts has been presented. Five hypotheses served as the primary motivation for Chapters 2 – 6, which are briefly summarized here:

Chapter 2 reviewed the asymmetries (e.g., mesovortices) observed by dual-Doppler analysis in Hurricane Harvey to determine their impact to the near-surface, instantaneous wind field. It was found that the mesovortices at the lowest analysis level (0.5 km altitude) exhibited winds that were on the order of 5-10 m s^{-1} stronger than their background flow. Using a simple logarithmic projection validated by radiosonde boundary layer observations, the 10 m standardized wind field was compared to Stick Net observations at the time of the maximum wind. The spatially contiguous maximum winds, often procured by mesovortex structures, were determined to be realistic and suggested that Hurricane Harvey was a Category 3 storm at landfall.

Given that asymmetries are integral to multi-scale interactions though VRW processes, the mesovortices in Hurricane Harvey were further explored in Chapter 3. As an explanation for the instantaneous impact to the wind field, mesovortices were found to promote the redistribution of potential vorticity from the radius of maximum wind radially inward. Although PV is not conserved in a hurricane, the radial transport of PV on the downwind portion of the mesovortex is consistent with the conservation of angular momentum and a local increase in the wind

magnitude. Alternatively on the upwind portion of the mesovortices, transport of PV radially outward across the radius of maximum wind was found. Rainband formation was noted in these regions, which was shown to be analogous to VRW formation. While over water, the radial transport of eddy vorticity was shown to promote an increase in the mean tangential wind near the radius of maximum wind. This is the first observational evidence examining wave-mean flow interactions discussed in MK97 and suggests that VRWs can indeed transport angular momentum inward toward the source asymmetries.

To further explore VRW formation, Chapter 4 reviewed the rainbands in Chapter 3 to determine if they are indeed coupled to VRWs. Inner core rainband formation was shown to occur preferentially in the vicinity of trailing spirals of vertical vorticity that intersected the eyewall near vorticity and reflectivity perturbations. While the kinematic data was not continuously observable around a closed circuit, the contiguous reflectivity data was compared to the mean tangential wind around a radius circle at 35 km from the center of circulation. Rainbands propagating through the closed circuit were shown to often propagate slower than the mean tangential wind, confirming consistency with VRWs. Thus, it was concluded that VRWs were active in rainband formation prior to and during the landfall of Hurricane Harvey.

With a unique and unprecedented observational dataset with which to observe VRW processes, Chapter 5 reviewed several similarities and differences of modeled VRW-driven rainbands to observations. It was found that the rainbands were more azimuthally contiguous in terms of their vertical updraft structure and reflectivity. Similar to observations, trailing spiraled vertical vorticity maxima accompanied the bands and were similarly more continuous in azimuth than their observed counterparts. Nonetheless, the propagation behavior of VRWs was shown to manifest most strongly in the azimuthal wavenumber 1 and 2 modes, consistent with

observations. Unfortunately, however, the wave-mean flow interactions calculated in terms of the radial eddy vorticity flux were shown to converge angular momentum outside the radius of maximum wind, rather than across the radius of maximum wind in observations. Additionally, the eddies within the radius of maximum wind acted to reduce the tangential wind more strongly than in reality. Two modes of improvement (namely microphysics and model diffusion) were suggested based on the modeled character of the VRW processes and will be the subject of future work.

Finally, observations of the hurricane boundary layer were presented to document in detail the response of the low-level wind field. Using NOAA P-3 and U.S. Air Force dropwindsondes data, the structure of the boundary layer over the ocean was, for the first time, compared in detail to the boundary layer structure over land observed via dual-Doppler analysis and near-coastal VADs. An internal boundary layer response to the step-function increase in aerodynamic surface roughness in the onshore flow was found but was only found to affect the lowest 1 km of the atmosphere in the vicinity of the coast. The over-land boundary layer structure was also shown to vary in time with three distinct boundary layer regimes being documented in the outer bands, inner core, and eyewall across the spatially averaged domain. In order to understand and improve the boundary layer representation of mesoscale flow features including outer rainband-induced perturbations to the wind field, VRWs in the inner core, and mesovortices/asymmetries in the eyewall, further work examining the boundary layer in the presence of these features is needed.

7.2 Significance and Concluding Remarks

The representation of asymmetric dynamic processes in numerical models is one of the priorities to the hurricane research community today. Observations using aircraft radar-based analyses have procured invaluable knowledge on physical processes leading to rapid intensification but have unfortunately been unable to document rapidly evolving asymmetric processes. This dissertation is largely the result of the unique observational capability of the Shared Mobile Atmospheric Research and Teaching Radar program that is capable of high spatial resolution observations of such processes at novel temporal resolution. While mostly at landfall, this dissertation has demonstrated the utility of examining VRWs with ground-based C-band Doppler weather radar. Furthermore, the datasets and discussion presented here augment the understanding of VRWs both at landfall and over the ocean where the evolution of TCs is often challenging to observe. In the future, datasets of this nature should be used to observe rapidly evolving processes and offer a unique way in which to validate numerical weather prediction. As the atmospheric science community moves toward more sophisticated remote sensing platforms such as phased array weather radar, improved in situ fixed and mobile wind monitoring, and more detailed water-hazard monitoring, ground-based observations will offer significant opportunity to improve TC modeling, hazard mitigation, and forecast communication.

Appendix 1: Dealiasing Details

For each case described in this dissertation, the Doppler velocity data were quality controlled using the method described herein from Alford et al. (2019a). The SR Doppler velocity data were passed to an automated dealiasing algorithm after several pre-processing steps were taken. First, a threshold based on the dual-polarization correlation coefficient was applied to the Doppler velocity to remove regions of noise. Velocities associated with correlation coefficient values <0.01 were removed. While the 0.01 threshold value seems extremely low, the purpose of this step was to conservatively remove regions of non-meteorological echo before proceeding. Next, a local neighborhood standard deviation of Doppler velocity at each gate was calculated using a rolling, centered, 20-gate sample. Standard deviations in both the radial and azimuthal directions were computed and the *minimum* of the two estimates was retained. The minimum was used to assure both radial and azimuthal standard deviations were representative of noise. If the radar reflectivity of a gate was below 5 dBZ and the local neighborhood standard deviation exceeded 16 m/s, the gate of data was removed. Effectively, this removed most of the remaining noise in the Doppler velocity field in regions of low signal-to-noise (SNR) ratio. Solely using a threshold on correlation coefficient (e.g. < 0.9) often resulted in edges of echoes being removed. A despeckling function over a width of five gates removed any remaining isolated velocity-outlier gates in low SNR regions. After pre-processing, the Py-ART (Helmus and Collis, 2016) software package was used to objectively dealias the Doppler velocity data for all sector and 360° volumes, excluding RHI and surveillance volumes. Within Py-ART, the four-dimensional Doppler dealiasing scheme (James and Houze, 2001) objectively processed all data collected between 2058 UTC 25 August and 0600 UTC 26 August in the case of Hurricane Harvey only. In Harvey, the shear of the horizontal wind was large, which resulted in the sweep-

wide aliasing of the Doppler velocities into the incorrect Nyquist interval. The 4DD scheme affords the ability to use a previous radar volume to constrain the current volume being dealiased. As a result, the 4DD method resulted in significantly less dealiasing errors than the region-based scheme during the 2058 to 0600 UTC time period. For all other cases (Isabel, Matthew, and Irene), the region-based method was chosen as the preferred dealiasing scheme. After all Doppler velocities were dealiased objectively, data were further quality controlled subjectively using the National Center for Atmospheric Research Solo3 software package (Oye et al., 1995) to produce a final quality controlled version of the data. Subjective dealiasing was required to correct regions that were aliased into the incorrect Doppler velocity interval. In addition, gates in low signal-to-noise regions were sometimes not captured by the above-described standard deviation and despeckling functions and had to be removed manually using Solo3.

WSR-88D data in Level II format were retrieved from the National Centers for Environmental Information (NCEI, Available online at https ://www.ncdc.noaa.gov/data-acces s/ radar-data) and were processed in a similar fashion. Using Py-ART, radial velocity data were excluded if the gate's reflectivity was <0 dBZ. The data were also passed through the same standard deviation filter as above, but almost no data were removed as a result of pre-processing performed on the Level II data. The data were passed into Py-ART's region-based dealiasing scheme for all cases in order to correct the aliasing of Doppler velocities for the entire dataset. While the data were processed in Solo3 as well, very few subjective edits were needed.

References

Abarca, S. F., and K. L. Corbosiero, 2011: Secondary eyewall formation in WRF simulations of Hurricanes Rita and Katrina (2005). *Geophys. Res. Lett.*, **38**, 1–5, doi:10.1029/2011GL047015.

Aberson, S. D., and J. L. Franklin, 1999: Impact on Hurricane Track and Intensity Forecasts of GPS Dropwindsonde Observations from the First-Season Flights of the NOAA Gulfstream-IV Jet Aircraft. *Bull. Am. Meteorol. Soc.*, **80**, 421–427, doi:10.1175/1520-0477(1999)080<0421:IOHTAI>2.0.CO;2.

——, M. L. Black, R. A. Black, R. W. Burpee, J. J. Cione, C. W. Landsea, and F. D. Marks, 2006: Thirty years of tropical cyclone research with the NOAA P-3 aircraft. *Bull. Am. Meteorol. Soc.*, **87**, 1039–1055, doi:10.1175/BAMS-87-8-1039.

——, A. Aksoy, K. J. Sellwood, T. Vukicevic, and X. Zhang, 2015: Assimilation of High-Resolution Tropical Cyclone Observations with an Ensemble Kalman Filter Using HEDAS: Evaluation of 2008–11 HWRF Forecasts. *Mon. Weather Rev.*, **143**, 511–523, doi:10.1175/MWR-D-14-00138.1. http://journals.ametsoc.org/doi/10.1175/MWR-D-14-00138.1.

——, J. A. Zhang, K. Nuñez Ocasio, S. D. Aberson, J. A. Zhang, and K. N. Ocasio, 2017: An extreme event in the eyewall of Hurricane Felix on 2 September 2007. *Mon. Weather Rev.*, MWR-D-16-0364.1, doi:10.1175/MWR-D-16-0364.1. http://journals.ametsoc.org/doi/10.1175/MWR-D-16-0364.1.

Alaka, G. J., X. Zhang, S. G. Gopalakrishnan, S. B. Goldenberg, and F. D. Marks, 2017: Performance of basin-scale HWRF tropical cyclone track forecasts. *Weather Forecast.*, **32**, 1253–1271, doi:10.1175/WAF-D-16-0150.1.

——, ——, ——, Z. Zhang, F. D. Marks, and R. Atlas, 2019: Track uncertainty in high-resolution HWRF ensemble forecasts of Hurricane Joaquin. *Weather Forecast.*, **34**, 1889–1908, doi:10.1175/WAF-D-19-0028.1.

Alford, A. A., and M. I. Biggerstaff, 2017: Mesoscale processes observed in the inner cores of Hurricanes Hermine and Matthew. *18th Cyclone Workshop*, Montreal, Canada, State University of New York at Albany.

——, M. I. Biggggerstaff, C. L. Zieglgler, D. P. Jorgensen, and G. D. Carrie, 2018: A method for correcting staggered pulse repetition time (PRT) and dual pulse repetition frequency (PRF) processor errors. doi:10.5281/zenodo.1306295.

——,——,——,——,——, in preparation: A method for correcting staggered pulse repetition time (PRT) and dual pulse repetition frequency (PRF) processor errors.

——, M. I. Biggerstaff, and G. D. Carrie, 2019a: Mobile ground-based SMART radar observations and wind retrievals during the landfall of Hurricane Harvey (2017). *Geosci. Data J.*, doi:10.1002/gdj3.82.

——, ——, ——, J. L. Schroeder, B. D. Hirth, and S. M. Waugh, 2019b: Near-surface maximum winds during the landfall of Hurricane Harvey. *Geophys. Res. Lett.*, **46**, doi:10.1029/2018GL080013.

Avila, L. A., and J. Cangialosi, 2012: *Tropical Cyclone Report: Hurricane Irene (AL092011)*. 45 pp. http://www.nhc.noaa.gov/data/tcr/AL092011_Irene.pdf.

Baradaranshoraka, M., J.-P. Pinelli, K. Gurley, X. Peng, and M. Zhao, 2017: Hurricane Wind versus Storm Surge Damage in the Context of a Risk Prediction Model. *J. Struct. Eng.*, **143**, 1–10, doi:10.1061/(ASCE)ST.1943-541X.0001824.

Barnes, G. M., E. J. Zipser, D. Jorgensen, and F. Marks, 1983: Mesoscale and convective

structure of a hurricane rainband. *J. Atmos. Sci.*, **40**, 2125–2137, doi:10.1175/1520-0469(1983)040<2125:MACSOA>2.0.CO;2.

——, J. F. Gamache, M. A. Lemone, and G. J. Stossmeister, 1991: A convective cell in a hurricane rainband. *Mon. Weather Rev.*, **119**, 776–794, doi:10.1175/1520-0493(1991)119<0776:ACCIAH>2.0.CO;2.

Bell, M. M., and W. C. Lee, 2012: Objective tropical cyclone center tracking using single-doppler radar. *J. Appl. Meteorol. Climatol.*, **51**, 878–896, doi:10.1175/JAMC-D-11-0167.1.

Betten, D. P., M. I. Biggerstaff, and C. L. Ziegler, 2018: Three-Dimensional Storm Structure and Low-Level Boundaries at Different Stages of Cyclic Mesocyclone Evolution in a High-Precipitation Tornadic Supercell. **2018**, 24 pp, doi:10.1155/2018/9432670.

Beven, J. L., and H. Cobb, 2003: *Tropical Cyclone Report: Hurricane Isabel*. 30 pp. http://www.nhc.noaa.gov/data/tcr/AL132003_Isabel.pdf.

Biggerstaff, M. I., and R. A. Houze, 1991: Midlevel Vorticity Structure of the 10–11 June 1985 Squall Line. *Mon. Weather Rev.*, **119**, 3066–3079, doi:10.1175/1520-0493(1991)119<3066:MVSOTJ>2.0.CO;2.

——, and Coauthors, 2005: The Shared Mobile Atmospheric Research and Teaching Radar: A Collaboration to Enhance Research and Teaching. *Bull. Am. Meteorol. Soc.*, **86**, 1263–1274, doi:10.1175/BAMS-86-9-1263.

Biswas, M. K., and Coauthors, 2018: *Hurricane Weather Research and Forecasting (HWRF) Model: 2017 Scientific Documentation*. 111 pp.

Black, P. G., S. J. Buchan, and R. L. Cohen, 1999: The Tropical Cyclone Eyewall Mesovortex: A Physical Mechanism Explaining Extreme Peak Gust Occurrence in TC Olivia, 4 April 1996 on Barrow Island, Australia. *Offshore Technology Conference*, Houston, TX, OTC

10792.

Blake, E. S., and D. A. Zelinsky, 2018: *National Hurricane Center Tropical Cyclone Report: Hurricane Harvey*. 1–77 pp.

Braun, S. A., 2006: High-Resolution Simulation of Hurricane Bonnie (1998). Part II: Water Budget. *J. Atmos. Sci.*, **63**, 43–64, doi:10.1175/JAS3609.1.

——, M. T. Montgomery, and Z. Pu, 2006: High-Resolution Simulation of Hurricane Bonnie (1998). Part I: The Organization of Eyewall Vertical Motion. *J. Atmos. Sci.*, **63**, 19–42, doi:10.1175/JAS3598.1. http://dx.doi.org/10.1175/JAS3598.1.

——, and Coauthors, 2013: Nasa's Genesis and Rapid Intensification Processes (Grip) Field Experiment. *Bull. Am. Meteorol. Soc.*, **94**, 345–363, doi:10.1175/BAMS-D-11-00232.1.

Browning, K. A., and R. Wexler, 1968: The determination of kinematic properties of a wind field using Doppler radar. *J. Appl. Meteorol.*, **7**, 105–113, doi:10.1175/1520-0450(1968)007%3C0105:TDOKPO%3E2.0.CO;2.

Bryan, G. H., and R. Rotunno, 2009: The maximum intensity of tropical cyclones in axisymmetric numerical model simulations. *Mon. Weather Rev.*, **137**, 1770–1789, doi:10.1175/2008MWR2709.1.

Burgess, D. W., M. A. Magsig, J. Wurman, D. C. Dowell, and Y. Richardson, 2002: Radar Observations of the 3 May 1999 Oklahoma City Tornado. *Weather Forecast.*, **17**, 456–471, doi:10.1175/1520-0434(2002)017<0456:ROOTMO>2.0.CO;2. http://journals.ametsoc.org/doi/abs/10.1175/1520-0434%282002%29017%3C0456%3AROOTMO%3E2.0.CO%3B2.

Cavallo, S. M., R. D. Torn, C. Snyder, C. Davis, W. Wang, and J. Done, 2012: Evaluation of the Advanced Hurricane WRF data assimilation system for the 2009 Atlantic hurricane season.

Mon. Weather Rev., 121017144007007, doi:10.1175/MWR-D-12-00139.1.

Chen, Y., and M. K. Yau, 2001: Spiral bands in a simulated hurricane. Part I: Vortex rossby wave verification. *J. Atmos. Sci.*, **58**, 2128–2145, doi:10.1175/1520-0469(2001)058<2128:SBIASH>2.0.CO;2.

Chen, Y., and M. K. Yau, 2003: Asymmetric structures in a simulated landfalling hurricane. *J. Atmos. Sci.*, **60**, 2294–2312, doi:10.1175/1520-0469(2003)060<2294:ASIASL>2.0.CO;2.

Chow, K. C., K. L. Chan, and A. K. H. Lau, 2002: Generation of Moving Spiral Bands in Tropical Cyclones. *J. Atmos. Sci.*, **59**, 2930–2950, doi:10.1175/1520-0469(2002)059<2930:GOMSBI>2.0.CO;2.

Corbosiero, K. L., and J. Molinari, 2003: The Relationship between Storm Motion, Vertical Wind Shear, and Convective Asymmetries in Tropical Cyclones. *J. Atmos. Sci.*, **60**, 366–376, doi:10.1175/1520-0469(2003)060<0366:TRBSMV>2.0.CO;2. http://journals.ametsoc.org/doi/abs/10.1175/1520-0469%282003%29060%3C0366%3ATRBSMV%3E2.0.CO%3B2.

——, ——, A. R. Aiyyer, and M. L. Black, 2006: The Structure and Evolution of Hurricane Elena (1985). Part II: Convective Asymmetries and Evidence for Vortex Rossby Waves. *Mon. Weather Rev.*, **134**, 3073–3091, doi:10.1175/MWR3250.1.

Cotto, A., I. Gonzalez, and H. E. Willoughby, 2015: Synthesis of vortex Rossby waves. Part I: Episodically forced waves in the inner waveguide. *J. Atmos. Sci.*, **72**, 3940–3957, doi:10.1175/JAS-D-15-0004.1.

Crum, T. D., and R. L. Alberty, 1993: The WSR-88D and the WSR-88D Operational Support Facility. *Bull. Am. Meteorol. Soc.*, **74**, 1669–1687, doi:10.1175/1520-0477(1993)074<1669:TWATWO>2.0.CO;2.

Curry, R. A., 2010: Dual-Doppler analysis of Hurricane Isabel (2003) as it made landfall. School of Meteorology, University of Oklahoma, 80 pp.

DeHart, J. C., R. A. Houze, and R. F. Rogers, 2014: Quadrant Distribution of Tropical Cyclone Inner-Core Kinematics in Relation to Environmental Shear. *J. Atmos. Sci.*, **71**, 2713–2732, doi:10.1175/JAS-D-13-0298.1. http://journals.ametsoc.org/doi/abs/10.1175/JAS-D-13-0298.1.

Didlake, A. C., and R. A. Houze, 2013: Dynamics of the Stratiform Sector of a Tropical Cyclone Rainband. *J. Atmos. Sci.*, **70**, 1891–1911, doi:10.1175/JAS-D-12-0245.1. http://journals.ametsoc.org/doi/abs/10.1175/JAS-D-12-0245.1.

——, G. M. Heymsfield, L. Tian, and S. R. Guimond, 2015: The coplane analysis technique for three-dimensional wind retrieval using the HIWRAP Airborne Doppler Radar. *J. Appl. Meteorol. Climatol.*, **54**, 605–623, doi:10.1175/JAMC-D-14-0203.1.

Doviak, R. J., V. Bringi, A. V. Ryzhkov, A. Zahrai, and D. Zrnić, 2000: Considerations for polarimetric upgrades to operational WSR-88D radars. *J. Atmos. Ocean. Technol.*, **17**, 257–278, doi:10.1175/1520-0426(2000)017<0257:CFPUTO>2.0.CO;2.

Elliott, W. P., 1958: The growth of the atmospheric internal boundary layer. *Eos, Trans. Am. Geophys. Union*, **39**, 1048–1054, doi:10.1029/TR039i006p01048.

Emanuel, K., 2018: 100 Years of Progress in Tropical Cyclone Research. *Meteorol. Monogr.*, AMSMONOGRAPHS-D-18-0016.1, doi:10.1175/AMSMONOGRAPHS-D-18-0016.1. http://journals.ametsoc.org/doi/10.1175/AMSMONOGRAPHS-D-18-0016.1.

Feng, Y. C., and M. M. Bell, 2019: Microphysical Characteristics of an Asymmetric Eyewall in Major Hurricane Harvey (2017). *Geophys. Res. Lett.*, **46**, 461–471, doi:10.1029/2018GL080770.

Fernandez-Caban, P. L., and Coauthors, 2019: Observing Hurricane Harvey's eyewall at landfall. *Bull. Am. Meteorol. Soc.*, doi:10.1175/BAMS-D-17-0237.1.

Fischer, M. S., R. F. Rogers, and P. D. Reasor, 2020: The Rapid Intensification and Eyewall Replacement Cycles of Hurricane Irma (2017). *Mon. Weather Rev.*, **148**, 981–1004, doi:10.1175/mwr-d-19-0185.1.

Franklin, C. N., G. J. Holland, and P. T. May, 2006: Mechanisms for the generation of mesoscale vorticity features in tropical cyclone rainbands. *Mon. Weather Rev.*, **134**, 2649–2669, doi:10.1175/MWR3222.1.

Franklin, J. L., M. L. Black, and K. Valde, 2003: GPS Dropwindsonde Wind Profiles in Hurricanes and Their Operational Implications. *Weather Forecast.*, **18**, 32–44, doi:10.1175/1520-0434(2003)018<0032:GDWPIH>2.0.CO;2.

Gall, R., J. Franklin, F. Marks, E. N. Rappaport, and F. Toepfer, 2013: The hurricane forecast improvement project. *Bull. Am. Meteorol. Soc.*, **94**, 329–343, doi:10.1175/BAMS-D-12-00071.1.

Gao, C., and P. Zhu, 2016: Vortex Rossby wave propagation in baroclinic tropical cyclone-like vortices. *Geophys. Res. Lett.*, **43**, 12,578-12,589, doi:10.1002/2016GL071662.

Garratt, J. R., 1990: The internal boundary layer - A review. *Boundary-Layer Meteorol.*, **50**, 171–203, doi:10.1007/BF00120524.

Giammanco, I. M., J. L. Schroeder, and M. D. Powell, 2012: GPS Dropwindsonde and WSR-88D Observations of Tropical Cyclone Vertical Wind Profiles and Their Characteristics. *Weather Forecast.*, **28**, 77–99, doi:10.1175/waf-d-11-00155.1.

——, ——, F. J. Masters, P. J. Vickery, R. J. Krupar, and J. A. Balderrama, 2016: Influences on observed near-surface gust factors in landfalling U.S. Gulf coast hurricanes: 2004-08. *J.*

Appl. Meteorol. Climatol., **55**, 2587–2611, doi:10.1175/JAMC-D-16-0053.1.

Gopalakrishnan, S., Q. Liu, and T. Marchok, 2011: Hurricane Weather Research and Forecasting (HWRF) model: 2011 scientific documentation. *Dev. Testbed Cent.*, 1–81. http://www.dtcenter.org/HurrWRF/users/docs/scientific_documents/HWRFScientificDocumentation_August2011.pdf.

Guimond, S. R., P. D. Reasor, G. M. Heymsfield, and M. M. McLinden, 2020: the Dynamics of Vortex Rossby Waves and Secondary Eyewall Development in Hurricane Matthew (2016): New Insights From Radar Measurements. *J. Atmos. Sci.*, 2349–2374, doi:10.1175/jas-d-19-0284.1.

Guinn, T. A., and W. H. Schubert, 1993: Hurricane Spiral Bands. *J. Atmos. Sci.*, **50**, 3380–3403.

Hall, J. D., M. Xue, L. Ran, and L. M. Leslie, 2013: High-Resolution Modeling of Typhoon Morakot (2009): Vortex Rossby Waves and Their Role in Extreme Precipitation over Taiwan. *J. Atmos. Sci.*, **70**, 163–186, doi:10.1175/JAS-D-11-0338.1.

Halverson, J. B., J. Simpson, G. Heymsfield, H. Pierce, T. Hock, and L. Ritchie, 2006: Warm Core Structure of Hurricane Erin Diagnosed from High Altitude Dropsondes during CAMEX-4. *J. Atmos. Sci.*, **63**, 309–324, doi:10.1175/JAS3596.1. http://journals.ametsoc.org/doi/abs/10.1175/JAS3596.1.

Helmus, J. J., and S. M. Collis, 2016: The Python ARM Radar Toolkit (Py-ART), a Library for Working with Weather Radar Data in the Python Programming Language. *J. Open Res. Softw.*, **4**, e25, doi:10.5334/jors.119.

Hirth, B. D., J. L. Schroeder, C. C. Weiss, D. A. Smith, and M. I. Biggerstaff, 2012: Research Radar Analyses of the Internal Boundary Layer over Cape Canaveral, Florida, during the Landfall of Hurricane Frances (2004). *Weather Forecast.*, **27**, 1349–1372,

doi:10.1175/WAF-D-12-00014.1.

Hock, T. F., and J. L. Franklin, 1999: The NCAR GPS dropwindesonde. *Bull. Am. Meteorol. Soc.*, **80**, 407–420, doi:10.1175/1520-0477(1999)080<0407:TNGD>2.0.CO;2.

Hogsett, W., and D.-L. Zhang, 2009: Numerical Simulation of Hurricane Bonnie (1998). Part III: Energetics. *J. Atmos. Sci.*, **66**, 2678–2696, doi:10.1175/2009JAS3087.1.

Holton, J. R., and G. J. Hakim, 2013: *An Introduction to Dynamic Meteorology*. 5th ed. Elsevier, Waltham, MA, 552 pp.

Homeyer, C. R., and Coauthors, 2021: Polarimetric signatures in landfalling tropical cyclones. *Mon. Weather Rev.*, **149**, 131–154, doi:10.1175/MWR-D-20-0111.1.

Houze, R. A., 2010: Clouds in Tropical Cyclones. *Mon. Weather Rev.*, **138**, 293–344, doi:10.1175/2009MWR2989.1. http://journals.ametsoc.org/doi/abs/10.1175/2009MWR2989.1.

——, F. D. Marks, and R. A. Black, 1992: Dual-aircraft investigation of the inner core of Hurricane Norbert. Part II: Mesoscale distribution of ice particles. *J. Atmos. Sci.*, **49**, 943–963, doi:10.1175/1520-0469(1992)049<0943:DAIOTI>2.0.CO;2. http://journals.ametsoc.org/doi/abs/10.1175/1520-0469(1992)049%3C0943:DAIOTI%3E2.0.CO;2.

Hristova-Veleva, S., and Coauthors, 2021: Impact of Microphysical Parameterizations on Simulated Hurricanes—Using Multi-Parameter Satellite Data to Determine the Particle Size Distributions that Produce Most Realistic Storms. *Atmosphere (Basel).*, **12**, 154, doi:10.3390/atmos12020154.

Huang, Z., D. V. Rosowsky, and P. R. Sparks, 2001: Hurricane simulation techniques for the evaluation of wind-speeds and expected insurance losses. *J. Wind Eng. Ind. Aerodyn.*, **89**,

605–617, doi:10.1016/S0167-6105(01)00061-7.

Janic, Z. I., 1990: The step-mountain coordinate: physical package. *Mon. Wea. Rev.*, **118**, 1429–1443.

Jorgensen, D. P., and P. T. Willis, 1982: A Z-R Relationship for Hurricanes. *J. Appl. Meteorol.*, **21**, 356–366, doi:10.1175/1520-0450(1982)021<0356:AZRRFH>2.0.CO;2.

——, E. J. Zipser, M. A. LeMone, D. P. Jorgensen, E. J. Zipser, and M. A. LeMone, 1985: Vertical Motions in Intense Hurricanes. *J. Atmos. Sci.*, **42**, 839–856, doi:10.1175/1520-0469(1985)042<0839:VMIIH>2.0.CO;2. http://journals.ametsoc.org/doi/abs/10.1175/1520-0469%281985%29042%3C0839%3AVMIIH%3E2.0.CO%3B2.

——, C. L. Ziegler, E. N. Rasmussen, A. S. Goldstein, and A. A. Alford, 2017: Improvements to the NOAA P-3 Airborne Doppler Tail-Mounted Radar: Super Cell Observations from VORTEX-Southeast. *38th Conf. on Radar Meteor.*, Chicago, IL, Amer. Meteor. Soc.

Judt, F., and S. S. Chen, 2010: Convectively Generated Potential Vorticity in Rainbands and Formation of the Secondary Eyewall in Hurricane Rita of 2005. *J. Atmos. Sci.*, **67**, 3581–3599, doi:10.1175/2010JAS3471.1. http://journals.ametsoc.org/doi/abs/10.1175/2010JAS3471.1.

Kepert, J., 2001: The Dynamics of Boundary Layer Jets within the Tropical Cyclone Core . Part I : Linear Theory. *J. Atmos. Sci.*, **58**, 2469–2484, doi:10.1175/1520-0469(2001)058<2469:TDOBLJ>2.0.CO;2.

Knight, R. I., and F. Khalid, 2015: Evaluation of the potential of friction surface analysis in modelling hurricane wind damage in an urban environment. *Nat. Hazards*, **76**, 891–911, doi:10.1007/s11069-014-1527-3.

Knupp, K. R., J. Walters, and M. Biggerstaff, 2006: Doppler Profiler and Radar Observations of

Boundary Layer Variability during the Landfall of Tropical Storm Gabrielle. *J. Atmos. Sci.*, **63**, 234–251, doi:10.1175/JAS3608.1. http://journals.ametsoc.org/doi/abs/10.1175/JAS3608.1.

Ko, M. C., F. D. Marks, G. J. Alaka, and S. G. Gopalakrishnan, 2020: Evaluation of Hurricane Harvey (2017) rainfall in deterministic and probabilistic HWRF forecasts. *Atmosphere (Basel).*, **11**, 1–17, doi:10.3390/atmos11060666.

Kosiba, K. A., and J. Wurman, 2014: Finescale dual-Doppler analysis of hurricane boundary layer structures in hurricane Frances (2004) at landfall. *Mon. Weather Rev.*, **142**, 1874–1891, doi:10.1175/MWR-D-13-00178.1.

——, ——, F. J. Masters, and P. Robinson, 2013: Mapping of Near-Surface Winds in Hurricane Rita Using Finescale Radar, Anemometer, and Land-Use Data. *Mon. Weather Rev.*, **141**, 4337–4349, doi:10.1175/MWR-D-12-00350.1. http://journals.ametsoc.org/doi/abs/10.1175/MWR-D-12-00350.1.

Krupar, R. J., J. L. Schroeder, D. A. Smith, S.-L. Kang, and S. Lorsolo, 2016: A Comparison of ASOS Near-Surface Winds and WSR-88D-Derived Wind Speed Profiles Measured in Landfalling Tropical Cyclones. *Weather Forecast.*, **31**, 1343–1361, doi:10.1175/WAF-D-15-0162.1. http://journals.ametsoc.org/doi/10.1175/WAF-D-15-0162.1.

Laurencin, C. N., A. C. Didlake, S. D. Loeffler, M. R. Kumjian, and G. M. Heymsfield, 2020: Hydrometeor Size Sorting in the Asymmetric Eyewall of Hurricane Matthew (2016). *J. Geophys. Res. Atmos.*, **125**, 1–19, doi:10.1029/2020JD032671.

Lee, W.-C., and F. D. Marks, 2000: Tropical cyclone kinematic structure retrieved from single-Doppler radar observations. Part II: The GBVTD-simplex center finding algorithm. *Mon. Weather Rev.*, **128**, 1925–1936, doi:10.1175/1520-

0493(2000)128<1925:TCKSRF>2.0.CO;2.
http://journals.ametsoc.org/doi/abs/10.1175/1520-0493(2000)128%3C1925:TCKSRF%3E2.0.CO;2%5Cnhttp://journals.ametsoc.org/doi/pdf/10.1175/1520-0493(2000)128%3C1925:TCKSRF%3E2.0.CO;2.

——, B. Jou, P.-L. Chang, and S.-M. Deng, 1999: Tropical cyclone kinematic structure retrieved from single-Doppler radar observations. Part I: Interpretation of Doppler velocity patterns and the GBVTD technique. *Mon. Weather Rev.*, **127**, 2419–2440, doi:10.1175/1520-0493(1999)127<2419:TCKSRF>2.0.CO;2.
http://journals.ametsoc.org/doi/full/10.1175/1520-0493(1999)127%3C2419:TCKSRF%3E2.0.CO;2.

Leighton, H., S. Gopalakrishnan, J. A. Zhang, R. F. Rogers, Z. Zhang, and V. Tallapragada, 2018: Azimuthal distribution of deep convection, environmental factors, and tropical cyclone rapid intensification: A perspective from HWRF ensemble forecasts of Hurricane Edouard (2014). *J. Atmos. Sci.*, **75**, 275–295, doi:10.1175/JAS-D-17-0171.1.

Li, L. ., G. . Heymsfield, J. . Carswell, D. . Schaubert, J. . Creticos, and M. . Vega, 2008: High-altitude imaging wind and rain airborne radar (HIWRAP). *Int. Geosci. Remote Sens. Symp.*, **3**, III354–III357, doi:10.1109/IGARSS.2008.4779356.

Lorsolo, S., J. L. Schroeder, P. Dodge, and F. Marks, 2008: An Observational Study of Hurricane Boundary Layer Small-Scale Coherent Structures. *Mon. Weather Rev.*, **136**, 2871–2893, doi:10.1175/2008MWR2273.1.
http://journals.ametsoc.org/doi/abs/10.1175/2008MWR2273.1.

Lu, X., and X. Wang, 2019: Improving Hurricane analyses and predictions with TCI, IFEX field campaign observations, and CIMSS AMVs using the advanced hybrid data assimilation

system for HWRF. Part I: What is missing to capture the rapid intensification of Hurricane Patricia (2015) . *Mon. Weather Rev.*, **147**, 1351–1373, doi:10.1175/MWR-D-18-0202.1.

——, and ——, 2020: Improving hurricane analyses and predictions with TCI, IFEX field campaign observations, and CIMSS AMVs using the advanced hybrid data assimilation system for HWRF. Part II: Observation impacts on the analysis and prediction of Patricia (2015). *Mon. Weather Rev.*, **148**, 1407–1430, doi:10.1175/MWR-D-19-0075.1.

——, ——, M. Tong, and V. Tallapragada, 2017: GSI-based, continuously cycled, dual-resolution hybrid ensemble-variational data assimilation system for HWRF: System description and experiments with edouard (2014). *Mon. Weather Rev.*, **145**, 4877–4898, doi:10.1175/MWR-D-17-0068.1.

MacDonald, N. J., 1968: The evidence for the existence of Rossby-like waves in the hurricane vortex. *Tellus*, **20**, 138–150, doi:10.1111/j.2153-3490.1968.tb00358.x.

Marks, F. D., and R. A. Houze, 1987: Inner Core Structure of Hurricane Alicia from Airborne Doppler Radar Observations. *J. Atmos. Sci.*, **44**, 1296–1317, doi:10.1175/1520-0469(1987)044<1296:ICSOHA>2.0.CO;2. http://journals.ametsoc.org/doi/abs/10.1175/1520-0469(1987)044%3C1296:ICSOHA%3E2.0.CO;2.

McWilliams, J. C., L. P. Graves, and M. T. Montgomery, 2003: A Formal Theory for Vortex Rossby Waves and Vortex Evolution. *Geophys. Astrophys. Fluid Dyn.*, **97**, 275–309, doi:10.1080/0309192031000108698.

Menelaou, K., and M. K. Yau, 2014: On the role of asymmetric convective bursts to the problem of hurricane intensification. Radiation of vortex Rossby waves and wave-mean flow interactions. *J. Atmos. Sci.*, 140212115924008, doi:10.1175/JAS-D-13-0343.1.

http://journals.ametsoc.org/doi/abs/10.1175/JAS-D-13-0343.1.

Ming, J., J. A. Zhang, R. F. Rogers, F. D. Marks, Y. Wang, and N. Cai, 2014: Multiplatform observations of boundary layer structure in the outer rainbands of landfalling typhoons. *J. Geophys. Res. Atmos.*, **119**, 7799–7814, doi:doi:10.1002/2014JD021637.

Möller, J. D., and M. T. Montgomery, 2000: Tropical Cyclone Evolution via Potential Vorticity Anomalies in a Three-Dimensional Balance Model. *J. Atmos. Sci.*, **57**, 3366–3387, doi:10.1175/1520-0469(2000)057<3366:tcevpv>2.0.co;2.

Montgomery, M. T., and R. J. Kallenbach, 1997: A theory for vortex Rossby-waves and its application to spiral bands and intensity changes in hurricanes. *Quart. J. Roy. Meteor. Soc.*, **123**, 435–465, doi:10.1002/qj.49712353810. http://dx.doi.org/10.1002/qj.49712353810.

——, and R. K. Smith, 2016: Recent developments in the fluid dynamics of tropical cyclones. 1–23.

——, J. A. Zhang, and R. K. Smith, 2014: An analysis of the observed low-level structure of rapidly intensifying and mature hurricane Earl (2010). *Q. J. R. Meteorol. Soc.*, **140**, 2132–2146, doi:10.1002/qj.2283.

——, S. F. Abarca, and R. K. Smith, 2015: On the applicability of linear , axisymmetric dynamics in intensifying and mature tropical cyclones. **9**, 1–9.

Moon, Y., and D. S. Nolan, 2015: Spiral Rainbands in a Numerical Simulation of Hurricane Bill (2009). Part II: Propagation of Inner Rainbands. *J. Atmos. Soc.*, 141016121051006, doi:10.1175/JAS-D-14-0056.1. http://journals.ametsoc.org/doi/abs/10.1175/JAS-D-14-0056.1.

Morrison, I., S. Businger, F. Marks, P. Dodge, and J. A. Businger, 2005: An observational case for the prevalence of roll vortices in the hurricane boundary layer. *J. Atmos. Sci.*, **62**, 2662–

2673, doi:10.1175/JAS3508.1.

Naftel, J. C., 2009: *NASA Global Hawk: A New Tool for Earth Science Research*. 13 pp. http://ntrs.nasa.gov/archive/nasa/casi.ntrs.nasa.gov/20090023138.pdf.

NOAA, O. for C. M., 2018: National Land Cover Database. www.coast.noaa.gov/ccapftp (Accessed August 20, 2006).

Nolan, D. S., Y. Moon, and D. P. Stern, 2007: Tropical Cyclone Intensification from Asymmetric Convection: Energetics and Efficiency. *J. Atmos. Sci.*, **64**, 3377–3405, doi:10.1175/JAS3988.1. http://journals.ametsoc.org/doi/abs/10.1175/JAS3988.1.

——, D. P. Stern, and J. A. Zhang, 2009a: Evaluation of planetary boundary layer parameterizations in tropical cyclones by comparison of in situ observations and high-resolution simulations of Hurricane Isabel (2003). Part II: Inner-core boundary layer and eyewall structure. *Mon. Weather Rev.*, **137**, 3675–3698, doi:10.1175/2009MWR2786.1.

——, J. A. Zhang, and D. P. Stern, 2009b: Evaluation of planetary boundary layer parameterizations in tropical cyclones by comparison of in situ observations and high-resolution simulations of Hurricane Isabel (2003). Part I: Initialization, maximum winds, and the outer-core boundary layer. *Mon. Weather Rev.*, **137**, 3651–3674, doi:10.1175/2009MWR2785.1.

——, B. D. McNoldy, and J. Yunge, 2021a: Evaluation of the Surface Wind Field over Land in WRF Simulations of Hurricane Wilma (2005). Part I: Model Initialization and Simulation Validation. *Mon. Weather Rev.*, 1–49, doi:10.1175/mwr-d-20-0199.1.

——, ——, ——, F. J. Masters, and I. M. Giammanco, 2021b: Evaluation of the Surface Wind Field over Land in WRF Simulations of Hurricane Wilma (2005). Part II: Surface Winds, Inflow Angles, and Boundary Layer Profiles. *Mon. Weather Rev.*, 1–47, doi:10.1175/mwr-

d-20-0201.1.

Oye, R. C., C. Mueller, and S. Smith, 1995: Software for radar translation, visualization, editing, and interpolation. *27th Conference on Radar Meteorology*, Vail, CO, Amer. Meteor. Soc., 359–361.

Pazmany, A. L., J. B. Mead, H. B. Bluestein, J. C. Snyder, and J. B. Houser, 2013: A mobile rapid-scanning X-band polarimetric (RaXPol) doppler radar system. *J. Atmos. Ocean. Technol.*, **30**, 1398–1413, doi:10.1175/JTECH-D-12-00166.1.

Potvin, C. K., D. Betten, L. J. Wicker, K. L. Elmore, and M. I. Biggerstaff, 2012: 3DVAR vs. traditional dual-Doppler wind retrievals of a simulated supercell thunderstorm. *Mon. Weather Rev.*, 120525114116000, doi:10.1175/MWR-D-12-00063.1.

Powell, M. D., 1993: Wind Measurement and Archival under the Automated Surface Observing System (ASOS): User Concerns and Opportunity for Improvement. *Bull. Am. Meteorol. Soc.*, **74**, 615–623, doi:10.1175/1520-0477(1993)074<0615:WMAAUT>2.0.CO;2. http://dx.doi.org/10.1175/1520-0477(1993)074%3C0615:WMAAUT%3E2.0.CO%5Cnhttp://2.

——, and S. H. Houston, 1996: Hurricane Andrew's Landfall in South Florida. Part II: Surface Wind Fields and Potential Real-Time Applications. *Weather Forecast.*, **11**, 329–349, doi:10.1175/1520-0434(1996)011<0329:HALISF>2.0.CO;2.

——, and ——, 1998: Surface Wind Fields of 1995 Hurricanes Erin, Opal, Luis, Marilyn, and Roxanne at Landfall. *Mon. Weather Rev.*, **126**, 1259–1273, doi:10.1175/1520-0493(1998)126<1259:SWFOHE>2.0.CO;2.

——, ——, and T. a. Reinhold, 1996: Hurricane Andrew's Landfall in South Florida. Part I: Standardizing Measurements for Documentation of Surface Wind Fields. *Weather*

Forecast., **11**, 304–328, doi:10.1175/1520-0434(1996)011<0304:HALISF>2.0.CO;2.

——, P. J. Vickery, and T. A. Reinhold, 2003: Reduced drag coefficient for high wind speeds in tropical cyclones. *Nature*, **422**, 279–283, doi:10.1038/nature01481.

Rappaport, E. N., 2014: Fatalities in the United States from Atlantic Tropical Cyclones: New Data and Interpretation. *Bull. Am. Meteorol. Soc.*, **95**, 341–346, doi:10.1175/BAMS-D-12-00074.1. http://journals.ametsoc.org/doi/abs/10.1175/BAMS-D-12-00074.1.

Reasor, P. D., M. T. Montgomery, F. D. Marks, and J. F. Gamache, 2000: Low-Wavenumber Structure and Evolution of the Hurricane Inner Core Observed by Airborne Dual-Doppler Radar. *Mon. Weather Rev.*, **128**, 1653–1680, doi:10.1175/1520-0493(2000)128<1653:LWSAEO>2.0.CO;2.

Rogers, R. F., S. Lorsolo, P. Reasor, J. Gamache, and F. Marks, 2012: Multiscale Analysis of Tropical Cyclone Kinematic Structure from Airborne Doppler Radar Composites. *Mon. Weather Rev.*, **140**, 77–99, doi:10.1175/MWR-D-10-05075.1.

——, P. Reasor, and S. Lorsolo, 2013: Airborne Doppler Observations of the Inner-Core Structural Differences between Intensifying and Steady-State Tropical Cyclones. *Mon. Weather Rev.*, **141**, 2970–2991, doi:10.1175/MWR-D-12-00357.1. http://journals.ametsoc.org/doi/abs/10.1175/MWR-D-12-00357.1.

——, and Coauthors, 2017: Rewriting the tropical record books: The extraordinary intensification of Hurricane Patricia (2015). *Bull. Am. Meteorol. Soc.*, **98**, 2091–2112, doi:10.1175/BAMS-D-16-0039.1.

Savelyev, S. A., and P. A. Taylor, 2005: Internal boundary layers: I. Height formulae for neutral and diabatic flows. *Boundary-Layer Meteorol.*, **115**, 1–25, doi:10.1007/s10546-004-2122-z.

Schroeder, J., B. Edwards, and I. Giammanco, 2009: Observed tropical cyclone wind flow

characteristics. *Wind Struct.*, **12**, doi:10.12989/was.2009.12.4.349.

Sibson, R., 1981: A brief description of natual neighbor interpolation. *Interpreting Multivariate Data*, John Wiley, 21–36.

Smith, R. K., and M. T. Montgomery, 2014: On the existence of the logarithmic surface layer in the inner core of hurricanes. *Q. J. R. Meteorol. Soc.*, **140**, 72–81, doi:10.1002/qj.2121.

——, J. A. Zhang, and M. T. Montgomery, 2017: The dynamics of intensification in a Hurricane Weather Research and Forecasting simulation of Hurricane Earl (2010). *Q. J. R. Meteorol. Soc.*, **143**, 293–308, doi:10.1002/qj.2922.

Sparks, P. R., S. D. Schiff, and T. A. Reinhold, 1994: Wind damage to envelopes of houses and consequent insurance losses. *J. Wind Eng. Ind. Aerodyn.*, **53**, 145–155, doi:10.1016/0167-6105(94)90023-X.

Stern, D. P., G. H. Bryan, and S. D. Aberson, 2016: Extreme Low-Level Updrafts and Wind Speeds Measured by Dropsondes in Tropical Cyclones. *Mon. Weather Rev.*, **144**, 2177–2204, doi:10.1175/MWR-D-15-0313.1. http://journals.ametsoc.org/doi/10.1175/MWR-D-15-0313.1.

Stewart, S. R., 2017: National Hurricane Center Tropical Cyclone Report: Hurricane Matthew (AL 142016) 28 Septmeber - 9 October 2016. 1–32. http://www.nhc.noaa.gov/data/tcr/AL142016_Matthew.pdf.

Tang, X., and Z. Tan, 2006: Boundary-layer wind structure in a landfalling tropical cyclone. *Adv. Atmos. Sci.*, **23**, 737–749, doi:10.1007/s00376-006-0737-3.

Torres, S. M., Y. F. Dubel, and D. S. Zrnić, 2004: Design, implementation, and demonstration of a staggered PRT algorithm for the WSR-88D. *J. Atmos. Ocean. Technol.*, **21**, 1389–1399, doi:10.1175/1520-0426(2004)021<1389:DIADOA>2.0.CO;2.

Tuleya, R. E., M. DeMaria, and R. J. Kuligowski, 2007: Evaluation of GFDL and simple statistical model rainfall forecasts for U.S. landfalling tropical storms. *Weather Forecast.*, **22**, 56–70, doi:10.1175/WAF972.1.

UCAR/NCAR, 2005: *NSF/NCAR GV HIAPER Aircraft*. http://doi.org/10.5065/D6DR2SJP.

Uhlhorn, E. W., and P. G. Black, 2003: Verification of remotely sensed sea surface winds in hurricanes. *J. Atmos. Ocean. Technol.*, **20**, 99–116, doi:10.1175/1520-0426(2003)020<0099:VORSSS>2.0.CO;2.

Vickery, P. J., D. Wadhera, M. D. Powell, and Y. Chen, 2009: A hurricane boundary layer and wind field model for use in engineering applications. *J. Appl. Meteorol. Climatol.*, **48**, 381–405, doi:10.1175/2008JAMC1841.1.

Vukicevic, T., A. Aksoy, P. Reasor, S. D. Aberson, K. J. Sellwood, and F. Marks, 2013: Joint Impact of Forecast Tendency and State Error Biases in Ensemble Kalman Filter Data Assimilation of Inner-Core Tropical Cyclone Observations. *Mon. Weather Rev.*, **141**, 2992–3006, doi:10.1175/MWR-D-12-00211.1. http://journals.ametsoc.org/doi/abs/10.1175/MWR-D-12-00211.1.

Wakimoto, R. M., and R. Srivastava, 2017: *Radar and atmospheric science: A collection of essays in honor of david atlas*. 1716 pp.

——, H. V. Murphey, D. C. Dowell, and H. B. Bluestein, 2003: The Kellerville Tornado during VORTEX: Damage Survey and Doppler Radar Analyses. *Mon. Weather Rev.*, **131**, 2197–2221, doi:10.1175/1520-0493(2003)131<2197:TKTDVD>2.0.CO;2.

Wang, W., B. Liu, L. Zhu, Z. Zhang, A. Mehra, V. Tallapragada, and W. Wang, 2021: A New Horizontal Mixing-Length Formulation for Numerical Simulations of Tropical Cyclones. *Weather Forecast.*, doi:10.1175/WAF-D-20-0134.1.

Wang, X., D. Parrish, D. Kleist, and J. Whitaker, 2013: GSI 3Dvar-based ensemble-variational hybrid data assimilation for NCEP global forecast system: Single-resolution experiments. *Mon. Weather Rev.*, **141**, 4098–4117, doi:10.1175/MWR-D-12-00141.1.

Wang, Y., 2002a: Vortex Rossby Waves in a Numerically Simulated Tropical Cyclone. Part I: Overall Structure, Potential Vorticity, and Kinetic Energy Budgets. *J. Atmos. Sci.*, **59**, 1213–1238, doi:10.1175/1520-0469(2002)059<1239:VRWIAN>2.0.CO;2.

——, 2002b: Vortex Rossby Waves in a Numerically Simulated Tropical Cyclone. Part II: The Role in Tropical Cyclone Structure and Intensity Changes. *J. Atmos. Sci.*, **59**, 1239–1262, doi:10.1175/1520-0469(2002)059<1239:VRWIAN>2.0.CO;2.

——, 2008: Rapid Filamentation Zone in a Numerically Simulated Tropical Cyclone*. *J. Atmos. Sci.*, **65**, 1158–1181, doi:10.1175/2007JAS2426.1.

Wei, Z., L. Han-Cheng, and D. Zhang, 2010: Mesoscale Barotropic Instability of Vortex Rossby Waves in Tropical Cyclones. *Adv. Atmos. Sci.*, **27**, 243–252, doi:10.1007/s00376-009-8183-7.1.Introduction. http://link.springer.com/article/10.1007/s00376-009-8183-7.

Weiss, C. C., and J. L. Schroeder, 2008: StickNet: A New Portable Rapidly Deployable Surface Observation System. *Bull. Am. Meteorol. Soc.*, **89**, 1502–1503, doi:https://doi.org/10.1175/1520-0477-89.10.1469.

Williams, G. J., 2019: Idealized Simulations of the Inner Core Boundary Layer Structure in a Landfalling Tropical Cyclone. Part I: Kinematic Structure. *Trop. Cyclone Res. Rev.*, **8**, 47–67, doi:10.1016/j.tcrr.2019.07.006. http://dx.doi.org/10.1016/j.tcrr.2019.07.006.

Willoughby, H. E., 1977: Inertia buoyancy waves in hurricanes. *J. Atmos. Sci.*, **34**, 1028–1039. http://adsabs.harvard.edu/abs/1977JAtS...34.1028W.

——, and M. B. Chelmow, 1982: Objective Determination of Hurricane Tracks from Aircraft

Observations. *Mon. Weather Rev.*, **110**, 1298–1305, doi:10.1175/1520-0493(1982)110<1298:odohtf>2.0.co;2.

Wingo, S. M., and K. R. Knupp, 2016: Kinematic Structure of Mesovortices in the Eyewall of Hurricane Ike (2008) Derived from Ground-Based Dual-Doppler Analysis. *Mon. Weather Rev.*, **144**, 4245–4263, doi:10.1175/MWR-D-16-0085.1. http://journals.ametsoc.org/doi/10.1175/MWR-D-16-0085.1.

Wurman, J., and J. Winslow, 1998: Intense sub-kilometer-scale boundary layer rolls observed in hurricane Fran. *Science (80-.).*, **280**, 555–557, doi:10.1126/science.280.5363.555.

——, and K. Kosiba, 2018: The role of small-scale vortices in enhancing surface winds and damage in Hurricane Harvey (2017). *Mon. Weather Rev.*, MWR-D-17-0327.1, doi:10.1175/MWR-D-17-0327.1. http://journals.ametsoc.org/doi/10.1175/MWR-D-17-0327.1.

Zhang, J. A., and M. T. Montgomery, 2012: Observational Estimates of the Horizontal Eddy Diffusivity and Mixing Length in the Low-Level Region of Intense Hurricanes. *J. Atmos. Sci.*, **69**, 1306–1316, doi:10.1175/JAS-D-11-0180.1.

——, and F. D. Marks, 2015: Effects of Horizontal Diffusion on Tropical Cyclone Intensity Change and Structure in Idealized Three-Dimensional Numerical Simulations. **143**, 3981–3995, doi:10.1175/MWR-D-14-00341.1.

——, R. F. Rogers, D. S. Nolan, and F. D. Marks, 2011: On the Characteristic Height Scales of the Hurricane Boundary Layer. *Mon. Weather Rev.*, **139**, 2523–2535, doi:10.1175/MWR-D-10-05017.1. http://journals.ametsoc.org/doi/abs/10.1175/MWR-D-10-05017.1.

——, ——, P. D. Reasor, E. W. Uhlhorn, and F. D. Marks, 2013: Asymmetric Hurricane Boundary Layer Structure from Dropsonde Composites in Relation to the Environmental

Vertical Wind Shear. *Mon. Weather Rev.*, **141**, 3968–3984, doi:10.1175/mwr-d-12-00335.1.

——, D. S. Nolan, R. F. Rogers, and V. Tallapragada, 2015: Evaluating the impact of improvements in the boundary layer parameterization on hurricane intensity and structure forecasts in HWRF. *Mon. Weather Rev.*, **143**, 3136–3155, doi:10.1175/MWR-D-14-00339.1.

——, F. D. Marks, J. A. Sippel, R. F. Rogers, X. Zhang, S. G. Gopalakrishnan, Z. Zhang, and V. Tallapragada, 2018: Evaluating the impact of improvement in the horizontal diffusion parameterization on hurricane prediction in the operational Hurricane Weather Research and Forecast (HWRF) Model. *Weather Forecast.*, **33**, 317–329, doi:10.1175/WAF-D-17-0097.1.